Heinrich Heine
Universität
Düsseldorf

Metabolic Investigations of the Human Liver using Phosphorus-31 Magnetic Resonance Spectroscopy at 3 Tesla

Inaugural-Dissertation

zur Erlangung des Doktorgrades
der Mathematisch-Naturwissenschaftlichen Fakultät
der Heinrich-Heine-Universität Düsseldorf

vorgelegt von

Marc Jonuscheit
aus **Viersen**

Düsseldorf, Juli 2025

aus dem Institut für Klinische Diabetologie des Deutschen Diabetes-Zentrums,
Leibniz-Zentrum für Diabetes-Forschung an der Heinrich-Heine-Universität Düsseldorf
Direktor: Univ. Prof. Dr. Michael Roden

Gedruckt mit der Genehmigung der
Mathematisch-Naturwissenschaftlichen Fakultät der
Heinrich-Heine-Universität Düsseldorf

Berichterstatter:

1. Univ. Prof. Dr. Thomas Heinzel
   Institut für Experimentelle Physik der kondensierten Materie
   Heinrich-Heine-Universität Düsseldorf (HHU)

2. Univ. Prof. Dr. Michael Roden
   Klinik für Endokrinologie und Diabetologie
   Universitätsklinikum Düsseldorf (UKD)
   Heinrich-Heine-Universität Düsseldorf (HHU)
   Deutsches Diabetes-Zentrum Düsseldorf (DDZ)

Tag der mündlichen Prüfung: 17.12.2025

Meinen Eltern.

Acknowledgments

I would like to take this opportunity to thank all those who have supported me in completing this doctoral thesis.

First of all, I would like to thank Prof. Dr. Michael Roden for giving me the opportunity to write my PhD thesis at his institute. I am very grateful for your excellent advice, scientific guidance, and support, which have been continuous over the years. The trust you placed in me has enabled me to develop freely, both personally and academically.

Special thanks go to Prof. Dr. Thomas Heinzel for taking on the supervision of this thesis and for his interest in my work.

Furthermore, I want to thank Prof. Dr. Vera Schrauwen-Hinderling for being my mentor during the past years. Your consistently proven coexistence of professional brilliance and great personality has reliably guided me and will serve as a great role model for me in the future. You always had an open ear for any questions and problems that arose - thank you.

I would also like to thank the entire Metabolic Imaging working group (Benedict Korzekwa, Yuliya Kupriyanova, Filippo Michelotti, Neele Midding, Franziska Paumen and Stefan Wierichs) for their constant, uninterrupted support and assistance during my investigations. I would like to thank Benedict for the many hours we spent together at the scanners and for your long endurance during the measurements. Yuliya, you always infected us with your good humour and created a good atmosphere. I would also like to thank Filippo for his technical help in solving complex problems in the scripts I used. Neele and Franziska, we had a great time with measurements in the early mornings during the routine measurements and mastered them brilliantly. Last but not least, thanks to Stefan for all that fun in the lab and outside of it. We have both grown personally and professionally during this time and have successfully overcome a number of situations together.

I would also like to thank my former colleagues in the group (Jong-Hee Hwang, Andrea Nagel, Maik Rothe, and Frithjof Wickrath). Special thanks to Maik and Frithjof, who inspired me during my early days in the high art of spectroscopy and thus ensured that this fascination has not faded away to this day.

Certainly, none of this would have been possible without my dearest family, my mum, dad, and grandma, who always stood behind me and never doubted me, although I believe they still have no comprehensive idea what I actually do in Düsseldorf. I would not be here today without you. Bernie, I think I speak on behalf of the entire working group when I explicitly thank you here for the delicious cakes that you have kindly baked so often, sometimes even without explicit request, but nobody will ever complain.

Thank you, Bettina, from the bottom of my heart for your emotional support on this long journey. You were always there, and with your positive attitude, you turned every dark day into a bright one. Please excuse the countless times when I did not make it out of the institute on time because I just wanted to finish something (“ens jüss”).

Author's Declaration

I hereby declare that I wrote the dissertation 'Metabolic Investigations of the Human Liver using Phosphorus-31 Magnetic Resonance Spectroscopy at 3 Tesla' independently and without other resources as indicated in according to 'Grundsätze zur Sicherung guter wissenschaftlicher Praxis an der Heinrich-Heine-Universität Düsseldorf'.

Furthermore, I declare that I did not submit this dissertation, either in full or modified, to any other academic institute and did not absolve any promotion trials before.

Friday 11th July, 2025
Date

Marc Jonuscheit

First Authorships

This doctoral thesis is based on the two following publications. Personal contributions and impact factors are listed in the Appendix on page 153.

- M. Jonuscheit, S. Wierichs, M. Rothe, B. Korzekwa, J. Mevenkamp, P. Bobrov, Y. Kupriyanova, M. Roden, and V. B. Schrauwen-Hinderling. "Reproducibility of absolute quantification of adenosine triphosphate and inorganic phosphate in the liver with localized 31P-magnetic resonance spectroscopy at 3-T using different coils," *NMR in Biomedicine*, vol. 37, no. 8, p. e5120, 2024. doi: 10.1002/nbm.5120.
- M. Jonuscheit, B. Korzekwa, M. Schär, J. Mevenkamp, S. Wierichs, P. Bobrov, T. Sarabhai, S. Kahl, M. Roden, and V. B. Schrauwen-Hinderling. "31P-MRS saturation transfer for assessing human hepatic ATP synthesis at clinical field strength," *European Radiology Experimental*, vol. 9, no. 1, p. 51, 2025. doi: 10.1186/s41747-025-00588-9.

Abstract

The liver is a key organ in maintaining overall physiological homeostasis. Being the central hub of glucose and lipid metabolism, it strictly regulates the storage, production, and distribution of glucose and fatty acids. Adenosine triphosphate (ATP), the primary energy currency of the cell, plays a crucial role in biochemical reactions as it represents the moiety providing energy for conversion of substrates. The liver itself is able to generate ATP mainly in the mitochondria of the cells via oxidative ATP synthesis. Understanding hepatic ATP homeostasis in the healthy and diseased state is of critical importance, as changes in ATP concentration and synthesis have been implicated in metabolic disorders, such as metabolic dysfunction-associated steatotic liver disease (MASLD) and diabetes mellitus. For this reason, the need and search for – ideally non-invasive – methods to assess energy metabolism and monitor ATP concentrations in the liver has gained a lot of attention in recent years.

This doctoral thesis used a state of the art clinical magnetic resonance (MR) system in combination with new coil and sequence design to investigate pure hepatic metabolism with focus on the high-energy phosphate (HEP) ATP. In this process, suitable magnetic resonance spectroscopy (MRS) protocols for detection of phosphorus-31 (^{31}P)-metabolites were established. First, a pipeline for assessment of absolute concentrations of main hepatic ^{31}P-metabolites, including ATP and inorganic phosphate (P_i), was established using a three-dimensional localized MRS sequence. In this course, the whole process was performed using the phantom replacement technique and two different surface coils. Afterwards, the reproducibility of the method was tested in an in-vivo study in healthy volunteers. The obtained absolute concentrations with the two surface coils were compared in order to judge whether the established procedure was able to report coil-independent results. Being able to assess physiological concentrations of metabolites paves the way for more advanced methods, which were applied in a second study to obtain metabolic fluxes. Using this method, the ATP synthesis rate of the liver was assessed. For this purpose, an additional MRS method was developed, which included implementation of a saturation pulse to be able to selectively saturate a specific moiety of the ^{31}P-spectrum and evaluate the effects. The saturation sequence was tested in vitro and in vivo before being more broadly applied in a healthy cohort to assess the reproducibility of the method. Furthermore, in order to investigate the sensitivity of the method to detect clinically relevant differences, a second group of people with type 1 diabetes (T1D) was included. Both studies do not only demonstrate a way of non-invasive assessment of hepatic parameters, but also investigate the reproducibility of the respective method, which is of great importance for future application of the techniques in clinical trials.

In the first study, a localized three-dimensional MRS sequence was used to establish a pipeline that allows to report absolute hepatic metabolite concentrations in millimoles per liter (mM). The study employs the phantom replacement technique, which makes use of extensive phantom measurements that mimic the in-vivo measurement and make it possible to correct for any kind of sequence-, coil-, or metabolite-related characteristics and for factors related to the varying geometrical and electrical properties of the volunteer under investigation. In the course of this process, the fitted metabolite amplitudes obtained from the MRS spectrum were corrected

for individual longitudinal relaxation (T_1), the excitation pulse profile of the coil, the spatial excitation and detection field distribution of the coil (sensitivity profile), and the coil loading of the volunteer. Two surface coils differing in both size and geometry were extensively tested with the ultimate aim to evaluate consistency of the results with regard to the obtained concentrations and reproducibility. Whereas one coil was a multi-purpose vendor-provided flat, single-loop surface coil, the second was a newly designed, curved quadrature surface coil explicitly manufactured for application in human liver. In this course, both day-to-day reproducibility and intra-day repeatability were assessed. For the in-vivo part, a cohort of eleven volunteers with a broad range of body mass index (BMI) between 20.6–32.4 kg/m^2 were examined. Eight volunteers underwent measurements on three different days within a week under standardized conditions with both coils to assess day-to-day reproducibility and five of them returned after three months for a fourth measurement in order to examine potential long-term variations. Furthermore, six volunteers were measured in total seven times within one day to gain information on inter-day repeatability (without repositioning) and reproducibility (with repositioning of the volunteer) of the (more sophisticated) quadrature coil, which would be the coil of choice for future experiments. For analysis of hepatic spectra, a custom-written script was established, including prior knowledge, to ensure consistent and reproducible peak fitting. As parameters of quality control, signal-to-noise ratio (SNR) was assessed and the phosphocreatine (PCr) to ATP ratio was used as marker for potential signal contamination from abdominal muscle. Analysis of all obtained spectra was processed in the same way, with the individual coil correction factors being applied with the aim to provide coil-unbiased absolute concentrations.

As result, similar high SNR spectra with mean SNR of 8.2 ± 1.5 (mean ± standard deviation (SD)) for ATP and 7.3 ± 2.3 for P_i were achieved for the single loop and 8.0 ± 1.5 and 6.8 ± 1.9 for the quadrature coil, respectively, in an acquisition time of 13 minutes per spectrum. This was achieved in combination with low signal contamination from muscle, as evaluated by a mean PCr contamination of 18 ± 16% and 25 ± 12% of ATP signal intensity for the two coils, respectively. The comparison of the calculated absolute concentrations of the two coils in the day-to-day measurements yielded similar, and not statistically different, values. Concentrations of 2.31 mM [2.10; 2.53] (mean [95% confidence interval (CI)]) for ATP and 1.73 mM [1.58; 1.87] for P_i were obtained using the single loop and 2.32 mM [2.11; 2.53] and 1.73 mM [1.59; 1.87] for the quadrature surface coil, respectively. The coefficients of variation (CV) of these measurements were 7.3 ± 3.1% vs. 6.7 ± 3.3% for ATP and 8.8 ± 3.4% vs. 10.6 ± 11.3% for P_i, respectively. The similarity of the results indicates the robustness of the method. This was similar for the intra-day measurements of the quadrature coil: Three consecutive acquisitions without repositioning resulted in low CVs of 4.7 ± 2.2% and 6.8 ± 2.1% for ATP and P_i, respectively. Measurements with full repositioning yielded slightly higher CVs of 6.3 ± 5.3% and 7.1 ± 6.1%. All results were comparable for the used coil or positioning of the volunteer, showing that if applied correctly, the phantom replacement technique is a very powerful tool for consistent assessment of tissue concentrations. The results of this study show that the phantom replacement technique is capable of providing coil-independent metabolite concentrations and that coils can be used interchangeably. Although this procedure is usually not likely to be done during an ongoing study, it is sometimes unavoidable due to coil defects or studies that run for many years. The

method further underlines its reliability and suitability for clinical applications and studies on metabolic diseases such as diabetes. The precise measurement of the main hepatic metabolites may help to gain new mechanistic insights into etiology of disease and provides means for monitoring energy metabolism during treatments.

In the second study, a new method was developed and applied to assess hepatic ATP synthesis rates. The overall aim was to develop a robust and reproducible ^{31}P-MRS saturation transfer (ST) technique, which is able to assess the hepatic ATP synthesis rate and is sensitive enough to detect differences in synthesis rates between people with T1D and healthy controls. Furthermore, the new method should be applicable at clinical field strength. This is important for future clinical applicability of the method. The proposed method was able to assess ATP synthesis rates within one session of about 90 minutes without any contamination from skeletal muscle. This was possible due to a two-dimensional localization sequence, which stands in contrast to previous studies where two sessions were required and total measurement times of about two hours were needed, and a lower degree of signal localization was achieved. Importantly, also data on reproducibility were lacking for these methods. First, a vendor-provided two-dimensional localization sequence was extended by implementation of a saturation pulse in front of the sequence. In-vitro experiments were then conducted in order to determine optimal sequence parameters to be capable to continuously saturate specifically the ATP signal. Saturation was achieved using Delays Alternating with Nutations for Tailored Excitation (DANTE) pulse trains, which saturated the ATP resonance with minimal influence on the neighboring signals. Afterwards, the most promising parameters were tested in vivo in two healthy volunteers and the best performing pulse train was used for further experiments. To shorten the total acquisition time, the ten-point inversion recovery (IR) protocol that is usually used in the literature for determination of the apparent longitudinal magnetization of P_i, $T'_{1,Pi}$, was replaced by a five-point saturation recovery protocol, from which the three repetition times (TR) that most robustly described $T'_{1,Pi}$ were assessed. For consistent analysis of spectra, a custom-written analysis script was established which enables simultaneously processing of all spectra of a saturation experiment. This allows for consistent pre-processing of all spectra. For example, the mean phase angle that was applied was identical, minimizing variation due to random factors, allowing a precise estimation of peak differences caused by the presence of saturation. Further, SNR and the PCr/ATP ratio were used as markers for high spectral quality. Additionally, all saturated spectra were analyzed regarding the achieved strength of ATP saturation with the aim of residual ATP <5%. After protocol optimization, nine young, healthy volunteers were examined twice with full repositioning to evaluate the reproducibility of the method and comparison of the obtained synthesis rates with other approaches used in the literature. Using the established protocol, $T'_{1,Pi}$ and the forward rate constant of ATP synthesis k_f were assessed. Finally, the protocol was applied in eight individuals with T1D and a broad age range to test the new protocol regarding its sensitivity to detect differences between a population of healthy volunteers and individuals with chronic disease.

The resulting spectra showed high SNRs with mean values of 12.0 ± 1.9 for ATP and 6.2 ± 1.2 for P_i, respectively, in the mirrored spectra, and negligible contamination from muscle, as indicated by a low PCr/ATP ratio, with the highest ratio being <11%. This confirms successful

signal localization to hepatic tissue. The reproducibility in healthy volunteers showed acceptable CVs with 7.1% for $T'_{1,Pi}$ and 21.3% for k_f, respectively. These values are comparable to CVs reported at ultrahigh field (UHF, 7 T), proving that the ST method can also be applied at clinical field strength. The comparison of controls and T1D showed significantly lower values in T1D, mean k_f was assessed to be 0.34 $^1/_s$ [0.26; 0.42] (mean [95% CI]) and 0.16 $^1/_s$ [0.08; 0.23], $p = .001$, but no difference in $T'_{1,Pi}$ (482 ms [431; 533] vs. 517 ms [449; 585], $p = .340$, respectively), was found. Performing the absolute quantification protocol in a separate measurement, as described in the first study, one is able to report the forward ATP synthesis rate F_{ATP}, which amounted 35.3 $^{mM}/_{min}$ [27.3; 43.3] in controls and 16.4 $^{mM}/_{min}$ [8.2; 24.7], $p = .002$, in T1D, respectively. All significant differences remained, even after correction for sex, age, and BMI. The results of this study show that the newly developed method is sensitive for investigations of hepatic energy metabolism between different cohorts and can be applied at clinical field strength, which does not limit its application to UHF systems. Reduced k_f and F_{ATP} values indicate an impaired mitochondrial function in people with T1D. The non-invasive nature of the technique makes it suitable for future implementation for characterization of liver metabolism in chronic metabolic diseases, as invasive methods such as biopsies are normally not justified in these conditions.

Both studies demonstrate the feasibility to perform reproducible ^{31}P-MRS for studying hepatic energy metabolism using a clinical scanner. Being able to perform measurements at 3 T is a big advantage, because UHF systems are usually not available in clinical routine. The results of the current studies show that despite the challenge of low SNR at clinical field strength, it is possible to conduct robust and reproducible measurements.

To summarize, this doctoral thesis describes the use of non-invasive techniques to investigate hepatic energy metabolism at clinical field strength. The two protocols discussed allow both the determination of absolute metabolite concentrations and the measurement of hepatic synthesis rates, thus providing in-depth insights into metabolism. Showing acceptable reproducibility, it is possible to use them for individual characterization of metabolism and for future biomedical research studies. The presented techniques have the potential to improve our basic understanding of liver metabolism and contribute to the diagnosis and monitoring of treatments, making them valuable tools for future clinical applications.

Kurzzusammenfassung

Die Leber ist das zentrale Organ für die Aufrechterhaltung der allgemeinen physiologischen Homöostase. Als zentraler Knotenpunkt des Glukose- und Lipidstoffwechsels besteht eine ihrer Hauptaufgaben in der strengen Steuerung der Speicherung, Produktion und Verteilung von Glukose und Fettsäuren. Als primäre Energiewährung der Zelle spielt Adenosintriphosphat (ATP) eine entscheidende Rolle bei biochemischen Reaktionen, da es die universelle Energieeinheit für die Umwandlung von Substraten darstellt. Die Leber erzeugt ATP hauptsächlich in den Mitochondrien ihrer Zellen durch oxidative ATP-Synthese. Aus diesem Grund ist ein grundlegendes Verständnis der hepatischen ATP-Homöostase im gesunden und im kranken Zustand von entscheidender Bedeutung. Von besonderem Interesse sind hierbei Veränderungen der ATP-Konzentration und -Synthese bei Stoffwechselstörungen wie der metabolisch assoziierten steatotischen Lebererkrankung, engl. metabolic dysfunction-associated steatotic liver disease (MASLD), und Diabetes mellitus. Aus diesem Grund wuchs das Interesse an idealerweise nicht-invasiven Methoden zur Bewertung des Energiestoffwechsels und zur Überwachung der ATP-Konzentration in der Leber in den letzten Jahren stark an.

Diese Doktorarbeit nutzte ein klinisches Magnetresonanztomographie (MRT)-System in Kombination mit neuartiger Spulen- und Sequenzentwicklung, um den Leberstoffwechsel mit Fokus auf das energiereiche Phosphat ATP zu untersuchen. Dabei wurden geeignete Magnetresonanzspektroskopie (MRS)-Protokolle für den Nachweis von Phosphor-31 (^{31}P)-Metaboliten etabliert. Zunächst wurde eine Methode zur Bestimmung absoluter Konzentrationen der wichtigsten hepatischen ^{31}P-Metaboliten, u.a. ATP und anorganisches Phosphat (P_i), mittels einer dreidimensional lokalisierten MRS-Sequenz entwickelt. Hierbei kam die Phantomaustauschtechnik mit zwei unterschiedlichen Oberflächenspulen zum Einsatz. Anschließend wurde die Reproduzierbarkeit in einer in-vivo Studie an gesunden Studienteilnehmern validiert. Die mit beiden Spulen ermittelten ATP-Konzentrationen wurden im weiteren Verlauf verglichen, um die Spulenunabhängigkeit der Methode bewerten zu können. Die Möglichkeit zur Erfassung physiologischer Metabolitenkonzentrationen ebnete den Weg für eine komplexere Methode: In einer zweiten Studie wurden metabolische Flussraten gemessen, insbesondere die ATP-Syntheserate der Leber. Dazu wurde ein zusätzliches MRS-Verfahren entwickelt, in welchem ein Sättigungspuls zur selektiven Sättigung spezifischer ^{31}P-Signale implementiert wurde. Diese Sättigungssequenz wurde zunächst in-vitro und in-vivo getestet, bevor sie anschließend an gesunden Studienteilnehmern auf Reproduzierbarkeit validiert wurde. Um das Protokoll auf klinisch detektierbare Unterschiede zu prüfen, wurde zusätzlich eine Subkohorte von Menschen mit Typ-1-Diabetes (T1D) rekrutiert und gemessen. Beide durchgeführten Studien demonstrieren nicht nur nicht-invasive Methoden zur Detektion hepatischer Konzentrationen und Flussraten, sondern belegen auch deren Reproduzierbarkeit, was eine entscheidende Voraussetzung für den künftigen Einsatz in klinischen Studien darstellt.

In der ersten Studie wurde eine lokalisierte dreidimensionale MRS-Sequenz verwendet und eine Auswertungsroutine etabliert, die es ermöglicht, absolute hepatische Metabolitenkonzentrationen in physiologischen Einheiten (Millimol pro Liter, mM) anzugeben. Die Studie nutzt hierbei die Phantomaustauschtechnik, bei der umfangreiche Messungen am Phantom durchgeführt werden. Ziel ist es, die in-vivo Messung zu simulieren und dadurch zu ermöglichen, diese sowohl für sequenz-, spulen- oder metabolitspezifische Eigenschaften als auch für Faktoren zu korrigieren, die mit den variierenden geometrischen und elektrischen Eigenschaften der gemessenen Person zusammenhängen. Weiterhin wurden die aus dem MRS-Spektrum gewonnenen angepassten Metabolitenamplituden für ihre jeweils individuelle longitudinale Relaxation (T_1), das Anregungspulsprofil der Spule, die räumliche Anregungs- und Sensitivitätsverteilung der Spule (Empfindlichkeitsprofil) und die Spulenbelastung der Person korrigiert. In diesem Zusammenhang wurden zwei Oberflächenspulen mit unterschiedlicher Größe und Geometrie umfassend getestet, um die Konsistenz der Ergebnisse im Hinblick auf die ermittelten Konzentrationen und die Reproduzierbarkeit zu bewerten. Während es sich bei der ersten Spule um eine flache, universell-einsetzbare Einzelschleifen-Oberflächenspule des MRT-Herstellers handelte, wurde die zweite Spule, eine gekrümmte Quadratur-Oberflächenspule, speziell für die Anwendung in der menschlichen Leber neu entwickelt und konzipiert. Für beide Spulen wurden sowohl die tagesübergreifende Reproduzierbarkeit (inter-day) als auch die tagesinterne Wiederholbarkeit (intra-day) bewertet. Für den in-vivo Teil wurde eine Kohorte von elf Studienteilnehmern (Body-Mass-Index (BMI): 20,6–32,4 $\mathrm{kg/m^2}$) untersucht. Acht Studienteilnehmer wurden hierfür an drei verschiedenen Tagen innerhalb einer Woche unter standardisierten Bedingungen mit beiden Spulen gemessen, um die Reproduzierbarkeit über einen Tag hinaus zu beurteilen, wobei fünf von ihnen nach drei Monaten nochmals für eine vierte Messung zurückkehrten, um ebenfalls mögliche Langzeitschwankungen zu untersuchen. Darüber hinaus wurden sechs Studienteilnehmer insgesamt sieben Mal innerhalb eines Tages gemessen, um Informationen über die Wiederholbarkeit (ohne Spulenneupositionierung) und die Reproduzierbarkeit (mit Spulenneupositionierung) der Quadraturspule zu erhalten, die als Spule der Wahl für künftige Experimente vorgesehen ist. Für die Analyse der Leberspektren wurde ein hierfür speziell angefertigtes Skript erstellt, das auch Vorkenntnisse (prior-knowledge) zu festen Beziehungen der einzelnen Metabolite untereinander enthält, um eine konsistente und reproduzierbare Peak-Auswertung zu gewährleisten. Als Parameter für die Qualitätskontrolle wurde das Signal-zu-Rausch-Verhältnis, engl. signal-to-noise ratio (SNR), bewertet und das Verhältnis von Phosphokreatin (PCr) zu ATP als Marker für eine mögliche Signalkontamination durch die über der Leber befindliche Bauchmuskulatur verwendet. Die Analyse aller aufgenommenen Spektren wurde auf die gleiche Weise durchgeführt, wobei die individuellen Spulen-Korrekturfaktoren angewendet wurden, um letztendlich spulenunabhängige absolute Konzentrationen zu erhalten.

Als Ergebnis wurden für beide Spulentypen vergleichbar hohe SNR-Werte mit einem mittleren SNR von 8,2 ± 1,5 (Mittelwert ± Standardabweichung) für ATP und 7,3 ± 2,3 für P_i bei der Einzelspule bzw. 8,0 ± 1,5 und 6,8 ± 1,9 bei der Quadraturspule erzielt. Die Aufnahmezeit eines Spektrums betrug dabei 13 Minuten. Dies gelang bei gleichzeitig geringer Signalkontamination durch den Muskel, bewertet anhand einer mittlere PCr-Kontamination von 18 ± 16% bzw.

25 ± 12% der ATP-Signalintensität für die beiden Spulen. Der Vergleich der berechneten absoluten Konzentrationen der beiden Spulen in den tagesübergreifenden Messungen ergab ähnliche, statistisch nicht unterschiedliche Werte: Konzentrationen von 2,31 mM [2,10; 2,53] (Mittelwert [95% Konfidenzintervall (KI)]) für ATP und 1,73 mM [1,58; 1,87] für P_i wurden mit der Einzelspule bzw. 2,32 mM [2,11; 2,53] und 1,73 mM [1,59; 1,87] für die Quadraturspule ermittelt. Die Variationskoeffizienten (CV) dieser Messungen betrugen 7,3 ± 3,1% bzw. 6,7 ± 3,3% für ATP und 8,8 ± 3,4% bzw. 10,6 ± 11,3% für P_i. Die Ähnlichkeit der erhaltenen Ergebnisse zeigt die Robustheit der etablierten Methode. Ähnliches gilt für die tagesinternen Messungen der Quadraturspule: Drei aufeinanderfolgende Messungen ohne Neupositionierung ergaben niedrige CVs von 4,7 ± 2,2% und 6,8 ± 2,1% für ATP bzw. P_i. Messungen mit vollständiger Repositionierung ergaben leicht höhere CVs von 6,3 ± 5,3% und 7,1 ± 6,1%. Alle Ergebnisse waren unabhängig von der verwendeten Spule oder der Positionierung des Studienteilnehmers vergleichbar. Dies zeigt, dass die Anwendung der Phantomaustauschtechnik bei korrekter Anwendung ein hocheffektives Werkzeug für die konsistente Bestimmung von Metabolitenkonzentrationen in der Leber ist. Die Ergebnisse dieser Studie demonstieren, dass die Phantomaustauschtechnik damit in der Lage ist, spulenunabhängige Metabolitenkonzentrationen zu liefern, und dass die Spulen austauschbar verwendet werden können. Obwohl ein Spulenwechsel während laufender Studien normalerweise vermieden wird, ist er bei Spulendefekten oder Langzeitstudien (mehrere Jahre) manchmal unumgänglich. Die Methode unterstreicht damit ihre Zuverlässigkeit und Eignung für klinische Anwendungen und Studien zu Stoffwechselkrankheiten wie Diabetes. Die präzise Messung der wichtigsten hepatischen Metaboliten kann dazu beitragen, neue mechanistische Erkenntnisse über die Ätiologie von Krankheiten zu gewinnen, und bietet Mittel zur Überwachung des Energiestoffwechsels während einer Behandlung.

In der zweiten Studie wurde eine neue Methode entwickelt und angewandt, um die hepatische ATP-Syntheserate zu bestimmen. Das Hauptziel bestand darin, eine robuste und reproduzierbare ^{31}P-MRS Sättigungstransfer (ST)-Technik zu entwickeln, die in der Lage ist, die hepatische ATP-Syntheserate zu quantifizieren und gleichzeitig empfindlich genug ist, um Unterschiede in den Syntheseraten zwischen Menschen mit T1D und einer gesunden Kontrollgruppe zu erkennen. Darüber hinaus sollte die neue Methode bei klinischer Magnetfeldstärke (3 T) einsetzbar sein, was für die zukünftige klinische Anwendung von großer Bedeutung ist. Die hier vorgeschlagene Methode konnte die ATP-Syntheserate innerhalb einer Messung von etwa 90 Minuten und ohne Kontamination durch die Bauchmuskulatur erfassen. Dies gelang durch Anwendung einer zweidimensionalen Lokalisierungssequenz. Frühere Studien, welche die ATP-Syntheserate bestimmten, benötigten hingegen zwei separate Sitzungen im MRT, die Gesamtmesszeit betrug etwa zwei Stunden und es wurde ein geringerer Grad an Signallokalisierung erreicht. Zudem fehlten bei den bisherigen Methoden auch Daten zur Reproduzierbarkeit. Zunächst wurde eine vom MR-Hersteller bereitgestellte zweidimensionale Lokalisierungssequenz durch die Implementierung eines Sättigungspulses erweitert. In anschließenden in-vitro Experimenten wurden optimale Sequenzparameter ermittelt, um eine kontinuierliche und selektive Sättigung des ATP-Signals zu ermöglichen. Die Sättigung erfolgte hierbei durch die Verwendung von DANTE-Pulszügen (engl. delays alternating with nutations for tailored excitation), welche das ATP-Resonanzsignal mit minimalem Einfluss auf be-

nachbarte Signale sättigten. Anschließend wurden die vielversprechendsten Parameter in-vivo an zwei gesunden Studienteilnehmern getestet, und der am besten geeignete DANTE-Pulszug wurde für weitere Experimente verwendet. Um die Gesamterfassungszeit zu verkürzen, wurde das in der Literatur übliche 10-Punkt Inversionserholungsprotokoll (engl. inversion recovery) zur Bestimmung der scheinbaren longitudinalen Magnetisierung von P_i, $T'_{1,Pi}$, durch ein 5-Punkt-Sättigungserholungsprotokoll (engl. saturation recovery) ersetzt. Aus diesem Protokoll wiederum wurden die drei Repetitionszeiten (TR) ausgewählt, die $T'_{1,Pi}$ am zuverlässigsten beschrieben. Für eine einheitliche Analyse der Spektren wurde ein eigens entwickelter Auswertungsskript erstellt, welcher die gleichzeitige Analyse aller Spektren eines Sättigungsexperiments erlaubt. Dies ermöglicht eine einheitliche Vorverarbeitung aller Spektren, wie z.B. die Ermittlung des mittleren Phasenwinkels aller Spektren, wodurch zufallsbedingte Schwankungen minimiert und Unterschiede in den Peaks, die durch die Sättigung verursacht wurden, präzise erfasst werden konnten. Zusätzlich wurden sowohl das SNR als auch das PCr/ATP-Verhältnis als Marker für eine hohe Spektrenqualität herangezogen. Alle gesättigten Spektren wurden weiterhin hinsichtlich der erreichten Stärke der ATP-Sättigung begutachtet, mit dem Ziel, das ATP-Restsignal auf <5% zu beschränken. Nach der Protokolloptimierung wurden neun junge, gesunde Studienteilnehmer zweimal mit vollständiger Repositionierung gemessen, um die Reproduzierbarkeit der Methode zu bewerten und die erfassten Syntheseraten mit anderen in der Literatur beschriebenen Ansätzen zu vergleichen. Unter Verwendung des etablierten Protokolls wurden $T'_{1,Pi}$ und die Vorwärtsratenkonstante der ATP-Synthese k_f bestimmt. Abschließend wurde das Protokoll bei acht Personen mit T1D und einer breiten Altersspanne angewandt, um die Sensitivität des neuen Protokolls bei der Erkennung von Unterschieden zwischen gesunden und chronisch kranken Studienteilnehmern zu testen.

Die quantifizierten Spektren wiesen hohe SNRs mit Mittelwerten von 12,0 ± 1,9 für ATP und 6,2 ± 1,2 für P_i in den Kontrollspektren auf. Eine potentielle Kontamination der Spektren durch Muskelsignal war vernachlässigbar, wie durch ein niedriges PCr/ATP-Verhältnis von maximal <11% bestätigt wurde. Hieraus ließ sich die erfolgreiche Lokalisierung des Signals im Lebergewebe verifizieren. Die Reproduzierbarkeit bei gesunden Probanden zeigte akzeptable CVs von 7,1% für $T'_{1,Pi}$ und 21,3% für k_f. Diese Werte sind vergleichbar mit CVs aus Ultrahochfeld-Messungen (7 T), was beweist, dass die ST-Technik auch bei klinischer Feldstärke angewendet werden kann. Der Vergleich zwischen gesunden Studienteilnehmern und Menschen mit T1D ergab signifikant verminderte Werte in der T1D Kohorte: Die mittlere k_f der Kontrollgruppe betrug 0,34 $^1/_s$ [0,26; 0,42] (Mittelwert [95% KI]) und war dadurch etwa doppelt so hoch als in T1D mit 0,16 $^1/_s$ [0,08; 0,23], $p = 0{,}001$. Dagegen zeigte sich kein Unterschied bei $T'_{1,Pi}$ (482 ms [431; 533] bzw. 517 ms [449; 585], $p = 0{,}340$. Bei Anwendung der Phantomaustauschtechnik zum Erhalt von absoluten Konzentrationen, wie in der ersten Studie beschrieben, kann die Vorwärts-ATP-Syntheserate F_{ATP} berechnet werden, welche 35,3 $^{mM}/_{min}$ [27,3; 43,3] in der Kontrollgruppe und 16,4 $^{mM}/_{min}$ [8,2; 24,7], $p = 0{,}002$ in T1D betrug. Alle signifikanten Unterschiede blieben auch nach Korrektur für Geschlecht, Alter und BMI bestehen. Die Ergebnisse dieser Studie belegen, dass die neu entwickelte Methode für Untersuchungen des hepatischen Energiestoffwechsels zwischen verschiedenen Kohorten sensitiv ist und bei klinischer Feldstärke eingesetzt werden kann, was ihre Anwendung nicht auf Ultrahochfeld-Systeme limitiert. Die

in Menschen mit T1D erfassten reduzierten Werte für k_f und F_{ATP} weisen auf eine beeinträchtigte mitochondriale Funktion hin. Da diese Methode nicht-invasiv ist, eignet sie sich besonders für die Charakterisierung des Leberstoffwechsels bei chronischen Stoffwechselerkrankungen, bei denen invasive Verfahren wie Biopsien klinisch nicht gerechtfertigt wären.

Beide hier beschriebenen Studien belegen, dass reproduzierbare ^{31}P-MRS Untersuchungen des hepatischen Energiestoffwechsels an klinischen MR-Scannern möglich sind. Die Durchführbarkeit der Messungen bei 3 T ist ein entscheidender Vorteil, da Ultrahochfeld-Systeme im klinischen Alltag kaum zur Verfügung stehen. Trotz der Herausforderung durch ein vergleichsweises geringes SNR bei klinischer Feldstärke zeigen die gewonnenen Ergebnisse, dass robuste und reproduzierbare Messungen realisierbar sind.

Zusammenfassend beschreibt diese Dissertation den Einsatz nicht-invasiver MR-Techniken zur Untersuchung des hepatischen Energiestoffwechsels bei klinischer Feldstärke. Die beiden entwickelten Messprotokolle ermöglichen sowohl die Bestimmung absoluter Metabolitenkonzentrationen als auch die Messung hepatischer Flussraten, wodurch sie tiefgreifende Einblicke in den Stoffwechsel liefern. Beide Protokolle weisen eine akzeptable Reproduzierbarkeit auf und eignen sich dadurch für eine individuelle Stoffwechselcharakterisierung sowie zukünftige biomedizinische Forschungsstudien. Die vorgestellten Techniken haben das Potenzial, das Grundverständnis des Leberstoffwechsels zu verbessern und zur Diagnose und Therapieüberwachung beizutragen - sie stellen damit wertvolle Werkzeuge für künftige klinische Anwendungen dar.

Table of Contents

Page

Acknowledgments v

Author's Declaration vii

First Authorships ix

Abstract xi

Kurzzusammenfassung xv

1 Introduction 1

2 Nuclear magnetic resonance (NMR) 5

2.1 Physical basics . . . 6

2.1.1 Nuclear spin and magnetic moment . . . 6

2.1.2 Nuclei in a magnetic field . . . 7

2.1.3 Dynamics of magnetization . . . 9

2.1.4 Resonance condition . . . 11

2.1.5 Relaxation processes . . . 12

2.1.6 Chemical shift . . . 14

2.1.7 Spin-spin coupling . . . 16

2.1.8 Spin decoupling . . . 18

2.1.9 Nuclear Overhauser effect (NOE) . . . 19

2.2 Fundamentals of MRI and MRS . . . 21

2.2.1 Basic experimental principle . . . 22

2.2.2 Static field gradients in MR . . . 24

2.2.3 Magnetic resonance spectroscopy (MRS) . . . 26

2.3 Surface coils . . . 28

2.4 Radio-frequency (RF) pulses . . . 29

2.4.1 Block RF pulses . . . 30

2.4.2 Selective RF pulses . . . 30

2.4.3 Adiabatic RF pulses . . . 31

2.5 Localization in MRS . . . 33

2.5.1 Stimulated echo acquisition mode (STEAM) . . . 34

2.5.2 Image selected in vivo spectroscopy (ISIS) . . . 34

2.5.3 Chemical shift displacement (CSD) . . . 36
2.6 Quantification of metabolites . . . 37
2.6.1 Correction factors for phantom replacement technique . . . 40
2.7 Saturation transfer (ST) . . . 45
2.7.1 Principle of chemical exchange . . . 45
2.7.2 ^{31}P-MRS of the liver . . . 46

3 Liver MRS **49**
3.1 Anatomy and function of the human liver . . . 49
3.2 Diabetes mellitus . . . 50
3.2.1 Diabetes in numbers . . . 50
3.2.2 Clinical classification and subtypes of diabetes . . . 52
3.3 Physiology / Pathway of ATP synthesis . . . 53
3.4 ^{1}H-MRS of the liver . . . 56
3.5 ^{31}P-MRS of the liver . . . 59

4 Aims **63**

5 Study 1: ^{31}P-MRS absolute quantification of hepatic ATP and P_i using different surface coils **65**

6 Study 2: ^{31}P-MRS saturation transfer for assessment of hepatic ATP synthesis rate **81**

7 Overall Discussion **95**

8 Conclusion and Outlook **103**

Bibliography **107**

Nomenclature **121**

Supplemental Material Study 1 **125**

Supplemental Material Study 2 **133**

Publications **153**

Co-author publications **154**

List of Figures **155**

List of Tables **156**

Chapter 1

1 Introduction

Diabetes mellitus is a serious chronic disease and a major global health challenge. It is characterized by chronic hyperglycemia resulting from defects in insulin secretion, insulin action, or both [1]. Diabetes is one of the four priority non-communicable diseases identified by international health organizations and policymakers as requiring urgent action [2]. The disease itself comes with a dual burden of rising morbidity and enormous economic costs, which have reached epidemic proportions. The global prevalence of people with diabetes, including both diagnosed and undiagnosed cases, has risen dramatically over the past decades. In 1990, approximately 198 million people were affected globally, but by 2022, this number increased to 828 million [3]. This represents a rise in global prevalence from 6.9% in 1990 to 14.1% in 2022 [3]. Recent projections suggest that the number of people with diabetes could exceed 1.3 billion by 2050, underlining the urgent need for effective prevention and management strategies [4]. The profound implications on the healthcare systems already amounted to annual expenditures of USD 1.015 billion worldwide in 2024 [5]. Diabetes is not only one of the most common chronic diseases, it is also a leading cause of death worldwide. In 2000, it ranked as the 14th most common cause of death globally, but by 2021, it had climbed to the 8th place, accounting for 2.4% of total deaths [6]. These data agree with earlier predictions which estimated that diabetes could rise to rank 7 by 2030 and even could reach the 4th place in high-income countries like Germany, where it may account for 4.8% of total deaths [7]. Taking also deaths caused by diabetes-related complications into account, the mortality rate in people with diabetes aged 20–79 years increases to 9.3% of total mortality (approximately 3.4 million deaths) in 2024 [5]. Beyond mortality, the disease drives substantial morbidity through accompanying comorbidities like cardiovascular disease, kidney failure, and neuropathy. In Germany alone, healthcare costs for diabetes are projected to amount to €81 billion per year by 2040 [8], showing that there is an urgent need for strategies addressing prevention, early diagnosis, and cost-effective therapies. This is exactly where the field is being reshaped as new treatment strategies like glucagon-like peptide-1 (GLP-1) receptor agonists influence both clinical outcomes and economic calculations [9].

This epidemic is primarily driven by an increase in the incidence of type 2 diabetes (T2D), a heterogeneous disease characterized by an insufficient insulin secretion by pancreatic beta cells in the context of impaired insulin sensitivity, termed insulin resistance [10]. T2D is closely linked to metabolic dysfunction-associated steatotic liver disease (MASLD), a hepatic manifestation of the metabolic syndrome, which is associated with obesity and insulin-resistance and affects up to 70% of people with T2D [11]. MASLD represents a disease continuum ranging from simple steatosis to metabolic dysfunction-associated steatohepatitis (MASH), which may progress through stages of fibrosis, compensated cirrhosis, decompensated cirrhosis, and

ultimately hepatocellular carcinoma (HCC). Due to insulin-resistance, hepatic glucose production and adipose tissue lipolysis are only partially suppressed by insulin, leading to increased fasting glucose levels and a rise in the concentration of free fatty acids [12]. As a result, the pancreas is stimulated to secrete more insulin, which, in the long term, is often not capable of compensating for the increasing insulin resistance, especially upon beta-cell dysfunction and a reduction of beta-cell mass. Recent advancements in precision diabetology aim to stratify people with diabetes into subgroups (subtypes) based on their risk profiles and clinical characteristics [13]. Cluster-based analyses in T2D have identified subtypes with distinct risks of complications, such as cardiovascular disease or neuropathy [14–16]. For example, the severe insulin-resistant diabetes (SIRD) subgroup exhibits pronounced hepatic steatosis, mitochondrial dysfunction, and fibrosis. These findings underscore the central role of hepatic metabolic dysregulation in shaping diabetes heterogeneity and complication profiles.

The liver is a central organ in energy metabolism, playing a pivotal role in maintaining physiological homeostasis and acting as a metabolic hub for the precise regulation of storage, production, and distribution of glucose and fatty acids. In order to maintain stable blood glucose levels, the liver is able to store excessive glucose as glycogen via glycogenesis and degrade the glycogen stores via glycogenolysis during prolonged fasting periods. Additionally, it regulates gluconeogenesis (de novo glucose synthesis) and de novo lipogenesis (conversion of excess carbohydrates into lipids). All these processes are often dysregulated in metabolic disorders such as diabetes and MASLD [10]. As a large number of biochemical reactions require energy for the conversion of substrates, adenosine triphosphate (ATP) has a critical role being the primary energy currency of the cell. Hepatic ATP is predominantly generated in the mitochondria of the cells via oxidative ATP synthesis, which uses glucose and fatty acids as substrates. The anaerobic process glycolysis is also able to provide fresh ATP. However, its ATP yield is secondary compared to the mitochondrial pathway. The ability of the liver to maintain stable ATP levels is crucial for metabolic flexibility and overall function. Lipid accretion in the liver, a hallmark of MASLD, reflects an imbalance between lipid uptake and oxidation rather than mere excessive uptake [10]. The fatty acid oxidation within the mitochondria is the key ATP-generating pathway, and its impairment is implicated in metabolic dysregulation. Any kind of disruption in ATP synthesis is strongly associated with metabolic disorders, including MASLD and diabetes, underscoring the need for studying hepatic energy metabolism. Assessing hepatic ATP dynamics is therefore essential for understanding both physiological and pathological states. For this reason, the need and search for - ideally non-invasive and reproducible - methods for absolute ATP quantification and detection of ATP synthesis rates have increased in recent years.

The phenomenon of nuclear magnetic resonance (NMR) forms the basis for magnetic resonance imaging (MRI) and extend beyond the acquisition of high-resolution anatomical images of arbitrary organs. NMR provides much more diverse insights into biological systems than merely mapping the spatial distribution of water molecules, proving to be an efficient tool for non-invasive diagnostic and analytical methods in living systems in medicine and science [17]. Although the continuous progress in MRI attracts a lot of attention, it is crucial to recognize that, by performing NMR spectroscopy, one can obtain deep insights into the realm of bio-

chemical processes. The frequency differences in NMR arise purely from endogenous physicochemical factors, enabling precise quantitative measurements of metabolite concentrations or even metabolic fluxes in cells. Therefore, in-vivo magnetic resonance spectroscopy (MRS) has grown as an important technique to study static and dynamic aspects of metabolism in disease and in health. Phosphorus-31 (^{31}P)-MRS leverages these principles, being an ideal tool for investigation of hepatic energy metabolism in vivo, since hepatic high-energy phosphates (HEP) and phosphorus-containing metabolites as the key metabolites adenosine triphosphate (ATP), inorganic phosphate (P_i), as well as grouped phosphomonoesters (PMEs), and grouped phosphodiesters (PDEs) can be detected. The technique is able to acquire spectra with high temporal resolution. Because MRS is non-invasive and does not employ ionizing radiation, it is ideal for repeated measurements within an individual, allowing both short-term intervention effects and long-term treatment effects to be studied. In addition to steady-state measurements of hepatic metabolite ratios or concentrations, it is also possible to assess in-vivo reaction kinetics of ^{31}P-metabolites using magnetization transfer (MT) techniques such as saturation transfer (ST) [18].

In-vivo spectroscopy itself has always struggled with the acquisition time needed to obtain a sufficient signal-to-noise ratio (SNR) to be widely applied in a clinical setting. This is even more serious in the case of ^{31}P-MRS, with signal intensity being more than tenfold less compared to proton-MRS (^{1}H-MRS), which is why the main application field of ^{31}P-MRS in the human organism is basic research in brain, skeletal muscle, and liver [19]. However, recent advances in magnet and gradient technology, higher magnetic field strengths, and new coil designs led to improvements in SNR, which can be invested to improve temporal or spatial resolution. This fact and the simultaneous development of new methods for detecting parameters that are otherwise difficult to assess clinically might open the door for more frequent application of ^{31}P-MRS in a clinical setting. Unlike percutaneous liver biopsies, which are invasive, carry risks of complications, and are only performed when clinically indicated, this non-invasive approach holds significant relevance for monitoring metabolic processes safely and repeatedly.

The present work highlights novel developments in diabetes research and magnetic resonance spectroscopy with particular focus on hepatic energy metabolism using a clinical scanner. For this, the following Chapter 2 first describes the theoretical physical basis for the magnetic resonance (MR) experiment and specific features of imaging (MRI) and spectroscopy (MRS). Subsequently, surface coils for signal excitation and detection are presented and the radiofrequency (RF) pulses used by them are characterized. This is followed by an explanation of the technique of spatial localization in MRS, which is particularly relevant for examinations in the liver, before a theoretical explanation of the quantification of metabolites is given. Finally, the technique of ^{31}P-MRS ST, which enables the assessment of biochemical reactions, is explained. Chapter 3 focuses on the application of MRS in the liver. First, a general description of the human liver is given, followed by a characterization of the metabolic disease diabetes mellitus. Subsequently, hepatic physiology is described, with a focus on the process of ATP generation. Finally, the application of both ^{1}H- and ^{31}P-MRS in the liver is explained, including an overview of the metabolites that can be characterized. Chapter 4 summarizes the aims of this thesis. Afterwards, the two main topics of this doctoral thesis, the absolute quantifica-

tion of ^{31}P-metabolites (Study 1) and the assessment of hepatic ATP synthesis rates (Study 2), are presented in the form of the original manuscripts in Chapters 5 and 6. Chapter 7 lists the key findings of the studies, classifies them within the literature, and discusses them. Lastly, the thesis is summarized, with Chapter 8 giving an outlook on the further application of the proposed methods.

Chapter 2

2 Nuclear magnetic resonance (NMR)

Spectroscopy itself is the study of how matter (atoms and molecules) interacts with electromagnetic radiation. Matter possesses discrete energy levels corresponding to different energy states. Electromagnetic radiation can induce transitions between these states through the absorption and emission of photons when applied with energy matching the energy level between two states. Due to the fact that the energy of a photon is directly proportional to its frequency, the different types of spectroscopy can be differentiated based on the applied frequency. For nuclear magnetic resonance (NMR) spectroscopy, the frequencies are in the range of 10–1000 MHz, commonly referred to as radio frequencies (RF), corresponding to wavelengths of about 30 m to 30 cm [17].

NMR is used to study the magnetic properties and associated energies of nuclei [17]. Specifically, NMR focuses on the behaviour of nuclei with non-zero spin in a magnetic field, since these nuclei can absorb and emit alternating radio frequencies while experiencing a constant, external magnetic field. NMR was simultaneously, but independently discovered in 1945 by Bloch et al. [20] and Purcell et al. [21], but it still took half a century until its outstanding suitability for in-vivo imaging and spectroscopy applications came into use. Lauterbur et al. [22] and Mansfield et al. [23] revolutionized NMR by adding additional local position-dependent magnetic fields to the main static magnetic field, which allows detection of the spatial distribution of the nuclear spins resulting in an image and therefore opened the door for magnetic resonance imaging (MRI) and localized magnetic resonance spectroscopy (MRS). While MRI primarily focuses on creating anatomical images using the signals from hydrogen (^{1}H)-nuclei in water and lipids, MRS is able to detect and quantify metabolites in tissues using different nuclei such as hydrogen-1 (^{1}H), carbon-13 (^{13}C), and phosphorus-31 (^{31}P) as signal source. From this point in time, MRI and MRS flourished and underwent rapid evolution to become one of the leading modalities for both anatomical and functional imaging as well as a powerful tool for investigation of the metabolism by assessing metabolite concentrations and even metabolic fluxes.

This chapter provides the theoretical background used in this doctoral thesis to understand the performed studies. At first the physical fundamentals of NMR are explained before an introduction about MRI and MRS is given. MRS itself allows the non-invasive and non-destructive analysis of structure of molecules and metabolites, and even metabolic changes and fluxes can be detected, making this technique ideal for in-vivo measurements in the human body. Next, an overview of RF coils and types of excitation pulses is given, before the principle of localization in MRS is described. Last, the process of metabolite quantification and the technique of saturation transfer (ST) are delineated.

2.1 Physical basics

The physical principles required for this thesis have been developed with the help of publications by Dale, Brown, and Semelka [24], de Graaf [17], and Friebolin [25]. As long as not otherwise stated, all illustrations have been newly created.

2.1.1 Nuclear spin and magnetic moment

NMR is based on the interaction between an applied magnetic field and a particle. All atoms consist of three fundamental particles which have both spin and charge: Positive charged protons and neutrons without charge in the atomic nucleus and negative charged electrons in shells or orbitals surrounding the nucleus. To categorize elements, one uses its individual properties which are i) the atomic number representing the number of protons in the nucleus, ii) the atomic weight which is the sum of protons and neutrons in the nucleus and iii) the nuclear spin or angular momentum quantum number I, which is quantized and depends on the atomic composition. All atoms of an element have the same atomic number and generally undergo the same chemical reactions. Atoms with identical atomic number but different atomic weight are called *isotopes*. Every element in the Periodic Table of Elements, except argon and cerium, has at least one naturally occurring isotope that possesses a spin [24]. The nuclear spin is key for NMR as it defines the magnetic properties of the individual nucleus and its interaction with an external magnetic field. The quantized spin of a nucleus is described by both atomic number and atomic weight and can be zero in case of even atomic number and atomic weight (e.g. ^{12}C), integral for even atomic weight and odd atomic number (e.g. ^{2}H), or half-integral in case of an odd atomic weight (e.g. ^{1}H, ^{13}C and ^{31}P). All nuclei with a non-zero spin are NMR visible and possess an intrinsic nuclear spin angular momentum $\boldsymbol{P}$, which can classically be described as a spherical nucleus which constantly rotates around its axis. From a quantum mechanical view, P is quantized and can be calculated using the spin I and the reduced Planck's constant ($\hbar = {}^{h}/_{2\pi}$) with a value for h of $h = 6.6256 \cdot 10^{-34}$ Js:

$$P = \hbar\sqrt{I(I+1)} \tag{2.1}$$

Because of the positive charge of a proton and the fact that every charge element represents a circle current, there is a magnetic moment $\boldsymbol{\mu}$ linked with $\boldsymbol{P}$. Both $\boldsymbol{\mu}$ and $\boldsymbol{P}$ are proportionally linked to each other through the gyromagnetic ratio γ, an isotope-specific constant.

$$\boldsymbol{\mu} = \gamma\boldsymbol{P} \text{ and } \mu = \gamma\hbar\sqrt{I(I+1)} \tag{2.2}$$

Executing spectroscopy, γ is a fundamental property of each nucleus as it heavily influences the precession frequency of $\boldsymbol{\mu}$ in a given external magnetic field (see subsection 2.1.2). To substantiate that dependence, receptivity is introduced, which gives an estimate of the expected signal strength and by convention receptivity is often specified relative to its proton (^{1}H)-value. Since receptivity has a cuboidal reliance on the gyromagnetic ratio $\left|\gamma^3\right|$, nuclei with high γ are favored for NMR. Considering clinical applications performed using NMR, the most widely

utilized signal source for an in-vivo examination are ^{1}H-nuclei. The ^{1}H-nucleus possesses a spin of $I = 1/2$, a high natural abundance (N) and one of the highest γ with $\gamma_{^{1}\mathrm{H}} = 2.675 \cdot 10^{8}$ Hz/T in comparison to other isotopes making it very sensitive for experiments (see Table 2.1). Performing NMR in the human body, other nuclei of interest are ^{13}C and ^{31}P for investigations of substrate (lipid and carbohydrate) and energy metabolism. While both nuclei also possess a spin of $I = 1/2$, especially ^{13}C-MRS suffers from low NMR-receptivity due to the fact that the most abundant isotope, ^{12}C, is NMR invisible ($I = 0$), while ^{31}P has no other stable isotopes but its gyromagnetic ratio is only about 41% compared to γ of ^{1}H. Calculations of receptivity are accomplished in subsection 2.2.3.

Table 2.1: Key nuclear properties of isotopes commonly used for in-vivo NMR spectroscopy, that include their nuclear composition, spin, gyromagnetic ratio, natural abundance, Larmor frequency at 3 Tesla, and receptivity relative to protons. Table modified from [24] and [26].

Element	Nuclear composition		Spin	Gyromagnetic ratio	Nat. abundance	Larmor frequency ν_L	Receptivity
	protons	neutrons	I	$\gamma/2\pi$ [MHz/T]	N [%]	at 3 T [MHz]	molar rel. to ^{1}H
^{1}H	1	0	$\frac{1}{2}$	42.58	99.9885	127.73	1.00
^{2}H	1	1	1	6.54	0.0115	19.61	$9.65 \cdot 10^{-3}$
^{13}C	6	7	$\frac{1}{2}$	10.71	1.07	32.12	$1.59 \cdot 10^{-2}$
^{31}P	15	16	$\frac{1}{2}$	17.25	100	51.71	$6.65 \cdot 10^{-2}$

2.1.2 Nuclei in a magnetic field

When a nucleus with nuclear spin angular momentum $\boldsymbol{P}$ and magnetic moment $\boldsymbol{\mu}$ is placed in a static magnetic field $\boldsymbol{B_0}$, as is the case in an MR scanner, the spins, which were previously randomly oriented in all spatial directions, will show a slight preference for alignment in the direction of the applied magnetic field, conventionally the z-direction, while the x- and y-components are completely randomly oriented and averaged out. Therefore, one can find the z-component of $\boldsymbol{P}$ in the following discrete angular orientation:

$$P_z = m\hbar \tag{2.3}$$

The character m represents the magnetic quantum number, which, according to quantum theory, can only take specific values from $m = I, I\text{-}1, ..., \text{-}I$. Therefore, for a given I, there are exactly $(2I + 1)$ possible values, leading to corresponding orientations of $\boldsymbol{P}$ and $\boldsymbol{\mu}$ in the magnetic field. This phenomenon is known as the QUANTIZATION OF DIRECTION. Additionally, it is important to note that each possible orientation corresponds to a specific energy level (consult subsection 2.1.3).

Both ^{1}H and ^{31}P with spin $I = 1/2$, which are the nuclei of interest in this thesis, can occupy two possible orientations: $m = 1/2$ and $m = \text{-}1/2$. Consequently, these nuclei can be described as magnetic dipoles. By connecting Equations 2.2 and 2.3, it is possible to calculate the component

of the magnetic moment μ_z in the direction of the applied field:

$$\mu_z = m\gamma\hbar \tag{2.4}$$

From a classical perspective, nuclei experience a torque in the magnetic field, causing them to precess on a cone shell around the z-axis, which has a slight preference to align with the direction of the exterior field $\boldsymbol{B_0}$, resembling the movement of gyroscopes in the gravitational field of the earth. The frequency of this precessional motion, known as the LARMOR FREQUENCY ν_L, is given by:

$$\nu_L = \left|\frac{\gamma}{2\pi}\right| B_0 \tag{2.5}$$

Equation 2.5 is fundamental for NMR as it defines the precise excitation frequency of a specific nucleus, which simultaneously is also the frequency of signal detection.

The individual gyromagnetic ratios of different nuclei allow the targeted investigation of specific nuclei, which is important for specific applications such as ^{31}P-MRS for studying energy metabolism. From examining Equation 2.5, it becomes clear that the Larmor frequency is proportional to the applied magnetic flux density B_0. Consequently, at a field strength of 3 T, which was used for all experiments in this thesis, the Larmor frequency amounts $\nu_L = 127.73\,\text{MHz}$ for ^{1}H and $\nu_L = 51.71\,\text{MHz}$ for ^{31}P. The corresponding twin-precess cone for both nuclei is illustrated in Figure 2.1a. Additionally, the angle θ between $\boldsymbol{B_0}$ and $\boldsymbol{\mu}$ is quantized, and the fixed angles for a nucleus with spin I and corresponding magnetic quantum numbers m can be calculated as follows:

$$\cos(\theta) = \frac{m}{\sqrt{I(I+1)}} \tag{2.6}$$

Inserting corresponding values for ^{1}H and ^{31}P, both spins precess at an angle of $\theta = 54°44'$ (consult Figure 2.1b).

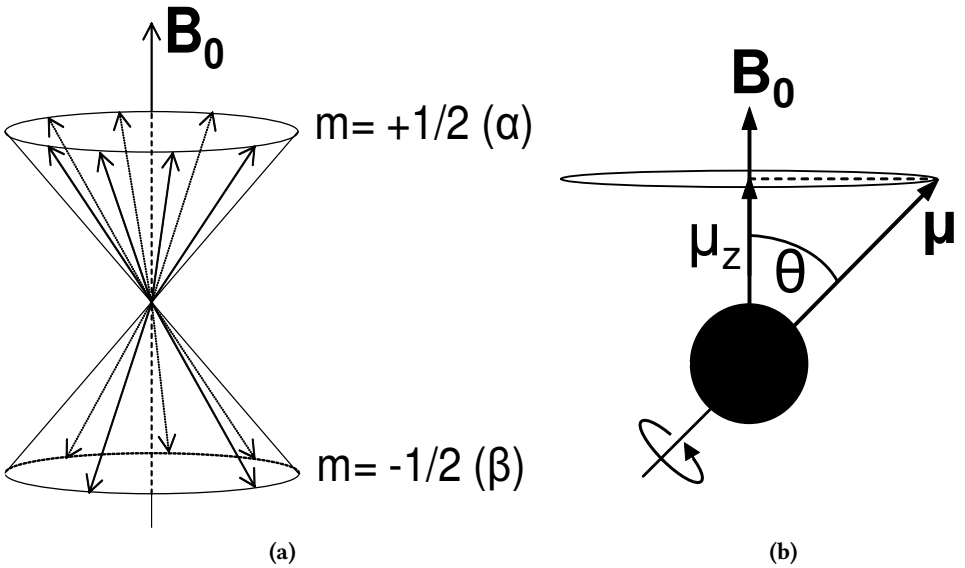

(a) **(b)**

Figure 2.1: (a) Double-precession cone illustrating the two quantized angular positions for both ^{1}H- and ^{31}P-nuclei. (b) Microscopic view of the precession of a single spin situated in a magnetic field $\boldsymbol{B_0}$. Its magnetic moment $\boldsymbol{\mu}$ is tilted by an angle θ from $\boldsymbol{B_0}$.

If one sums all z-components of the magnetic moment in a sample, it will result in a macroscopic bulk magnetization $\boldsymbol{M_0}$ in the direction parallel to the magnetic field. This is due to the constant interaction between $\boldsymbol{B_0}$ and the protons, known as the Zeeman interaction. Consequently, different energy levels are present, as described in the following subsection. Note that this energy will be only degenerate if a static magnetic field is present.

2.1.3 Dynamics of magnetization

When a magnetic dipole is situated in a magnetic field with a magnetic flux density B_0, its energy is given by:

$$E = -\mu_z B_0 \tag{2.7}$$

By combining Equation 2.4 with Equation 2.7, one can determine the different energy states for a given nucleus, also referred to as Zeeman spectral splitting, through the following relationship:

$$E = -m\gamma\hbar B_0 \tag{2.8}$$

The Zeeman splitting is fundamental for NMR spectroscopy and therefore for MRS, as it forms the basis for the resonance frequency and thus for signal detection. From this equation, it is evident that a nucleus with $2I + 1$ possible orientations also has $2I + 1$ energy levels. Consequently, ^{1}H- and ^{31}P-nuclei with $m = \pm 1/2$ exhibit two energy values. When the magnetic quantum number is $m = 1/2$, the magnetic moment μ_z is parallel to the direction of the field. This corresponds to the energetically more favorable arrangement, the lower energy level, known in quantum mechanics as the α spin state. Conversely, if $m = -1/2$, the magnetic moment points antiparallel to the field, which is an energetically unfavorable, higher energy level, and thus less frequently realized (β spin state). The energy gap between two neighboring states can be calculated by inserting both values for m into Equation 2.8 and subtracting one from the other, resulting in:

$$\triangle E = \gamma\hbar B_0 \tag{2.9}$$

An attentive reader can observe the proportionality between $\triangle E$ and B_0, as illustrated for $I = 1/2$ in Figure 2.2a.

The distribution of nuclei across different energy levels in a macroscopic sample in thermodynamic equilibrium can be predicted by the Boltzmann distribution. For nuclei with spin $I = 1/2$, the number of spins in the lower energy level is denoted by N_α, and the number of spins in the higher energy level is denoted by N_β. Thus:

$$\frac{N_\beta}{N_\alpha} = \exp\left(-\frac{\triangle E}{k_B T}\right) = \exp\left(-\frac{\gamma\hbar B_0}{k_B T}\right) \tag{2.10}$$

where k_B is the Boltzmann constant ($k_B = 1.3805 \cdot 10^{-23}\,\mathrm{J/K}$) and T is the absolute temperature in Kelvin, as shown in Figure 2.2b. From Equation 2.10, it can be observed that there is approximately an even distribution of spins at room temperature. This phenomenon is due to the small energy difference $\triangle E$, situated in the numerator of Equation 2.10, compared to the averaged thermal energy $k_B T$, situated in the denominator, at room temperature. This behavior

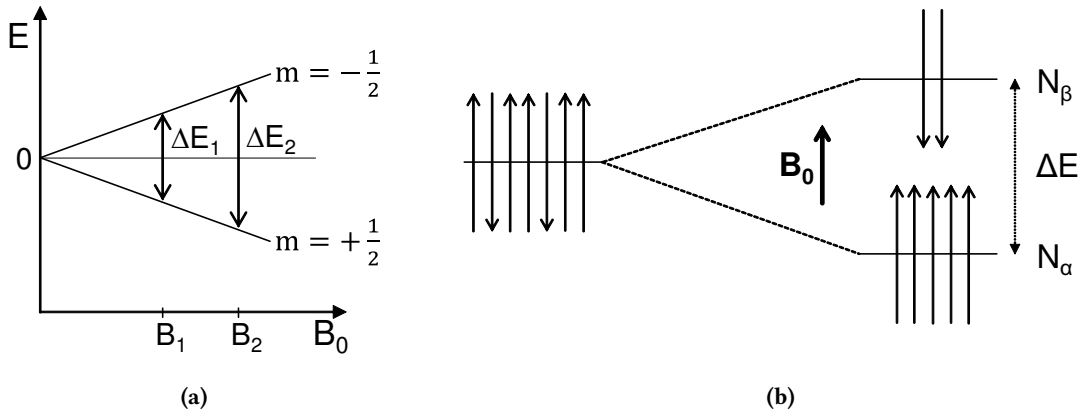

Figure 2.2: (a) Energy difference $\triangle E$ between two neighboring energy levels as a function of the external magnetic flux density B_0 for spin $I = 1/2$. (b) Distribution of nuclei with $I = 1/2$ across the energy levels in the presence of a magnetic field $\boldsymbol{B_0}$. Note that the difference is exaggerated in this illustration.

is independent of the type of nucleus being investigated. Calculating the energy and population difference between both states for ^{1}H- and ^{31}P-nuclei, one obtains $\triangle E \cong 5.1 \cdot 10^{-2}\,\mathrm{J/mol}$ and $N_\beta = 0.999980 N_\alpha$, as well as $\triangle E \cong 2.1 \cdot 10^{-2}\,\mathrm{J/mol}$ and $N_\beta = 0.999992 N_\alpha$, respectively, showing that the surplus of the lower energy levels is in the millionth range. Since the NMR signal is proportional to the population difference, the sensitivity of NMR is rather low compared to other modalities. Strategies to enhance the sensitivity are i) increasing B_0, ii) decreasing the temperature, or iii) the use of hyperpolarization techniques. Nevertheless, this small population difference is sufficient to obtain a macroscopic bulk magnetization along the field axis when summing up all magnetic moments $\boldsymbol{\mu}$ being present in the magnetic field, which can be represented as a vector $\boldsymbol{M_0}$, which remains constant over time. In contrast, for the direction perpendicular to $\boldsymbol{B_0}$, the result will not differ from that obtained without a magnetic field because spins are still randomly distributed despite the time-varying nature of each transverse component [27]. Using approximations, the magnitude of the vector $\boldsymbol{M_0}$ can be estimated by the following equation:

$$|\boldsymbol{M_0}| = (\gamma\hbar)^2 \left(\frac{N B_0}{4 k_B T}\right) \tag{2.11}$$

In this context, N denotes the total number of nuclei $N = N_\alpha + N_\beta$. Because $\boldsymbol{M_0}$ is directly proportional to the signal intensity in NMR, several important factors can be derived from Equation 2.11. Firstly, there is a quadratic dependence of $|\boldsymbol{M_0}|$ on the gyromagnetic ratio. Secondly, there is a linear dependence on the magnetic flux density B_0 and the number of nuclei N, which correlates with the observed sample volume. Finally, there is a reciprocal proportionality to the temperature T. In addition to these predicted factors, several others influence the magnitude of the magnetization, such as noise, natural abundance of the nuclei, relaxation parameters, or the magnetic susceptibility of the tissue. Notably, in the context of ^{31}P-spectroscopy, the amplitude of $\boldsymbol{M_0}$ also provides evidence for the sensitivity of the NMR experiment. The quadratic dependence on the gyromagnetic ratio leads to high intensities for nuclei like ^{1}H, which resonate at high frequencies, whereas ^{31}P suffers due to an about 60% lower γ compared to ^{1}H.

The alignment of $\boldsymbol{M_0}$ along the magnetic field $\boldsymbol{B_0}$ without a transverse component is the foundation of NMR. The entire field is based on the manipulation of $\boldsymbol{M_0}$, which is caused by spins situated in the lowest energy level and which tend to return to this state when excited.

2.1.4 Resonance condition

Technically, it is possible to stimulate MR visible nuclei using an additional high-frequency (HF) or radio-frequency (RF) field in the form of an electromagnetic wave, resulting in transitions between different energy levels. All transitions from a lower energy level to a higher level correspond to energy absorption, while the reverse process corresponds to energy emission. Both transitions are possible and equally likely, but because the lower energy level is more highly occupied, energy absorption predominates over energy emission when an electromagnetic wave is applied, enabling the detection of a signal. Importantly, the intensity of this signal is proportional to the total number of spins in the investigated sample and, therefore, to the concentration. According to quantum mechanical selection rules, only transitions with $\triangle m = \pm 1$ are allowed and, as a result, only transitions between adjacent energy levels are possible. However, this limitation does not affect investigations of ^{1}H- and ^{31}P-nuclei since both possess only two energy levels. During these experiments, the electromagnetic waves affecting the nuclei have to be applied perpendicular to $\boldsymbol{B_0}$ with a suitable central frequency ν_1 that matches the energy difference ΔE between two levels, according to Equation 2.9:

$$h\nu_1 = \triangle E \tag{2.12}$$

The characteristic frequency range for NMR is $\nu_1 = 10\text{–}1000\,\text{MHz}$, depending on the magnetic flux density and the observed nuclei [17]. From the spin perspective, it appears as if there is an additional field $\boldsymbol{B_1}$, e.g., $B_{1,max}\cos(\nu_1 t)$, with $B_{1,max}$ representing the maximum amplitude of the applied field. By combining Equations 2.9 and 2.12, the *resonance condition*, representing the frequency at which spins are affected by $\boldsymbol{B_1}$, can be defined as:

$$\nu_1 = \nu_L = \left|\frac{\gamma}{2\pi}\right| B_0 \tag{2.13}$$

Equation 2.13 shows that transitions can only occur when the Larmor frequency ν_L of the nuclei matches the irradiation frequency of the electromagnetic wave. In this case, the bulk magnetization $\boldsymbol{M_0}$ experiences a torque and can be nutated towards the xy-plane because $\boldsymbol{M_0}$ precesses about both $\boldsymbol{B_0}$ and $\boldsymbol{B_1}$. When B_0 is 3 T, these frequencies are present if the irradiation wave is applied with $\nu_L = 127.73\,\text{MHz}$ for ^{1}H- and $\nu_L = 51.71\,\text{MHz}$ for ^{31}P-nuclei, respectively (consult Table 2.1). However, during excitation, the applied electromagnetic waves have wavelengths of $\lambda = 2.35\,\text{m}$ for ^{1}H and $\lambda = 5.80\,\text{m}$ for ^{31}P, which is why they are known as *radio waves* or HF/RF waves.

To excite nuclei in NMR, an HF generator that operates at a fixed frequency ν_1 and generates $\boldsymbol{B_1}$ pulses of the order of microtesla lasting several milliseconds to microseconds is used. The generator frequency must be adjusted according to the type of nucleus being investigated and the amplitude of the external magnetic field $\boldsymbol{B_0}$. To excite as many nuclei as possible, effects

such as chemical shift (see subsection 2.1.6) and inhomogeneities of the magnet must be considered. Therefore, the excitation pulse must be applied with a certain bandwidth around the Larmor frequency ν_L. However, the amplitudes of frequency components from pulses decrease rapidly with increasing separation from ν_1. Therefore, short-duration pulses with high power, often several watts, are used to achieve homogeneous excitation of as many nuclei as possible [25]. These pulses are known as *hard pulses*. Additionally, to maximize the deviation effect, excitations with $\boldsymbol{B_1}$ are always perpendicular to $\boldsymbol{B_0}$. By varying the irradiation time τ_{pulse} or the intensity of the RF pulse ($\boldsymbol{B_1}$), arbitrary angles of the total magnetization relative to the z-axis can be achieved. This relationship is shown in the following Equation 2.14:

$$\Theta = \gamma B_1 \tau_{pulse} \tag{2.14}$$

The specific angle by which the spins are tipped away from their initial position is called impulse or flip angle (FA). When the overall magnetization is flipped into the xy-plane (90°-flip), the pulse is called a $\pi/2$-PULSE. If the overall magnetization is inverted into the negative z-direction (180°-flip), it is termed a π-PULSE. In this process, the tilted spins are synchronized in phase and precession frequency. The combination of different pulses with certain pulse durations, intensities, and orders, allows the development of specialized pulse sequences (see section 2.4), which is crucial for the type of investigation desired.
Immediately after stopping irradiation, the resulting magnetization vector returns to its initial state through relaxation processes, as described in the next subsection.

2.1.5 Relaxation processes

Once the excitation pulse has ended, the magnetization vector $\boldsymbol{M_0}$ precesses around the z-axis with a Larmor frequency ν_L, flipped by an angle Θ from its equilibrium position. Its current position can be described at any time t in a stationary coordinate system by three time-dependent components M_x, M_y, and M_z. Ultimately, the overall magnetization will return to its initial state, the thermal equilibrium, as spins release the energy absorbed during the RF pulse. During this process, M_z will increase to $|\boldsymbol{M_0}|$, and M_x as well as M_y will decrease to zero. This process is called *relaxation*. The exact characterization of the temporal evolution of the entire magnetization during relaxation is described by BLOCH'S EQUATIONS [20]. These first-order differential equations include two relaxation times, T_1 and T_2, which differ in the final deposition of energy. The full Bloch equations in the stationary coordinate system are as follows [20]:

$$\frac{dM_x(t)}{dt} = \gamma \left[M_y(t) B_0 - M_z(t) B_{1,y}(t) \right] - \frac{M_x(t)}{T_2} \tag{2.15}$$

$$\frac{dM_y(t)}{dt} = \gamma \left[M_z(t) B_{1,x}(t) - M_x(t) B_0 \right] - \frac{M_y(t)}{T_2} \tag{2.16}$$

$$\frac{dM_z(t)}{dt} = \gamma \left[M_x(t) B_{1,y}(t) - M_y(t) B_{1,x}(t) \right] - \frac{(M_z(t) - M_0)}{T_1} \tag{2.17}$$

T_1 relaxation

T_1 relaxation, also known as *longitudinal relaxation time* or *spin-lattice relaxation time*, describes the gradual increase of magnetization in z-direction. During this process, energy is transferred from the spin system to the surrounding atomic lattice. As a result, the excited spins return to the lower energy level, and the overall magnetization increases towards equilibrium. By solving Bloch's equations for the z-axis, the characteristic of T_1 relaxation is obtained:

$$M_z(t) = M_0 \left(1 - \exp\left(-\frac{t}{T_1}\right)\right) \tag{2.18}$$

Due to the exponential function in Equation 2.18, the overall magnetization will exponentially recover in the direction of the external magnetic field towards its initial state. T_1 represents the relaxation time, which varies for each molecule and metabolite. It corresponds to the time after which approximately 63% of the initial magnetization is recovered. After three T_1 periods, M_z will have regained ~95% of its equilibrium magnitude $|\boldsymbol{M_0}|$. The variable t in the equation represents the time following the RF pulse. Additionally, T_1 depends on the strength of $\boldsymbol{B_0}$ and the intrinsic motion of the molecule.

It is important to note that a continuously applied pulse would lead to a vanishing signal because populations of both energy levels would gradually equalize over time. This condition is referred to as *saturation*, which will be crucial for experiments aiming to assess biochemical reaction rates (see Study 2 in chapter 6). Therefore, a delay time between RF pulses is introduced, allowing nuclei to release energy by T_1 relaxation. However, the time between successive pulses is typically insufficient for full relaxation of all spins, as this would make in-vivo measurements too lengthy. Therefore, T_1 of individual metabolites is often assessed in separate scans using an inversion recovery (IR) sequence, where $\boldsymbol{M_0}$ is first inverted and then its return to equilibrium is observed over several time intervals. Knowing the individual T_1 relaxation time of a certain metabolite, one is able to correct for incomplete T_1 relaxation (see subsection 2.6.1).

T_2 relaxation

The process of gradual decrease of magnetization in the x- and y-direction is called T_2 relaxation, also referred to as *transverse relaxation time* or *spin-spin relaxation time*. This process is fundamentally driven by the interaction of spins among themselves, without any energy transfer to the surrounding, making it an entropy process [17].

After the excitation pulse ends, the tilted spins move in phase, or coherently. This means the spins are phase-synchronized in the xy-plane. However, each spin retains its specific Larmor frequency ν_L. Spin-spin relaxation involves energy transfer from an excited spin to a nearby spin of the same type and molecular environment, sharing the same Larmor frequency. These energy transitions occur repeatedly as long as the spins remain at a common frequency and are close to each other. However, due to factors such as molecular vibrations, the magnetic field of every spin, and the interaction with the non-uniform external magnetic field, the system

loses homogeneity. Consequently, spins begin to precess at different Larmor frequencies over time, according to Equation 2.5, leading to a breakdown of phase synchronicity, causing the spins to drift apart. Finally, magnetization in the xy-plane vanishes as the spins become fully distributed along the cone. Solving the Bloch equations for the x- and y-components, the temporal behavior of magnetization in the xy-plane is obtained:

$$M_{x/y}(t) = M_0 \exp\left(-\frac{t}{T_2}\right) \tag{2.19}$$

According to Equation 2.19, transverse magnetization originating from the initial magnetization decays exponentially until it reaches zero. The parameter T_2 denotes the T_2 relaxation time, which, like T_1, depends on the molecule being investigated. After a time interval of T_2, approximately 37% of phase coherency remains, after $2T_2$ ~14%, and after $5T_2$ it has nearly vanished. Both relaxation times are primarily molecule-specific. Experiments show that transverse magnetization decays much faster than predicted by T_2 relaxation time in practice. To account for this discrepancy, an additional relaxation time, known as T_2^* relaxation time, has been introduced. This parameter accounts for inhomogeneities in the external magnetic field or the sample, which further amplify dephasing. In an MR scanner, inhomogeneity is addressed by installing additional coils in every spatial direction to prevent signal loss during experiments. The process of homogenizing the external magnetic field is called *shimming*. In-vivo relaxation times are typically ordered as follows: $T_2^* < T_2 < T_1$.

2.1.6 Chemical shift

All previous explanations might suggest that every type of nucleus has a single nucleus resonance signal which is determined by the strength of the applied magnetic field $\boldsymbol{B_0}$ (see Equation 2.11). Consequently, every ^{1}H- or ^{31}P-spectroscopy would produce exactly one fixed resonance signal, making it impossible to characterize a specific metabolite.

In reality, every nucleus is influenced by its immediate surrounding. The nucleus is not only shielded by its own electron cloud but also by neighboring atoms or other molecules in its environment and tissues. As a result, nuclei do not experience the external magnetic field exactly. As electrons circulate within their orbitals in the presence of an external magnetic field, they induce a magnetic moment which, according to Lenz's law, opposes $\boldsymbol{B_0}$. Consequently, diamagnetic molecules (all electrons are paired together in an orbital or their total spin is zero) always have a lower effective magnetic field $\boldsymbol{B_{eff}}$ than the external one, a phenomenon called *shielding*. On the other hand, paramagnetic molecules (at least one unpaired electron and therefore an orbital with a net spin) always experience a higher magnetic field, known as *deshielding*. This occurs because their electrons circulate between ground and excited states and thus are further away from the nucleus. The effect of the electrons is not large but it is measurable:

$$B_{eff} = B_0 - \sigma B_0 = (1 - \sigma)\, B_0 \tag{2.20}$$

The dimensionless value σ is characterized as shielding constant and can be experimentally assessed by comparing the resonance frequency of the nucleus of interest in different chemical

environments. This constant arises from several effects that together produce a net effect, with electrons shielding the nucleus from the main magnetic field being the main reason. Among others, a diamagnetic term (from ground-state electrons) and an opposing paramagnetic term (from excited states) contribute to the shielding constant. Hydrogen bonding is another factor influencing the shielding constant because it causes deshielding by decreasing the electron density around the proton site. For protons, the strength of the shielding constant is around 10^{-5}, while for heavier nuclei, like ^{31}P, it increases due to the higher number of electrons shielding the nucleus [25].

Moreover, note that the shielding constant is independent of $\boldsymbol{B_0}$; it is only determined by the chemical group and overall molecular structure in which the nucleus is located. Electronegativity plays an important role in this context since it quantifies the force which nuclei in a molecule possess, enabling them to attract the electrons of their neighbors due to their tendency to achieve a full outer electron shell. For example, a nucleus surrounded by highly electronegative neighbors has lower shielding due to the attraction of its electrons. A local effective magnetic field $\boldsymbol{B_{eff}}$ that differs from the value of the external field causes a change in the resonance condition as follows:

$$\nu_1 = \frac{\gamma}{2\pi} (1 - \sigma) B_0 \tag{2.21}$$

From Equation 2.21, it can be shown that the resonance frequency ν_1 is proportional to two terms: First, the magnetic flux density B_0 and second the shielding term $(1 - \sigma)$. In the case of strong attraction of electrons by neighboring atoms, the resonance frequency of a nucleus rises due to weaker shielding. As a result, two chemically non-equivalent nuclei can be separately detected in a spectrum due to differing shielding constants, resulting in two distinct resonance signals. Additionally, the relaxation times exhibited by a nucleus depend on the chemical group it is part of and the physicochemical environment of the tissue in which it is located [28].

It should be noted that there is no absolute scale in NMR spectroscopy because B_0 and ν_1 are coupled, according to Equation 2.21. Hence, a relative scale, showing the frequency difference $\triangle\nu$ between the resonance signals of the investigated metabolite and a chosen reference substance, is employed. However, $\triangle\nu$ is also dependent on B_0. Therefore, in spectroscopy, a dimensionless variable δ, which is independent of B_0, known as *chemical shift*, was introduced:

$$\delta_{\text{sample}}[\text{ppm}] = \frac{\nu_{\text{sample}} - \nu_{\text{reference}}}{\nu_{\text{reference}}} = \frac{\triangle\nu}{\nu_{\text{reference}}} \frac{[\text{Hz}]}{[\text{MHz}]} \tag{2.22}$$

Since the denominator is on the order of several hundred MHz and therefore always significantly larger than the numerator, which is on the order of a few hundred Hz, all values for the chemical shift are reported in PARTS PER MILLION (ppm). Using Equation 2.22, one obtains a relative measurement of the influence of electromagnetic shielding on a specific nucleus, which is independent of the applied B_0 and thus comparable between different MR scanners. Under ideal conditions, the reference substance should have the following properties: The reference substance used should be chemically inert, have a chemical shift independent of external variables, and exhibit a strong singlet that is well-separated from other resonance signals [17]. While

tetramethylsilane (TMS) is primarily used for ^{1}H-MRS in-vitro measurements and cannot be used in vivo due to toxicity and natural absence in the body, in-vivo NMR relies on metabolites that naturally occur in the body. Commonly used internal references are the methyl resonance of N-acetyl aspartate (2.01 ppm) or water (mostly 4.7 ppm) for ^{1}H-spectroscopy of the brain and the phosphocreatine (PCr) resonance (0.00 ppm) for ^{31}P-spectroscopy of brain and muscle [17]. However, it should also be noted that not every metabolite can be found in every organ, which is why in the human liver a different metabolite is used as internal reference (see section 3.5). In ^{1}H-spectroscopy, the prominent water peak overlaps with many resonances of human metabolites, often necessitating the suppression of water spins (consult section 3.4). In contrast, ^{31}P-spectroscopy does not have this problem since water does not contain any ^{31}P-atoms, and therefore no water signal interferes. MRS is preferably applied at higher magnetic fields to improve spectral resolution due to small chemical shifts between metabolites.

For historical reasons, a conventional MRS spectrum shows an increasing frequency from right to left, while the shielding constant increases from left to right. For nuclei with weaker shielding σ than that of water, a more positive value of the chemical shift δ is obtained due to the higher resonance frequency ν_1. In the spectrum, the peak can be found to the left of the reference point (downfield). Figure 2.3 summarizes the various trajectories.

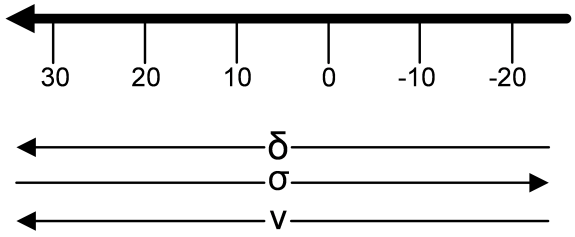

Figure 2.3: Range of ^{31}P-chemical shifts and tendencies of the chemical shift δ, the shielding constant σ, and the frequency ν.

2.1.7 Spin-spin coupling

In addition to chemical shift, there is another molecular interaction that changes the local environment of a nucleus. When examining a spectrum of molecules, it is noticeable that their resonance signals often consist of several resonances grouped together rather than a single resonance. This splitting into multiplets is caused by *spin-spin coupling*, an interaction between neighboring nuclei in a molecule that causes energy levels to split according to their energy level (see subsection 2.1.3). This interaction changes the apparent magnetic field at the nucleus, which may increase or decrease the original field. According to Equation 2.21, this leads to shifted resonance frequencies ν_1 as a consequence. Spin-spin coupling can occur in two ways:

When nuclei are directly coupled through space, which is typically intermolecular, this phenomenon is called *direct spin-spin coupling* or *dipolar coupling*. Conversely, when coupling occurs intramolecularly through a chemical bond, it is called *indirect spin-spin coupling*, *scalar coupling* or *J-coupling*. Since direct spin-spin coupling vanishes in fluid phase due to Brownian motion, although it is the main reason for relaxation, this thesis focuses on indirect

spin-spin coupling in the obtained spectra because this effect does not average to zero and causes the observed phenomena. The interval between two resonance signals of one spin, centered around their chemical shift, indicates the strength of the reciprocal influence between the spins. This is described by a coupling constant J, reported in Hz. Unlike chemical shift, the value of J is not dependent on the strength of the external magnetic field because the splitting is caused solely by the nuclei themselves. For example, a ^{1}H–^{1}H coupling typically has coupling constants in the range of 1–15 Hz and up to 100 Hz if other nuclei are involved [28]. However, spin-spin coupling will only emerge if the neighboring nucleus retains its alignment to the external field long enough. Its lifetime τ at the corresponding energy level must be larger than $1/J$. If $\tau < 1/J$, the interlinked nucleus changes its orientation so quickly that the additional field vanishes in the time-averaged spectrum.

Furthermore, a distinction is made between *homonuclear coupling*, which refers to interactions between nuclei of the same isotope, and *heteronuclear coupling,* which involves interactions between different types of nuclei. In the first case, spectra can be treated by a first-order analysis if the following conditions are met [29]: Firstly, the chemical shift difference between the examined nuclei must be considerably larger than the value of their spin coupling. Secondly, the nuclei must be both chemically and magnetically equivalent. Chemically equivalent nuclei have the same chemical shift, while magnetically equivalent nuclei belong to the same isotope and exhibit equal coupling with another nuclei in the molecule. If the nuclei of a molecule meet these requirements, their spectral splitting pattern can be predicted. When a nucleus is coupled to another functional group which consists of n nuclei with spin I, the resulting multiplicity M is composed of

$$M = 2nI + 1 \tag{2.23}$$

lines. For nuclei with a spin of $I = 1/2$, like ^{1}H and ^{31}P, the formula reduces to $M = n + 1$. The ratio of the intensities can be determined from the number of possible spin states. Each spin has two possibilities: Aligned with or against the external magnetic field $\boldsymbol{B_0}$. For ^{1}H- and ^{31}P-nuclei, the BINOMIAL SERIES determines relative intensities for a given M value. Additionally, all lines of one multiplet are equidistantly separated by the coupling constant J. However, magnetically equivalent nuclei of one functional group can couple, but this does not affect the spectrum. Note that the multiplet can have subsplitting, especially in aromatic rings, resulting in additional signals from spins located beyond the immediate neighbors. Couplings that do not meet the above conditions must be treated as second order and are often analyzed using simulations because symmetry, spacing and splitting are longer organized.

Considering the metabolite adenosine triphosphate (ATP) as an example, it consists of an adenine ring, a ribose sugar, and three phosphate groups (α–γ). Performing ^{31}P-MRS, one can typically obtain three distinct signals originating from chemical shift differences of the three phosphate groups with γ-phosphate at about −2.5 ppm, α-phosphate at −7.7 ppm and β-phosphate at −17.8 ppm in a solution at $pH = 9$ (see Figure 2.4). Please note that the individual chemical shifts are pH-dependent and differ in vivo (see section 3.5). Due to homonuclear spin-spin coupling, each signal splits up into a multiplet according to Equation 2.23 resulting in a doublet for each α- and γ-phosphate because of coupling with the neighboring β-phosphate and

in a triplet for β-phosphate as it couples with both α- and γ-phosphate. The typical coupling constant amounts 20 Hz in vitro [30] and 16 Hz in vivo [31, 32].

As one of the key metabolites in energy metabolism, ATP concentrations in the body are strictly regulated. Non-invasive assessment of its absolute concentration is of great interest in metabolic research, because changes in ATP levels have profound implications for energy regulation and disease pathogenesis. For example, it was shown that people with type 2 diabetes (T2D) exhibit decreased hepatic ATP concentrations [33–35] and reduced hepatic ATP synthesis rates [35], alterations associated with hepatic insulin sensitivity and lipid accumulation. Study 1 of this doctoral thesis presents a method to quantify physiological ATP concentrations (see chapter 5), while Study 2 addresses the assessment of hepatic ATP synthesis rates (see chapter 6).

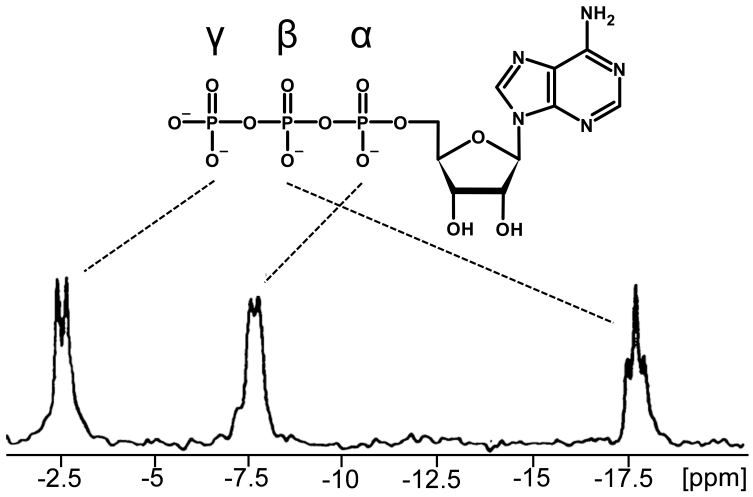

Figure 2.4: Structural formula and ^{31}P-MRS spectrum of adenosine triphosphate (ATP) in a solution with $pH = 9$. Each phosphate group shows an individual signal in the spectrum. Due to homonuclear spin-spin coupling, α- and γ-phosphate are detected as doublet, while β-phosphate resonates as a triplet. Adapted from [17].

2.1.8 Spin decoupling

While understanding and analyzing spin-spin couplings provide valuable information about the chemical structure of neighboring chemically shifted functional groups, from a clinical perspective, splitting can be disruptive. Human tissue contains many different molecules, resulting in overlapping multiplet structures. Clinical investigations typically deal with well-known metabolites, making it desirable to suppress line splitting, which only provides structural information. This allows for easier identification and quantification of metabolites in vivo, as a split signal from a functional group has a lower signal-to-noise ratio (SNR) than the same signal represented by a single resonance, simplifying peak fitting (see section 3.5).

For these reasons, a technique called *decoupling* was developed. This technique breaks down all multiplets of a functional group into a single peak by applying a second, *decoupling magnetic field* $\boldsymbol{B_1}$ to the group causing the coupling. Decoupling is achieved if the functional group

responsible for coupling changes its alignment relative to $\boldsymbol{B_0}$ at a higher rate than its coupling constant, leading to saturation of the multiplet states (compare subsection 2.1.7) [29]. The decoupling pulse is only present during signal acquisition, as decoupling is considered an instantaneous process. In practice, it is often used in combination with the nuclear Overhauser effect (NOE) to achieve higher SNR (see subsection 2.1.9). As a result of decoupling, spectra show increased signal intensities due to the energy that was previously distributed over multiple resonances of a multiplet now concentrated in a single, sharper peak, which is of special importance for the detection of low-concentration metabolites.

There are various modes of decoupling, with the two most frequently used being *broadband* and *narrowband*. Broadband decoupling simplifies complex spectra by combining all multiplets into singlets, affecting all nuclei of one type coupled to nuclei of another type in all functional groups. In contrast, narrowband or continuous wave decoupling prevents coupling in a single functional group of interest and requires the decoupling field to be precisely tuned to the frequency of the group of interest. Broadband decoupling is achieved by applying a frequency band that encompasses the entire bandwidth of the spectrum. The resulting spectrum contains at most n singlet signals from n ^{31}P-nuclei. However, it should be noted that especially broadband decoupling can lead to additional sample heating, which is why the decoupling power needs to be carefully optimized.

Proton decoupling is important in ^{31}P-spectroscopy because the ^{1}H–^{31}P bonds result in overlapping multiplets (see subsection 2.1.7). Irradiating protons during signal acquisition averages out couplings and ^{31}P-resonances narrow into singlets. Broadband proton decoupling is often enabled at about 4 ppm where the J-coupling is to $-O-CH_2$ methylene protons, so all ^{1}H–^{31}P couplings are decoupled by applying a frequency-modulated $\boldsymbol{B_1}$ pulse to the protons which saturates them all. In practice, the so-called Wideband Alternating-phase Low-power Technique for Zero-residual splitting (WALTZ) [36] sequence is employed, which achieves decoupling by the application of a specific sequence of composite RF pulses with different phases.

As one of the aims of this thesis is to quantify the main hepatic ^{31}P-metabolites in a single spectrum, a broadband decoupling technique was applied – essential for resolving overlapping hepatic metabolite signals.

2.1.9 Nuclear Overhauser effect (NOE)

The NOE is an NMR technique that facilitates the transfer of magnetization between spin systems through dipole-dipole interactions, resulting in altered signal intensities. This effect, which originated as a beneficial side effect of decoupling, operates through space rather than through chemical bonds (consult subsection 2.1.7).

Typically, NOE is applied to transfer magnetization from a nucleus with a high gyromagnetic ratio, such as ^{1}H, to one with a lower gyromagnetic ratio, like ^{31}P, thereby enhancing the SNR ratio of the latter. This is achieved by applying a second RF pulse ($\boldsymbol{B_1}$) to excite and saturate ^{1}H-spins, leading to equal spin populations across all energy levels. The subsequent relaxation processes transfer population differences from ^{1}H- to neighboring ^{31}P-nuclei, resulting

in increased population differences for ^{31}P and, consequently, higher signal amplitudes. In a two-spin system (*HP*) with dipole-dipole coupling, four energy levels exist ($\alpha\alpha$, $\alpha\beta$, $\beta\alpha$, $\beta\beta$), corresponding to different spin orientations (see Figure 2.5a). During an NOE experiment, spin H is continuously saturated, altering population ratios compared to the equilibrium state. Three types of transitions occur: *single-quantum transitions* (W_1), which belong to T_1 relaxation, and two new transitions, *double-quantum* (W_2) and *zero-quantum* (W_0) transitions. While these latter two are spectroscopically forbidden as they violate the resonance condition (compare subsection 2.1.4), they are allowed during relaxation and are crucial in determining the strength of the NOE effect (consult Figure 2.5b). The behavior of NOE varies depending on molecular size and the correlation time, the average time required for a molecule to rotate by one radian in solution. In small molecules with short correlation times, W_2 transitions dominate, resulting in positive NOE, whereas in large macromolecules with long correlation times, W_0 transitions lead to negative NOE.

$$NOE = 1 + \frac{\gamma_H}{\gamma_P}\left(\frac{W_2 - W_0}{W_0 + 2W_{1,P} + W_2}\right) \tag{2.24}$$

To estimate the maximum NOE, the case of the extreme narrowing limit, where molecular motion is much faster than the Larmor frequency of the observed nuclei ($W_2 > W_0$), can be assumed, simplifying the NOE equation to:

$$NOE = 1 + \frac{\gamma_H}{2\gamma_P} = 1 + \eta \tag{2.25}$$

The NOE enhancement factor η is a key parameter in understanding the effect's magnitude. For ^{1}H–^{31}P couplings, the maximum theoretical NOE enhancement is 2.235, though in practice, in-vivo values typically range from 1.4–1.8, because molecular motions in vivo are generally slower and more complex due to the viscous cellular environment and the presence of large biomolecules [17].

While NOE and spin decoupling may appear similar, they differ in several important aspects. NOE is continuously applied during experiments, except during signal acquisition when decoupling is performed. NOE is a slower spin-lattice process and operates through space via dipolar coupling, whereas decoupling is instantaneous and operates through chemical bonds via J-coupling. Furthermore, NOE improves signal intensity, while decoupling also enhances spectral resolution. However, since both techniques apply an additional $\boldsymbol{B_1}$, sample heating becomes unavoidable when these modules are activated, which is why their application must be carefully controlled and optimized.

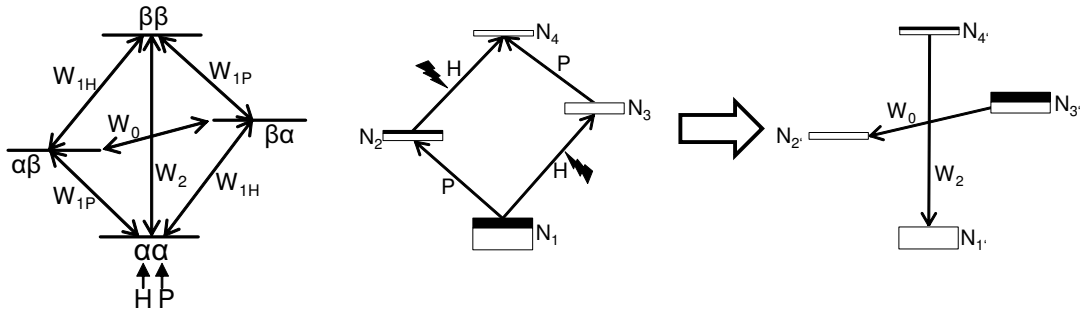

(a) **(b)**

Figure 2.5: Energy level diagrams and effects resulting from NOE on the energy levels regarding their population ratios for a dipolar coupled two-spin system ^{1}H–^{31}P. (a) The terms W_x represent transition probabilities for a transition. Whereas W_1 corresponds to single-quantum transition, W_0 represents zero-quantum and W_2 a double-quantum transition. (b) N_1 to N_4 denote the population of each energy level. Transition frequencies for H and P are identical. Left: Initial situation just before nucleus H is being saturated. Right: Situation in which both H transitions are saturated. The black rectangles show the shift of the spin populations. Here, only the transition probabilities responsible for signal manipulation of nucleus P are shown. Adapted from [25].

2.2 Fundamentals of MRI and MRS

This section outlines the fundamental principles of magnetic resonance (MR) before focusing on ^{31}P-spectroscopy, highlighting its advantages and limitations. Before exploring the experimental principles, it is crucial to understand the two primary distinctions between magnetic resonance imaging (MRI) and magnetic resonance spectroscopy (MRS).

First, MRS in principle can acquire spectra without using gradients. Consequently, all molecules are subjected to the same basic magnetic field ($\boldsymbol{B_0}$) without the slight variations induced by gradients. As described in the chemical shift subsection 2.1.6, this phenomenon becomes the primary source of magnetic field variation. Thus, chemical shift is the sole factor enabling the identification of different molecular species, contrasting with MRI where these shifts are often considered as artifacts [24]. Second, MRS aims to minimize all types of relaxation effects. This approach is necessary because the metabolites under investigation are typically present in low concentrations and often exhibit long T_1 and T_2 relaxation times. To achieve this, long repetition times (TR) are employed to prevent T_1 saturation, while T_2^* time is evaluated to account for T_2 effects. In contrast, MRI relies on relaxation effects to optimize image contrast. Finally, MRI generates anatomical images, whereas MRS produces spectra showing signal intensities as a function of chemical shift. It is worth noting that while MRI is widely used in medical centers, MRS is predominantly utilized in research facilities. This distinction underscores the different applications and focuses of these two MR techniques.

MRS can be conducted on any nucleus with a non-zero spin. Applications of in-vivo MRS focus on proton (^{1}H), carbon (^{13}C), phosphorus (^{31}P), and sodium (^{23}Na) nuclei which are naturally present in the human body and coincidentally provide extensive information as multiple signals from different metabolites can be simultaneously detected.

2.2.1 Basic experimental principle

An MR scanner is a complex system relying on the interplay of several key components for generating images or spectra. The three main components are:

1. Superconducting magnet: The magnet creates the external magnetic field $\boldsymbol{B_0}$, responsible for generating and maintaining bulk magnetization $\boldsymbol{M_0}$.

2. High-frequency (HF) technique: This component excites spins with a suitable resonance frequency. A transmitter coil generates an electromagnetic wave $\boldsymbol{B_1}$ in the shape of a pulse, whose intensity and duration time are chosen in a way that, for example, the bulk magnetization $\boldsymbol{M_0}$ is flipped from its original z-direction by 90° ($\pi/2$-pulse) into the xy-plane (see subsection 2.1.4).

3. Gradient technique: An MR scanner incorporates three main, individually selectable gradient coils, each aligned with one spatial direction. This technique allows for precise placement of the field of view (FOV), which represents the area from which signals are collected. Without these gradients, spatially resolved acquisitions would be impossible. The gradient field slightly distorts $\boldsymbol{B_0}$ in a linear and predictable manner, causing the resonance frequencies of nuclei to vary as a function of their position. This enables spatial encoding, slice selection, and frequency/phase encoding (consult subsection 2.2.2). In localized spectroscopy, gradients play a crucial role for spatial selection and signal encoding. However, non-localized spectroscopy (NLS) operates without the use of gradients, relying instead on the homogeneous $\boldsymbol{B_0}$ to acquire spectral information from the entire sample.

After the RF excitation pulse has finished, all spins precess according to Equation 2.21 phase-synchronously with their individual Larmor frequency ν_L in the xy-plane around the z-axis. Spin dephasing then occurs due to macroscopic and microscopic field inhomogeneities, resulting in different relaxation processes (see subsection 2.1.5). During this time, T_1 increases slowly, while transverse magnetization decays. The constantly changing magnetization induces an electric field (voltage) in the nearby antenna (RF receiver coil), which is directly detectable. This process utilizes *Faraday induction,* with the induced voltage proportional to the magnitude of transverse magnetization. Therefore, coils serve dual purposes: Applying RF pulses to the sample and detecting the NMR signal. However, different systems and applications might require separate coils for excitation and detection. It is noteworthy that the disappearing coherence in the transverse plane produces the detectable signal in NMR. By contrast, T_1 does not contribute to the detectable signal as it is never detected directly due to overwhelmingly larger contributions from magnetization associated with electron currents within atoms and molecules due to $\boldsymbol{B_0}$ [17]. Nevertheless, it reveals itself in repetitive experiments since signal magnitude is dependent on the extend to which T_1 can be flipped in the xy-plane.

The time-dependent electromotive force induced by transverse magnetization is called the free induction decay (FID). It appears as several exponentially decaying oscillations with different frequencies, corresponding to various nuclei with individual chemical shifts from distinct molecular environments. For that reason, the FID contains information about the observed

spins relative abundances and resonance frequencies. While the FID describes the signal intensity dependency in time (*time-domain* signal), it is difficult to interpret directly. In practice, a Fourier transformation (FT) is applied to convert the time-domain signal into a *frequency-domain* spectrum, which reveals discrete resonance frequencies, with relative abundances reflected by their intensities. Performing FT offers the advantage of simultaneous resonance of all nuclei while maintaining differentiation and enables signal averaging through multiple scans. The Fourier transform of a time-domain signal $f(t)$ results in a frequency-domain signal $F(\nu)$ according to:

$$F(\nu) = \int_{-\infty}^{+\infty} f(t) \exp(-i2\pi\nu t)\, dt \tag{2.26}$$

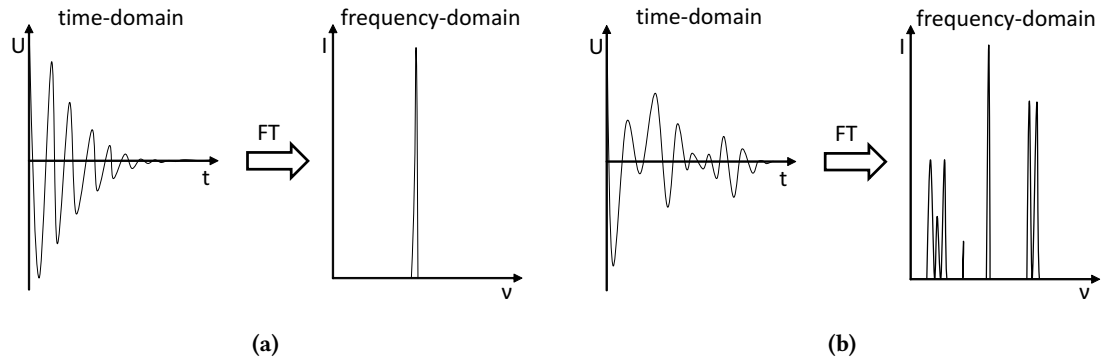

Figure 2.6: FID signal and Fourier transformed spectrum of (a) a single frequency and (b) a mixture of frequencies. Note that the recorded voltage U in the time-domain and the signal intensity I in the frequency-domain are shown in arbitrary units.

Signal intensity comparisons are relative to each other within a single measurement, which limits the interpretability to relative comparisons only. Obtaining absolute signal intensities require the knowledge about a constant metabolite concentration within the tissue of interest or an external reference standard (consult section 2.6). Analyzing the frequency-domain spectrum, the area under a peak corresponds to the abundance of a specific nucleus or molecule. The number of peaks depends on the bandwidth of the applied excitation pulse. A narrowband pulse around the resonance frequency of water would result in a single distinct peak (see Figure 2.6a), while a broadband pulse would affect multiple molecules simultaneously, resulting in a mixture of frequencies that, after FT, resolve into multiple peaks corresponding to different molecules (see Figure 2.6b).

Due to inhomogeneities of the external magnetic field and inherent background noise, sequences must be repeated multiple times. All FIDs are then stored and combined to create an accumulated spectrum. This method enhances SNR as the resonance signal becomes more prominent compared to noise with each sequence repetition. According to random process theory, signal intensity scales proportionally with the number of accumulations (n), while noise intensity only scales proportional to the square root of n. Consequently, the SNR improves by

a factor $n/\sqrt{n} = \sqrt{n}$, resulting in the following relationship:

$$SNR \propto \sqrt{n} \tag{2.27}$$

In practice, there are limitations to SNR improvement through repeated measurements. A tenfold increase in SNR requires a hundredfold increase in measurement time. This constraint particularly affects the widespread use of ^{31}P-MRS, as its low sensitivity necessitates numerous repetitions to obtain an interpretable spectrum. Alternative methods to enhance SNR include expanding the investigated volume or using higher magnetic field strengths.

2.2.2 Static field gradients in MR

Magnetic field gradients are one of the three main components of an MR scanner (see subsection 2.2.1). In classical MRI, they are extensively used to generate high-resolution anatomical images, but they are also needed to enable spatial localization in MRS. The main function of gradients is to generate a temporary additional static magnetic field orientated parallel to $\boldsymbol{B_0}$, which linearly varies in strength with position along the x-, y- or z-axis, or some oblique direction to these axes [28]. Gradients typically produce a total field variation of less than 1% [27]. This linear variation of $\boldsymbol{B_0}$ in a specific direction causes different Larmor frequencies along the gradient direction, according to Equation 2.5. This relationship is expressed as

$$\nu(\epsilon) = \frac{\gamma}{2\pi}(B_0 + G_\epsilon \epsilon), \tag{2.28}$$

where G_ϵ denotes the gradient strength along an arbitrary direction ϵ, often expressed in $^{\mathrm{mT}}/_{\mathrm{m}}$. When a gradient field is applied while magnetization is in the transverse plane, the precessional frequency of this magnetization will vary linearly along the gradient direction, allowing each nucleus to resonate at a unique frequency dependent on its exact position within the gradient field.

After switching off the gradients, the entire sample magnetization will again precess at the initial Larmor frequency. However, spins will have different phases due to their period of altered precession. This situation continues until a gradient in the opposite direction is applied with identical strength and duration. All MR images represent frequency and phase maps of nuclei produced by a special magnetic field strength at every point within the image. In the obtained digital image, volume elements, commonly called *voxels*, are represented as a collection of pixels, where pixel intensity indicates the overall number of nuclei situated in the voxel. Gradients in MR are able to serve different purposes:

Spoiling of magnetization

The gradient system can be used to induce rapid dephasing of transverse magnetization by applying an intense gradient pulse resulting in elimination of all frequencies within the excited volume. This helps to prevent artifacts caused by previous excitations and ensures that consistent initial conditions are present before the next excitation begins.

Refocusing of magnetization

In some cases, it is beneficial to delay the acquisition of a MR signal to allow additional time for the application of other necessary pulse sequence elements. Besides *a Spin-Echo*, a similar effect can be achieved with a *Gradient-Echo* sequence. This technique uses a gradient to consciously dephase magnetization; at a later specific moment, the gradient is inverted to rephase the spins. To achieve a complete rephasing of spins, the following condition has to be fulfilled:

$$\int G_\epsilon \epsilon \, dt = 0 \tag{2.29}$$

Implementing this condition completely rephases the spins within a pulse sequence, whereas careful attention has to be paid regarding pulse sequence timing. If very intense refocusing gradients are used, this rephasing can be achieved in a very short period.

Slice selection

Application of a gradient, e.g. in z-direction (G_z), simultaneously with a narrowband frequency RF pulse allows for the selective excitation of a well-defined slice of spins along the z-direction into the transverse plane. All other spins along this direction in the sample ideally remain unpertubed. A particular location or slice thickness can be chosen by varying the RF pulse bandwidth and gradient amplitude. In MRS, the choice of the applied pulse bandwidth is of particular importance, since a too narrow bandwidth fails to excite the magnetization across the whole chemical shift range of the obtained spectrum causing off-resonance effects and increased chemical shift displacement (CSD) (consult subsection 2.5.2).

Since most MRS voxels are quadratic or rectangular, it is desirable to select slices with a rectangular profile across the voxel because this leads to a rapid decay outside the selected volume and therefore minimal contamination. However, due to instrumental imperfections, the profile of the excited slice always resembles the frequency profile of the RF pulse, which is the Fourier transform of the pulse shape in the time-domain [28]. Therefore, an ideal rectangular slice profile requires the application of a sinc-shaped RF pulse of infinite duration [28]. Since fulfilling this condition is impossible, truncated sinc pulses, apodized with a Gaussian function, are used for slice selection in practice (see section 2.4).

Spatial encoding

This application is mainly used in MRI but also in spectroscopic imaging. Since this thesis deals exclusively with MRS and imaging is just performed for the purpose of planning the localized MRS voxel, this extensive topic will be briefly addressed.

Spatial encoding is performed to create images. It is achieved with the help of two additional gradients that encode spatial information into the collected signal. More precisely, one gradient is used for frequency encoding, the other for phase encoding. Usually, frequency encoding is done by applying a gradient in the x-direction during signal acquisition. This leads to a

variety of frequencies, detected in such a way that every spin precesses with a slightly different Larmor frequency along the x-axis. In contrast, phase encoding is done by applying a gradient in the y-direction at a certain time after excitation. While phase encoding is active, nuclei at different positions along the y-axis experience various amounts of phase shifts. After deactivating this gradient, every spin along the y-direction has a characteristic phase, which identifies itself clearly. By repeating the whole procedure several times with varying the amplitude of the y-gradient, a set of signals is obtained. In MR, all raw data are represented in a digital representation called *k-space*. Each measurement with a different y-gradient amplitude leads to a new row in this space. If this space is sufficiently filled, applying a 2D-FT produces two-dimensional images (see Figure 2.7). The image received through this procedure depicts the position-dependent distribution of the intensity of the spins.

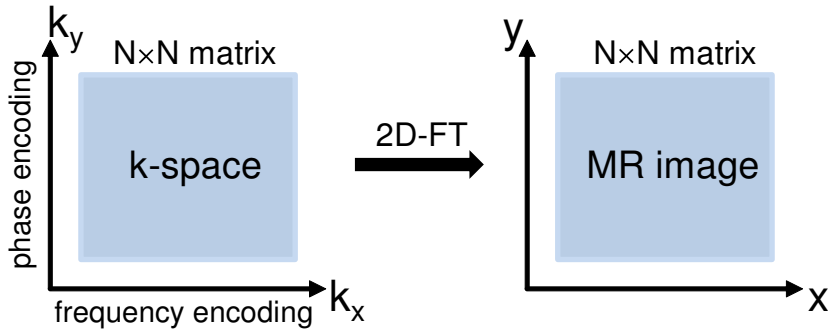

Figure 2.7: Emergence of an MR image from k-space data. Each pass with a different gradient strength in the y-direction fills one row in k-space. Performing a 2D-FT produces a two-dimensional image showing the intensity-coded distribution of spins.

2.2.3 Magnetic resonance spectroscopy (MRS)

Although MRI is the most common application of the MR phenomenon nowadays in clinics, its original usage is MRS. Transferring the NMR techniques onto whole-body scanners allow MRS to be applied for studying human biochemistry and detecting alterations in metabolites without any kind of invasive interventions, e.g. biopsies. The ^{1}H-nucleus is the most sensitive nucleus for in-vivo MRS regarding intrinsic NMR sensitivity ($\gamma_{proton} = 2.675 \cdot 10^8$ Hz/T) and natural abundance (>99.9%). Because almost all metabolites contain protons, ^{1}H-MRS can be applied for observation, identification and quantification of a wide range of metabolites in the whole human body. The most prominent areas of application are neurology and psychiatry in the brain, oncology in the whole body, cardiology in the heart, and diabetology in the skeletal muscle and liver. An overview of detectable metabolites in the human liver is given in sections 3.4 and 3.5.

However, from a spectroscopic point of view ^{1}H-MRS has several limitations: The omnipresence of water in the human body results in spectra where the water resonance is several orders of magnitude larger than any other signal from low-concentration metabolites, complicating detection of those. Therefore, sequences with water-suppression are often applied to increase visibility of non-water metabolites but also to be able to detect metabolites which signals are

superimposed by the water resonance. Another restriction of ^{1}H-MRS is the narrow chemical shift range of about 5 ppm causing signals to overlap each other [17]. This leads to the practice that at clinical field strengths in human brain, often the sum of overlapping metabolites rather than individual amplitudes is reported [37], whereas ultrahigh-field (UHF) studies in the rat brain have revealed that 18 different metabolites could be separately detected [38]. It has to be kept in mind that even though protons are the most sensitive nuclei for spectroscopy, MRS is an insensitive technique making the detection of low-concentration metabolites a compromise between time resolution and SNR [17].

Application of ^{31}P-spectroscopy enables another non-invasive assessment of important information regarding energy metabolism by detecting high-energy phosphates (HEP) and phospholipids in vivo. Additionally, it allows for observation of intracellular pH, magnesium concentration, and even reaction fluxes. In fact, ^{31}P-MRS is the only other nucleus commonly used in clinical routine because it has the most important property in common with protons, namely a spin of $I = 1/2$. Owning this characteristic, it can readily be derived that in an external magnetic field, the ^{31}P-nucleus splits into two approximately equally populated energy levels as protons do. Another advantage of ^{31}P-MRS is the relatively large spectral range with about 30 ppm due to the fact that ^{31}P has 15 electrons whereof five are situated in the outermost shell and can be manipulated from outside. For this reason, its shielding constant σ can vary much more than that of protons, resulting in good spectral resolution for the metabolites [17].

On the other hand, there are several drawbacks. Although the ^{31}P-nucleus possesses a natural abundance of 100% due to the absence of other stable isotopes, its Larmor frequency amounts $\nu_L = 51.71$ MHz, which is about 41% of the value for protons. The amplitude of $\boldsymbol{M_0}$ is highly affected by the quadratic dependence on the gyromagnetic ratio γ, as the low γ of ^{31}P compared to ^{1}H $\gamma_{^{31}P}/\gamma_{^{1}H} = 0.4051$ leads to a low sensitivity, as can be calculated by Equation 2.11, despite its smaller transition energy difference (compare Equation 2.9) which conversely increases the Boltzmann population difference (see Equation 2.10). According to Equation 2.4, the magnetic moment μ is also low, reducing signal intensity (see Equation 2.11). Additionally, the rate of precession decreases which is why the induced signal in the detection coil will also decrease. These factors, combined with resulting loss of macroscopic bulk magnetization, contribute to a much lower sensitivity for ^{31}P compared to ^{1}H. However, it is more common to characterize the sensitivity in terms of receptivity (compare subsection 2.1.1) [39], always relative to protons. The natural receptivity is calculated by multiplying the NMR sensitivity, represented by the term $\left|\gamma^3\right| I(I+1)$, and the natural abundance (N) of the corresponding nucleus. Inserting the data provided in Table 2.1 into the following formula, one obtains the natural receptivity of the ^{31}P-nucleus:

$$R_{^{31}\mathrm{P}}^{^{1}\mathrm{H}} = \left|\frac{\gamma_{^{31}\mathrm{P}}^3}{\gamma_{^{1}\mathrm{H}}^3}\right| \frac{N_{^{31}\mathrm{P}} I_{^{31}\mathrm{P}}(I_{^{31}\mathrm{P}}+1)}{N_{^{1}\mathrm{H}} I_{^{1}\mathrm{H}}(I_{^{1}\mathrm{H}}+1)} = \frac{R\left(^{31}\mathrm{P}\right)}{R\left(^{1}\mathrm{H}\right)} = 6.65 \cdot 10^{-2} \tag{2.30}$$

Despite these challenges, the utilization of the two techniques proton decoupling and NOE helps to partially overcome the inherent sensitivity limitations of ^{31}P-MRS (consult subsections 2.1.8 and 2.1.9). Executing in-vivo measurements is almost always done with a heteronuclear broadband decoupling to increase the appearance and sensitivity of the spectra [17]. A second frequency matching the resonance frequency of the coupled protons is applied during the ac-

quisition window, canceling the additional field generated by protons on time average, and, as a result, all signals in the spectrum are recorded as singlets. Application of NOE during the experiment via transfer of population differences from ^{1}H- to neighboring ^{31}P-nuclei triggers a larger occupation of the lower ^{31}P-energy state, yielding increased excitations in the higher energy level.

2.3 Surface coils

RF coils are an essential part of the whole MR system as they belong to the HF technique system (see subsection 2.2.1), which is capable of exciting the spin system with oscillating transverse $\mathbf{B_1}$ fields (excitation coil(s)) and also detect the induced signal afterwards (receive coil(s)). Being responsible for spin excitation and signal detection, there is the need for an optimal coil design in order to maximize the quality of the image or spectrum. However, due to the countless different areas of application and research questions, there are a large number of coil designs that are tailored to the respective case. From a geometric point of view, one can categorize coils into so-called *surface coils*, which are two-dimensional and placed directly on the region of interest, and *volume coils*, which possess a three-dimensional geometry surrounding the region of interest. Volume coils as for example the built-in *body coil* in clinical MRI scanners have the advantage of a homogeneous $\mathbf{B_1}$ field over a large volume, making it favorable for whole body examinations or situations in which a large volume should be covered in a short time span. However, for investigation of smaller volumes, surface coils show enhanced sensitivity and SNR because they are placed directly close to the voxel of interest (VOI). Additionally, surface coils show a high degree of flexibility due to their size and can apply locally stronger $\mathbf{B_1}$ fields, increasing sensitivity, and due to their design, offer a certain degree of localization by their limited detection range.

The aim of this thesis was to perform metabolic investigations in the human liver. Since the human liver itself possesses a huge cross section close to the body surface and is easily accessible within the abdomen, surface coils were used for both signal detection and collection. The simplest surface coil design is a circular single-turn coil. Assuming a uniform $\pi/2$-excitation of all spins in a sample, the detection sensitivity at a distance z along the axis of a circular coil of n turns and radius r which carries a current I is proportional to the magnitude of $\mathbf{B_1}$ per unit current at that position in free space and is given by [28]:

$$B_1 = \frac{\mu n I r^2}{(r^2 + z^2)^{3/2}} \tag{2.31}$$

By the principle of reciprocity, the detection range of a surface coil is, in a first estimation, limited to an approximately hemispherical region with a radius given by half of the coil loop diameter. However, because of existing $\mathbf{B_1}$ field inhomogeneity, the coil sensitivity is neither uniform within this hemisphere nor limited to this region. Moreover, the limited homogeneity of the coil leads to an uneven signal distribution in the obtained spectrum in a way that e.g. high concentrations of a certain metabolite produce an intense resonance in the spectrum although it is more distant from the coil compared to a metabolite with equal concentration in

close proximity. Thus, it is very important to determine the $\mathbf{B_1}$ *sensitivity profile* of a coil in order to correct for $\mathbf{B_1}$ inhomogeneity, which is mandatory for calculating absolute metabolite concentrations (consult section 2.6). Nevertheless, the inhomogeneous $\mathbf{B_1}$ field of a transmit-receive surface coil can also be used as an advantage as the nutation angle (θ) represents a function of position relative to the coil [28]:

$$S \propto B_1 \sin(\gamma B_1 \tau) \tag{2.32}$$

Since the obtained signal is proportional to both B_1 and τ and these are functions of position, one can modulate the localization of the coil by variation of these parameters. It should be noted that pushing $\mathbf{B_1}$ further away comes with lower signal intensity as the detection sensitivity sharply decreases with increased distance between coil and VOI.

Coil development significantly improved during recent years as a variety of coil designs enter the market, each desired for a specific application. Since each coil design has its advantages and disadvantages, it is also possible to separate spin excitation and signal detection to different coils. In practice, larger volume coils for spin excitation are often combined with smaller surface coils for signal detection. This method enables application of a homogeneous $\mathbf{B_1}$ field over a large volume while signal detection is done only at the VOI with high sensitivity and SNR.

2.4 Radio-frequency (RF) pulses

Regardless of whether MRI or MRS is performed, there exists a huge number of different pulses, each with its own purpose, to manipulate spins, e.g. $\pi/2$-excitation, sub-$\pi/2$ excitation, inversion, refocusing, saturation, or recovery. The RF transmitter as part of the HF technique (see section 2.2) is responsible for amplifying input waveforms. An RF waveform itself consists of a set of complex data points with amplitudes and phases that vary with time, typically comprising several hundreds of points [24]. Before the data points are mixed with the carrier frequency and are amplified, they need to be converted into analog format. However, all RF waveforms share the same parameters: center frequency, duration, phase, and amplitude.

The center frequency is typically fixed and selected in a way that it matches the resonance frequency of the nuclei being investigated, also referred to as *on resonance*. Pulse duration represents the length of the RF pulse and defines the bandwidth or rather range of frequencies being excited because of its inverse proportionality. The effective orientation of the RF energy deposited in the tissue is set by the phase of the pulse. More precisely, it sets the axis of rotation the net magnetization experiences during the influence of the pulse. Finally, the pulse amplitude defines the strength of the pulse in terms of how much energy is applied to the nuclei, which determines the amount of rotation they undergo. In brief, pulse amplitude determines the FA (consult Equation 2.14 in subsection 2.1.4). These waveforms need to be combined with the center frequency produced by a frequency synthesizer, also called *modulation*. There are two ways of mixing, the *amplitude modulation* where the energy is simultaneously distributed to all frequencies at the same time resulting in equal treatment of all frequencies or the *fre-*

quency/phase modulation describing sequential excitation of each frequency/phase, each with the same amplitude. The overall aim is to achieve an equal treatment of all frequencies in a way that all spins are rotated uniformly, leading to a common starting point after excitation. Pulses can be divided by their *pulse shape* representing the waveform in time:

2.4.1 Block RF pulses

Non-selective pulses, often known as *hard pulses*, *rectangular pulses* or *block pulses*, have a short duration and a constant amplitude. Their aim is to excite a broad frequency range with a uniform amplitude. Typical application scenarios are to determine the resonance frequency of the sample, volunteer, or in case very short RF pulses are needed. They are also often used in an experiment where T_1 and T_2 relaxation times of metabolites are measured. From a programming point of view these pulses are easiest to implement since they do not need a complex modulation function. FT of a block pulse in the time domain leads to a SINC function in the frequency domain representing the slice profile (consult Figure 2.8a). Another field of application for block pulses is to use them as saturation pulses in order to completely saturate certain resonances. For example, so-called *DELAY ALTERNATING WITH NUTATION FOR TAILORED EXCITATION* (DANTE) pulses consist of a series of short, non-selective pulses with low FA in order to selectively excite a small frequency range to suppress signal from a certain metabolite. In such a situation, the center frequency is precisely set to the resonance frequency of the metabolite to be saturated and the pulse bandwidth is adapted by pulse duration and repetition rate. This kind of RF pulse is used in Study 2 to achieve a complete saturation of the γ-ATP signal for calculation of ATP synthesis rates (consult chapter 6).

2.4.2 Selective RF pulses

In contrast, the second class of pulses is called *frequency-selective pulses* or *soft pulses*, which do not possess constant amplitudes at all times or at all frequencies during their transmission. These pulses are able to excite a narrower frequency bandwidth because of a longer pulse duration. Therefore, this kind of pulses is usually used for in-vivo MRI/MRS where selective excitation is desirable, e.g. spatial slice selection, water-suppression, and spectral editing, because excitation preferably should only occur within the targeted region.

The usual pulse of choice is a SINC-PULSE which represents an amplitude modulated pulse of short duration, which leads to an uniform amplitude and phase excitation in the requested slice. In order to be able to excite a certain frequency, that frequency has to be within the pulse bandwidth. Because several frequencies at the same phase are included in a pulse, its shape approaches that of a sinc function, an infinite function that contains all possible frequencies in the bandwidth [24]. However, as a sinc function possess an infinite span, and duration as well as bandwidth of pulses are limited, the real pulse shape is applied as a truncated sinc function at the n-th zero crossing:

$$B_1(t) = B_{1,max} \cdot f_B(t) = B_{1,max} \frac{\sin(2\pi nt/T)}{(2\pi nt/T)} \text{ for } -\frac{T}{2} \leq t \leq +\frac{T}{2} \tag{2.33}$$

$B_{1,max}$ represents the maximum amplitude of the RF pulse in Tesla and T denotes the pulse duration in seconds. A sinc pulse with five lobes ($n = 3$) and the corresponding slice profile is shown as an example in Figure 2.8b. Due to truncation, the pulse profile is not rectangular and exhibits oblique sides. Sinc pulses are commonly used as frequency-selective excitation and refocusing pulses.

Another type of RF pulse used for frequency-selective saturation is a Gaussian pulse. Since the Gaussian function is its own FT, the slice profile is smooth without 'wiggles' compared to the sinc function (see Figure 2.8c). Gaussian pulses possess a narrower excitation bandwidth making them ideal for water and lipid suppression.

2.4.3 Adiabatic RF pulses

In MRS it is often favored to achieve an exact $\pi/2$- or π-nutation of the magnetization in the VOI. All aforementioned RF pulses rely on the presence of a homogeneous $\mathbf{B_1}$ field, as the pulses are applied *on resonance* and the FA is given by Equation 2.14. Therefore, in presence of $\mathbf{B_1}$ inhomogeneities, different FAs are produced, resulting in signal loss and artifacts. In practice, most RF coils and especially surface coils provide only inhomogeneous excitation fields. To compensate for this circumstance, a special class of RF pulses, a so-called hyperbolic secant (HS) or *adiabatic pulse*, can be applied.

Adiabatic pulses feature simultaneous modulation of both the amplitude and frequency of the applied RF field (consult Figure 2.8d). Their strong tolerance against $\mathbf{B_1}$ inhomogeneities and therefore to frequency offsets is achieved by constantly varying the transmitter offset frequency from far off-resonance to on-resonance. The amplitude $B_1(t)$ and frequency $\Delta\nu(t)$ modulations of an adiabatic pulse can be described using the modulation functions $f_B(t)$ and $f_\nu(t)$ as

$$B_1(t) = B_{1,max} \cdot f_B(t) \tag{2.34}$$

$$\nu(t) - \nu_c = \Delta\nu(t) = \nu_{max} \cdot f_\nu(t) \tag{2.35}$$

with $B_{1,max}$ and ν_{max} representing the maximum RF amplitude and frequency offset (Hz), respectively, and ν_c being the RF carrier frequency. The HS1 pulse, which is typically used on clinical systems, shows the following modulations:

$$B_1(t) = B_{1,max}\,\mathrm{sech}\left(\beta(1 - \frac{2t}{T})\right) \tag{2.36}$$

$$\Delta\nu(t) = \nu_{max}\tanh\left(\beta(1 - \frac{2t}{T})\right) \tag{2.37}$$

In the above equations, β represents a dimensionless truncation factor, often defined as $sech(\beta) = 0.01$ and T is the pulse length, whereby $0 \leq t \leq T$. Applying an adiabatic pulse over its full duration causes $\mathbf{B_1}$ to rotate from the z-axis into the $-z$-direction (=inversion, adiabatic full passage (AFP)). Alternatively, executing it only over its half duration (0 till $T/2$), magnetization is flipped into the transverse plane (=excitation, adiabatic half passage (AHP)).

An adiabatic pulse leads to an excitation (AHP) or inversion (AFP) of all spins with frequencies in $-\nu_{max} \leq \nu \leq \nu_{max}$ in case the *adiabatic condition* is fulfilled. The adiabatic condition describes a state where the change in the effective magnetic field $B_{1,eff}$ is slow in order that it follows the field without energy exchange between the spin system and the lattice. Therefore, the rotation of $B_{1,eff}$ needs to be much slower than the precession of the magnetization around this field:

$$\mid \frac{d\theta}{dt} \mid \ll \gamma \mid B_{eff} \mid \tag{2.38}$$

The easiest way to achieve the adiabatic condition is to increase the amplitude of the pulse, as every pulse has a minimum amplitude threshold that needs to be transcended before the adiabatic condition is properly satisfied. The upper limit for amplitudes to stay within the condition is typically not reached in vivo, due to SAR limitations. In most multinuclear research applications, volume coils are unavailable. Therefore, typically surface coils in combination with AHP pulses are very common in MRS. However, drawbacks of AHP pulses are the high level of RF power needed, which increases SAR and the presence of an asymmetric excitation profile (consult Figure 2.8d). Adiabatic pulses also possess a larger pulse duration of several milliseconds compared to the other pulses and their effective bandwidth is B_1 dependent.

As this thesis attempts to detect ^{31}P-metabolites in the liver by localized MRS, an AHP excitation pulse was chosen, since this kind of excitation pulse provides a uniform excitation of all spins within the 3D-VOI, although the surface coils employed suffer from an inhomogeneous B_1 excitation field.

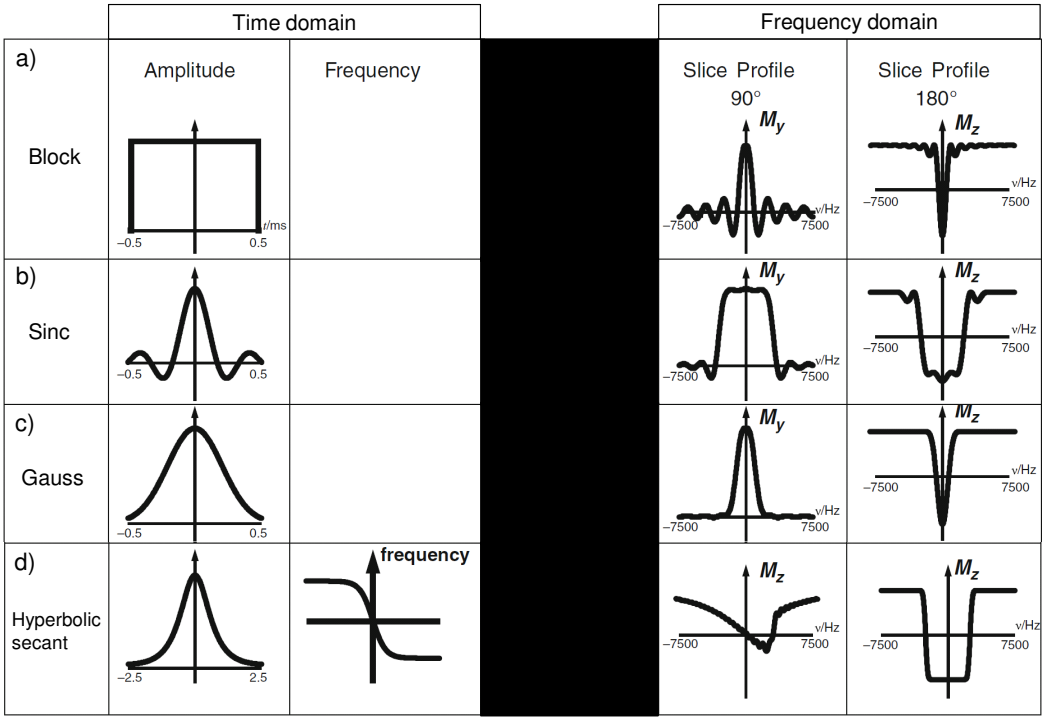

Figure 2.8: Overview of the most prominent RF pulses, pulse shapes and corresponding slice profiles for $\pi/2$- and π-excitation. All bandwidths are shown for pulse durations of 1 ms, except for the HS pulse (5 ms). Note that the HS pulse is the only one with frequency modulation and is displayed here as an AFP pulse, the AHP pulse profile can be obtained by truncating the pulse at its midpoint. Adapted from [40].

2.5 Localization in MRS

In-vivo MRS critically relies on the ability to perform signal detection from a precisely predefined region within the body in order to serve as a clinical tool. Optimally, the obtained spectra should contain signal exclusively originating from the selected volume, known as the VOI, without any signal loss from within the VOI and no contamination from outside it. Over the last 50 years, scientists have developed and optimized a variety of MRS sequences through enhancements in coil design, magnetic field gradients, and pulse sequence designs [28]. However, due to gradient system constraints the shape of the VOIs is still very limited which is why a cuboidal shape is often applied and acquisition of fully contamination-free spectra is difficult, especially in the case of higher concentrations of metabolites surrounding the VOI.

Although various localization sequences have been developed in the literature, only three are currently widely implemented on commercial scanners. These so-called volume selection sequences use the static gradient system for localization and provide a cuboidal VOI with minimal outside contamination (see Figure 2.9) [28]. In ^{1}H-MRS the two echo-based sequences Point RESolved Spectroscopy (PRESS) [41] and STimulated Echo Acquisition Mode (STEAM) [42] are often used, while for ^{31}P-MRS Image-Selected In vivo Spectroscopy (ISIS) [43] is a popular localization sequence. Different localization techniques are required because each nucleus exhibits distinct metabolite relaxation properties and may require additional pulse sequence elements, e.g. water-suppression for ^{1}H-MRS. However, these methods have in common that the result will be a single spectrum from one VOI and therefore they belong to the single-voxel localized spectroscopy (SVS). Additionally, there exists the non-localized spectroscopy (NLS) where the signal is localized by the geometry and $\mathbf{B_1}$ profile of the coil loops and the multi-voxel localized spectroscopy (MVS), a combination of MRI and MRS which yields multiple spectra across a defined volume. The results of this thesis rest upon utilization of the STEAM and ISIS sequences for ^{1}H- and ^{31}P-MRS, respectively.

Both sequences apply narrowband RF pulses in combination with static field gradients along all three orthogonal axes to localize the VOI. The spins are manipulated such that the obtained signal originates from the VOI while signal from outside is eliminated. In order to position and shape the VOI, RF pulse frequency and gradient strength are adjusted accordingly.

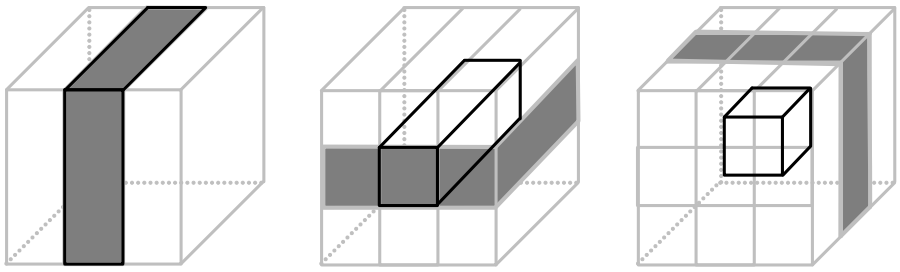

Figure 2.9: Volume selection using static magnetic field gradients. Gradients and RF pulses are applied sequentially to mark a specific slice along each of three orthogonal axes consecutively. Each pulse cluster defines a slice of magnetization (gray); the intersection of the first two slices forms a column, and the third defines a cuboidal region where magnetization is affected by all three clusters (black region).

2.5.1 Stimulated echo acquisition mode (STEAM)

The STEAM sequence consists of the application of three $\pi/2$-excitation pulses, each in combination with an active gradient in one of the three dimensions to generate an echo (see Figure 2.10a). At first, the initial $\pi/2$-excitation pulse (with gradient G_z) flips the magnetization into the xy-plane. A spoiler gradient then dephases the spins in this plane so that they are isotropically distributed before the second $\pi/2$-excitation pulse (applied along the x'-axis) with a coding gradient G_x flips the magnetization to the z-plane. Application of the third $\pi/2$-excitation pulse (with gradient G_y) returns magnetization into the xy-plane within a cuboidal VOI and the refocusing signal produces the *stimulated echo*.

The STEAM sequence can be combined with a frequency-selective RF pulse which suppresses unwanted magnetization signals, e.g. the dominant water peak. Immediately after exciting the unwanted spins, a powerful gradient is applied, resulting in complete phase dispersion of the spins. This process is referred to as *spoiling* the unwanted magnetization. It is particularly important in ^{1}H-spectroscopy to suppress the water signal because the concentration of water in biological tissue is several orders of magnitude higher than the concentration of any metabolite of interest (consult section 3.4).

2.5.2 Image selected in vivo spectroscopy (ISIS)

The ISIS sequence allows volume selection by post-acquisition signal combinations. Depending on the desired degree of localization, one to three π-pulses together with encoding gradients, each in one of the three orthogonal axes, are applied before a $\pi/2$-pulse for excitation and detection of the FID (see Figure 2.10b). In its most simplistic form, a gradient, e.g. in the x-direction (G_x), is applied in combination with a π-inversion pulse in the x' direction to invert a slice of the magnetization. After a certain delay t_d, a $\pi/2$-pulse is again applied in the x' direction to flip the magnetization into the xy-plane, whereas the signal from the defined slice is 180° out of phase and can be collected. By subtracting the obtained signal from a second experiment where only the $\pi/2$-pulse without application of a gradient is used, all signal from outside the desired slice is subtracted and only the previously selected signal is preserved. Higher-dimensional localization requires more combinations of selective inversion pulses and the number of necessary experiments for an n-dimensional ISIS is given by 2^n. Table 2.2 shows an exemplary scheme for application of a 3D-ISIS.

Due to the design of the ISIS sequence, it can be divided into the preparation phase (π-pulses) where localization takes place and is prepared, followed by a simple excitation ($\pi/2$-pulse) and acquisition of the FID. The excitation pulse itself can be a simple $\pi/2$-pulse, or a sequence of pulses designed to achieve measurements of relaxation times, water-suppression, or spectral editing [44]. The ISIS sequence is primarily dependent on T_1 relaxation because longitudinal magnetization constantly recovers between the preparation and excitation. The influence of T_2-weighting can be almost neglected since signal acquisition immediately starts after the excitation pulse, making ISIS the sequence of choice for metabolites with short T_2 relaxation times as it is for ^{31}P-metabolites, where T_2 is below 100 ms for most metabolites at 3 T.

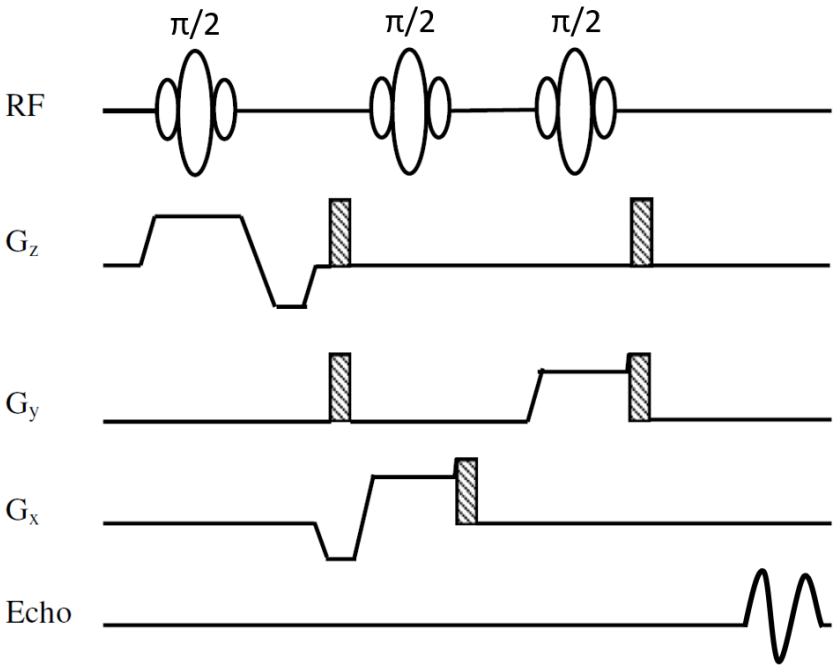

(a)

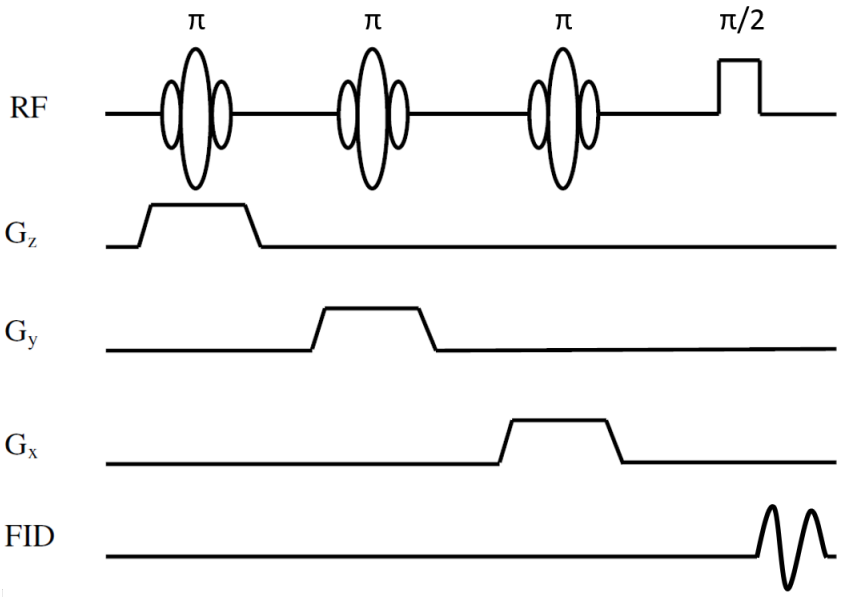

(b)

Figure 2.10: Typical pulse sequence diagrams for the (a) STEAM and (b) ISIS sequence. RF pulses are applied as $\pi/2$- or π-pulses, gradients $G_{x,y,z}$ enable slice excitation. Spoiler gradients are shown hatched. STEAM generates an echo while ISIS uses inversions before acquiring the FID. Adapted from [28].

Table 2.2: Experimental ISIS cycle diagram illustrating the subtractive localization method using eight scans and orthogonal inversion pulses for 3D-voxel selection as proposed by Ordidge et al. [43].

Experiment	Gradient G_x	Gradient G_y	Gradient G_z	Contribution to total spectrum
1	Off	Off	Off	+1
2	On	Off	Off	-1
3	Off	On	Off	-1
4	On	On	Off	+1
5	Off	Off	On	-1
6	On	Off	On	+1
7	Off	On	On	+1
8	On	On	On	-1

2.5.3 Chemical shift displacement (CSD)

The CSD describes a common artifact in localized MRS caused by the different chemical shifts of metabolites resulting in an impure spatial localization of the obtained signals. Applying the same RF pulse, metabolites with different chemical shifts and therefore Larmor frequency will be excited at slightly different spatial positions. Therefore the manually selected localization voxel in MRS only represents the exact origin of signal for the metabolite which resonates at the center frequency of the excitation pulse. The spatial displacement Δx between two metabolites can be calculated and depends on their frequency difference $\Delta\nu$, the bandwidth BW of the RF pulse, and the size of the VOI according to the following equation:

$$\Delta x = (\Delta\nu/BW) \cdot VOI \tag{2.39}$$

The CSD must be considered when performing quantification of metabolites, especially in heterogeneous tissues. Since for two- or three-dimensional localization multiple orthogonal pulses are necessary, each of these pulses may experience a different CSD in respect to the VOI size in each direction. Therefore, the excited volume may partially extend outside the desired VOI.

One strategy to minimize the CSD effect is the application of adiabatic pulses, since they provide a broader excitation bandwidth together with uniform excitation. The effect and extent of the CSD in absolute quantification of the ^{31}P-metabolites γ-ATP and inorganic phosphate (P_i) are discussed and exemplarily calculated in chapter 5.

2.6 Quantification of metabolites

The ability for quantification of metabolites is crucial for interpretation of spectra and aims to derive meaningful biochemical information. In contrast to qualitative approaches, quantitative methods allow for precise determination of metabolite concentrations which can reveal even minor changes not visible upon visual inspection. Quantification per se enables detection of differences in metabolite concentrations between tissues, organs, diseases, and time points. Therefore it opens the way for comparisons between people suffering from diseases and control groups, as well as tracking disease progression or therapeutic effects.

The simplest application is the *relative quantification* of metabolites by comparing their amplitudes and calculating relative ratios. Studies performing ^{31}P-MRS in liver often report relative ratios of metabolites with respect to the ATP-signal, e.g. PDE/ATP, PME/ATP, or P_i/ATP [45–48] or ratios of individual metabolites relative to the total ^{31}P-metabolite signal [49, 50]:

$$\left[^{31}P_{total}\right] = [PMEs] + [P_i] + [PDEs] + [\gamma\text{–}ATP] + [\alpha\text{–}ATP] + [NAD(P)H] + [\beta\text{–}ATP] \quad (2.40)$$

However, an interpretation of metabolite ratios can be difficult because a change in ratio can have multiple causes. Assuming a change in P_i/ATP ratio from 0.8 to 1.0 may be caused by i) an increase in P_i concentration, ii) a decrease in ATP concentration, or iii) changes in both metabolite concentrations. Therefore, it is important to be able to determine absolute concentrations to make reliable statements. Study 1 of this thesis presents one way to set up a pipeline to be able to report absolute values of ^{31}P-metabolites by absolute quantification in the human liver (consult chapter 5). In addition to that, the ability to perform absolute quantification is a prerequisite for calculation of quantitative fluxes through metabolic pathways as described for the ATP synthesis rate using the ^{31}P-MRS ST approach presented in Study 2 (see chapter 6).

One major advantage of MRS is the ability to assess absolute concentrations of metabolites in vivo. The concentrations can be reported in millimoles per liter ($^{mmol}/_{L}$ or mM) and micromol per gram of tissue ($^{\mu mol}/_{g}$). The foundation for this principle is the fact that the macroscopic bulk magnetization $\mathbf{M_0}$ is directly proportional to the number of spins in the sample (see Equation 2.11). In general, the signal intensity for a metabolite M, detected as an induced current proportional to the transverse magnetization in a receiver coil, is given by [17]:

$$S_M = NSA \cdot RG \cdot \nu_L \cdot c_M \cdot V \cdot f_{sequence} \cdot f_{coil} \quad (2.41)$$

In the above formula, NSA and RG denote the number of signal averages and receiver gain setting, ν_L denotes the Larmor frequency, c_M is the molar concentration of the metabolite, V represents the volume size of the VOI, and $f_{sequence}$ and f_{coil} are correction functions influencing the detected signal by the NMR pulse sequence and RF coil, respectively. Whereas $f_{sequence}$ depends on accessible parameters such as repetition time/echo time (TR/TE), number and kind of RF pulses, spectral bandwidth (BW) as well as on the individual T_1/T_2 relaxation times of the metabolites, f_{coil} is dependent on factors like coil geometry and coil quality which are not directly measurable, preventing direct calculation of c_M. Therefore, it is common practice to make use of a calibration or reference compound with a fixed, known concentration c_{ref} in

order to be able to report absolute metabolite concentrations according to:

$$c_M = c_{ref} \cdot \frac{S_M}{S_{ref}} \cdot c_{Mref} \tag{2.42}$$

In Equation 2.42, S_{ref} represents the obtained signal from the reference compound and c_{Mref} denotes the correction factor for differences between the reference and the metabolite of interest, e.g. relaxation times, gyromagnetic ratio, and spatial position relative to the coil. Nevertheless, calculation of c_{Mref} is a tedious process, which is why many in-vivo MRS studies report metabolite ratios as an alternative, because c_{Mref} is then identical for both metabolites and many of the unknown parameters of Equation 2.41 are not necessary.

For hepatic ^{31}P-MRS it is common in the literature to choose the γ-ATP signal as the *internal reference* metabolite (see Figure 2.11a). In order to obtain absolute concentrations using the internal reference method, usually the γ-ATP concentration is set to a specific fixed value for the entire cohort under investigation based on a literature-derived value. Most of the studies calculate the individual metabolite concentrations based on a fixed γ-ATP concentration between 2.5 mM [51–53] and 2.65 mM [54]; these concentrations are based on biopsies reported by Hultman et al. [55]. This kind of quantification allows to report absolute concentrations by comparing the individual peak amplitudes with that of γ-ATP, which ideally represents a stable endogenous reference. However, the significance of the results is subject to the variability of the reference metabolite. It is well known that in case the metabolism is slightly challenged or in the presence of certain pathologies, ATP concentration can vary. These changes may be obscured using this technique. For example, it was previously shown that the concentration of γ-ATP and P_i decrease at the same time by approximately 37% and 25% in people suffering from alcohol-associated hepatitis and cirrhosis [56] and type 2 diabetes (T2D) [33]. Relative ratios would fail to detect these alterations and lead to wrong conclusions.

In order to obtain real tissue concentrations in absolute units, the internal reference can be replaced by an *external reference* which has a well-known concentration so that normalization can be done in a calibration experiment (see Figure 2.11b). Here, c_{Mref} in Equation 2.42 becomes relevant again because in-vivo measurements need to be calibrated to in-vitro measurements. Because the calibration sample cannot be measured at the same position from which the in-vivo spectrum is acquired, especially $\boldsymbol{B_1}$ inhomogeneities need to be considered. For this, the in-vitro and in-vivo voxel sizes are kept constant and typically the in-vitro voxel is acquired at a position symmetrically about the center of the coil or the $\boldsymbol{B_1}$ field distribution of the used coil is determined beforehand and the spectrum is corrected for those (consult Figure 2.11b). During the whole process, the position of the volunteer remains the same and is not changed. However, it should be noted that this procedure is not possible using a surface coil, since its geometry, design, and sensitivity are entirely front-facing, which hampers signal acquisition on its backside. Due to this reason the external reference method is not applicable for ^{31}P-MRS using a surface coil.

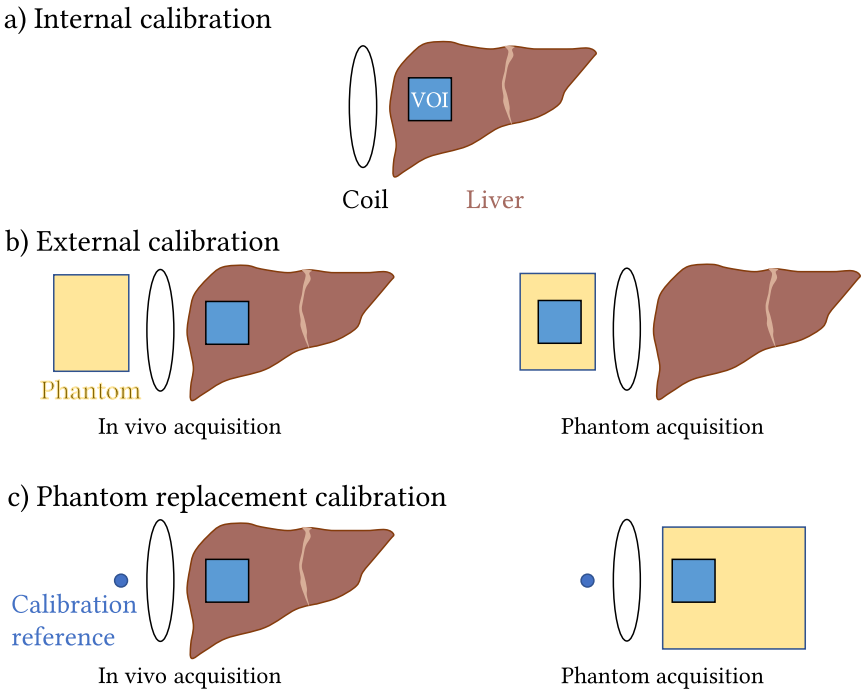

Figure 2.11: Overview of the different calibration methods for estimation of metabolite concentrations. (a) Internal calibration using a metabolite within the in-vivo spectrum as reference. (b) External calibration by putting a phantom in an equal sensitivity area as the in-vivo VOI. Two separate scans are acquired within one session, in vivo (left) and in a phantom (right). (c) Phantom replacement calibration consisting of two separate sessions, one in vivo (left) and one in vitro (right). Note that the position of the VOI is exactly reproduced in the phantom acquisition. A calibration reference is used to account for differences in coil loading. Please note that most surface coils do not possess a symmetric $\boldsymbol{B_1}$ field distribution, which is why option (b) is often not feasible. Adapted for the liver from [17].

In order to still use the advantage of the external reference, the elimination of the assumption of a reference concentration, another method of calibration experiment is aimed for, the so-called PHANTOM REPLACEMENT EXPERIMENT (see Figure 2.11c). Here, a previously mixed phantom of known composition and concentration, mimicking the human tissue, is measured after the volunteer measurement under conditions as close as possible to that in vivo. This procedure tries to minimize errors inlcuding $\boldsymbol{B_1}$ excitation inhomogeneities by placing the voxel at the identical position as previously used in vivo. Nevertheless, there are several correction factors which are important to be incorporated to allow assessment of valid absolute concentrations, e.g. differences in relaxation effects, pulse profile, and sensitivity of the coil (consult the following subsection 2.6.1). Although implementation of absolute quantification by the phantom replacement technique is very time consuming, it offers huge advantages in detecting physiological metabolite concentrations. Study 1 deals with the setup of a method which is able to detect absolute concentrations of ^{31}P-metabolites (consult chapter 5). The principle of absolute quantification by the phantom replacement technique in ^{31}P-MRS in the healthy human liver was first described by Meyerhoff et al. in 1990 [57], although he already applied the technique in 1989 in people with alcoholic hepatitis and was able to show that relative ratios are not a sensitive measure [56].

2.6.1 Correction factors for phantom replacement technique

In order to quantify the concentration of a metabolite in absolute units (mM), it is crucial to perform a calibration experiment using a phantom to account for several coil-dependent correction factors. It should be noted that the original method using the phantom replacement technique required moving the phantom to the same position post in-vivo measurement and repeating the protocol. This is perfectly feasible and practical for smaller studies; however, if the method is to be used permanently in large cohort studies, the repeated in-vitro experiment is not only time-consuming, but also limits volunteer throughput. Therefore, a comprehensive and very time-consuming but one-time series of measurements can be carried out as an alternative, which covers all VOI positions for subsequent in-vitro data reconstruction. This procedure considerably shortens the in-vitro measurement. It is only necessary to acquire a short spectrum of another reference sample during each in-vivo measurement in order to correct for coil loading, as shown in the next paragraph.

The following section gives a general description of mandatory correction factors, which need to be assessed in vitro to guarantee a meaningful application of the phantom replacement technique. The method for the one-time detailed measurement of the phantom is described here. As a reference standard for the phantom replacement technique, usually a 2–5 L phantom containing monopotassium phosphate (KH_2PO_4) is measured with the identical sequence and setup as in vivo [56–60]. The final concentration c^{ij} (in mM) for each corresponding ^{31}P-metabolite i in volunteer j can be obtained by the following Equation 2.43 [61]:

$$c^{ij} = \frac{A^{ij}}{A_{ph}} \cdot c_{ph} \cdot f^{i}_{offset} \cdot f_{B_{1,xyz}} \cdot f^{i}_{T_1} \cdot f^{j}_{loading} \cdot f^{j}_{HL} \tag{2.43}$$

Pulse profile

The excitation profile of the applied $\boldsymbol{B_1}$ excitation pulse is one crucial factor for correct assessment of metabolite concentrations. Since $\boldsymbol{B_1}$ excitation pulses always have a limited bandwidth and, depending on the pulse type, also exhibit differences in their slice profile (see section 2.4), metabolites experience a different excitation FA leading to differences in their signal amplitude. Correcting for these bandwidth-related excitation pulse imperfections ensures that the non-equivalent excitation of different metabolites is compensated in order to directly compare signal amplitudes.

From an experimental point of view, the individual correction of each metabolite f^{i}_{offset} can be conducted by an in-vitro experiment series of a single-resonance phantom where the transmitter frequency of the $\boldsymbol{B_1}$ excitation pulse is continuously varied to cover the entire frequency range of interest. In practice, one acquires a spectrum at the center frequency of the later desired in-vivo protocol, followed by n spectra at discrete frequencies corresponding to the frequencies of the metabolites of interest. Finally, the respective amplitudes of the metabolites can then be normalized to the amplitude at the center frequency.

Figure 2.12 shows an exemplary result of the pulse profile correction of a HS AHP used for detection of ^{31}P-metabolites, covering a spectral range of about 1400 Hz or 23 ppm. The ex-

perimentally obtained data agree with the mathematically derived pulse shape of the HS AHP in Figure 2.8d. As a result, resonances upfield from the center frequency, e.g. the three ATP resonances need to be corrected upwards, while downfield the amplitudes have to be lowered.

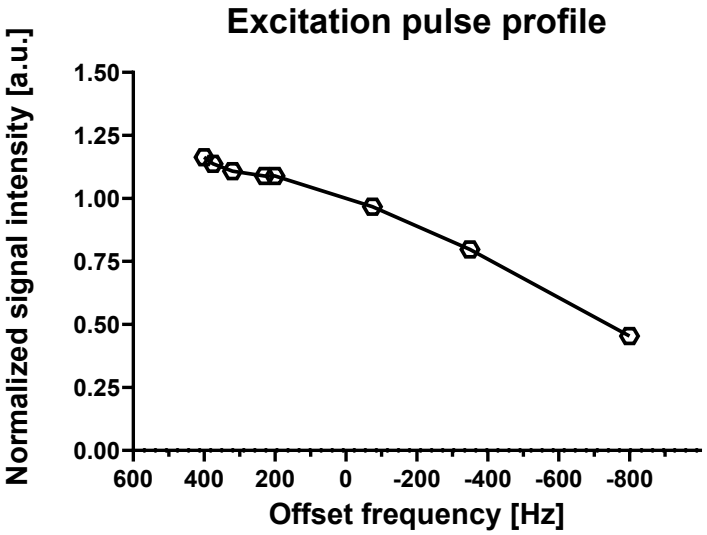

Figure 2.12: In vitro obtained $\boldsymbol{B_1}$ excitation pulse offset correction. Eight different frequency offsets corresponding to the positions of the most prominent ^{31}P-metabolites (PE, PC, P_i, GPE, GPC, γ-ATP, α-ATP, β-ATP) relative to the center of the excitation pulse offset (0 Hz) in the in-vivo experiment were set to correct for the HS AHP pulse profile. All signals were normalized to the respective amplitude at 0 Hz offset. Adapted from [62].

Spatial B_1 field distribution

Next to correction of excitation pulse frequency, the spatial distribution of the $\boldsymbol{B_1}$ excitation pulse needs to be considered, especially when applied using a surface coil which by its design suffers from an inhomogeneous excitation (compare section 2.3). In a first approximation, it can be assumed that the excitation profile of a surface coil is a hemispherical region with radius r, which corresponds to half the diameter of the coil element, but inhomogeneities quickly change this assumption. For this reason, the coil profile should always be measured and the amplitudes of metabolites within the VOI used later should be corrected accordingly. Since the VOI can be placed three-dimensionally in the volunteer in relation to the coil position, a correction in all three spatial directions is necessary. While in theory a continuous grid of offsets could be acquired, a more practical solution is to move the VOI at discrete intervals, e.g. ±1 cm steps, to obtain a profile. Please note that this procedure is conducted for detailed, one-time measurement of the phantom to assess $f_{B_{1,xyz}}$, while the original approach exactly reproduces the position of the VOI within the phantom immediately after the in-vivo experiment for each volunteer.

Figure 2.13 shows the experimentally obtained excitation pulse profiles of a HS AHP pulse, acquired in vitro using two different surface coils. The hemispherical excitation profile is clearly visible and there is a homogeneous area of excitation close to the surface coil, which decreases rapidly towards higher distances and RL-offsets. An exemplary mathematical description of

such a spatial distribution map is given in Figure 2.14. While for single-loop surface coils the y-offset, representing the distance between VOI perpendicular to the coil plane, follows a linear function (Figure 2.14a), the x- and z-offsets show a distance dependency better described by a quadratic function (Figure 2.14b).

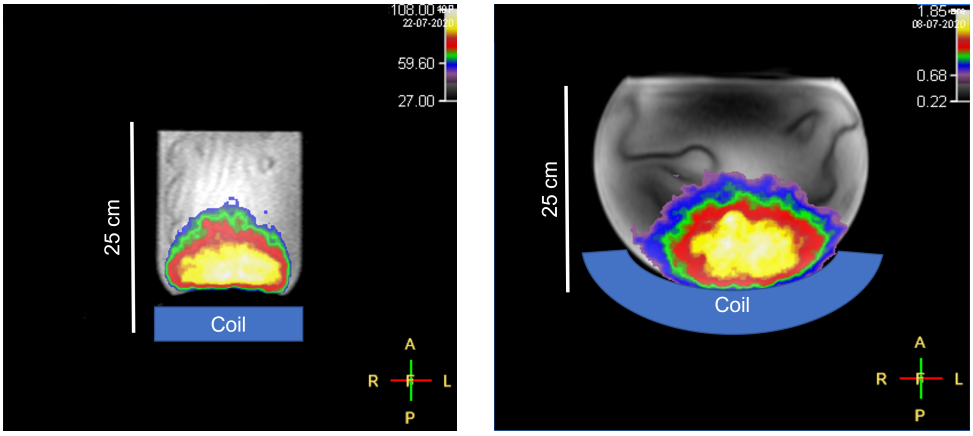

(a) (b)

Figure 2.13: Spatial B_1 excitation profiles of a HS AHP pulse, acquired in vitro using two different surface coils. The sensitivity profiles are shown in rainbow colors for (a) a flat circular single-loop coil and (b) a curved rectangular quadrature surface coil. The sensitivity values represent arbitrary units.

T_1 correction

T_1 correction is a very important factor for quantifying metabolite concentrations because each metabolite possesses a different relaxation time. The individual relaxation time of a metabolite is influenced by its molecular structure and electromagnetic environment leading to different T_1 values even for the same metabolite dependent on the investigated organ and applied magnetic field strength. In MRS, the applied TR is typically shorter than the T_1 relaxation of the metabolites being investigated, which is why without proper correction, T_1 weighting can lead to inaccurate quantification of metabolite levels. The correction process involves determining individual T_1 correction factors $f_{T_1}^i$ for each metabolite i. Because an individual assessment of T_1 relaxation times is time-consuming, either literature values are used or performed on a separate group using an IR sequence. Table 2.3 shows T_1 relaxation times of the most prominent ^{31}P-metabolites which are typically used for T_1 correction in the human liver at 3 T. Note that there is a large span of T_1 relaxation times from <0.5 s for γ-ATP to almost ~7 s for glycero-phosphoethanolamine (GPE), which is why ^{31}P-MRS protocols are applied at different TRs dependent on the metabolites of interest.

$$f_{T_1}^i = \frac{A^{ij}}{1 - \exp\left(-TR/T_1\right)} \tag{2.44}$$

In addition to the T_1 correction of the metabolites in vivo, it should be noted that the phantom used may have a considerably longer T_1 time. Therefore, it is essential to ensure that this is determined experimentally and corrected.

Table 2.3: T_1 relaxation times of the most prominent ^{31}P-metabolites acquired at 3 T in the human liver. Values represent means obtained from six volunteers [51].

Metabolite	PE	PC	P_i	GPE	GPC	γ-ATP	α-ATP	β-ATP
T_1 [ms]	1810	2240	730	6980	4260	430	580	550

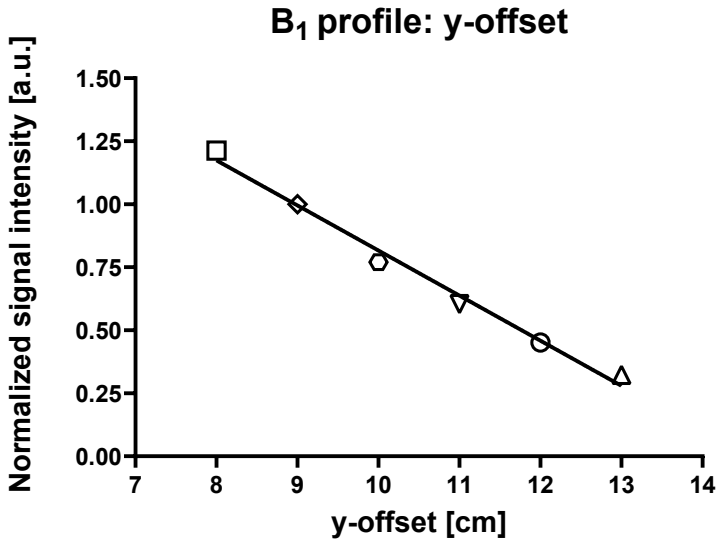

(a)

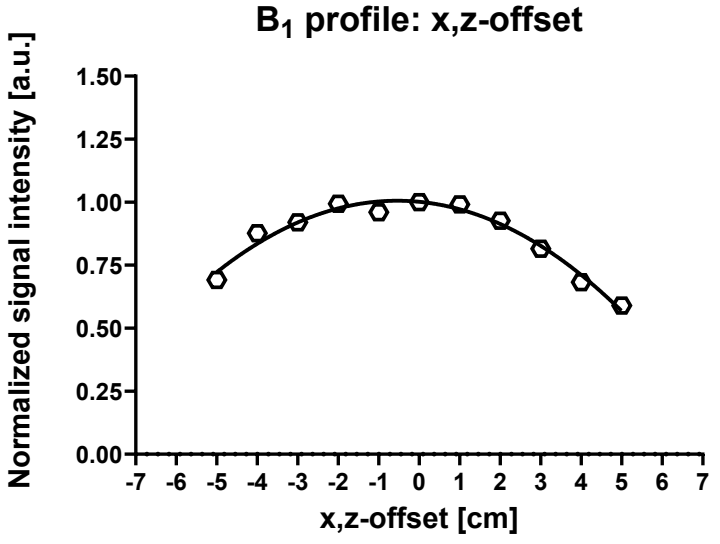

(b)

Figure 2.14: In vitro obtained B_1 excitation pulse correction in all three spatial dimensions to correct imperfect VOI placement relative to the central position using a single-loop surface coil. (a) Sensitivity profile perpendicular to coil plane (y). (b) Profile along coil axes (x, z). To assess profiles, the VOI was moved in discrete intervals of ±1 cm steps. Figures adapted from [62].

Coil loading

Since the desired in-vivo concentrations are derived from a separate phantom experiment, differences in coil loading between the human tissue and the phantom need to be considered. During each measurement, the coil is subjected to a loading by the sample (tissue or phantom) to be analyzed, i.e. there is an interaction between the coil and the sample. Samples considerably influence the coil loading through their electrical conductivity and dielectric properties. As a result, the coil changes its electrical properties, particularly with regard to its impedance and resonance frequency. This can lead to coil heating accompanied by a reduction in coil sensitivity. Even small signal changes may have a significant effect on the detection of metabolite signals resulting in an incorrect estimation of concentrations.

Since the in-vivo metabolite amplitudes are normalized to an in-vitro phantom of known concentration, phantom coil loading must be taken into account. Experimentally, a small external reference sphere is placed on the coil's backside or interior and its signal is measured using a non-localized sequence in both in-vitro and in-vivo sessions. This external reference can be used to determine the interaction between the coil and different samples, as it is a constant factor in every measurement. Amplitudes are compared as a ratio and thus provide a correction factor accounting for different coil loading according to Equation 2.45:

$$f^{j}_{loading} = \frac{A^{ph}_{ref}}{A^{j}_{ref}} \tag{2.45}$$

It should be noted that the compound used should resonate far from any metabolite of interest which is why formic acid or methylphosphorustriamide are typically used for ^{31}P-MRS.

Hepatic lipid (HL) content

For accurate absolute quantification, it is mandatory to ensure that the in-vivo voxel is not only completely localized in the liver, but also the VOI purely contains ^{31}P-signal. This is important because 100% of the volume acquired in vitro contains ^{31}P-signal. Since the liver is generally considered homogeneous, an often not negligible amount of lipids may occupy space within the acquired VOI. This presence of lipids effectively dilutes the in-vivo ^{31}P-metabolite signal, leading to an underestimation of concentrations. Especially when performing measurements in people with T2D, this underestimation even increases since a significant amount of people suffering from metabolic dysfunction-associated steatotic liver disease (MASLD) build up high amounts of HL content [34].
Therefore, the not bioenergetically active lipid signal needs to be assessed with a suitable ^{1}H-MRS protocol. In the end, all ^{31}P-signals have to be corrected for the amount of HL content in the liver.

2.7 Saturation transfer (ST)

In addition to ^{31}P-MRS for relative or absolute quantification of metabolites, it is also possible to perform ^{31}P-MRS for assessment of reaction kinetics of chemical reactions [18]. This technique is called magnetization transfer (MT) and its most common form is the so-called saturation transfer (ST) technique, allowing a transfer of magnetization between two nuclei coupled by chemical exchange. A ST experiment enables assessment of unidirectional exchange rates and metabolic fluxes while still maintaining steady-state conditions. This brings the advantage of tracer-free assessment of chemical reaction kinetics, because no exogenous agents are required. Performing the ^{31}P-MRS ST technique in humans, one is able to assess reaction kinetics in several organs as the brain [63–67], the heart [68–72], the liver [19,35,51,52,73–76] and skeletal muscle [77–86]. Here, the measured metabolic fluxes include the creatine kinase (CK) reaction and ATP synthesis rate (compare section 3.3). It is to note that in the liver, only ATP synthesis rates are observed due to the absence of PCr (see section 3.5).

2.7.1 Principle of chemical exchange

The underlying principle of ST involves observing chemical reactions between two metabolites A and B [18] (see Equation 2.46):

$$X + A \underset{k_r}{\overset{k_f}{\rightleftharpoons}} B + Y \tag{2.46}$$

In order to calculate the pseudo-first order equilibrium forward rate constant (k_f) of a reaction, a two-site chemical exchange model between metabolites A and B, as shown in Equation 2.46, is typically assumed. This model assumes that metabolite B is continuously synthesized from a metabolite X and A.

In order to assess k_f, the signal of metabolite A is continuously saturated by perturbation of its relaxation using a highly-selective RF pulse right before the acquisition of the spectrum. The saturated spins of metabolite A, whose magnetization is zero and therefore MR invisible, then exchange with metabolite B causing its signal to decrease from $M_{0,B}$ to $M'_{0,B}$. Additionally, due to chemical exchange of B with the saturated metabolite A, the T_1 relaxation of metabolite B also changes from $T_{1,B}$ to an apparent $T'_{1,B}$. The longitudinal magnetization of metabolite B at an arbitrary time t during active saturation of metabolite A, $M'_B(t)$, is derived by:

$$M'_B(t) = M'_{0,B} + (M'_B(t=0) - M'_{0,B}) \cdot \exp\left(\frac{t}{T'_{1,B}}\right) \tag{2.47}$$

with

$$\frac{1}{T'_{1,B}} = \frac{1}{T_{1,B}^{intrinsic}} + k_f \tag{2.48}$$

and

$$M'_{0,B} = \frac{M_{0,B}}{1 + T_{1,B}^{intrinsic} \cdot k_f} \tag{2.49}$$

In Equation 2.48 and 2.49, $T_{1,B}^{intrinsic}$ denotes the *intrinsic longitudinal relaxation time* of metabolite B when no chemical exchange is present. From these formulas, the unidirectional reaction

rate can be deduced:

$$k_f = \frac{1}{T'_{1,B}} \left(1 - \left(\frac{M'_{0,B}}{M_{0,B}}\right)\right) \tag{2.50}$$

In summary, three variables are required to assess k_f: The apparent spin-lattice relaxation time of B ($T'_{1,B}$), the equilibrium magnetization ($M_{0,B}$) and apparent longitudinal magnetization of B ($M'_{0,B}$).

Knowing k_f, one is able to calculate the forward synthesis rate of metabolite A (F_A) by multipliying k_f by the concentration of metabolite B:

$$F_A = k_f \cdot [B] \tag{2.51}$$

2.7.2 ^{31}P-MRS saturation transfer

There exist different approaches in the literature to assess k_f. Typically, two spectra are acquired to determine $M_{0,B}$ and $M'_{0,B}$ which represent the difference in metabolite B's signal, $\triangle B$, caused by zeroing the magnetization of metabolite A. One spectrum is acquired with active saturation on metabolite A to obtain $M'_{0,B}$ and the other without saturation for determination of $M_{0,B}$. However, note that although the saturation pulse is intended to be sharply applied on the frequency of metabolite A, it may affect the overall magnetization and signal intensity of the spectrum, and thereby also on metabolite B, which is called *off-resonance* or *spill-over effect.* For this reason, a *control spectrum* is acquired with saturation at a mirrored frequency which is symmetrically mirrored around the frequency of metabolite A by the absolute amount of difference in chemical shift to metabolite B. This so-called *control* or *mirrored spectrum* intends to account for possible imperfection of the frequency-selective RF pulse, causing it to affect the resonance of metabolite B and thereby solving the direct saturation problem. However, it was shown that this procedure cannot fully compensate for the spill-over effect, especially for cases with small frequency differences between A and B and if the RF pulse is applied with high intensity [87]. For the assessment of hepatic ATP synthesis rates (see section 3.3), the amount of spill-over is rather low because of the large frequency difference between γ-ATP and P_i, which amounts to ~400 Hz at 3 T. For assessment of CK reaction, this difference only amounts ~130 Hz, making spill-over much more likely. To solve this issue, researchers have proposed mathematical equations to account for the spill-over effect [88, 89]. Another limitation to note is that Equation 2.50 does not account for any kind of incomplete (residual) magnetization of metabolite A.

The desired saturation of the resonance A is best achieved by very long pulses that apply continuous radiation, which are not possible in practice. Therefore, typically a train of saturation pulses with short inter-pulse delays is implemented on scanners. One example is the application of DANTE RF pulses consisting of a pulse train with short, non-selective RF pulses applied with low amplitude and separated by short delay intervals [90]. To enable frequency-selective saturation, DANTE pulses are combined with the application of gradients.

To ensure continuous saturation of a resonance over its full linewidth, the amplitude of the DANTE pulse train can be modulated according to the flip angle function $\alpha(k)$ to produce

multiple adjacent suppression bands according to the following equation:

$$\alpha(k) = \beta \sum_{n=0}^{m-1} \cos\left(2\pi\left(n - \tfrac{m-1}{2}\right) k\tau\delta\right) \tag{2.52}$$

In Equation 2.52, k denotes the number of subpulses, m represents the number of suppression bands, δ is the frequency separation in Hz between the individual suppression bands, β denotes the average subpulse FA per suppression band and τ represents the TR of the subpulses. The application of these short hard pulses enables application of a narrow suppression band at a specific frequency. Splitting the applied irradiation into subpulses creates aliased suppression bands in the spectrum at frequency intervals equal to the inverse of τ. Figure 2.15 shows an example of a DANTE saturation pulse applied on γ-ATP (red) and mirrored saturation (blue) for investigating hepatic ATP synthesis rates using ^{31}P-MRS ST (compare chapter 6).

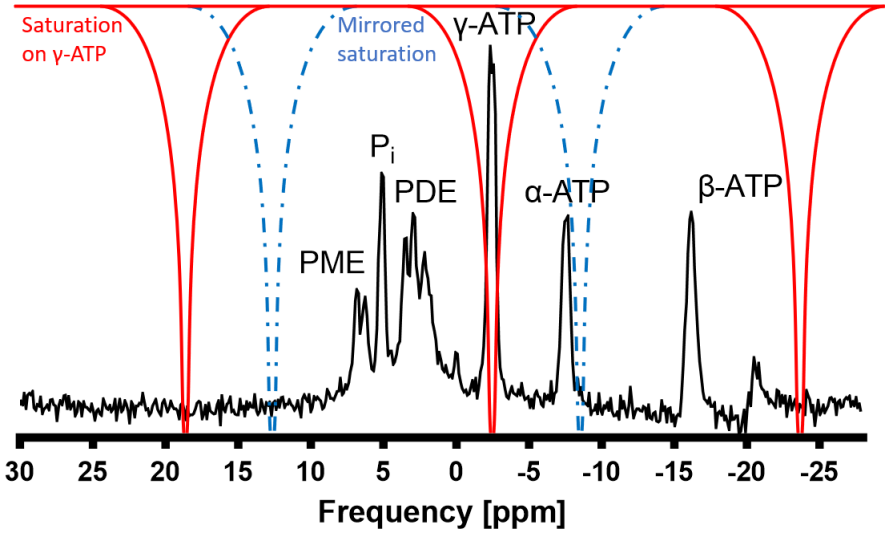

Figure 2.15: Position of the DANTE saturation bands on an entire hepatic ^{31}P-MRS spectrum for determination of ATP synthesis rate. In the saturation experiment, the saturation pulse was centered on the γ-ATP resonance at ~−2.48 ppm (saturation bands shown in red). Two aliased saturation bands (~−23.6 ppm and ~18.7 ppm) appear at intervals of ~21.2 ppm ($1/\tau$ = 1100 Hz) from the center of the saturation frequency due to a subpulse duration of τ = 0.91 ms. In the mirrored experiment, the frequency was mirrored around the P_i resonance and the saturation frequency was set to ~12.7ppm, resulting in aliased saturation bands at ~33.82ppm (not shown) and ~−8.5 ppm (blue dashed lines). The spectrum is apodized with a 5 Hz Gaussian filter. Adapted from [91].

Finally, $T'_{1,B}$ must be determined in order to calculate k_f. This approach is conventionally done using an IR experiment in the presence of continuous saturation of metabolite A. Briefly, a π-pulse inverts the magnetization of metabolite B, followed by a variable delay τ which allows partial recovery of magnetization before a $\pi/2$-pulse converts the longitudinal magnetization into a detectable signal. Fitting the amplitude of metabolite B over a range of τ using a mono-exponential function, $T'_{1,B}$ is obtained. Application of ^{31}P-MRS ST in the liver has typically used ten inversion times at 3 T [51, 52] and eight at 7 T [75]. Study 2 of this doctoral thesis aims to accelerate $T'_{1,B}$ determination by replacing the IR with a saturation recovery approach, as it has been shown to provide comparable results while reducing the number of spectra to two [92].

Chapter 3

3 Liver MRS

3.1 Anatomy and function of the human liver

The human liver is a dark brownish-red, intraperitoneal organ located in the right upper abdomen beneath the diaphragm and protected by the rib cage. Its surface is smooth and glistening due to its peritoneal covering (*peritoneum viscerale*) with the exception of three regions: The bare area (*area nuda*), where it is directly attached to the diaphragm, the gallbladder fossa (*fossa vesicae biliaris*), and the *porta hepatis* and *vena cava inferior*. Being the largest internal organ, liver weight varies between sexes with approximately 1400 g in women to 1600 g in men [93].

Macroscopically, the liver has a rounded, triangular, and wedge-shaped morphology and can be divided into two major lobes, the right lobe (*lobus dexter*) and the left lobe (*lobus sinister*) through a crescent-shaped peritoneal duplicature, the *ligamentum falciforme hepatis*, which extends towards anterior-posterior direction (see Figure 3.1) [93]. The right lobe is more voluminous than the left lobe and occupies most of the upper abdominal cavity. Next to these two, there exist two additional lobes, *lobus quadratus* and *lobus caudatus*. While this lobular structure, characterized by furrows and fissures, reflects anatomical divisions, it does not correspond to the functional organization of the organ structure. Therefore, the liver is further divided into eight segments following the segmentation described by Couinaud [94]. The segmentation is based on the branching pattern of the portal triad (portal vein, hepatic artery, and bile duct), whose vascular-biliary pathways define autonomous metabolic and surgical units (segments I–$VIII$).

In distinction from all other internal organs, the liver receives blood from two afferent vascular ports: Both *arteria hepatica propria* and *vena portae* (displayed in red and purple in Figure 3.1, respectively) supply the liver with oxygenated, nutrient-rich blood. In the case of the portal vein, it carries blood directly from the gastrointestinal tract. The hepatic artery proper contributes approximately 25% to the liver's blood supply, while the portal vein provides the remaining 75% [93]. The large intrahepatic veins (left, middle, right; blue in Figure 3.1), which run in the intersegmental clefts and drain the blood from neighboring segments, converge into two anatomical groups of hepatic veins: The upper group (left, middle, right hepatic veins) which drain into the suprahepatic *vena cava inferior* and the lower group (several accessory veins) draining into the caudate lobe and parts of the right lobe into the retrohepatic *vena cava inferior*.

The liver performs a wide array of functions which are essential for maintaining homeostasis. Besides various tasks in energy metabolism, it is also responsible for detoxification, immune de-

fense, storage of essential nutrients, biotransformation, and synthesis of urea, bile, hormones, and plasma proteins [95]. The variety of functions fits its strategic anatomical position, as the liver is able to absorb nutrients, vitamins, and electrolytes directly from the intestine during the absorption phase. These can be stored in the liver and released into the bloodstream during post-absorptive or fasting periods in order to maintain energy balance.

The ^{31}P-MRS measurements reported in this doctoral thesis were all conducted in the *lobus dexter*, as this lobe has the largest area next to the body surface and therefore exhibits sufficient signal for detecting metabolites using surface coils. Due to its soft consistency, its shape varies significantly. Especially the shape of the wall of the upper abdominal cavity and the filling condition of neighboring organs, particularly the gallbladder and stomach, have a great influence on its actual shape. Also, due to its connection to the diaphragm through ligaments and the bare area, the liver's position and shape alter with respiration. All these factors must be considered when planning the VOI in ^{31}P-MRS experiments (see chapter 5).

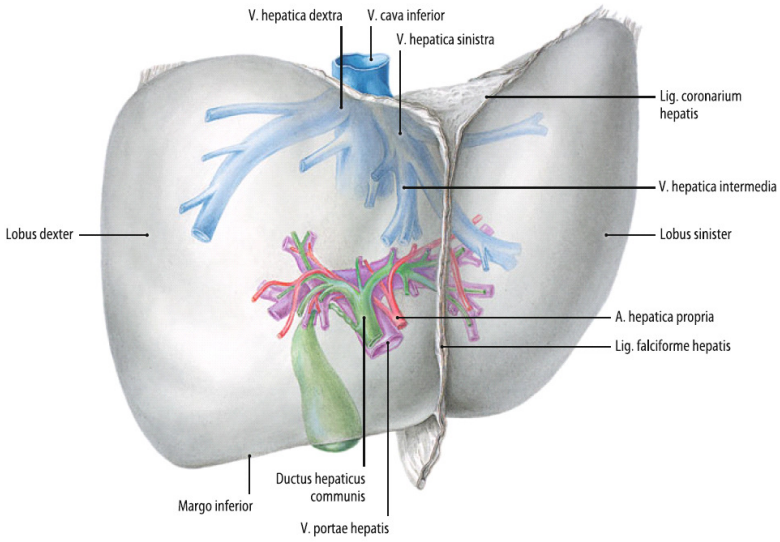

Figure 3.1: Frontal view of the human liver, showing the left and right lobes, major hepatic veins, the hepatic artery, portal vein, bile duct, and key ligaments. Figure retrieved from [93].

3.2 Diabetes mellitus

3.2.1 Diabetes in numbers

Diabetes mellitus is a serious chronic disease and a significant public health problem. It represents one of four priority non-communicable diseases which have been targeted for action by world leaders [2]. The recently published *Diabetes Atlas* (11th edition) by the International Diabetes Federation (IDF) reports that about 589 million people aged between 20–79 years worldwide lived with diabetes in 2024 and a global age-standardized prevalence of 11.1% was found [5]. In addition, it is assumed that a further 252 million people worldwide live with undiagnosed diabetes, increasing the total number to 841 million [5]. A projection for the year 2050 predicts that the number of people living with diabetes between 20–79 years worldwide will

rise by 44.8% to 853 million and the global prevalence by 11.1% to 13.0%, respectively [5]. Another study reporting the crude prevalence of diabetes shows an even more drastic scale of this disease. According to the latest results of pooled analysis of 1108 population-representative studies presented in 2024, the number of people living with diabetes (diagnosed and undiagnosed) rose from 198 million in 1990 to 828 million in 2022 [3]. This shows that the global prevalence has more than doubled from 6.9% in 1990 to 14.1% in 2022 [3]. The increasing prevalence of diabetes constitutes a considerable burden on the global health systems.

According to the results from a former publication of the IDF *Diabetes Atlas* (9th edition), the total global diabetes-related health expenditure was estimated at USD 760 billion in adults aged 20–79 years in 2019 [96]. Projections at this time showed that the total expenditures will rise further to USD 825 billion in 2030 and might reach USD 845 billion per year by 2045 [96]. However, the updated numbers from 2024 (11th edition) show that these estimates were severely underestimated because with total costs of USD 1.015 billion, the USD 1 billion mark was already exceeded in 2024 [5]. Overall, the total costs have risen by 338% over 17 years from 2007 (USD 232 billion) to 2024, and from 2019 to 2021 alone they have risen by a further approximate 20% [5]. These numbers emphasize the significant economic impact of diabetes and underline the necessity for effective prevention as well as management strategies. However, it should be noted that the projections from 2019 could not take into account the latest developments of glucagon-like peptide-1 (GLP-1) receptor agonists, which dramatically changed the landscape of diabetes care and costs. According to a recent analysis, the total annual spending on GLP-1 receptor agonists rose from USD 13.7 billion in 2018 to USD 71.7 billion in 2023 in the United States alone [9]. The most recent data from 2022 to 2023 show that this trend is likely to continue in recent years and in the years to come, as spending increased by 62% in just one year [9]. However, it should be noted that these initially high short-term costs of medication could lead to an overall reduction in costs in the long term, as considerable savings could be made by avoiding follow-up costs such as hospitalization. Data on this and on the broader long-term application of these drugs are currently still insufficient.

Being responsible for 1.6% of total global deaths, diabetes has been on the 14th rank among causes of deaths in 2000 and rose to 8th place by 2021, accounting for 2.4% of total deaths [6]. This agrees with predictions from an older study, projecting diabetes to climb worldwide to rank 7 in 2030 and in high-income countries like Germany even to rank 4, making diabetes responsible for 4.8% of total deaths in 2030 [7]. Complementary data from the *Diabetes Atlas* reveals an even broader impact when including deaths caused by diabetes-complications. Among people aged 20–79 years, diabetes and its complications together caused about 3.4 million deaths in 2024, representing 9.3% of total mortality in this age group [5]. It is to note, that this analysis included both diagnosed (2.4 million) and undiagnosed diabetes-related (1.0 million) deaths [5].

In Germany, the standardized prevalence of diabetes also increased from 8.9% of the study population counting 70,413,747 people in 2009 to 9.8% in a population of 69,818,047 people in 2015 [97]. Consequently, the fraction of people suffering from T2D rose from 8.5% to 9.5%. In contrast to this trend, the prevalence of type 1 diabetes (T1D) decreased readily from 0.33% to 0.28% [97]. Other data have shown a stagnation, albeit at a very high level, in the age- and

sex-standardized prevalence of total diabetes from 9.3% between 1997–1999 and 9.2% between 2008–2011, however, the prevalence of diagnosed diabetes increased from 5.6% to 7.2%, whereas undiagnosed diabetes decreased from 3.8% to 2.0% [98]. The latest available data confirm this stagnation, reporting a prevalence in T2D of 9.5% in 2023 and an incidence 0.87% [99]. For Germany alone, the annual healthcare costs for diabetes in 2010 were estimated at about €1 billion for T1D and almost €29 billion for T2D, respectively [8]. A projection for 2040 shows increases to approximately €2 and €79 billion, reflecting rises of 100% and 171% for T1D and T2D, respectively [8]. According to the World Health Organization (WHO), the major risk factors for the development of diabetes in 2022 in Germany were overweight, obesity, smoking, and physical inactivity with prevalences of 54%, 20%, 21%, and 23.4%, respectively [100].

3.2.2 Clinical classification and subtypes of diabetes

From a clinical point of view, diabetes is considered a prevalent disease characterized by chronic hyperglycemia. Currently, classification of diabetes is recommended in four general categories by the American Diabetes Association (ADA), which are distinguishable by pathophysiological and clinical criteria [1]:

1. Type 1 diabetes: Autoimmune β-cell destruction, causing absolute insulin deficiency
2. Type 2 diabetes: Non-autoimmune progressive loss of adequate β-cell insulin secretion which often originates from insulin resistance and metabolic syndrome
3. Specific types of diabetes: Diabetes due to other causes, e.g., monogenic diabetes syndromes (neonatal diabetes and maturity-onset diabetes of the young (MODY)), diseases of the exocrine pancreas, and drug- or chemical-induced diabetes.
4. Gestational diabetes: Diagnosis of diabetes in the second or third trimester of pregnancy without clear diabetes prior to gestation or other types of diabetes occurring throughout pregnancy.

According to ADA, there exist four diagnostic criteria for diagnosis of diabetes in non-pregnant individuals [1]: i) Hemoglobin A1c (HbA1c) value ≥6.5% (≥48 mmol/mol), being a long-term average blood sugar indicator; ii) fasting plasma glucose ≥126 mg/dl (7.0 mM), showing short-term blood glucose levels after an at least 8 hour fast; iii) 2 hour plasma glucose during an Oral Glucose Tolerance Test (OGTT) ≥200 mg/dl (11.1 mM), a diagnostic test measuring blood glucose levels 2 hours after consuming a glucose-rich drink usually consisting of 75 g glucose; iv) random plasma glucose ≥200 mg/dl (11.1 mM) with classic hyperglycemia symptoms (e.g. polyuria, polydipsia, weight loss), measuring blood glucose at any random time without regard of timing of meals. These four tests were also recognized by the WHO [101].

While there is a rough classification of diabetes into four general categories, it should be noted that each category may itself be heterogeneous with various differences in its clinical presentation and disease progression. From a clinical context, precise classification of an individual's diabetes is very important for selecting an appropriate treatment strategy. Therefore, in the last years a lot of effort and work has been conducted with the aim to classify and characterize subgroups (subtypes) within each category. In this context, the term precision diabetology

has been developed. In the context of T1D and T2D, the ultimate purpose of precision diabetology is to develop stratified prevention and treatment strategies for subgroups of people with different risk profiles [13]. In 2018, Ahlqvist et al identified five replicable clusters of patients with diabetes in a Swedish cohort study, leading to a paradigm shift in classification of diabetes based on different pathophysiological and genetic profiles [14]. The group showed that the five clusters had significantly different characteristics and risks of diabetic complications. The accumulation of lipids in the liver represents a significant risk factor for the development of T2D, as hepatic steatosis impairs insulin signaling and increases hepatic glucose production, thereby promoting systemic insulin resistance [10]. This risk is especially pronounced in individuals with the highest insulin resistance, such as those classified in the 'severe insulin-resistant diabetes' (SIRD) subtype, who exhibit higher levels of ectopic HLs and face an increased risk for diabetes and related complications [15]. A more recent study mapped people with T2D onto a tree structure based on nine easily accessible clinical variables which could stratify risks of complications, e.g. cardiovascular disease, neuropathy, and kidney disease based on individuals' position and therefore shows the potential of this method for precision diagnosis and risk stratification [16]. In addition to T2D, there are also approaches to dissect heterogeneity in T1D [102]. However, the overall aim, regardless of diabetes type, is always to lower high blood glucose levels and to minimize diabetes-related complications.

3.3 Physiology / Pathway of ATP synthesis

This section provides a concise overview of ATP synthesis pathways and their physiological context in the liver. While the biochemical complexity of these processes extends beyond the scope of this doctoral thesis, principal concepts will be introduced to illustrate advantages and limitations of ^{31}P-MRS ST, and address the special case of these processes in the liver.

ATP represents the universal cellular energy currency due to its high-energy phosphate bonds. Tissues like muscle and liver exhibit particularly high ATP demands. For example, a man with sedentary lifestyle and body weight of 70 kg needs about 8400 kJ of energy for his daily activity, which equates to about 83 kg of ATP required, but the human body only has 250 g available [103]. This highlights the critical role of continuous ATP regeneration. In the human body, ATP is constantly regenerated from ADP and this recycling takes place primarily through oxidative phosphorylation within the mitochondria. The reverse reaction, energy release, occurs via ATP hydrolysis into ADP and P_i. In total, three hierarchically organized ATP provision processes exist, which differ in speed of provision of ATP, ATP yield, oxygen dependence, and key location:

1. Creatine kinase reaction - immediate ATP buffer (1 ATP/PCr)
2. Glycolytic ATP synthesis - rapid but inefficient (2 ATP/glucose)
3. Oxidative ATP synthesis - slow but high-ATP yield (30–32 ATP/glucose)

The hepatic ATP dynamics are uniquely complex due to some idiosyncrasies: First, in the liver there exists a concurrent reciprocal process between ATP consumption (e.g. detoxification and

gluconeogenesis) and ATP production, which is dominated by oxidative ATP synthesis (fueled by glycogenolysis and β-oxidation). Second, the liver has to provide continuous, basal ATP turnover to maintain whole-body homeostasis. This is in sharp contrast to skeletal muscle, where ATP demand spikes occur during exercise. Third, unlike in muscle, hepatic CK reaction is minimal or not typically detectable in healthy liver tissue. Using the ^{31}P-MRS ST method, one is able to assess both the CK reaction and ATP synthesis in various organs, however, in the liver, only ATP synthesis can be detected.

Creatine kinase reaction

Performing ^{31}P-MRS ST studies, the CK reaction pathway is the most extensively studied pathway due to its central role in cellular energy buffering, especially in skeletal muscle. The generation of ATP can be described by:

$$ADP + PCr + H^+ \underset{k_r}{\overset{k_f}{\rightleftharpoons}} ATP + Cr \tag{3.1}$$

In cases of high ATP demand, such as during physical exertion, fresh ATP is immediately provided by consumption of energy reserves stored in PCr. Equation 3.1 is catalyzed by the CK enzyme and serves as a temporal buffer, since the reaction is very fast and can be considered as almost instantaneous [104]. During this process, PCr is split into creatine (Cr) and a phosphate group, which is then attached to ADP to build one ATP per molecule of PCr. This instantaneous process takes place anaerobically in the cytosol of the cell. The maximum rate of ATP formation amounts to 73.3 $^{\text{mmol}}/_{\text{s}}$ in skeletal muscle, however, the pool of 446 mmol PCr will be rapidly depleted, so that ATP can only be provided within the first seconds of exercise until the glycolytic and oxidative pathways are activated [103]. As Cr is simultaneously released with ATP, the total creatine (tCr) pool does not change ($tCr = PCr + Cr$). It is to mention that Equation 3.1 is reversible, so that the surplus of ATP, which is still being produced by the oxidative pathway, can be used for PCr resynthesis after finishing exercise [104].

In contrast to other organs, the above-described process of CK reaction cannot be observed in the healthy human liver, due to the reason that the CK enzyme is not present [105]. Out of this reason, little to no PCr is present in hepatocytes. Therefore, hepatic ^{31}P-MRS ST experiments focus on ATP synthesis dynamics rather than CK phosphate transfer.

Glycolytic ATP synthesis

The second ATP-producing pathway uses glucose as a source material in an anaerobic process within the cytosol, called glycolytic ATP synthesis. Glucose is provided from the bloodstream or by glycogenolysis (degradation of stored glycogen molecules in the liver or muscle). During glycolysis, one glucose molecule undergoes a 10-step enzymatic process, which ultimately provides two molecules of pyruvate and a net gain of 2 ATP and 2 NADH molecules [103]:

$$2ADP + 2P_i + 2NAD^+ + glucose \longrightarrow 2ATP + 2H_2O + 2NADH + 2H^+ + 2pyruvate \tag{3.2}$$

The resulting pyruvate is then converted into either lactate (anaerobic condition, also called *fermentation*) or carbon dioxide in the mitochondria (aerobic condition, see oxidative ATP synthesis). In the former process, lactate dehydrogenase catalyzes the reduction of pyruvate to lactate and simultaneously regenerates NAD^+ from NADH. The fermentation reaction of anaerobic glycolysis is as follows:

$$H^+ + NADH + pyruvate \longrightarrow NAD^+ + lactate \tag{3.3}$$

The glycolytic ATP synthesis is a fast-running process that provides ATP when energy demand is high and oxygen is limited, such as during the early phase of exercise, when the oxidative pathway is not yet operating at full capacity. In muscle, the maximum rate of ATP formation amounts 39.1 $^{\text{mmol}}/_{\text{s}}$ and the pool of available phosphate amounts 6700 mmol [103]. However, glycolysis requires constant NADH, which is known as the fermentation process (see Equation 3.3). This pathway is limited because it produces lactate and H^+, which can lead to acidosis. Compared to CK, its speed is decreased but it provides 2 ATP molecules per cycle.

Oxidative ATP synthesis

The third and most important ATP-producing pathway occurs in the mitochondria of the cell and is called oxidative ATP synthesis. Unlike anaerobic glycolysis, which is able to gain only minimal energy from one glucose molecule (2 ATP; <10% of glucose's potential), the oxidative pathway yields significantly more energy of about 30–32 ATP per glucose molecule under aerobic conditions via the citrate cycle (tricarboxylic acid/TCA cycle) and the electron transport chain (ETC) [103]. For this process, pyruvate molecules provided by glycolysis are first transported via pyruvate carriers into the mitochondrial matrix. In the mitochondria, pyruvate undergoes oxidative decarboxylation to form acetyl coenzyme A (acetyl-CoA), catalyzed by the pyruvate dehydrogenase complex.

$$pyruvate + NAD^+ + CoA \longrightarrow acetyl\text{–}CoA + CO_2 + NADH + H^+ \tag{3.4}$$

The acetyl-CoA enters the TCA cycle, generating as end products: $3NADH$, $1FADH_2$, $2CO_2$, CoA, H^+ and one molecule ATP.

$$Acetyl\text{–}CoA + 3NAD^+ + FAD + ADP + P_i + 2H_2O \longrightarrow 2CO_2 + 3NADH + FADH_2 + ATP + 2H^+ + CoA \tag{3.5}$$

Subsequently, NADH and $FADH_2$ are oxidized in the ETC, establishing a proton gradient across the inner mitochondrial membrane and creating an electrochemical gradient that drives the ATP synthesis:

$$ADP + P_i \underset{k_r}{\overset{k_f}{\rightleftharpoons}} ATP \tag{3.6}$$

This process is slow compared to the other two ATP-generating pathways, but results in provision of about 30–32 ATP from one molecule of glucose [103]. For this process, the oxygen is needed as the terminal electron acceptor to form water. This process is the basis for all higher life forms and the reason why we have to breathe oxygen. It is to mention that under fast-

ing conditions where limited amounts of glucose are available, the liver uses fatty acids as a supplier for acetyl-CoA.

Due to the fact that oxidative ATP synthesis is the primary energy source for cellular processes, a non-invasive tool for assessment of its turnover rates would be very helpful for investigations of mitochondrial function. ^{31}P-MRS represents such a tool, allowing dynamic monitoring of active, living tissue, which may help guide therapies and interventions for metabolic diseases. Study 2 describes a new method for the assessment of hepatic ATP synthesis rates using the ST technique (see chapter 6).

3.4 ^{1}H-MRS of the liver

^{1}H-MRS in the liver is an important non-invasive tool for characterization of triglycerides (TGs). In the pathogenesis of insulin resistance, lipids are not only found in the subcutaneous adipose tissue and intra-abdominal or visceral adipose tissue compartments, but also as ectopic lipids in organs that usually do not store lipids, such as the liver [106]. The accumulation of hepatic lipids (HL) often occurs in individuals with metabolic dysfunction and HL content is strongly associated with an elevated risk of T2D. Therefore, this condition is termed metabolic dysfunction-associated steatotic liver disease (MASLD) [107, 108]. The more severe form, termed metabolic dysfunction-associated steatohepatitis (MASH), denotes progressive liver inflammation that significantly raises the risk of fibrosis and hepatocellular carcinoma (HCC).

To investigate abnormal accumulation of HLs, which represents a risk of metabolic disease, several techniques such as ultrasound (US), computer tomography (CT) as well as MRI and MRS have been used for HL quantification. Comparing these techniques with histopathologic examinations as the reference standard, MRS showed a sensitivity of 73–89% compared with 73–91% for US and 82–97% for CT and a specificity of 92–96% compared to 70–85% for US and 88–95% for CT, respectively [109]. Being highly sensitive and specific, as shown in an intra- and inter-examination repeatability study yielding intra- and inter-examination standard deviations (SD) of 0.49% and 0.46%, respectively [110], MRS is currently seen as gold standard for non-invasive determination of HL quantification [111, 112]. Recent developments in MRI sequences also allow to determine HL content using imaging techniques showing high correlation with MRS [111–114].

Performing ^{1}H-MRS in the liver, one obtains prominent signals from water and lipids (consult Figure 3.2a). However, in metabolically healthy individuals, lipid levels are very low compared to the water signal, making detection of the lipid signal challenging. For this reason, water-suppression sequences were developed and applied in order to detect signals from low-concentration metabolites and lipids. In a TG molecule, up to 10 distinct resonances originating from different chemical groups can be individually detected [17]. Figure 3.2 shows representative MRS spectra acquired without and with water-suppression. Chemical shift assignment of all ^{1}H-MRS resonances in a human liver is stated in Table 3.1. The most prominent lipid signal originates from methylene protons at 1.3 ppm (peak 2) as these protons form the CH_2 backbone

of TGs. This resonance is of high interest for calculation of HL content, which is widely used in both clinical and metabolic research due to the fact that only the most prominent resonance needs to be assessed. However, taking the other lipid resonances into account, one is able to investigate the fatty acid composition of lipids in terms of their degree of saturation such as saturated fatty acids (SFA), mono-, and polyunsaturated fatty acids (MUFA/PUFA) [115]. Since the SNR is much lower for these resonances and some of them overlap each other in the liver at clinical field strengths, advanced protocols with long acquisition times and sophisticated fitting algorithms with prior knowledge are necessary [116].

Table 3.1: Peak identification and chemical shift values for hepatic triglycerides and water in the ^{1}H-MRS spectrum, with the signal-generating chemical group highlighted in bold. Assignments based on [117–120].

Peak	Chemical shift [ppm]	Chemical group	Type
1	0.90	$-(CH_2)_n-C\mathbf{H}_3$	Methyl protons
2	1.30	$-(C\mathbf{H}_2)_n-$	Methylene protons
	1.60	$O-CO-CH_2-C\mathbf{H}_2-$	Methylene protons β to COO
3	2.02	$-C\mathbf{H}_2-CH=CH-C\mathbf{H}_2-$	Methylene protons α to $C=C$
4	2.24	$O-CO-C\mathbf{H}_2-CH_2-$	Methylene protons α to COO
5	2.75	$-CH=CH-C\mathbf{H}_2-CH=CH-$	Diallylic methlene protons
6	4.07	$-C\mathbf{H}_2-O-CO-$	Glycerol protons
	4.20	$-C\mathbf{H}_2-O-CO-$	Glycerol protons
7	4.70	$\mathbf{H}_2O$	Water
8	5.19	$-C\mathbf{H}-O-CO-$	Glycerol protons
	5.29	$-C\mathbf{H}=C\mathbf{H}-$	Methine protons

To determine HL content, the signal fat fraction (η) can be calculated as the signal from lipid protons divided by the sum of the signals from lipid and water protons according to Equation 3.7 [119]:

$$\eta\ (\%) = \frac{S_{lipid}}{S_{lipid} + S_{water}} \cdot 100 \tag{3.7}$$

The HL content in this thesis was calculated using the fitted peak areas of methylene protons and methylene protons in the β-carbonyl position (peak 2) in the water-suppressed spectrum for S_{lipid} and the peak area of water (peak 7) in the non-water-suppressed spectrum for S_{water} (compare Figure 3.2). Before calculating HL content, the individual metabolite amplitudes were corrected for T_2 relaxation time using $T_{2,lipid} = 62$ ms and $T_{2,water} = 23$ ms, respectively, based on [117].

From a clinical point of view, the current agreement of 'upper limit of normal' HL content without any risk factors for hepatic steatosis is reported to be 5.56%, assessed via ^{1}H-MRS in 345 volunteers at 1.5 T in 2005 [121]. However, a recent study questions this value and suggests to decrease the threshold to 1.85%, based on extensive data analysis of 1, 506 volunteers [122].

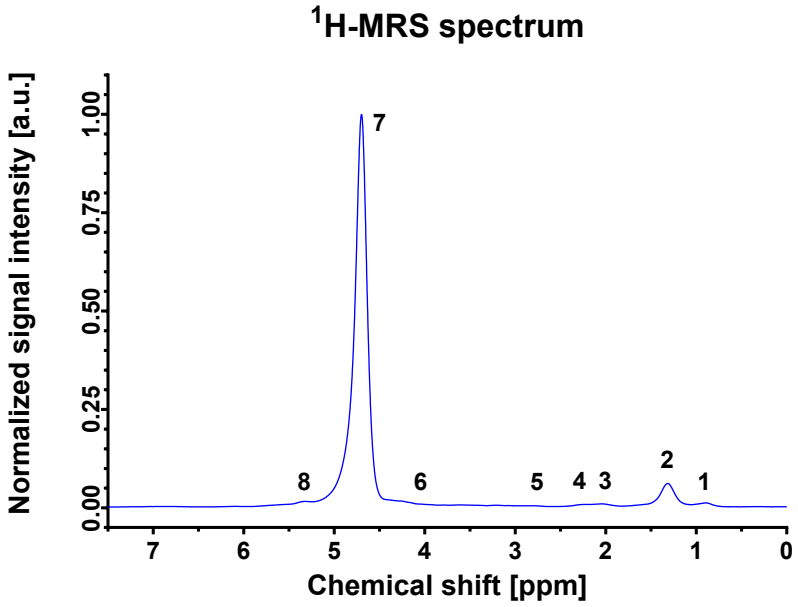

(a)

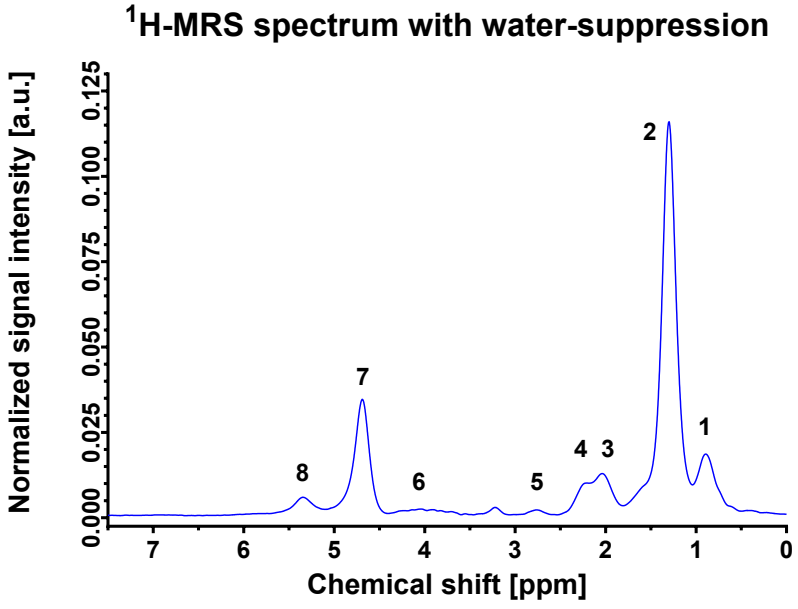

(b)

Figure 3.2: Representative 3D-localized ^{1}H-MRS spectra (STEAM, TR = 4.5 s, TE = 20 ms, voxel size = $30 \times 30 \times 30\,\mathrm{mm}^3$) of the human liver (a) without and (b) with water-suppression at 3 T. Shown are seven characteristic peaks of triacylglycerol (1–6, 8) and the resonance of water (7), corresponding to the peaks in Table 3.1.

In this thesis, ^{1}H-MRS was applied to assess HL content in humans to be able to correct for it when calculating absolute concentrations of ^{31}P-MRS metabolites. A correction for HL content is necessary because the method used for calculation of ^{31}P-metabolite concentrations assumes that the signal obtained from the VOI contains solely ^{31}P-metabolites. In the presence of significant HL content, the ^{31}P-signal is diluted leading to an apparent decrease in the signal and therefore an underestimation of absolute concentrations.

3.5 ^{31}P-MRS of the liver

Application of ^{31}P-MRS in the liver opens the door for investigation of energy metabolism. In addition to information on metabolite ratios or concentrations assessed by static MRS spectra, dynamic MRS allows investigation of chemical reaction rates of hepatic energy metabolism.

A representative (decoupled) hepatic ^{31}P-MRS spectrum is displayed in Figure 3.3. A total of 12 distinct resonances can be obtained (see Table 3.2). Please note that the reported chemical shifts of hepatic ^{31}P-metabolites in Table 3.2 are not fixed since they are sensitive to physiological parameters like intracellular pH and ionic strength (e.g. magnesium) [17]. ATP, the universal energy supplier, shows three different resonances (α-, β- and γ-) at −7.61 ppm, −16.12 ppm, and −2.48 ppm, respectively, based on the three non-equivalent phosphate groups in the molecule. In a non-decoupled spectrum, line splitting of the ATP signals can be observed, resulting in doublets for α- and γ-ATP, and a triplet for β-ATP (see Figure 2.4). For all ^{31}P-MRS spectra in this study the γ-ATP resonance was used as internal chemical shift reference and was assigned to a chemical shift of −2.48 ppm. By convention, PCr is typically used as internal reference and is assigned to 0.00 ppm. However, since PCr is absent in the liver, γ-ATP was used. P_i can be detected at 5.18 ppm and serves as a substrate or product in chemical reactions of energy metabolism. Downfield from P_i, phosphomonoesters (PMEs), like phosphoethanolamine (PE) at 6.82 ppm and phosphocholine (PC) at 6.35 ppm, represent cell membrane precursors, and upfield from P_i, phosphodiesters (PDEs), such as glycero-phosphoethanolamine (GPE) at 3.51 ppm and glycero-phosphocholine (GPC) at 2.94 ppm, denote cell membrane degradation products. For a long time, the resonance at 1.99 ppm, often overlapping with the PDEs, was referred to as phosphoenolpyruvate (PEP) [123,124]. Recent studies explicitly analyzed the resonance which is reported here to be a mixture of PEP and phosphatidylcholine (PtdC) [125,126]. It was shown that under physiological conditions this signal originates mainly from hepatic PtdC due to its 3.5 times higher concentration compared to PEP [126] and that this peak is strongly increased if there is signal interference from the gallbladder, which is why it can be used to estimate signal contamination [125]. UHF MRS determined a PtdC concentration in the gallbladder of 9.64 mM in healthy volunteers, which is about 3.5 times higher than hepatic γ-ATP and P_i concentrations, making it an easy visual quality criterion for liver spectra contamination [127]. Nevertheless, both metabolites reflect different aspects of hepatobiliary function. PEP serves as a precursor in gluconeogenesis and is an important metabolite for glycolysis since the enzyme pyruvate kinase transfers its phosphate group to ADP, generating ATP and pyruvate [103]. PtdC is a phospholipid produced in the liver and excreted to the bile fluid to be stored in the gallbladder. Nicotinamide adenine dinucleotide (NAD) exists in both its oxidized (NAD^+) and reduced form (NADH), acting as electron acceptor and donor during substrate oxidation. Recent studies have shown that NAD^+, a coenzyme essential for ATP production and a substrate for enzymes involved in cellular homeostasis, plays a key regulatory role in mitochondrial biogenesis [128]. In ^{31}P-MRS spectra at clinical field strength, only the combined signal of NAD^+ and NADH can be detected at −8.24 ppm due to broad linewidths. However, recent advances in editing techniques indicate that separation of these signals is possible in skeletal muscle [129]. Please note that in ^{31}P-MRS sometimes NAD^+/NADH are labeled as $NAD(P)^+$/NAD(P)H as

the molecules are identical with the exception of an additional ^{31}P-atom on the second position of the adenosine ribose ring. The last detectable metabolite is uridine diphosphate glucose (UDPG), which is located at −9.67 ppm. In the liver, it represents an essential intermediate for glyconeogenesis, as it serves as a substrate for the enzyme glycogen synthase, which builds up the glycogen molecule. The short-term energy reserve for producing ATP, PCr is not naturally abundant in the liver. Therefore, when evaluating a hepatic ^{31}P-spectrum, one can judge the quality of signal localization by the amount of signal obtained at about 0.31ppm, corresponding to PCr's expected resonance. If a small peak is visible, there is probably signal contamination from the abdominal muscle, in which PCr is the most prominent resonance.

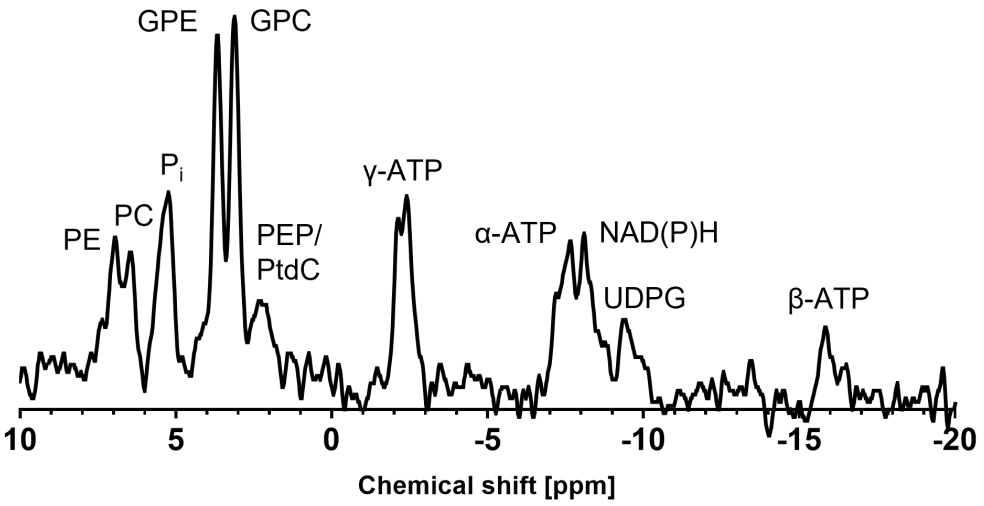

Figure 3.3: Representative 3D-localized ^{31}P-MRS spectrum (apodization 15 Hz) of the human liver at a field of 3 T. ATP, α–, β–, γ–adenosine triphosphate; GPC, glycero-phosphocholine; GPE, glycero-phosphoethanolamine; NAD(P)H, nicotinamide adenine dinucleotide (phosphate); P_i, inorganic phosphate; PC, phosphocholine; PE, phosphoethanolamine; PEP/PtdC, phosphoenolpyruvate/phosphatidylcholine; UDPG, uridine diphosphate glucose. Adapted from [62].

Table 3.2: Peak identification and chemical shift values for hepatic metabolites in the ^{31}P-MRS spectrum. Adapted from [62].

Peak	Chemical shift [ppm]	Abbreviation	Metabolite
1	6.82	PE	Phosphoethanolamine
2	6.35	PC	Phosphocholine
3	5.18	P_i	Inorganic phosphate
4	3.51	GPE	Glycero-phosphoethanolamine
5	2.94	GPC	Glycero-phosphocholine
6	1.99	PEP/PtdC	Phosphoenolpyruvate/ Phosphatidylcholine
7	0.31	PCr	Phosphocreatine
8	−2.48	γ-ATP	γ-adenosine triphosphate
9	−7.61	α-ATP	α-adenosine triphosphate
10	−8.24	NAD(P)H	Nicotinamide adenine dinucleotide (phosphate)
11	−9.67	UDPG	Uridine diphosphate glucose
12	−16.20	β-ATP	β-adenosine triphosphate

Chapter 4

4 Aims

The doctoral thesis at hand aims to present two methods using ^{31}P-MRS that allow one to assess hepatic metabolite concentrations and ATP synthesis rates in vivo in the human liver. Both methods were applied at clinical field strength, allowing their widespread use for both research and clinical studies. Likewise, the reproducibility of each method was assessed in order to judge the feasibility of the corresponding method to be applied on an individual basis for precision medicine or for calculating sample sizes for conducting clinical studies.

Study 1 deals with the assessment of reproducibility of absolute quantification of hepatic metabolites with a special focus on ATP and P_i. Two different surface coils were used for the measurements, and SNR was examined. Ultimately, the calculated absolute concentrations for both coils were analyzed and contrasted using the phantom replacement technique. In this course, a custom-designed post-processing pipeline for spectral fitting was established together with determining all relevant factors correcting coil- and sequence-dependent influences. The comparability between the results of both coils was assessed in both day-to-day and intra-day measurements and additionally the individual coefficients of variation (CV) were assessed.

Thus the aims of Study 1 were:

- Assessment and comparison of the technical performance of a clinical 3 T ^{31}P-MRS method for detection and quantification of hepatic metabolites using two surface coil designs (single loop vs. quadrature)
- Validation of the phantom replacement technique for calculation of absolute metabolite concentrations, ensuring consistency across coils and minimizing hardware-dependent variability
- Evaluation of reproducibility in both intra-day (short-term) and day-to-day (long-term) measurements of the method in both coils

Study 2 aims to introduce a new ^{31}P-MRS ST method which is able to assess hepatic ATP synthesis rates. This new sequence was designed to overcome central problems with this technique at clinical field strength, such as measurement times of about two hours, insufficient localization to hepatic tissue resulting in signal contamination from abdominal muscle, and, furthermore, to address the lack of reproducibility data of this technique in the literature. Further on, its sensitivity was tested by applying the method in people with T1D and the outcome was compared with measurements in healthy controls.

The aims of Study 2 were:

- Implementation of a new ^{31}P-MRS ST method for assessment of hepatic ATP synthesis rates with acceptable measurement time and reproducibility on a clinical system

- Overcome typical problems of signal localization and perform measurements in the liver without muscle contamination
- Assess ATP synthesis rates and compare them with data obtained at UHF systems
- Test the ability of the method to detect differences between healthy controls and people with T1D

The ultimate aim of this doctoral thesis was to validate and further develop ^{31}P-MRS methodologies for non-invasive characterization of hepatic energy metabolism in a clinical setting. The results show that ^{31}P-MRS offers valuable information about hepatic energy metabolism and should not be considered as a technique which can only be applied on UHF research scanners. Therefore, the application of these techniques may be expanded for further assessment and study of energy metabolism in states of disease such as diabetes with the overall aim to improve precision medicine.

Chapter 5

5 Study 1: ^{31}P-MRS absolute quantification of hepatic ATP and P_i using different surface coils

Received: 31 May 2023 | Revised: 19 December 2023 | Accepted: 20 January 2024

DOI: 10.1002/nbm.5120

RESEARCH ARTICLE

NMR IN BIOMEDICINE WILEY

Reproducibility of absolute quantification of adenosine triphosphate and inorganic phosphate in the liver with localized ^{31}P-magnetic resonance spectroscopy at 3-T using different coils

Marc Jonuscheit[1,2] | Stefan Wierichs[1,2] | Maik Rothe[1,2,3] | Benedict Korzekwa[1,2] | Julian Mevenkamp[4] | Pavel Bobrov[2,5] | Yuliya Kupriyanova[1,2] | Michael Roden[1,2,6] | Vera B. Schrauwen-Hinderling[1,2,4]

[1]Institute for Clinical Diabetology, German Diabetes Center, Leibniz Institute for Diabetes Research at Heinrich Heine University Düsseldorf, Düsseldorf, Germany

[2]German Center for Diabetes Research (DZD e.V.), München-Neuherberg, Germany

[3]University Clinic and Outpatient Clinic for Radiology, University Hospital Halle (Saale), Halle (Saale), Germany

[4]Department of Radiology and Nuclear Medicine, Maastricht University Medical Center, Maastricht, The Netherlands

[5]Institute for Biometrics and Epidemiology, German Diabetes Center, Leibniz Institute for Diabetes Research at Heinrich Heine University Düsseldorf, Düsseldorf, Germany

[6]Department of Endocrinology and Diabetology, Medical Faculty and University Hospital Düsseldorf, Heinrich Heine University Düsseldorf, Düsseldorf, Germany

Correspondence
Vera B. Schrauwen-Hinderling, Metabolic Imaging Group, German Diabetes Center, Auf'm Hennekamp 65, 40225 Düsseldorf, Germany.
Email: vera.schrauwen-hinderling@ddz.de

Abstract

Concentrations of the key metabolites of hepatic energy metabolism, adenosine triphosphate (ATP) and inorganic phosphate (P_i), can be altered in metabolic disorders such as diabetes mellitus. ^{31}Phosphorus (^{31}P)-magnetic resonance spectroscopy (MRS) is used to noninvasively measure hepatic metabolites, but measuring their absolute molar concentrations remains challenging. This study employed a ^{31}P-MRS method based on the phantom replacement technique for quantifying hepatic ^{31}P-metabolites on a 3-T clinical scanner. Two surface coils with different size and geometry were used to check for consistency in terms of repeatability and reproducibility and absolute concentrations of metabolites. Day-to-day ($n = 8$) and intra-day ($n = 6$) reproducibility was tested in healthy volunteers. In the day-to-day study, mean absolute concentrations of γ-ATP and P_i were 2.32 ± 0.24 and 1.73 ± 0.26 mM (coefficient of variation [CV]: 7.3% and 8.8%) for the single loop, and 2.32 ± 0.42 and 1.73 ± 0.27 mM (CVs 6.7% and 10.6%) for the quadrature coil, respectively. The intra-day study reproducibility using the quadrature coil yielded CVs of 4.7% and 6.8% for γ-ATP and P_i without repositioning, and 6.3% and 7.1% with full repositioning of the volunteer. The results of the day-to-day data did not differ between coils and visits. Both coils robustly yielded similar results for absolute concentrations of hepatic ^{31}P-metabolites. The current method, applied with two different surface coils, can be

Abbreviations: ^{31}P, phosphorus; AMARES, advanced method for accurate, robust, and efficient spectral fitting; ATP, adenosine triphosphate; BMI, body mass index; BW, spectral bandwidth; CI, confidence interval; CSD, chemical shift displacement; CV, coefficient of variation; CW, continuous wave; FOV, field of view; Gd-DTPA, gadolinium-diethylenetriaminepentaacetic acid; GDS, German Diabetes Study; GLMM, generalized linear mixed model; GPC, glycero-phosphocholine; GPE, glycero-phosphoethanolamine; HS, hyperbolic secant; ISIS, image-selected in vivo spectroscopy; jMRUI, Java magnetic resonance user interface; K_2HPO_4, dipotassium phosphate; KH_2PO_4, monopotassium phosphate; MeP, methylphosphonic acid; MRS, magnetic resonance spectroscopy; N, sample points; NAD(P)H, nicotinamide adenine dinucleotide (phosphate); NOE, nuclear Overhauser enhancement; NSA, number of signal averages; PC, phosphocholine; PCr, phosphocreatine; PDE, phosphodiester; PE, phosphoethanolamine; PEP, phosphoenolpyruvate; P_i, inorganic phosphate; PME, phosphomonoester; PtdC, phosphatidylcholine; SD, standard deviation; SNR, signal-to-noise ratio; T1DM, type 1 diabetes mellitus; T2DM, type 2 diabetes mellitus; TE, echo time; TR, repetition time; UDPG, uridine diphosphate glucose; VOI, volume of interest.

Funding information
This study was supported in part by the German Diabetes Center (DDZ), which is funded by the Ministry of Culture and Science of the State of North Rhine Westphalia and the German Federal Ministry of Health (BMG), by grants of the Federal Ministry for Research (BMBF) to the German Center for Diabetes Research (DZD e. V.). MR is also supported by grants from the European Community (HORIZON-HLTH-2022-STAYHLTH-02-01: Panel A) to the INTERCEPT-T2D consortium, the German Research Foundation (DFG, GRK 2576) and the Schmutzler-Stiftung. VSH was supported by an ERC starting grant (grant no. 759161 "MRS in diabetes"). The funding sources had no role in study design, data collection, data analysis, data interpretation, or writing of the report.

readily utilized in long-term and interventional studies. In comparison with the single loop coil, the quadrature coil also allows measurements at a greater distance between the coil and liver, which is relevant for studying people with obesity.

KEYWORDS
absolute quantification, hepatic adenosine triphosphate, hepatic inorganic phosphate, reproducibility of ^{31}P-MRS, surface coil

1 | INTRODUCTION

The application of ^{31}phosphorus (^{31}P)-magnetic resonance spectroscopy (MRS) methods for measurements in the liver at clinical field strengths offers novel insights into energy metabolism. ^{31}P-MRS enables the detection of key metabolites such as adenosine triphosphate (γ-, α-, and β-ATP) and inorganic phosphate (P_i), as well as grouped phosphomonoesters (PMEs) and grouped phosphodiesters (PDEs).[1–23] Changes in their hepatic concentrations have been implicated in several diseases such as hepatocellular carcinoma,[1] liver cirrhosis,[1–6] and lymphoma,[7] but also in type 1 diabetes mellitus (T1DM),[8–10] type 2 diabetes mellitus (T2DM),[10–16] and other diseases.[17–19]

Qualitative MRS studies express the intensities of hepatic ^{31}P-metabolites as relative ratios compared with a reference metabolite. Mostly, the ATP signal is used as reference and studies report relative ratios of PME/ATP, PDE/ATP, PME/PDE, and P_i/ATP,[1,2,7,20–22] or ratios of single metabolites relative to the total ^{31}P-metabolite signal.[3,11,23] Assuming a certain concentration for the reference metabolite, for example, a γ-ATP concentration of 2.5–2.65 mmol/L [mM] based on liver biopsy data,[24] ratios can be converted to absolute concentrations.[25–28] The major drawback of this procedure is the variability of the reference metabolite. In that regard, it was previously shown that both hepatic γ-ATP and P_i decrease by approximately 37% in people with alcoholic hepatitis[4] and 25% in people with T2DM,[13] an effect that would have been missed when using ATP as reference. In order to measure tissue concentrations in absolute terms, it is necessary to normalize the obtained signals in a calibration measurement of a phantom with known concentration employing a so-called phantom replacement experiment.[29] Typically, a 2–5 L phantom containing monopotassium phosphate (KH_2PO_4) is measured with the identical protocol and setup as in vivo to take into account several methodological and coil-specific factors, such as coil loading, coil sensitivity, inhomogeneity of the excitation field B_1 and the excitation pulse profile to obtain absolute concentrations.[4,29–32]

The majority of people with T2DM are characterized by overweight or obesity, making the measurement of hepatic ^{31}P-metabolites challenging because of the large distance of the region of interest (liver) from the coil and the limited sensitivity of standard single loop coils. It was reported earlier that obesity is the strongest predictor of failed data acquisition for T2DM and that every unit increase in body mass index (BMI) lowered the amount of successful ^{31}P-MRS by 14%.[11] One possibility to counter this trend is the utilization of coils with improved coil design. For example, quadrature coils consist of multiple coil loops and in theory increase the signal-to-noise ratio (SNR) by a factor of $\sqrt{2}$ and simultaneously halve the necessary transmission power.[33]

For longitudinal cohort studies like the German Diabetes Study (GDS), which investigates the course of diabetes and its subtypes (endotypes) as well as its comorbidities for 20 years,[34,35] liver ATP and P_i are quantified repetitively over a long period of time and thus consistency of values over decades is mandatory. So far, a multipurpose standard single loop coil was used for this purpose in this study. To reduce missing values due to obesity and still guarantee continuity of the measured values, a newly designed quadrature coil was tested and the obtained values were compared with the outcome of the previously used single loop coil. Furthermore, the reproducibility using the new coil was assessed within a single session (intra-day repeatability and reproducibility) and between sessions on different days (day-to-day reproducibility). The latter is important for calculating the sample size in longitudinal studies.

Thus, we aimed (i) to compare the performance and stability of the same ^{31}P-method to detect and quantify hepatic ^{31}P-metabolites in molar concentrations on a 3-T clinical scanner using two different coil designs, a single loop and a quadrature coil; (ii) to evaluate the day-to-day and intra-day reproducibility of this method; and (iii) to assess the potential replacement of the single loop coil by the quadrature coil for its use in clinical intervention and larger cohort studies.

2 | MATERIALS AND METHODS

2.1 | Volunteers

Eleven volunteers (seven males/four females) aged 24 to 56 years, with a broad range of BMI (20.6–32.4 kg/m^2), participated in this study (Table 1). The study was approved by the local ethics committee and all volunteers gave their written informed consent before participation in the study.

2.2 | Study design

Two surface coils with different coil geometry (single loop and quadrature) and from different manufacturers were used to determine absolute values of ^{31}P-metabolites and day-to-day reproducibility. Furthermore, the quadrature coil was used to determine the intra-day repeatability and reproducibility of ^{31}P-metabolites assessment and was compared with the intra-day reproducibility as determined for the single loop coil in an earlier study.[36] The study design is visualized in Figure 1.

2.2.1 | Day-to-day reproducibility

Eight volunteers aged 27 to 56 years, with a BMI range of 20.8–32.4 kg/m^2, underwent ^{31}P-MRS of the liver in three visits each within a week (4 to 7 days, stated as V1–V3 in Figure 1A; Table 1). To achieve standardized physiological conditions, each volunteer was measured at the same time of the day after a 4.5-h fast. Moreover, volunteers were requested to record their food intake before the first examination to replicate their diet prior to the following measurement days. All participants were asked to refrain from strenuous exercise as well as from alcohol and caffeine intake on the day preceding the examination. Volunteers were repositioned every time before switching the coil to enhance their comfort, secure full repositioning, and reset scanner adjustments.

For the quadrature coil, long-term reproducibility was also tested in five out of the eight volunteers. These volunteers participated in a fourth visit (Figure 1A, V4) after approximately 3 months (11 to 14 weeks after the third measurement) to reassess metabolite concentrations (Table 1).

2.2.2 | Intra-day repeatability and reproducibility

To assess the intra-day repeatability and reproducibility of the ^{31}P-MRS measurements acquired with the quadrature coil, a subgroup of six healthy volunteers (Table 1) aged 24 to 50 years, with a BMI range of 20.6–29.4 kg/m^2, was examined several times within a day to judge methodological variations (Figure 1B). The first five spectra were consecutively acquired to assess (a) repeatability without coil repositioning ($n = 6$, Figure 1B, M1–M3); and (b) reproducibility of voxel replacement ($n = 3$, Figure 1B, M3–M5) to account for sensitivity of the method regarding different placement of the volume of interest (VOI) while the volunteer was not moved. Next, two more measurements ($n = 6$, Figure 1B, M6–M7) with full volunteer repositioning and "optimal" VOI placement, just as in M1-M3, were acquired to evaluate reproducibility with coil repositioning. For this, the volunteers were asked to leave the scanner each time for a break of 5 min. Additionally, no markers for coil positioning

TABLE 1 Participants' characteristics. A total of eight volunteers participated in the three-visit day-to-day study. Longitudinal day-to-day and intra-day repeatability and reproducibility were assessed in groups of $n = 5$ and $n = 6$, respectively. All values are reported as mean ± SD.

	^{31}P day-to-day variability liver (3 visits)	**^{31}P day-to-day variability liver (4 visits)**	**^{31}P intra-day variability liver (1 visit)**
No. of volunteers	8	5	6
Sex (male/female)	7/1	4/1	2/4
Age (years)	37.1 ± 11.0	29.6 ± 2.1	34.2 ± 9.6
Weight (kg)	91.4 ± 17.4	85.8 ± 20.3	80.0 ± 21.1
Height (m)	1.83 ± 0.11	1.84 ± 0.13	1.77 ± 0.15
BMI (kg/m^2)	27.3 ± 4.2	25.2 ± 3.8	25.3 ± 3.5
Coil used	Single loop and quadrature	Quadrature	Quadrature
Data used for	Day-to-day reproducibility + coil comparison	Day-to-day reproducibility	Intra-day repeatability and reproducibility

Abbreviation: BMI, body mass index.

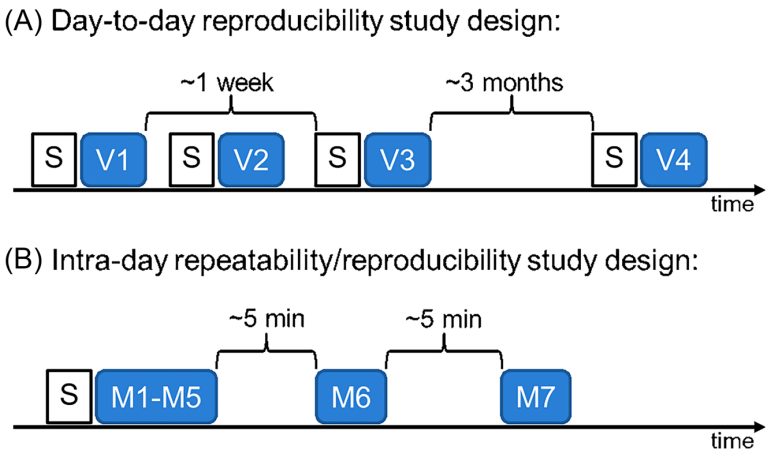

FIGURE 1 Study design. S, standardization protocol including measurement at the same time of the day and 4.5-h fasting after standard meal. (A) Day-to-day reproducibility study: hepatic ^{31}P-metabolites were measured with ^{31}P-MRS at each visit V1–V4 (V1–V3 within 1 week using both single loop and quadrature coils, V4 after 3 months using only the quadrature coil). (B) Intra-day repeatability/reproducibility study (quadrature coil only): M1–M5, five consecutive ^{31}P-measurements to evaluate (i) repeatability of the method without coil repositioning (M1–M3); and (ii) sensitivity of the method regarding different volume of interest (VOI) placement (M3–M5). M6 and M7 denote additional measurements to evaluate reproducibility of the method with coil repositioning; just as for M1–M3, the most optimal VOI position was sought.

were used, to guarantee a full repositioning with new adjustments. Moreover, the same physiological standardization protocol as in the day-to-day sessions was applied. Intra-day reproducibility of the single loop coil was previously reported by our group.[36]

2.3 | MR system and surface coils

All the examinations were conducted on a clinical 3-T MR system with the multinuclear option (bore diameter 60 cm, Philips Achieva dStream, Best, the Netherlands) using two different surface coils (Figure 2C,F). The first coil was a vendor-provided flat 14-cm circular single loop ^{31}P-surface coil (transmit-receive coil; Philips Healthcare, Best, the Netherlands) and the second coil was a newly designed curved quadrature ^{31}P-surface coil (transmit-receive coil; RAPID Biomedical, Rimpar, Germany) with total ^{31}P-loop size of 220 mm × 160 mm. Shimming, ^{1}H decoupling, and nuclear Overhauser enhancement (NOE) were performed by the ^{1}H-body coil (transmit-receive birdcage coil; Philips Healthcare). To correct for coil loading effects, both ^{31}P-coils had notches where methylphosphonic acid (MeP)-filled glass spheres were positioned inside the housing. While the MeP reference of the single loop coil was provided by the manufacturer and located in a sealed cavity in the center of the 140 mm loop, the MeP (98%, Sigma-Aldrich, Schnelldorf, Germany) references of the quadrature coil were custom made using two 530 µL spheres, whereas one is placed in the center of each ^{31}P-loop (the positions are highlighted in red in Figure 2C,F).

2.4 | Acquisition and localization of the ^{31}P-signal in human liver

First, scout images in three orientations were acquired (five slices of 15 mm thickness, 10 mm gap, field of view [FOV] 450 × 450 mm^2) followed by transverse T_2-weighted images acquired with multislice 2D single-shot turbo spin echo (repetition time [TR]/echo time [TE] 883/80 ms; 23 slices of 6mm thickness, 1mm gap, FOV 450 × 378 mm^2). After verification of correct coil positioning on the right lateral lobe of the liver, ^{31}P-MRS acquisition was planned by carefully placing a 60 × 60 × 60 mm^3 VOI within the liver tissue, avoiding immediate proximity to the lung, gallbladder, and abdominal muscle. Liver spectra were acquired using a 3D-localized image-selected in vivo spectroscopy (ISIS)[37] sequence with a 5.43 or 3.83 ms hyperbolic secant (HS) adiabatic half passage pulse for excitation (excitation bandwidth 1.15 or 1.63 kHz) for the single loop and quadrature coil, respectively, TR 6 s, number of signal averages (NSA) 128, total acquisition time 13 min, sample points (N) 2048, spectral bandwidth (BW) 3 kHz, excitation pulse center ~1.0 ppm, broadband decoupling (WALTZ-4) with offset frequency −100 Hz and B_1 amplitude 7 µT, continuous wave (CW) NOE with mixing time 3500 ms, offset frequency −100 Hz, and B_1 amplitude 0.5 µT. The duration of the HS inversion pulse for slice selection was 5.66 and 4.0 ms, while the HS inversion bandwidth was 2.25 and 3.18 kHz for the single loop and quadrature coil, respectively. No respiratory triggering was used. Shimming typically reached a linewidth of ~30 Hz for both coils.

Spectra of the external reference MeP spheres were acquired to account for coil loading in separate scans using a pulse-acquire sequence with the identical HS adiabatic pulse of the corresponding coil for excitation, TR 8 s, NSA 16, total acquisition time ~2 min, N 8192, BW 6 kHz,

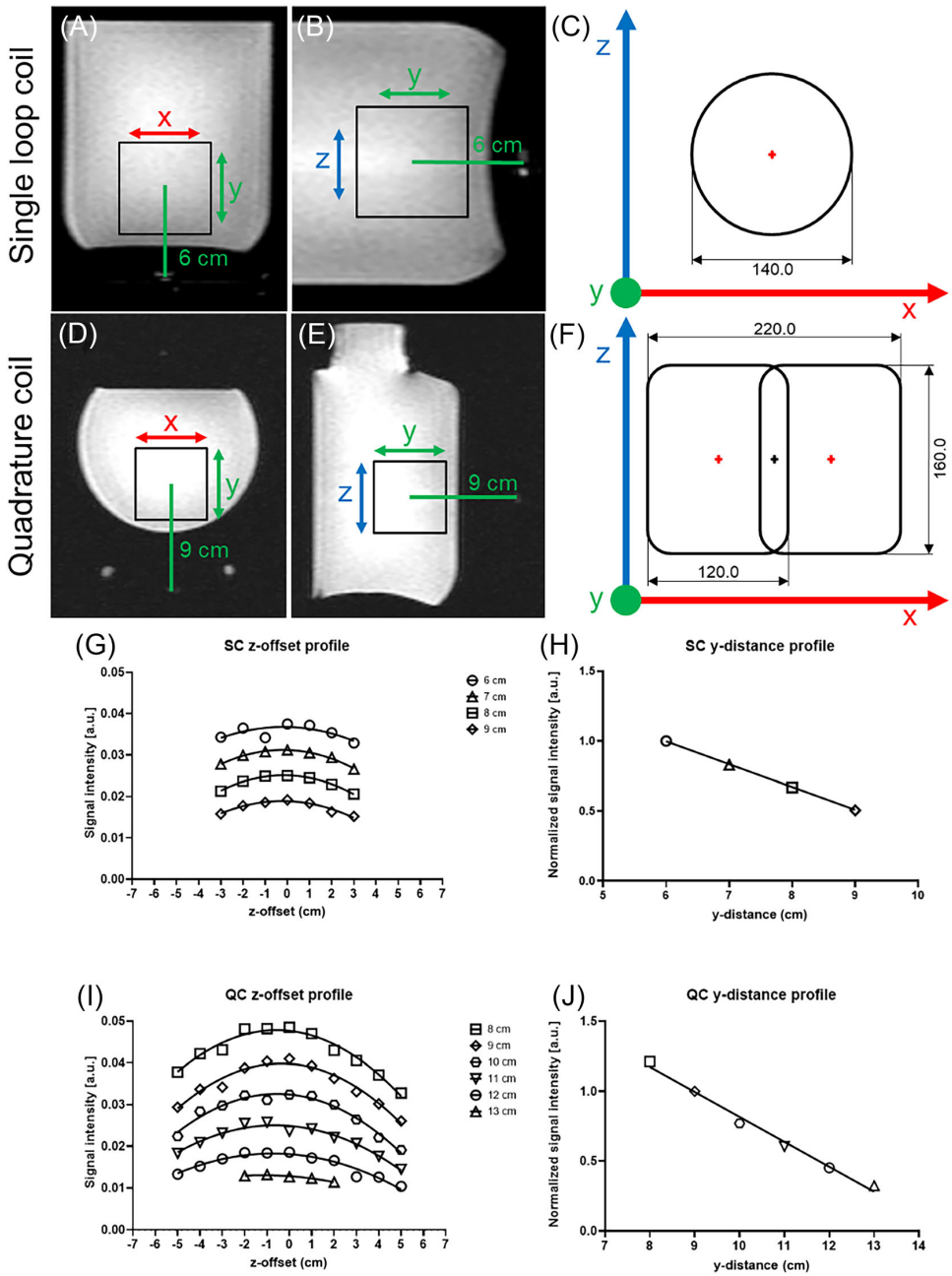

FIGURE 2 In vitro setup to determine correction factors for absolute quantification. The volume of interest (VOI) was shifted in all dimensions to compensate for different placements in the liver. For the single loop coil setup the phantom was placed upright on the coil (A, B), while it was laid down for the quadrature coil setup due to its curved housing (D, E). (C, F) Schematic overview of both ^{31}P-coil designs including coil orientation for (C) flat circular single loop, and (F) curved quadrature coil. Reference cavities are visualized as crosses. Red crosses highlight the location of the MeP spheres in the coil, the black cross symbolizes a sphere filled with water. All displayed dimensions are expressed in mm. (G, I) Offset profile of both coils to account for imperfect placement of the VOI in the central position of the coil. (H, J) Depth profile of both coils to account for variations in distance between VOI and the central coil reference. MeP, methylphosphonic acid; SC, single loop coil; QC, quadrature coil.

no proton decoupling, NOE, or localization. Shim voxel size was adjusted to the position of the external reference and varied in size for the two coils (single loop 80 × 80 × 80 mm^3, quadrature coil 130 × 80 × 80 mm^3). All details of the acquisition procedure are listed in Table S1.[38]

2.5 | ^{31}P-MRS in vitro measurements and correction factors for absolute quantification

In order to enable absolute quantification of ^{31}P-metabolites in the liver, an in-house mixed phantom containing 50 mM dipotassium phosphate (K_2HPO_4) (Sigma Aldrich) and 0.1 mM gadolinium-diethylenetriaminepentaacetic acid (Gd-DTPA) (Sigma Aldrich) was measured as matching phantom (cylindrical phantom, volume 3 L, diameter 16 cm, height 19 cm, T_1 10.36 s).[36] The phantom was placed in a similar position inside the scanner as the liver and spectra were acquired with the same geometries and parameters as used for the in vivo protocol (Figure 2A,B,D,E).

Spectra were acquired while the distance between the VOI and central coil reference (y-distance) varied, ranging from 6 to 10 cm in 1 cm steps (Figure 2H). In each of these steps, nine different frequency offsets corresponding to the position of the prominent ^{31}P-metabolites were set to be able to correct for the pulse profile (Figure S1). Additionally, to account for imperfect placement in the central position of the coil of the VOI, further spectra with positions towards the edge of the coil, ranging from −3 to 3 cm in 1 cm steps, were acquired (Figure 2G). In the final quantification table, these profiles allow to correct the in vivo spectrum resonances regarding offset frequency for each individual peak and x-, y-, and z-distance for each volunteer and metabolite.

Because of the different size and geometry of the quadrature coil, spectra for distance correction ranged from 8 to 13 cm (1 cm steps) and VOI placement towards the edge of the coil from −5 to 5 cm in steps of 1 cm, respectively (Figure 2I,J).

2.6 | Quantification procedure using the phantom replacement method

Absolute quantification of ^{31}P-metabolites in molar concentration was achieved using the phantom replacement method as introduced by Meyerhoff et al.[29] For correction of coil loading, the signal from the small glass sphere(s) containing MeP located in the coil housing was used.

In summary, corrections were applied for coil loading, T_1 relaxation times, the excitation profile of the adiabatic pulse, and B_1 inhomogeneities of the surface coil in all three spatial directions. The final concentration c^{ij} (in mM) of each corresponding ^{31}P-metabolite i of volunteer j can be obtained by the following equation[36]:

$$c^{ij} = \frac{A^{ij}}{A_{ph}} \cdot \frac{A^{ph}_{ref}}{A^{j}_{ref}} \cdot c_{ph} \cdot f^{i}_{T_1} \cdot f^{i}_{offset} \cdot f_{B_{1,xyz}} \cdot f_{liver\ lipid\ content}$$

A^{ij} represents the fitted peak area of a ^{31}P-metabolite in the liver of a volunteer, A_{ph} is the fitted peak area of the K_2HPO_4 phantom, which is corrected for T_1 and temperature, A^{ph}_{ref} denotes the fitted peak area of the MeP reference in the phantom measurement, A^{j}_{ref} is the fitted peak area of the MeP reference in a volunteer measurement, c_{ph} represents the known concentration of K_2HPO_4 in mM (50 mM), f^{i}_{T1} is referred to the correction factor for the corresponding T_1 relaxation time of the ^{31}P-compound, f^{i}_{offset} is the correction factor accounting for signal intensity of the different chemical shifts of the metabolites due to the nonuniform excitation pulse profile, $f_{B1,xyz}$ denotes the correction factor for the distance between the center of the coil to the center of the voxel in all three spatial directions, and $f_{liver\ lipid\ content}$ represents the correction factor for the amount of liver lipid content.

T_1 relaxation times of the ^{31}P-metabolites in the liver were corrected by using the reported values at 3-T by Schmid et al.[27] A correction for hepatic lipid content was not applied in this study. As volunteers were scanned within a short time period when they did not change their nutritional behavior, we assumed that the hepatic lipid content was the same in each session and did not influence reproducibility.

2.7 | Data processing

In line with best practice,[38,39] all spectra were reviewed regarding quality and were processed in a blinded fashion to the origin of the spectra (volunteer and session no.). To ensure good data quality, all spectra were analyzed regarding SNR using the definition[39] $SNR = \frac{Signal}{\sigma_{Noise}}$. After application of a 15 Hz Gaussian filter, the signal was defined as the fitted amplitude of the metabolite of interest and noise (σ) as standard deviation (SD) of the spectrum between 10 and 20 ppm both in the frequency domain using a custom written MATLAB script (MathWorks Inc. R2021a, Natick, MA, USA). Two quality criteria were applied: SNR of γ-ATP less than 4 and SNR of P_i less than 2.5 as marker for low spectral quality. Moreover, to account for potential signal contamination from abdominal skeletal muscle, the phosphocreatine (PCr) to γ-ATP peak ratio was calculated and spectra with PCr/γ-ATP more than 0.5 were excluded.

Spectra were processed using Java magnetic resonance user interface (jMRUI) software.[40,41] All spectra were apodized with a Gaussian line shape of 15 Hz, manually zero order-phased and frequency adjusted by setting the γ-ATP resonance to −2.48 ppm. Peak fitting was performed using

the advanced method for accurate, robust, and efficient spectral fitting (AMARES)[42,43] algorithm in jMRUI. Twelve peaks were quantified to account for 11 hepatic metabolite resonances and one additional peak to additionally account for potential PCr contamination from abdominal muscles. Chemical shift assignment was adapted from previous publications[44,45] and a custom-created prior knowledge file was used for fitting (Table S2).

The external reference spectra were processed using a 20 Hz Gaussian line shape apodization and manual zero order phasing. Next, the resonance of MeP was fitted as a single Gaussian peak, whereas amplitude, linewidth, and frequency were not constrained (set to "estimated").

2.8 | Statistical analysis

Statistical analysis was performed with GraphPad Prism v. 9.5 for Windows (GraphPad Software, San Diego, CA, USA). All reported data for absolute concentrations of ^{31}P-metabolites are presented as mean ± SD or mean (95% confidence interval [CI]). To assess the intra-volunteer variability, the coefficient of variation (CV), defined as the ratio of the SD to the mean, was calculated for all ^{31}P-measurements. Bland–Altman analysis was performed to assess the agreement between concentrations obtained for γ-ATP and P_i using both coils.

In order to test for significant differences in the estimated absolute quantification results obtained from the two different coils in the day-to-day reproducibility study (three visits with both coils), an analysis of covariance (ANCOVA) for generalized linear mixed model[46] (GLMM) with repeated measures adjusted for both coil and visit was performed in SAS v. 9.4 for Windows (SAS Institute, Cary, NC, USA) with significance level $\alpha = 0.05$.

3 | RESULTS

3.1 | ATP and P_i concentration

Valid results were obtained for ATP and P_i from all participants, on all occasions, except for one spectrum acquired during day-to-day measurements with the single loop coil, which was excluded due to low SNR. The mean absolute concentrations of γ-ATP and P_i were similar for both coils, amounting to 2.32 ± 0.24 and 1.73 ± 0.26 mM for the single loop and 2.32 ± 0.42 and 1.73 ± 0.27 mM for the quadrature coil, respectively (n.s., Tables 2 and 3). Values are given as the mean ± SD of the three measurement days. The Bland–Altman comparison of inter-coil variability shows a mean difference in concentration between both coils of −0.00522 ± 0.398 mM for γ-ATP and 0.000870 ± 0.233 mM for P_i (Figure 3). Of the 23 compared pairs of values, 22 (95%) and 21 (91%) were within 2 SDs for γ-ATP of P_i, respectively. Taking into account data from the fourth measurement, acquired approximately 3 months later, did not significantly change the results for γ-ATP (2.42 ± 0.45 mM) and P_i (1.76 ± 0.31 mM). Even although the main focus of this study was on assessing γ-ATP and P_i, for completeness we also analyzed the other prominent ^{31}P-metabolites glycero-phosphocholine (GPC), glycero-phosphoethanolamine (GPE), phosphocholine (PC), and phosphoethanolamine (PE) regarding metabolite concentrations, CVs, and statistical differences between both coils (Tables S3–S5).

3.2 | Variability of ATP and P_i

The mean intra-volunteer CVs of the three sessions day-to-day reproducibility study of γ-ATP and P_i were 7.3% ± 3.1% and 8.8% ± 3.4% for the single loop and 6.7% ± 3.3% and 10.6% ± 11.3% for the quadrature coil, respectively. Taking into account the fourth measurement after 3 months, the

TABLE 2 Estimated CVs and absolute concentrations of γ-ATP and P_i of the day-to-day and intra-day repeatability and reproducibility studies of the ^{31}P-MRS method including both coils.

	No. of volunteers	% CV intra-volunteer ± SD		Concentration, mM (mean ± SD)	
		γ-ATP	P_i	γ-ATP	P_i
Single loop coil—three sessions (V1–V3)	8	7.3 ± 3.1	8.8 ± 3.4	2.32 ± 0.24	1.73 ± 0.26
Quadrature coil—three sessions (V1–V3)	8	6.7 ± 3.3	10.6 ± 11.3	2.32 ± 0.42	1.73 ± 0.27
Quadrature coil—four sessions (V1–V4)	5	6.5 ± 3.7	15.2 ± 8.6	2.42 ± 0.45	1.76 ± 0.31
Quadrature coil—single session without repositioning (M1–M3)	6	4.7 ± 2.2	6.8 ± 2.1	2.24 ± 0.28	1.62 ± 0.25
Quadrature coil—single session with different VOI placement (M3–M5)	3	7.4 ± 2.0	8.2 ± 2.7	2.24 ± 0.22	1.40 ± 0.18
Quadrature coil—single session with volunteer repositioning (M1, M6, M7)	6	6.3 ± 5.3	7.1 ± 6.1	2.35 ± 0.32	1.69 ± 0.27

Abbreviations: CV, coefficient of variation; VOI, volume of interest.

TABLE 3 Analytical results using a repeated measures ANCOVA for GLMM adjusted for both coil and visit for the metabolites γ-ATP and P_i of the single loop and quadrature coil day-to-day reproducibility study (three visits). Estimated absolute concentrations of γ-ATP and P_i with 95% CI are listed for each individual coil or visit and their individual differences are shown.

	Concentration, mM (95% CI)	
Effect	**γ-ATP**	**P_i**
Least squares means		
All spectra of SC coil	2.31 [2.10; 2.53]	1.73 [1.58; 1.87]
All spectra of QC coil	2.32 [2.11; 2.53]	1.73 [1.59; 1.87]
Visit 1 (SC and QC)	2.28 [2.05; 2.50]	1.68 [1.52; 1.83]
Visit 2 (SC and QC)	2.34 [2.12; 2.56]	1.77 [1.61; 1.92]
Visit 3 (SC and QC)	2.34 [2.11; 2.56]	1.75 [1.58; 1.91]
Differences of least squares means		
SC–QC	−0.00554 [−0.146; 0.135]	−0.00066 [−0.131; 0.129]
Visit 1–Visit 2 (SC and QC)	−0.0618 [−0.231; 0.108]	−0.0899 [−0.247; 0.0671]
Visit 1–Visit 3 (SC and QC)	−0.0591 [−0.232; 0.114]	−0.0696 [−0.230; 0.0905]
Visit 2–Visit 3 (SC and QC)	0.00263 [−0.170; 0.175]	0.0203 [−0.140; 0.180]

Abbreviations: ANCOVA, analysis of covariance; CI, confidence interval; GLMM, generalized linear mixed model; QC, quadrature coil; SC, single loop coil.

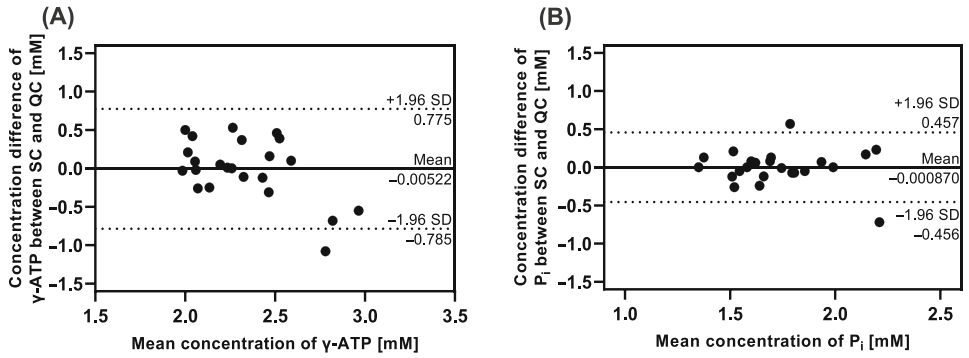

FIGURE 3 Bland–Altman plots for intercoil variability of (A) γ-ATP, and (B) P_i concentrations. 22 out of 23 datapoints are within 2 SDs for γ-ATP and 21 out 23 points for P_i. SC, single loop coil; QC, quadrature coil.

CVs were similar, with 6.5% ± 3.7% for γ-ATP and 15.2% ± 8.6% for P_i. For the intra-day reproducibility, the mean CVs of γ-ATP and P_i amounted to (a) 4.7% ± 2.2% and 6.8% ± 2.1% in a single session without repositioning; (b) 7.4% ± 2.0% and 8.2% ± 2.7% in a single session with different VOI placement; and (c) 6.3% ± 5.3% and 7.1% ± 6.1% in a single session with full repositioning of the volunteer, respectively (Figure 4). An overview of individual obtained values for other prominent ^{31}P-metabolites including the main CVs can be reviewed for both coils in Figure S2.

3.3 | Spectral quality

The mean SNRs of γ-ATP and P_i in the day-to-day study (three visits) were 8.2 ± 1.5 and 7.3 ± 2.3 for the single loop and 8.0 ± 1.5 and 6.8 ± 1.9 for the quadrature coil, respectively. The PCr signal, which indicates signal contamination from muscle, was low in all cases (18% ± 16% and 25% ± 12% of ATP signal intensity for the single loop and quadrature coil, respectively). Figure 5 shows representative ^{31}P-MRS spectra with all 11 prominent hepatic ^{31}P-metabolites.

4 | DISCUSSION

This study used a slightly modified version of an established ^{31}P-MRS method, allowing robust absolute quantification of hepatic γ-ATP and P_i concentrations within 15 min at 3-T with a quadrature coil. Results were compared with the results obtained with the previously used single loop

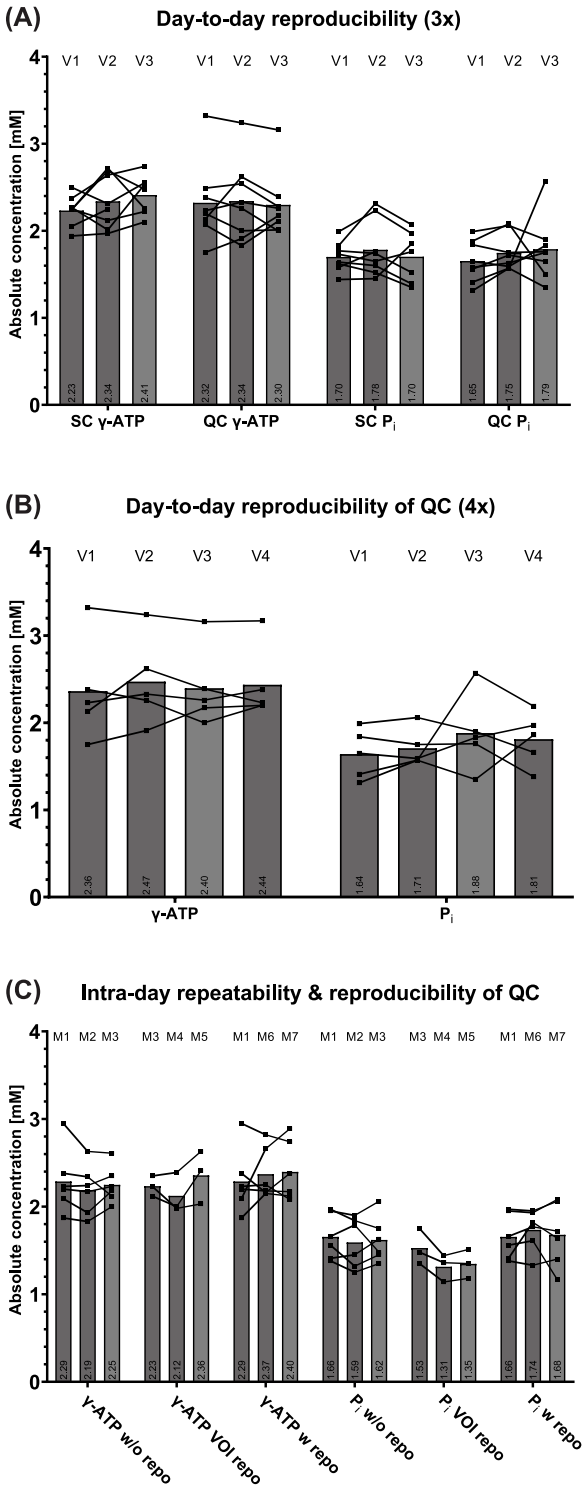

FIGURE 4 Legend on next page.

FIGURE 4 Results of the day-to-day (three and four visits) and intra-day repeatability and reproducibility study. For each study all obtained metabolite concentrations are denoted as a single datapoint. Black bars indicate mean values of one visit or session. Metabolite concentrations are presented in mM concentrations, quantified by the replacement method using a phantom with known concentration. (A) Results of the day-to-day reproducibility study to assess absolute concentrations of γ-ATP and P_i with both coils. All volunteers underwent the same MR sessions on three different days within a week (V1–V3). (B) Results of the day-to-day reproducibility study of the quadrature coil (V1–V3) with an additional measurement approximately 3 months later (V4) to assess the long-term variability of γ-ATP and P_i concentration. (C) Results of the intra-day repeatability and reproducibility study of the quadrature coil. Repeatability and reproducibility of measurements (i) without volunteer repositioning; (ii) with volume of interest (VOI) repositioning; and (iii) with volunteer repositioning between measurements were assessed. SC, single loop coil; QC, quadrature coil.

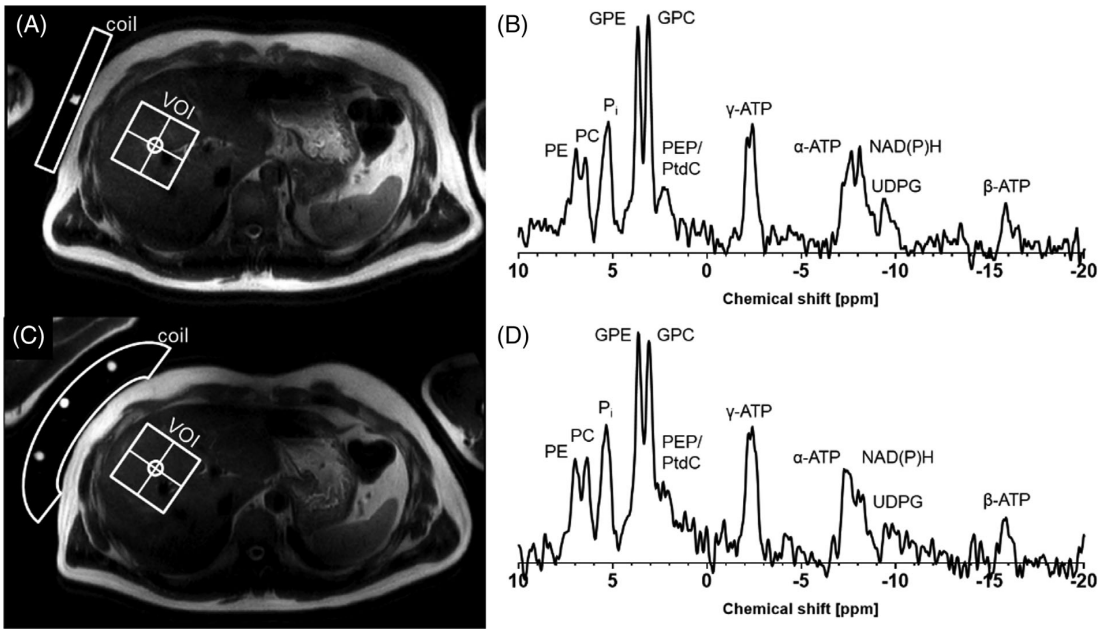

FIGURE 5 Top: single loop coil, bottom: quadrature coil. (A, C) Transversal slices of the liver showing coil placement and position of the volume of interest (VOI). White dots within the coil housing show the position of the reference spheres. (B, D) Representative ^{31}P-MR spectra (apodization 15 Hz) of human liver at a field of 3-T. ATP, α-,β-,γ-adenosine triphosphate; GPC, glycero-phosphocholine; GPE, glycero-phosphoethanolamine; NAD(P)H, nicotinamide adenine dinucleotide (phosphate); P_i, inorganic phosphate; PC, phosphocholine; PE, phosphoethanolamine; PEP/PtdC, phosphoenolpyruvate/phosphatidylcholine; UDPG, uridine diphosphate glucose.

surface coil,[36] and excellent agreement was found between the two coils. The consistency of measurements of absolute concentrations of metabolites in prospective studies over years to decades, like the GDS cohort,[34] can be challenging because coil replacement during the study is inevitable. If a new coil is introduced, the consistency of the results always needs careful validation. This is even more so when the coil geometry is changed. By introducing a slightly larger quadrature coil, we aimed to increase the success rate of hepatic ^{31}P-measurements in people with obesity while making sure that the measured ATP and P_i concentrations were not affected. Measurements in people with obesity using the single loop coil often fail, especially for a high distance between coil and VOI, which results in low SNR and therefore poor quality spectra.

Our results show that the absolute concentrations of ATP and P_i were very similar for both the single loop and quadrature coil and therefore the quadrature coil can indeed replace the single loop coil. This shows the importance of the exact procedures in terms of phantom setup and quantification of spectra, as this seems to be a more important source of variation than the coil used. Indeed, the range reported at different field strengths in the literature is rather large, with 1.39–3.7 mM for γ-ATP and 1.18–2.8 mM for P_i[5,6,8,12,13,17,18,29–32,36,44,47–49] suggesting that differences in site-specific procedures introduce relevant biases. However, the values of this study are well in range with those concentrations reported by other groups.[6,13,18,31,32,36,48]

In terms of quality of the measurement, the coils also performed very similarly. The mean intra-volunteer CVs for both coils were very similar (7.3% and 6.7% for γ-ATP and 8.8% and 10.6% for P_i) and agree with the literature,[1,11,32] which is the typical range for in vivo MRS measurements. The larger coil element size in the quadrature coil was expected to introduce more noise; however, the quadrature geometry should compensate for this by increasing the sensitivity and, therefore, also the signal. Indeed, the SNR results show a very similar outcome for both coils with mean SNRs of γ-ATP and P_i of 8.2 and 7.3 using the single loop and 8.0 and 6.8 using the quadrature coil, respectively.

A fourth measurement in five volunteers after approximately 3 months did not introduce additional variation, showing that basal concentrations of γ-ATP and P_i remain stable in healthy volunteers and when using a simple standardization protocol.

One of the volunteers showed a large deviation in P_i and especially in γ-ATP concentrations using the quadrature coil compared with the results obtained with the single loop coil. In the Bland–Altman analysis, the three most negative outliers for γ-ATP and the most negative point in the P_i plot can be assigned to him. This may originate from difficulties with consistent coil positioning in this volunteer. Being very lean and having a small waist circumference, the rigid, curved design of the quadrature coil did not fit to the volunteer's abdomen, and, during fasting, one of the coil elements was always at a greater distance, with a large air gap between the coil and the body. This appears to be a disadvantage of the quadrature coil, which was intentionally designed to perform ^{31}P-MRS in people with overweight or obesity, and reveals limitations for lean people with a small waist circumference due to its geometry.

Methodological variation, for example, due to respiratory motion or differences in shim, was determined by the consecutive repetition of the protocol (without repositioning). Intra-volunteer CVs of 4.7% for γ-ATP and 6.8% for P_i highlight that the method is highly reproducible and comparable with the literature.[32]

Robustness of the method for nonoptimal VOI placement was checked by purposely placing the VOI in a suboptimal position. In such cases, we detected an increase in CVs to 7.4% and 8.2% for γ-ATP and P_i. These are the highest CVs detected in the intra-day measurements. Although this variability is somewhat higher than with a consistent voxel position, it can still be acceptable for physiological studies and demonstrates that the method can compensate for small deviations from the most ideal VOI placement.

The CVs after full repositioning of the volunteer were slightly higher with 6.3% and 7.1% for γ-ATP and P_i than without repositioning (4.7% and 6.8%), but still below CVs of the day-to-day study (6.7% and 10.6%). Laufs et al.[36] reported comparable intra-day CVs of 9% and 7% assessed in five volunteers twice on different days with three scans including full repositioning. These values are of importance for sample size calculations for interventional studies where volunteers enter the scanner on different days.

In the current study, only one out of 86 spectra had to be excluded due to low SNR. The excluded spectrum was acquired with the single loop coil and excluded because of low SNR (γ-ATP < 4). It should be mentioned that no spectrum was excluded due to an inacceptable degree of abdominal muscle signal contamination resulting in a prominent PCr resonance (PCr/γ-ATP > 0.5). To minimize muscle contamination, a gap between abdominal muscle tissue and VOI was always maintained (Figure 5). Similarly, attempts were made to avoid the gallbladder as much as possible, although this was not always possible because of the limited liver size and the voxel size that was used. It was reported earlier that the resonance at ∼2.06 ppm originates mainly from the gallbladder, which is why it can be used for estimation of signal contamination.[50,51] A voxel size of 60 mm in each direction was applied to achieve a reasonable SNR within a scan time of approximately 13 min. Because a significant number of our cohort study in which this protocol is applied are overweight or obese, the big voxel size is necessary to compensate for signal loss due to the high distance between coil and liver tissue, which would otherwise lead to noisy spectra. In terms of chemical shift displacement (CSD), the chemical shift between γ-ATP and P_i amounts to ∼7.7 ppm, corresponding to ∼400 Hz at 3-T and will result in a CSD of ∼6.7 mm between these two metabolites. As the center of the HS AHP excitation pulse is located between the two metabolites, the CSD will be lower in our experiments, but in opposite directions. When planning measurements, care was taken that the voxel position was well within the liver for both metabolites. Although small, it is important to note that the CSD is taken into account for the absolute quantification, as the in vitro measurements are performed with the same settings as the in vivo measurements.

The main objective of this study was the comparison between two different surface coils for assessing hepatic γ-ATP and P_i. However, it is also possible to gain information about other prominent ^{31}P-metabolites from the acquired spectra. This study used γ-ATP as ATP representative for ATP concentration, although it should be noted that the γ-ATP signal contains a contribution of β-ADP.[52] The only pure ATP resonance is the β-ATP signal; however, due to the big chemical shift of the β-ATP resonance and the limited excitation pulse bandwidth, which resulted in low SNR for β-ATP, it was not possible to reliably quantify this peak. The remaining prominent metabolites GPC, GPE, PC, and PE were also analyzed between both coils and no significant differences were found between both individual visits and coils, except for a difference between the first two visits for GPC and between both coils for GPE (Tables S3 and S4). Furthermore, the CVs of GPC and GPE were less than 10% in the day-to-day study, whereas PC and PE showed more variations (CVs < 20%) (Table S5). Here, the trend also shows that the inaccuracy of the determination of concentrations increases with larger chemical shifts from the excitation pulse center.

This study used jMRUI with the AMARES algorithm for data processing and peak fitting. Establishing custom prior knowledge files including chemical shifts, linewidths, and line shapes allowed both a precise and highly reproducible fitting as well as a fast analysis (Figure 6). Consistent analysis is important, because in the early beginning of employing absolute quantification in liver, the results reported diverged significantly,[6,29,30,44] which was found to be partly caused by differences in processing and quantification methods.[25] Including fitting of the minor resonances uridine diphosphate glucose (UDPG), nicotinamide adenine dinucleotide (phosphate) (NAD(P)H), PCr, phosphoenolpyruvate (PEP), and phosphatidylcholine (PtdC) led to an almost flat residue (Figure 6, top section). PCr, fitted as peak 6, was always included in the fitting procedure as an indicator for signal contamination from superficial muscle and was used as the basis for exclusion of spectra. Noticeable is a continuous decrease of peak amplitude of the three ATP resonances from γ- to α- and especially β-ATP, which is caused by the limited excitation bandwidth (1.15 and 1.63 kHz) of the HS adiabatic pulse of the single loop and quadrature coil and the fact that the center frequency was set in between the metabolites of interest γ-ATP and P_i.

This study has certain limitations:

1. For the day-to-day reproducibility study there was no randomization of the protocols and coils, which might lead to a bias if customization to the measurements is needed. However, all the volunteers were familiar with MRS studies. Furthermore, all volunteers left the scanner after the single loop coil measurement without markers, allowing for identification of the coil setup. Thus, positioning of the quadrature coil was performed independently from the previous setup.
2. This study did not apply a correction for liver lipid content, which is usually performed for hepatic ATP measurements. However, the participants had a stable lifestyle without changes in meal pattern and physical activity during the short period of this study. Thus, hepatic lipid content will not affect the reproducibility and consistency of results under these conditions. Still, it might have influenced the spread of the obtained data, especially in the case of the two obese volunteers.

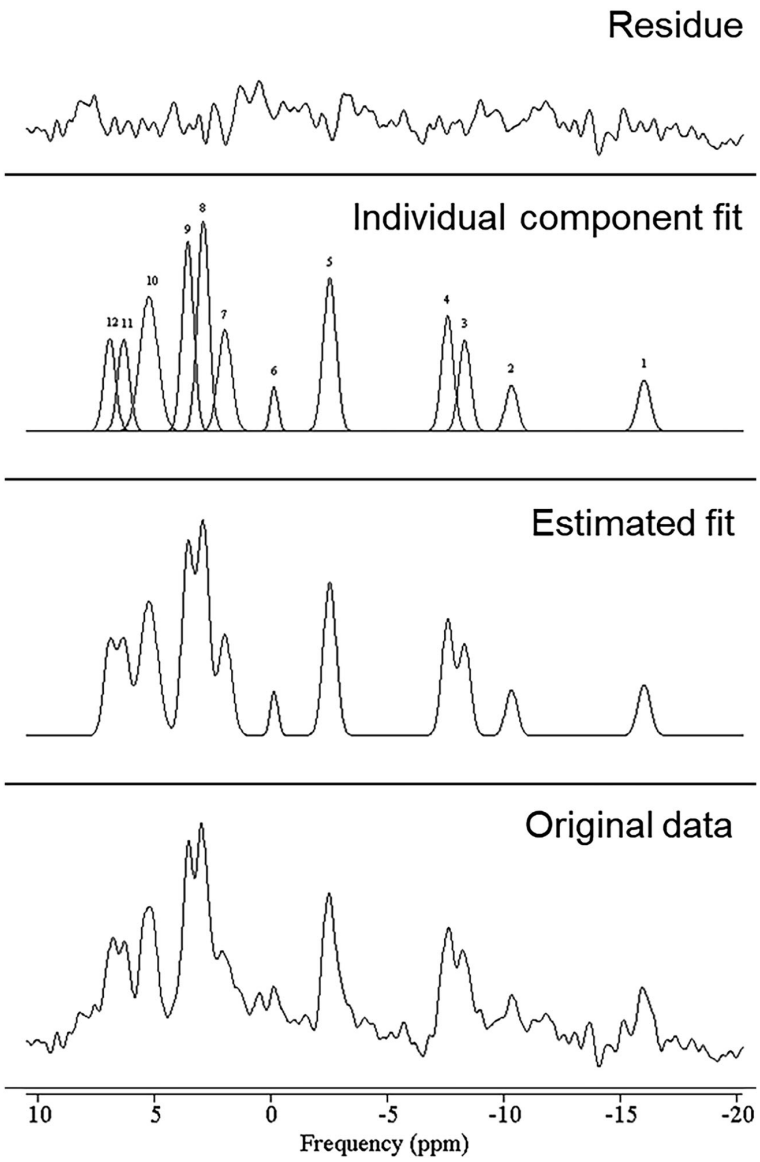

FIGURE 6 Exemplary result of the advanced method for accurate, robust, and efficient spectral fitting (AMARES) fitting routine of a human hepatic ^{31}P-spectrum (quadrature coil). Graphs from bottom to top: original data, sum of fitting result, individual peak fitting (1,4,5: β-,α-,γ-adenosine triphosphate [ATP], 2: uridine diphosphate glucose [UDPG], 3: nicotinamide adenine dinucleotide (phosphate) [NAD(P)H], 6: phosphocreatine [PCr], 7: phosphoenolpyruvate/phosphatidylcholine [PEP/PtdC], 8,9: phosphodiester [PDE], 10: inorganic phosphate [P_i], 11,12: phosphomonoester [PME]) and residue of the spectrum after fitting.

3. The obtained absolute concentrations for both γ-ATP and P_i are slightly lower compared with previous data of our group.[36] Lower absolute concentrations may result from the absence of correction for liver lipid content or from a different duration of fasting before the measurements. Nevertheless, dietary intervention studies revealed conflicting results on meal ingestion and fasting on ATP concentrations.[16,23,53,54]
4. A recent publication indicated that the absolute concentrations obtained using the phantom replacement technique can be biased when the conductivity of the phantom does not match the in vivo situation.[49] An acceptable range of conductivity of a phosphate phantom at 3-T field strength was found to be between $0.39-0.58\,\frac{S}{m}$. The 50 mM K_2HPO_4 phantom used in this study has an estimated conductivity of appoximately $0.89\,\frac{S}{m}$, which may introduce a 20% bias. Correcting our results according to Purvis et al.[49] would lead to concentrations of 2.78 and 2.08 mM for γ-ATP and P_i, which is still in agreement with the literature.

In summary, 3D-ISIS ^{31}P-MRS allows for robust measurement of hepatic γ-ATP and P_i concentrations within a reasonable time frame of ~13 min when a single loop or a quadrature coil is used. High reproducibility was shown for both day-to-day (CV < 11%) and intra-day studies with full repositioning (CV < 8%). The similarity of the metabolite concentrations between both coils and visits shows the robustness of the phantom-replacement method for obtaining absolute concentrations. This justifies switching between coils without introducing a coil-dependent bias. The larger coil loops of the quadrature coil may increase the success rate of measurements in people with obesity and in those with BMI values exceeding 32 kg/m^2.

AUTHOR CONTRIBUTIONS

Marc Jonuscheit designed the study, conducted the measurements, analyzed and interpreted the data, and wrote the manuscript. Stefan Wierichs analyzed the data and reviewed/edited the manuscript. Maik Rothe conducted the measurements and reviewed/edited the manuscript. Julian Mevenkamp helped with data analysis. Pavel Bobrov performed statistical analysis. Benedict Korzekwa, Yuliya Kupriyanova, and Michael Roden reviewed/edited the manuscript. Vera B. Schrauwen-Hinderling supervised the study, interpreted data, and reviewed/edited the manuscript. Vera B. Schrauwen-Hinderling is the guarantor of this work and, as such, had full access to all the data in the study and takes responsibility for the integrity of the data and the accuracy of the data analysis. All authors read and approved the final manuscript.

ACKNOWLEDGMENTS

The authors thank Prof. Oliver Kuß, Institute for Biometrics and Epidemiology, German Diabetes Center at Heinrich Heine University, for helpful discussions.

CONFLICT OF INTEREST STATEMENT

MR received lecture fees and/or served on advisory boards for Astra-Zeneca, Boehringer-Ingelheim, Eli Lilly, Novartis, Novo Nordisk, and Target RWE. No conflicts of interest, financial or otherwise, are declared by the other authors.

ORCID

Marc Jonuscheit https://orcid.org/0009-0003-3875-3382

REFERENCES

1. Cox IJ, Menon DK, Sargentoni J, et al. Phosphorus-31 magnetic resonance spectroscopy of the human liver using chemical shift imaging techniques. *J Hepatol.* 1992;14(2–3):265-275. doi:10.1016/0168-8278(92)90169-P
2. Menon DK, Sargentoni J, Taylor-Robinson SD, et al. Effect of functional grade and etiology onin vivo hepatic phosphorus-31 magnetic resonance spectroscopy in cirrhosis: biochemical basis of spectral appearances. *Hepatology.* 1995;21(2):417-427. doi:10.1002/hep.1840210224
3. Munakata T, Griffiths RD, Martin PA, Jenkins SA, Shields R, Edwards RH. An in vivo ^{31}P MRS study of patients with liver cirrhosis: progress towards a non-invasive assessment of disease severity. *NMR Biomed.* 1993;6(2):168-172. doi:10.1002/nbm.1940060211
4. Meyerhoff DJ, Boska MD, Thomas AM, Weiner MW. Alcoholic liver disease: quantitative image-guided P-31 MR spectroscopy. *Radiology.* 1989; 173(2):393-400. doi:10.1148/radiology.173.2.2798871
5. Corbin IR, Ryner LN, Singh H, Minuk GY. Quantitative hepatic phosphorus-31 magnetic resonance spectroscopy in compensated and decompensated cirrhosis. *Am J Physiol Gastrointest Liver Physiol.* 2004;287(2):G379-G384. doi:10.1152/ajpgi.00418.2003
6. Rajanayagam V, Lee RR, Ackerman Z, Bradley WG, Ross BD. Quantitative P-31 MR spectroscopy of the liver in alcoholic cirrhosis. *J Magn Reson Imaging.* 1992;2(2):183-190. doi:10.1002/jmri.1880020211
7. Dixon RM, Angus PW, Rajagopalan B, Radda GK. Abnormal phosphomonoester signals in ^{31}P MR spectra from patients with hepatic lymphoma. A possible marker of liver infiltration and response to chemotherapy. *Br J Cancer.* 1991;63(6):953-958. doi:10.1038/bjc.1991.208
8. Wolf P, Fellinger P, Pfleger L, et al. Reduced hepatocellular lipid accumulation and energy metabolism in patients with long standing type 1 diabetes mellitus. *Sci Rep.* 2019;9(1):2576. doi:10.1038/s41598-019-39362-4
9. Gancheva S, Bierwagen A, Kaul K, et al. Variants in genes controlling oxidative metabolism contribute to lower hepatic ATP independent of liver fat content in type 1 diabetes. *Diabetes.* 2016;65(7):1849-1857. doi:10.2337/db16-0162
10. Kupriyanova Y, Zaharia OP, Bobrov P, et al. Early changes in hepatic energy metabolism and lipid content in recent-onset type 1 and 2 diabetes mellitus. *J Hepatol.* 2021;74(5):1028-1037. doi:10.1016/j.jhep.2020.11.030

11. Solga SF, Horska A, Hemker S, et al. Hepatic fat and adenosine triphosphate measurement in overweight and obese adults using ^{1}H and ^{31}P magnetic resonance spectroscopy. *Liver Int.* 2008;28(5):675-681. doi:10.1111/j.1478-3231.2008.01705.x
12. Schmid AI, Szendroedi J, Chmelik M, Krssák M, Moser E, Roden M. Liver ATP synthesis is lower and relates to insulin sensitivity in patients with type 2 diabetes. *Diabetes Care.* 2011;34(2):448-453. doi:10.2337/dc10-1076
13. Szendroedi J, Chmelik M, Schmid AI, et al. Abnormal hepatic energy homeostasis in type 2 diabetes. *Hepatology.* 2009;50(4):1079-1086. doi:10.1002/hep.23093
14. Sarabhai T, Mastrototaro L, Kahl S, et al. Hyperbaric oxygen rapidly improves tissue-specific insulin sensitivity and mitochondrial capacity in humans with type 2 diabetes: a randomised placebo-controlled crossover trial. *Diabetologia.* 2023;66(1):57-69. doi:10.1007/s00125-022-05797-0
15. Gancheva S, Koliaki C, Bierwagen A, et al. Effects of intranasal insulin on hepatic fat accumulation and energy metabolism in humans. *Diabetes.* 2015;64(6):1966-1975. doi:10.2337/db14-0892
16. Fritsch M, Koliaki C, Livingstone R, et al. Time course of postprandial hepatic phosphorus metabolites in lean, obese, and type 2 diabetes patients. *Am J Clin Nutr.* 2015;102(5):1051-1058. doi:10.3945/ajcn.115.107599
17. Norén B, Lundberg P, Ressner M, Wirell S, Almer S, Smedby O. Absolute quantification of human liver metabolite concentrations by localized in vivo ^{31}P NMR spectroscopy in diffuse liver disease. *Eur Radiol.* 2005;15(1):148-157. doi:10.1007/s00330-004-2434-x
18. Fellinger P, Wolf P, Pfleger L, et al. Increased ATP synthesis might counteract hepatic lipid accumulation in acromegaly. *JCI Insight.* 2020;5(5):e134638. doi:10.1172/jci.insight.134638
19. Gancheva S, Caspari D, Bierwagen A, et al. Cardiometabolic risk factor clustering in patients with deficient branched-chain amino acid catabolism: a case-control study. *J Inherit Metab Dis.* 2020;43(5):981-993. doi:10.1002/jimd.12231
20. Wylezinska M, Cobbold JFL, Fitzpatrick J, et al. A comparison of single-voxel clinical in vivo hepatic ^{31}P MR spectra acquired at 1.5 and 3.0 Tesla in health and diseased states. *NMR Biomed.* 2011;24(3):231-237. doi:10.1002/nbm.1578
21. Zakian KL, Koutcher JA, Malhotra S, et al. Liver regeneration in humans is characterized by significant changes in cellular phosphorus metabolism: assessment using proton-decoupled ^{31}P-magnetic resonance spectroscopic imaging. *Magn Reson Med.* 2005;54(2):264-271. doi:10.1002/mrm.20560
22. Oberhaensli RD, Galloway GJ, Hilton-Jones D, et al. The study of human organs by phosphorus-31 topical magnetic resonance spectroscopy. *Br J Radiol.* 1987;60(712):367-373. doi:10.1259/0007-1285-60-712-367
23. Hakkarainen A, Lundbom J, Tuominen EK, Taskinen M-R, Pietiläinen KH, Lundbom N. Measuring short-term liver metabolism non-invasively: post-prandial and post-exercise ^{1}H and ^{31}P MR spectroscopy. *MAGMA.* 2015;28(1):57-66. doi:10.1007/s10334-014-0450-7
24. Hultman E, von Nilsson LH, Sahlin K. Adenine nucleotide content of human liver. Normal values and fructose-induced depletion. *Scand J Clin Lab Invest.* 1975;35(3):245-251. doi:10.3109/00365517509095736
25. Sijens PE, Dagnelie PC, Halfwerk S, van Dijk P, Wicklow K, Oudkerk M. Understanding the discrepancies between ^{31}P MR spectroscopy assessed liver metabolite concentrations from different institutions. *Magn Reson Imaging.* 1998;16(2):205-211. doi:10.1016/S0730-725X(97)00246-4
26. Purvis LAB, Clarke WT, Valkovič L, et al. Phosphodiester content measured in human liver by in vivo ^{31}P MR spectroscopy at 7 Tesla. *Magn Reson Med.* 2017;78(6):2095-2105. doi:10.1002/mrm.26635
27. Schmid AI, Chmelík M, Szendroedi J, et al. Quantitative ATP synthesis in human liver measured by localized ^{31}P spectroscopy using the magnetization transfer experiment. *NMR Biomed.* 2008;21(5):437-443. doi:10.1002/nbm.1207
28. Buehler T, Kreis R, Boesch C. Comparison of ^{31}P saturation and inversion magnetization transfer in human liver and skeletal muscle using a clinical MR system and surface coils. *NMR Biomed.* 2015;28(2):188-199. doi:10.1002/nbm.3242
29. Meyerhoff DJ, Karczmar GS, Matson GB, Boska MD, Weiner MW. Non-invasive quantitation of human liver metabolites using image-guided ^{31}P magnetic resonance spectroscopy. *NMR Biomed.* 1990;3(1):17-22. doi:10.1002/nbm.1940030103
30. Buchli R, Meier D, Martin E, Boesiger P. Assessment of absolute metabolite concentrations in human tissue by ^{31}P MRS in vivo. Part II: muscle, liver, kidney. *Magn Reson Med.* 1994;32(4):453-458. doi:10.1002/mrm.1910320405
31. Chmelík M, Schmid AI, Gruber S, et al. Three-dimensional high-resolution magnetic resonance spectroscopic imaging for absolute quantification of ^{31}P metabolites in human liver. *Magn Reson Med.* 2008;60(4):796-802. doi:10.1002/mrm.21762
32. Pfleger L, Gajdošík M, Wolf P, et al. Absolute quantification of phosphor-containing metabolites in the liver using ^{31}P MRSI and hepatic lipid volume correction at 7T suggests no dependence on body mass index or age. *J Magn Reson Imaging.* 2019;49(2):597-607. doi:10.1002/jmri.26225
33. Hoult DI, Chen CN, Sank VJ. Quadrature detection in the laboratory frame. *Magn Reson Med.* 1984;1(3):339-353. doi:10.1002/mrm.1910010305
34. Szendroedi J, Saxena A, Weber KS, et al. Cohort profile: the German Diabetes Study (GDS). *Cardiovasc Diabetol.* 2016;15:59. doi:10.1186/s12933-016-0374-9
35. Zaharia OP, Strassburger K, Knebel B, et al. Role of patatin-like phospholipase domain-containing 3 gene for hepatic lipid content and insulin resistance in diabetes. *Diabetes Care.* 2020;43(9):2161-2168. doi:10.2337/dc20-0329
36. Laufs A, Livingstone R, Nowotny B, et al. Quantitative liver ^{31}P magnetic resonance spectroscopy at 3T on a clinical scanner. *Magn Reson Med.* 2014;71(5):1670-1675. doi:10.1002/mrm.24835
37. Ordidge R, Connelly A, Lohman J. Image-selected in vivo spectroscopy (ISIS). A new technique for spatially selective NMR spectroscopy. *J Magn Reson.* 1986;66(2):283-294. doi:10.1016/0022-2364(86)90031-4
38. Lin A, Andronesi O, Bogner W, et al. Experts' Working Group on Reporting Standards for MR Spectroscopy Minimum reporting standards for in vivo magnetic resonance spectroscopy (MRSinMRS): experts' consensus recommendations. *NMR Biomed.* 2021;34(5):e4484. doi:10.1002/nbm.4484
39. Kreis R, Boer V, Choi I-Y, et al. Experts' Working Group on Terminology for MR Spectroscopy Terminology and concepts for the characterization of in vivo MR spectroscopy methods and MR spectra: background and experts' consensus recommendations. *NMR Biomed.* 2020;34(5):e4347. doi:10.1002/nbm.4347
40. Naressi A, Couturier C, Castang I, de Beer R, Graveron-Demilly D. Java-based graphical user interface for MRUI, a software package for quantitation of in vivo/medical magnetic resonance spectroscopy signals. *Comput Biol Med.* 2001;31(4):269-286. doi:10.1016/S0010-4825(01)00006-3
41. Stefan D, Cesare FD, Andrasescu A, et al. Quantitation of magnetic resonance spectroscopy signals: the jMRUI software package. *Meas Sci Technol.* 2009;20(10):104035. doi:10.1088/0957-0233/20/10/104035
42. Mierisová S, van den Boogaart A, Tkác I, van Hecke P, Vanhamme L, Liptaj T. New approach for quantitation of short echo time in vivo ^{1}H MR spectra of brain using AMARES. *NMR Biomed.* 1998;11(1):32-39. doi:10.1002/(SICI)1099-1492(199802)11:13.0.CO;2-#

43. Vanhamme L, van den Boogaart A, van Huffel S. Improved method for accurate and efficient quantification of MRS data with use of prior knowledge. *J Magn Reson*. 1997;129(1):35-43. doi:10.1006/jmre.1997.1244
44. Li CW, Negendank WG, Murphy-Boesch J, Padavic-Shaller K, Brown TR. Molar quantitation of hepatic metabolites in vivo in proton-decoupled, nuclear Overhauser effect enhanced ^{31}P NMR spectra localized by three-dimensional chemical shift imaging. *NMR Biomed*. 1996;9(4):141-155. doi:10.1002/(SICI)1099-1492(199606)9:43.0.CO;2-P
45. de Graaf RA. *In Vivo NMR Spectroscopy: Principles and Techniques*. 2nd ed. John Wiley & Sons; 2013. http://gbv.eblib.com/patron/FullRecord.aspx?p=4037486
46. Stroup WW. *Generalized Linear Mixed Models: Modern Concepts, Methods and Applications*. Chapman and Hall/CRC Texts in Statistical Science Ser. CRC Press; 2013. https://ebookcentral.proquest.com/lib/kxp/detail.action?docID=1570060
47. Tosner Z, Dezortová M, Tintěra J, Hájek M. Application of two-dimensional CSI for absolute quantification of phosphorus metabolites in the human liver. *MAGMA*. 2001;13(1):40-46. doi:10.1007/BF02668649
48. Bashir A, Gropler R, Ackerman J. Absolute quantification of human liver phosphorus-containing metabolites in vivo using an inhomogeneous spoiling magnetic field gradient. *PLoS ONE*. 2015;10(12):e0143239. doi:10.1371/journal.pone.0143239
49. Purvis LAB, Valkovič L, Robson MD, Rodgers CT. Feasibility of absolute quantification for ^{31}P MRS at 7 T. *Magn Reson Med*. 2019;82(1):49-61. doi:10.1002/mrm.27729
50. Bierwagen A, Begovatz P, Nowotny P, et al. Characterization of the peak at 2.06 ppm in ^{31}P magnetic resonance spectroscopy of human liver: phosphoenolpyruvate or phosphatidylcholine? *NMR Biomed*. 2015;28(7):898-905. doi:10.1002/nbm.3323
51. Chmelík M, Valkovič L, Wolf P, et al. Phosphatidylcholine contributes to in vivo ^{31}P MRS signal from the human liver. *Eur Radiol*. 2015;25(7):2059-2066. doi:10.1007/s00330-014-3578-y
52. Sedivy P, Dusilova T, Hajek M, Burian M, Krššák M, Dezortova M. In vitro ^{31}P MR chemical shifts of in vivo-detectable metabolites at 3T as a basis set for a pilot evaluation of skeletal muscle and liver ^{31}P spectra with LCModel software. *Molecules*. 2021;26(24):7571. doi:10.3390/molecules26247571
53. Hernández EÁ, Kahl S, Seelig A, et al. Acute dietary fat intake initiates alterations in energy metabolism and insulin resistance. *J Clin Invest*. 2017;127(2):695-708. doi:10.1172/JCI89444
54. Bawden SJ, Stephenson MC, Ciampi E, et al. Investigating the effects of an oral fructose challenge on hepatic ATP reserves in healthy volunteers: a (31)P MRS study. *Clin Nutr*. 2016;35(3):645-649. doi:10.1016/j.clnu.2015.04.001

SUPPORTING INFORMATION

Additional supporting information can be found online in the Supporting Information section at the end of this article.

How to cite this article: Jonuscheit M, Wierichs S, Rothe M, et al. Reproducibility of absolute quantification of adenosine triphosphate and inorganic phosphate in the liver with localized ^{31}P-magnetic resonance spectroscopy at 3-T using different coils. *NMR in Biomedicine*. 2024;37(8):e5120. doi:10.1002/nbm.5120

Chapter 6

6 Study 2: ^{31}P-MRS saturation transfer for assessment of hepatic ATP synthesis rate

Jonuscheit *et al. European Radiology Experimental* (2025)9:51
https://doi.org/10.1186/s41747-025-00588-9

EUROPEAN SOCIETY OF RADIOLOGY
European Radiology
EXPERIMENTAL

ORIGINAL ARTICLE Open Access

^{31}P-MRS saturation transfer for assessing human hepatic ATP synthesis at clinical field strength

Marc Jonuscheit[1,2], Benedict Korzekwa[1,2], Michael Schär[3], Julian Mevenkamp[4], Stefan Wierichs[1,2], Pavel Bobrov[2,5], Theresia Sarabhai[1,2,6], Sabine Kahl[1,2,6], Michael Roden[1,2,6] and Vera B. Schrauwen-Hinderling[1,2,5*]

Abstract

Background ^{31}P-magnetic resonance spectroscopy (MRS) saturation transfer (ST) allows for noninvasive investigation of liver energy metabolism by assessing flux rates of adenosine triphosphate (ATP) synthesis. However, this technique has rarely been applied at clinical field strengths because of long examination times and contamination from muscle tissue. Our aim was to establish a new method to robustly assess ATP synthesis using a clinical scanner.

Methods A prospective single-center study was performed (January 2023–August 2024) within the German Diabetes Study. We established a suitable ^{31}P-MRS ST protocol, tested it *in vitro* and *in vivo* and assessed its reproducibility. We assessed the hepatic apparent spin-lattice relaxation time of inorganic phosphate ($T'_{1,Pi}$), equilibrium forward rate constant (k_f), and forward ATP synthesis rate (F_{ATP}) in nine control volunteers (CON) (six females) and eight patients (five females) with type 1 diabetes (T1D) and compared differences by ANOVA.

Results Reproducibility assessment in nine CON, aged 27 ± 4 years (mean ± standard deviation), yielded coefficients of variation for repeated measurements of 7.1% and 21.3% for $T'_{1,Pi}$ and k_f, respectively. Group comparison revealed higher hepatic k_f (0.34 ± 0.03 s^{-1} *versus* 0.16 ± 0.03 s^{-1}; $p = 0.001$) and F_{ATP} (35.3 ± 3.5 mM/min *versus* 16.4 ± 3.5 mM/min; $p = 0.002$) in CON than in T1D, aged 42 ± 15 years, respectively.

Conclusion This ^{31}P-MRS ST method allowed for robust assessment of hepatic ATP synthesis at clinical field strength and was sensitive enough to detect differences between CON and T1D volunteers.

Relevance statement Noninvasive methods to investigate hepatic energy metabolism are urgently needed to evaluate liver health while preventing unnecessary biopsies. For broad clinical applicability, the robustness shown by the proposed method at clinical field strength is crucial.

Trial registration ClinicalTrials.gov: NCT01055093—Prospective study on diabetes mellitus and its complications in newly diagnosed adult patients (GDC), NCT01055093, Registered: 01/22/2010, https://clinicaltrials.gov/study/NCT01055093?term=NCT01055093&rank=1#study-overview.

*Correspondence:
Vera B. Schrauwen-Hinderling
vera.schrauwen-hinderling@ddz.de
Full list of author information is available at the end of the article

Key Points

- The proposed magnetic resonance spectroscopy method calculates hepatic ATP synthesis rates at clinical field strength.
- The protocol shows acceptable reproducibility and spectra without contamination from muscle.
- The method can detect differences between participants with type 1 diabetes and controls.

Keywords Adenosine triphosphate, Diabetes mellitus (type 1), Energy metabolism, Liver, Magnetic resonance spectroscopy

Graphical Abstract

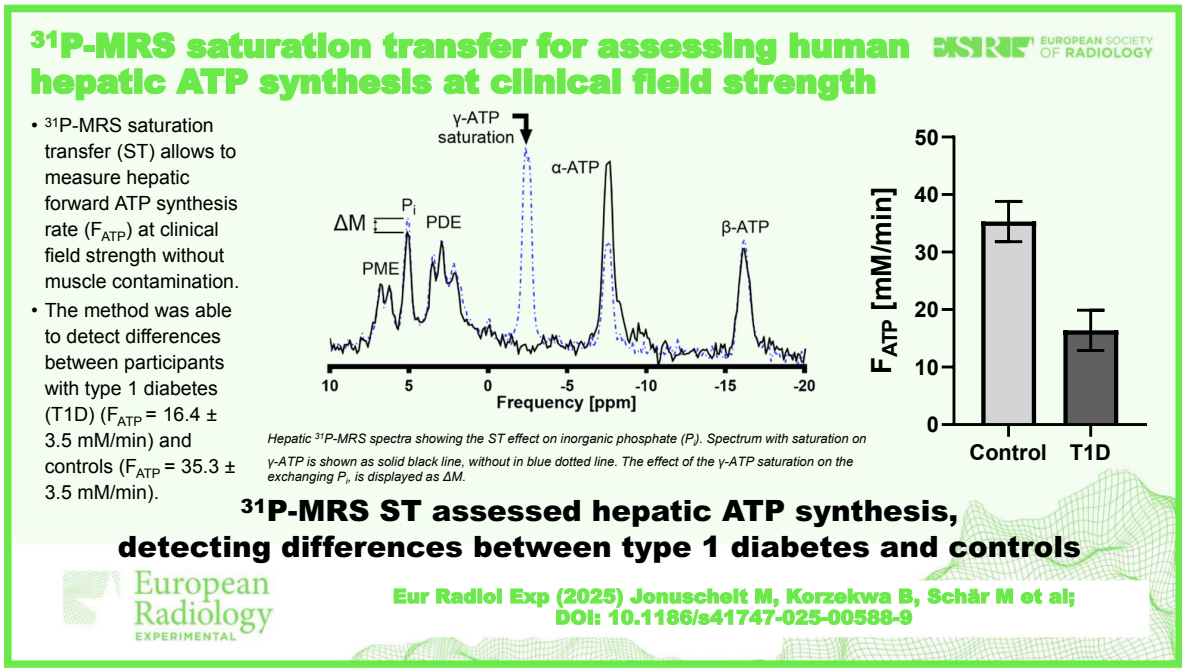

Background

Intact mitochondrial function is required for sufficient adenosine triphosphate (ATP) production for cellular demands [1]. In the liver, oxidative capacity changes during the development of metabolic dysfunction-associated steatotic liver disease (MASLD) and steatohepatitis (MASH). In surgical biopsies, *ex vivo* measured energy metabolism is upregulated in steatotic livers, but is impaired in MASH and fibrosis, associated with excessive lipid accumulation and oxidative stress, likely contributing to worsening liver damage and disease progression [1, 2]. As percutaneous liver biopsies are only taken upon clinical indication, noninvasive techniques are pivotal for further studies. Moreover, given the recent U.S. Food and Drug Administration approval of the liver-selective thyroid hormone receptor ß-agonist, resmetirom, for MASH [3], mechanistic studies monitoring mitochondrial function in the liver and thereby treatment efficacy are important. While diagnosis and treatment of MASH in obesity and type 2 diabetes (T2D) is a well-documented unmet clinical need and people with MASH and T2D feature lower hepatic oxidative capacity [4], it is less well known that also type 1 diabetes (T1D) shows derangements of hepatic energy metabolism, that deserve further study.

^{31}P-magnetic resonance spectroscopy (MRS) has been established for the detection of metabolite ratios and absolute concentrations [5, 6]. The few studies available show an impaired hepatic energy metabolism in people with T1D/T2D, indicated by decreased absolute concentrations of ATP and inorganic phosphate (P_i) [7, 8]. Furthermore, the saturation transfer (ST) technique allows to observe the reaction kinetics of ATP synthesis [9], which has been previously applied in brain [10, 11], skeletal muscle [12, 13], and liver [14–16]. Up to now, the method was mainly applied at ultrahigh field (UHF)

[16–21] and not at clinical field strength, because for the liver, spatial localization is mandatory, resulting in low signal-to-noise ratio (SNR) and long measurement times of > 2 h at clinical field strength. So far, the reproducibility of this method has only been assessed at UHF, and its variance during repeated measurements at clinical field strength is currently unknown.

The current study introduces "four repetition time ST" (FRiST) to robustly assess ATP synthesis using a clinical scanner with a high degree of spatial localization within 90 min. This method is based on TRiST ("triple repetition time ST") introduced by Schär et al for measurements of creatine kinase reaction rates in human calf and heart [22]. After extensive phantom testing, the reproducibility of the method was evaluated and applied in participants with T1D to detect differences as compared to control volunteers.

Methods

Study design, volunteers and MRS system

This prospective, cross-sectional study was performed as a single-center study between January 2023 and August 2024, utilizing a subcohort from the ongoing German Diabetes Study (GDS) [23] (ClinicalTrials.gov: NCT01055093). The study was approved by the local ethics committee (Medical Faculty, Heinrich Heine University, Düsseldorf; ref#4508), and all participants provided written informed consent. Nine control volunteers were included for protocol optimization and determination of reproducibility, and nine T1D volunteers for clinical relevance assessment (Table 1). Inclusion and exclusion criteria are described in Supplementary Material S1. Participants fasted overnight and refrained from caffeine, alcohol, and strenuous exercise on the day preceding measurements. All examinations were performed on a clinical 3-T system (Philips Achieva dStream) using a quadrature surface coil [24].

Table 1 Participants' characteristics

Volunteer group	Control volunteers	Type 1 diabetes	*p*-value
Number	9	8	
Sex (m/f)	3/6	3/5	1.000[a]
Age (years)	25.0 ± 3.43	42.1 ± 15.2	0.015*[b]
Weight (kg)	69.4 ± 11.5	74.5 ± 15.7	0.457[b]
Height (m)	1.70 ± 0.08	1.75 ± 0.11	0.395[b]
BMI (kg/m^2)	23.8 ± 2.16	24.2 ± 2.65	0.734[b]
Data used for	Assessment of $T'_{1,Pi}$, ΔM, k_f and F_{ATP} and reproducibility	Assessment of $T'_{1,Pi}$, ΔM, k_f and F_{ATP}	

All values are reported as numbers of participants or mean ± standard deviation
ΔM Difference of P_i between saturating and control irradiation, F_{ATP} Forward adenosine triphosphate synthesis rate, k_f Forward rate constant, $T'_{1,Pi}$ Apparent spin-lattice relaxation time of P_i
* $p < 0.05$ indicates statistical significance
[a] Fisher's test
[b] Welch *t*-test

^{31}P-MRS ST FRiST protocol

A detailed description of the *in vitro* and *in vivo* protocols is given in Supplementary Material S2. First, *in vitro* experiments were performed to optimize γ-ATP resonance saturation in the liver using a pulse train of delays alternating with nutations for tailored excitation (DANTE) [25] pulses. Two effective pulse schemes were identified with either 5 suppression bands, which were 9 Hz apart (M5D9) or 3 with 12 Hz (M3D12). The necessary DANTE subpulse flip angle β was determined to achieve < 5% γ-ATP residual. For *in vivo* validation of the protocols, the measurements were repeated in two male control volunteers aged 24 and 29 years, with body mass index (BMI) of 26.3 and 24.8 kg/m^2.

In order to accelerate the determination of the apparent spin-lattice relaxation time of P_i ($T'_{1,Pi}$), a saturation recovery experiment with two-dimensional-localization and a range of five different repetition times (TRs) was tested in two control volunteers and checked which 3TRs best reflect the 5TR value.

All measurements were performed by two experienced spectroscopists (M.J. and B.K., with 6 and 4 years of experience, respectively), including segmentation of the liver and calculation of resonance frequency of the saturation pulse. Scout images were acquired and shimming was performed, using a dedicated shim tool, as described by Schär et al [26]. With this method, a B_0 map was acquired, the liver was manually segmented in 16 slices, and the resulting calculated B_0 shim was maintained for all measurements in that session. Mean SD linewidths of the water peak before and after shimming amounted to 47 Hz and 18 Hz, respectively, and the water peak was visually inspected to confirm a single, narrow, symmetrical peak. Transverse T_2-weighted images acquired with multislice two-dimensional single-shot turbo spin-echo (TR/echo time 571/80 ms; 23 slices of 6-mm thickness, 1 mm gap, field of view 450 × 302 mm^2) served together with coronal images from the scout images for further planning of the ^{31}P-MRS measurements (Supplementary Fig. S1). To correctly apply the saturation pulse, the exact resonance frequencies of γ-ATP and P_i were determined from a nonlocalized ^{31}P-MRS scan (Supplementary Material S3).

All ST experiments were acquired using a two-dimensional-localized "image-selected *in vivo* spectroscopy" [27] sequence with a 40 × 90 mm^2 volume of interest (open in feet-head direction) and a hyperbolic secant adiabatic pulse for excitation and inversion (Supplementary Material S3). Four spectra were acquired with

varying TRs and number of signal averages (TR_{short} = 0.7 s, TR_{center} = 1.7 s, $TR_{mirrored}$ = 1.7 s, and TR_{long} = 2.7 s). Further details of the acquisition procedure are listed in Supplementary Table S1, and a representative raw MRS spectrum acquired with TR 1.7 s is shown in Supplementary Fig. S2 [28].

In the T1D participants, three-dimensional-localized "image-selected *in vivo* spectroscopy" spectra were collected for quantification of absolute P_i concentration with correction for hepatic lipid content, as assessed by ^{1}H-MRS as previously described [24].

Data processing and quantification procedure

In line with best practices, all spectra were reviewed and processed by experienced spectroscopists (M.J., B.K., and S.W. with 6, 4, and 6 years of experience). To ensure good quality data, all spectra were analyzed in terms of SNR using the consensus definition $SNR = \frac{Signal}{\sigma_{Noise}}$ [28, 29]. After application of a 15 Hz Gaussian filter, the signal was defined as the fitted amplitude of the metabolite of interest and noise (σ) as standard deviation of the spectrum between 10 and 20 ppm (Supplementary Fig. S2) both in the frequency domain using a custom written MATLAB script (MathWorks Inc. R2021a, Natick, MA, USA). As criteria for good quality, spectra with SNR of γ-ATP < 4, P_i < 2.5, and minimal phosphocreatine (PCr) contamination (PCr to γ-ATP peak ratio > 0.15) were excluded. A sophisticated, fully automated, custom-written MATLAB script was used to analyze all ST spectra (Supplementary Material S4).

In the ^{31}P-MRS ST experiments, the pseudo-first-order equilibrium forward exchange rate constant (k_f) was calculated according to (Supplementary Material S5): $k_f = \frac{1}{T'_{1,Pi}}\left(1 - \frac{M'_{0,Pi}}{M_{0,Pi}}\right)$

$T'_{1,Pi}$ was fitted from the signal amplitudes of the 3TR experiment using a mono-exponential equation. For assessment of the equilibrium ($M_{0,Pi}$) and apparent longitudinal magnetization of P_i ($M'_{0,Pi}$), the corresponding P_i amplitude at $TR_{mirrored}$ and TR_{center} were individually T_1 corrected for partial saturation by using $T_{1,Pi}$ of 730 ms obtained from literature [15] and the mean measured $T'_{1,Pi}$ of the corresponding group. F_{ATP} was calculated by multiplying k_f with the corresponding P_i concentration. ^{31}P-spectra for absolute P_i quantification were evaluated as previously described [24, 30]. Further details for the quantification process are given in Supplementary Material S4.

Statistical analysis

All results are reported as individual values, mean ± standard error of the mean or mean [95% confidence interval], with the exception of age, weight, height, and BMI, reported as mean ± standard deviation. For the reproducibility study in control volunteers, the coefficient of variation (CV) was determined for repeated measurements of $T'_{1,Pi}$, ΔM (difference in P_i between saturated and mirrored experiment), and k_f. Testing for outliers was performed using Grubbs's test in R (version 4.0.5). For inter-group comparison $T'_{1,Pi}$, ΔM, k_f, and F_{ATP} were compared between the control and T1D participants, using ANOVA for generalized linear model without and with adjusting for covariates at a statistical significance level of $p < 0.05$. Sample size calculation used Cohen's d method based on previously published data [21] and resulted in a power of 0.85 when investigating $n = 8$ participants per group, calculated using the POWER procedure in SAS software (SAS Institute Inc., Cary, NC, USA, Version 9.4) with $\alpha = 0.05$, Cohen's $d = 1.6$ and nominal power = 0.8. For deciding on the best TRs to determine $T'_{1,Pi}$, the coefficient of determination (R^2) was calculated using least squares regression without weighting and special handling for outliers.

Results

Participant characteristics and quality of spectra

The characteristics were similar in both groups, except for higher mean age in the group of T1D (Table 1). The mean age of T1D patients was 42 ± 15 years (mean ± standard deviation), that of controls 25 ± 3 years ($p = 0.015$), BMI was 24 ± 3 kg/m^2 *versus* 24 ± 2 kg/m^2, respectively ($p = 0.734$). Three of eight T1D patients were males (38%), three of nine controls were males (33%). Valid MRS results were obtained from all participants, except for two people. One T1D patient was excluded from the analyses due to a physiologically impossible negative k_f value, confirmed being an outlier by Grubbs's test (Fig. 1). In a second T1D patient, a spectrum for absolute P_i concentration was excluded due to low SNR, but group average P_i was used to calculate F_{ATP}.

^{31}P-MRS ST spectra showed mean SNRs of 5.7 ± 0.2, 5.8 ± 0.3, and 6.0 ± 0.2 for P_i in the saturated spectra using TR 0.7, 1.7, and 2.7 s, respectively. In the mirrored spectra, mean SNRs of 12.0 ± 0.4 and 6.2 ± 0.3 for γ-ATP and P_i were achieved. Absolute P_i quantification spectra had SNRs of 8.0 ± 0.8 and 6.3 ± 0.3 for γ-ATP and P_i, respectively. PCr was completely absent or negligible with highest PCr/γ-ATP ratio of 11%, indicating good liver localization. ATP was fully saturated with residual γ-ATP < 5%, except for two spectra with 6% and 11% of residual γ-ATP. As almost the complete data set (26/28) had very good saturation (> 95%), no correction for partial saturation was applied. The suppression sideband in the mirrored spectrum (Supplementary Fig. S3) leads to a partial saturation of α-ATP, which, however, was considered as negligible based on the result of a previous study [31].

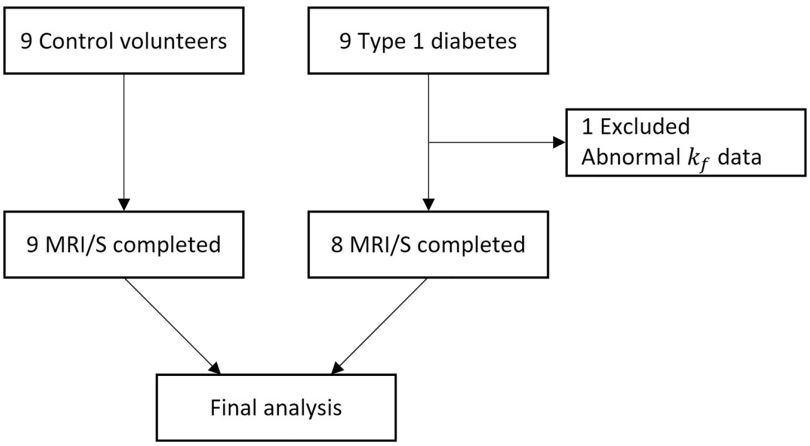

Fig. 1 Flowchart of the study participants. k_f, Forward rate constant; MRS, Magnetic resonance spectroscopy

Optimization of the FRiST method

The *in vitro* testing for suitable DANTE pulse train schemes with the voxel of interest at a distance of 10 cm between coil and voxel of interest to simulate measurements in the liver are shown in Fig. 2a, b. In both tested pulse schemes, it was possible to saturate the γ-ATP moiety to < 5% of its original signal. For M5D9, two local minima areas were found (β = 1.5–2.0° and β = 3.5–4.0°), while the scheme M3D12 also showed two, but wider minima (β = 2.5–4.0° and β = 5.0–6.0°). The spillover (Q), representing the amount of signal decrease resulting from off resonance saturation, is constantly decreasing with higher flip angles, with a minimum of 59% of the initial signal amplitude at β = 6° for both schemes (see Fig. 2a, b). Application of these experiments in two control volunteers showed local minima at β = 1.8°, 2.7°, 5.7°, and 6.0° in one volunteer each for M5D9, while for M3D12 both volunteers exhibit a complete γ-ATP saturation for β > 3.5° (Fig. 2c, d) which is why M3D12 was further used in this study. Additionally, in order to keep Q high while maintaining complete saturation and minimizing specific absorption rate levels, the flip angle β = 4.0° was chosen. Using this protocol, Q amounted to 0.67 at β = 4.0° in both volunteers. A complete overview of the resulting DANTE saturation bands, including their sidebands in a typical (mirrored) ^{31}P-MRS ST spectrum, is given in Supplementary Fig. S3. In the γ-ATP saturation experiments, the main saturation band is applied at -2.48 ppm with its sidebands far off from other ^{31}P-resonances. In the mirrored experiment, the main saturation band is applied mirrored to the P_i resonance at 12.7 ppm.

For shorter measurement time during $T'_{1,Pi}$ determination, a set of 3TRs with the least deviation from a 5TR saturation recovery experiment was extracted for two control volunteers. The 5TR fit yielded a $T'_{1,Pi}$ of 699 and 432 ms, respectively (solid lines in Fig. 3). Starting from five TRs, mono-exponential fits were executed with all TR combinations in order to find a TR triplet which is able to replicate the 5TR $T'_{1,Pi}$. Here, fitting the combination of TR 0.7, 1.7, and 2.7 s yielded $T'_{1,Pi}$ of 645 and 465 ms with R^2 of 0.9993 and 0.9995, which differ by 8 and 9% from the five-point fit, respectively (dotted lines in Fig. 3), resulting in applying these TRs for all future measurements. A list of all TR sets for $T'_{1,Pi}$ fitting including R^2 can be reviewed in Supplementary Table S2. An example fit of the final TR set (TR 0.7, 1.7, and 2.7 s) and their position on the predicted $T'_{1,Pi}$ relaxation curve is depicted in Fig. 4.

Reproducibility of the method

The reproducibility of the method was assessed by performing a second measurement after full repositioning and resulted in mean CVs of 7.1%, 20.9%, and 21.3% for $T'_{1,Pi}$, ΔM, and k_f, respectively, and decreases to 14.0% and 14.6% for ΔM and k_f when omitting one datapoint which was identified as statistical outlier ($p = 0.006$, control volunteer #7). Table 2 lists all individual data for the reproducibility measurements.

Application of FRiST in individuals with T1D and comparison to control volunteers

Representative spectra of the hepatic ST experiment at TR 1.7 s with saturation on γ-ATP (dashed blue line) and mirrored frequency (solid black line) are shown in Fig. 5. As with the $T'_{1,Pi}$ measurements (Fig. 4), the γ-ATP resonance is completely suppressed in the saturation experiment and residual PCr signal is absent indicating a high degree of signal localization.

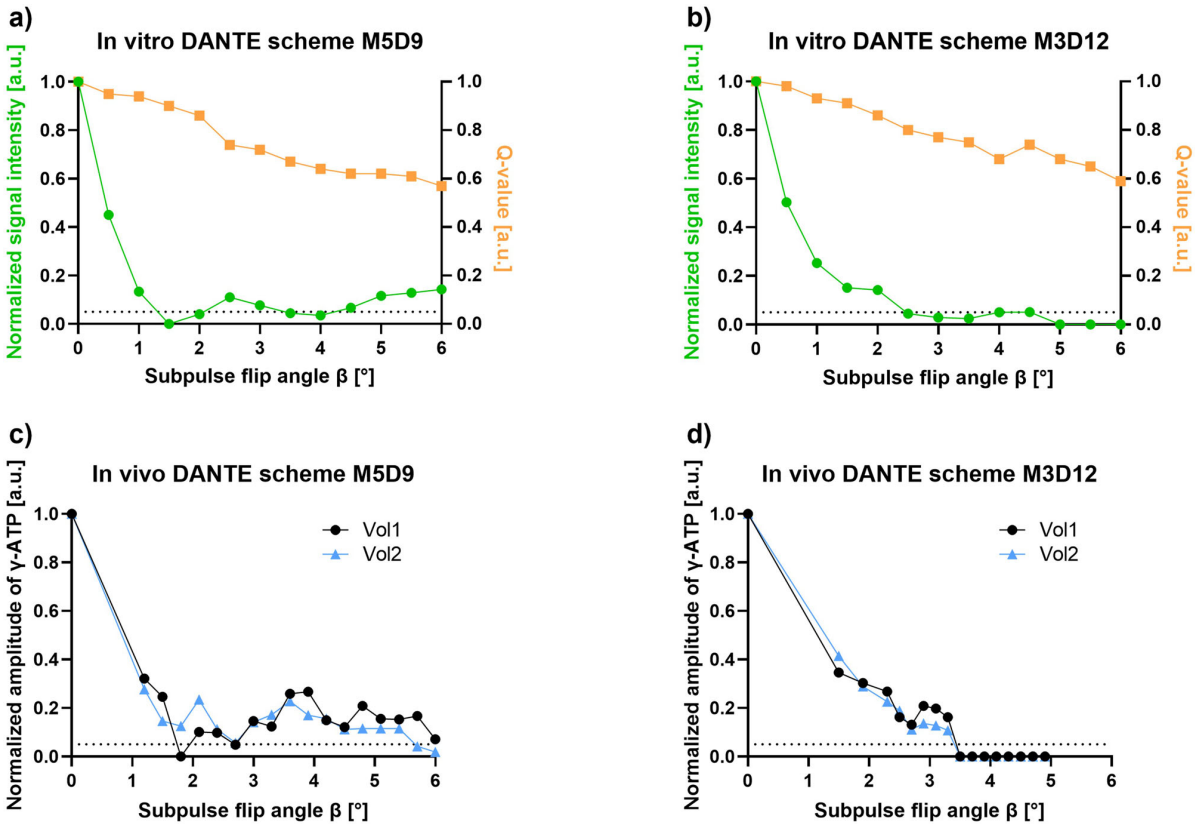

Fig. 2 Amplitude modulation of the delays alternating with nutations for tailored excitation (DANTE) saturation pulse scheme. **a**, **b** *In vitro* results of the calculated normalized magnetization of γ-adenosine triphosphate (γ-ATP) with varying subpulse flip angle (β) at repetition time (TR) of 0.7 s for the scheme: (i) M5D9 (5 saturation bands each 9 Hz apart); and (ii) M3D12 (3 saturation bands each 12 Hz apart). **c**, **d** *In vivo* results of the same DANTE pulse train schemes for two control volunteers. The dashed line symbolizes a γ-ATP saturation of 5%. Q, Spillover; Vol, Volunteer

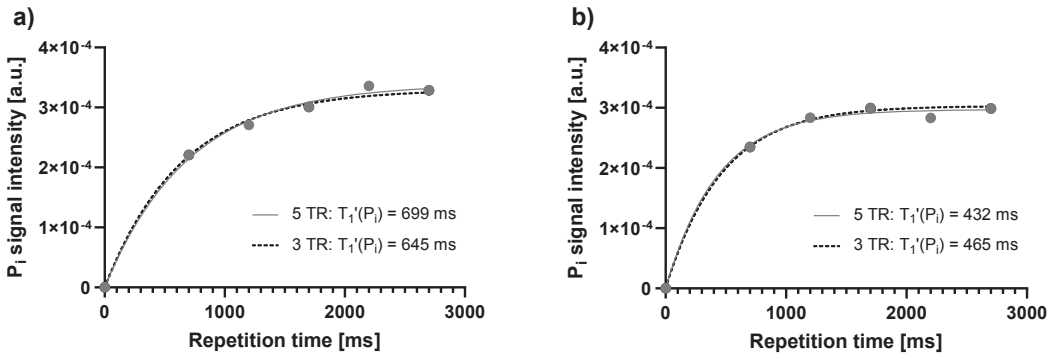

Fig. 3 **a**, **b** Results of the saturation recovery experiment for determination of the apparent spin-lattice relaxation time of P_i ($T'_{1,Pi}$) during active saturation of γ-adenosine triphosphate (γ-ATP) for two control individuals. $T'_{1,Pi}$ was determined by fitting five data points (dotted line) and by the 3TR method using only data points at 0.7, 1.7, and 2.7 s (solid line). P_i, Inorganic phosphate; TR, Repetition time

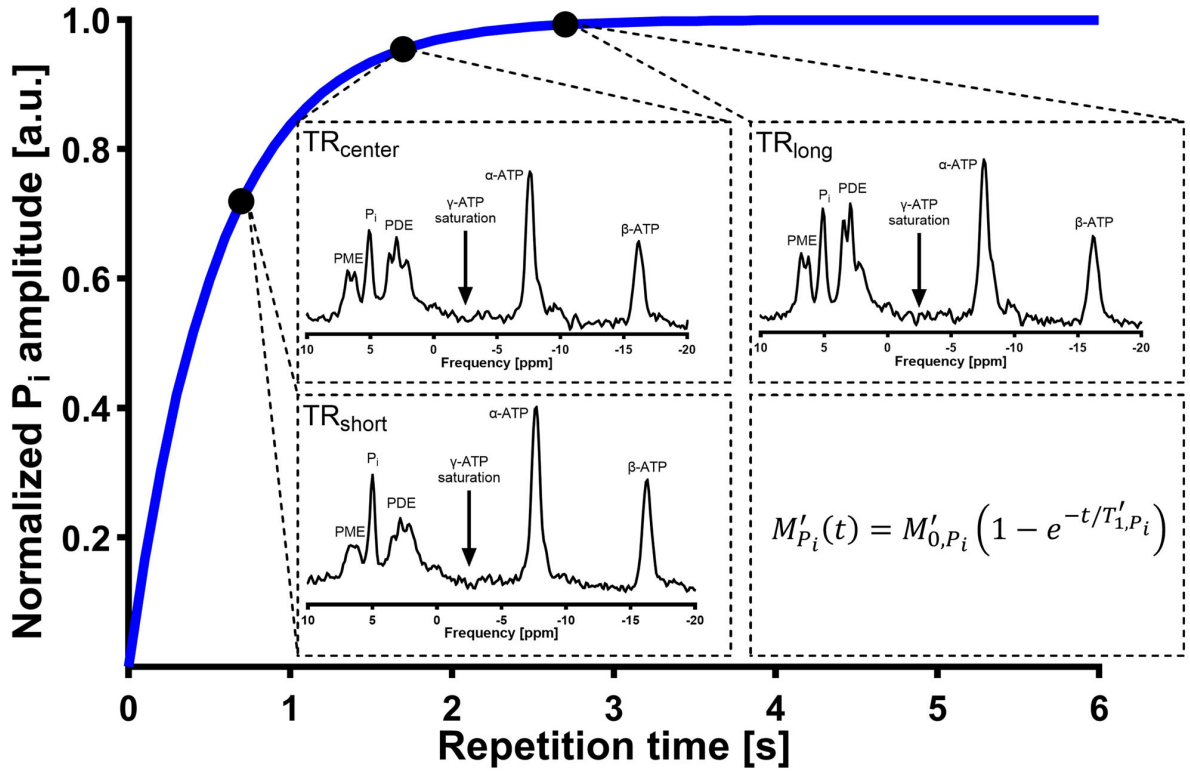

Fig. 4 Determination of the apparent spin-lattice relaxation time of P_i ($T'_{1,Pi}$) by a saturation recovery experiment in a control volunteer. Active saturation on the γ-adenosine triphosphate (γ-ATP) resonance was applied at three different TRs (0.7, 1.7, and 2.7 s) and $T'_{1,Pi}$ was obtained by fitting the inorganic phosphate (P_i) amplitudes according to the displayed formula. The blue curve represents the relaxation behavior for $T'_{1,Pi} = 520$ ms. Spectra are apodized by a 10 Hz Gaussian filter. ATP, Adenosine triphosphate; PDE, Phosphodiesters; PME, Phosphomonoesters; TR, Repetition time

Table 2 Individual data from the control volunteer group saturation transfer experiments

Volunteer	$T'_{1,Pi}$ (ms)	$T'_{1,Pi}$ (ms)	$T'_{1,Pi}$ (ms) (% CV)	ΔM (%)	ΔM (%)	ΔM (%) (% CV)	k_f (s^{-1})	k_f (s^{-1})	k_f (s^{-1}) (% CV)
1	500	467	484 ± 17 (4.8%)	13.6	14.3	14.0 ± 0.4 (4.0%)	0.27	0.31	0.29 ± 0.02 (8.8%)
2	591	550	571 ± 21 (5.1%)	14.3	15.8	15.1 ± 0.8 (7.1%)	0.24	0.29	0.26 ± 0.02 (12.1%)
3	469	427	448 ± 21 (6.6%)	17.5	13.9	15.7 ± 1.8 (16.4%)	0.37	0.33	0.35 ± 0.02 (9.8%)
4	540	443	492 ± 49 (14.0%)	14.9	15.9	15.4 ± 0.5 (4.7%)	0.28	0.36	0.32 ± 0.04 (18.5%)
5	618	519	569 ± 50 (12.3%)	17.5	14.9	16.2 ± 1.3 (11.3%)	0.28	0.29	0.29 ± 0.001 (1.0%)
6	385	423	404 ± 19 (6.7%)	19.1	16.9	18.0 ± 1.1 (8.5%)	0.50	0.40	0.45 ± 0.05 (15.1%)
7	388	389	389 ± 1.0 (0.2%)	6.7	21.9	14.3 ± 7.6 (75.5%)	0.17	0.56	0.37 ± 0.20 (75.3%)
8	566	548	557 ± 9.0 (2.3%)	13.3	18.3	15.8 ± 2.5 (22.1%)	0.24	0.33	0.28 ± 0.05 (24.3%)
9	482	573	528 ± 46 (12.2%)	6.5	11.4	9.0 ± 2.4 (38.4%)	0.14	0.20	0.17 ± 0.03 (26.8%)
Mean	504	482	493 ± 26 (7.1%)	13.7	15.9	14.8 ± 2.0 (20.9%)	0.28	0.34	0.31 ± 0.05 (21.3%)
Mean*	519	494	506 ± 29 (8.0%)	14.6	15.2	14.9 ± 1.3 (14.0%)	0.29	0.31	0.30 ± 0.03 (14.6%)

Values are reported as mean or mean ± standard error of the mean and coefficient of variation (CV) in parentheses
*Mean** mean without the outlier volunteer #7, *ΔM* Percentage difference in P_i amplitude between saturating and control irradiation, k_f Forward rate constant, $T'_{1,Pi}$ Apparent spin-lattice relaxation time of P_i

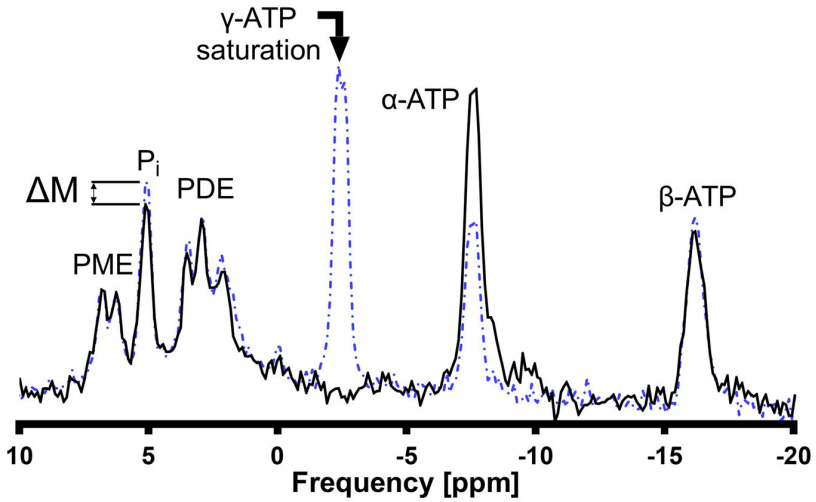

Fig. 5 Hepatic ^{31}P-magnetic resonance spectroscopy saturation transfer (ST) spectra showing the ST effect on inorganic phosphate (P_i). The black arrow indicates the frequency where the delays alternating with nutations for tailored excitation saturation pulse scheme was applied (directly on γ-ATP), and the resulting spectrum is shown as a solid black line. The spectrum of a second experiment performed with the same saturation pulse scheme applied at the mirrored frequency is shown in blue dotted line. The effect of the γ-ATP saturation on the exchanging P_i, is displayed as ΔM. Spectra are apodized by a 5 Hz Gaussian filter. ΔM percentage difference in P_i amplitude between saturating and control irradiation. ATP, Adenosine triphosphate; PDE, Phosphodiesters; PME, Phosphomonoesters

We found no evidence of a difference in $T'_{1,Pi}$ between the participants with (517 ± 29 ms) and without T1D (482 ± 22 ms, $p = 0.340$) (Fig. 6). Individuals with T1D had markedly lower ΔM with 7.7 ± 1.4% *versus* control volunteers with 15.9 ± 0.9% ($p < 0.001$) and in line, k_f was also lower with 0.16 ± 0.03 s^{-1} *versus* 0.34 ± 0.03 s^{-1} ($p = 0.001$), respectively (Fig. 6). For the calculation of the forward ATP synthesis rate, P_i concentration is required. In the T1D group, the individual absolute concentrations of P_i were determined by using the phantom-replacement technique, which yielded $P_i = 1.70 \pm 0.11$ mM and a hepatic lipid content of 0.67 ± 0.07%, resulting in F_{ATP} of 16.4 ± 3.5 mM/min. For controls, a fixed value for P_i of 1.73 mM was assumed as determined in a previous study [24], and subsequently, a mean F_{ATP} of 35.3 ± 3.5 mM/min was obtained. Data is summarized for both groups in Table 3. Additional analysis with adjustment for age, sex, and BMI still showed the same significant differences (Supplementary Table S3).

Discussion

This study developed FRiST, a robust ^{31}P-MRS ST method, to investigate hepatic energy metabolism on a clinical 3-T system. FRiST was able to: (1) successfully quantify hepatic k_f and F_{ATP} with acceptable reproducibility; (2) provide high spectral quality and purely hepatic measurements; (3) obtain results which are comparable to data acquired at UHF; and (4) detect significant changes in hepatic k_f and F_{ATP} between patients with T1D and controls (the significance remained when adjusting for age, sex, and BMI). These results, comparable to those that can be obtained at UHF [20, 21], show that the FRiST method is sensitive enough to be applied in future clinical studies.

The protocol optimizes the acquisition scheme, shimming, and spatial localization to obtain high spectral quality while keeping the total acquisition time to 90 min, allowing to assess purely hepatic fluxes, which is shown by minimal PCr signal. To reduce the acquisition time, FRiST uses a 3TR saturation recovery method to obtain $T'_{1,Pi}$ instead of a 10-point inversion recovery approach [14, 15] and allows dual use of the TR 1.7 s spectrum for both, $T'_{1,Pi}$ and ΔM assessment. FRiST shows acceptable CVs in repeated measurements. To the best of our knowledge, no data on the reproducibility of ST protocols in the liver at 3-T has been published so far, despite some reports of applying ST to the liver at 3-T. However, these protocols were very long and required two separate sessions [15] or the signal was not confined to the liver [14].

ST applied at UHF showed increased sensitivity compared to 3-T, with greater signal intensity differences (ΔM) of 21% *versus* 15%. Valkovič [20] reported CVs of 11.2% and 9.0% for $T'_{1,Pi}$ and k_f at 7-T in six controls. The CVs presented here were only slightly higher, with one outlier significantly affecting the mean CV of k_f ($CV_{No.7} = 75.3\%$). Excluding this outlier, confirmed by Grubbs's test, would reduce k_f's CV to 14.6%. It is unclear

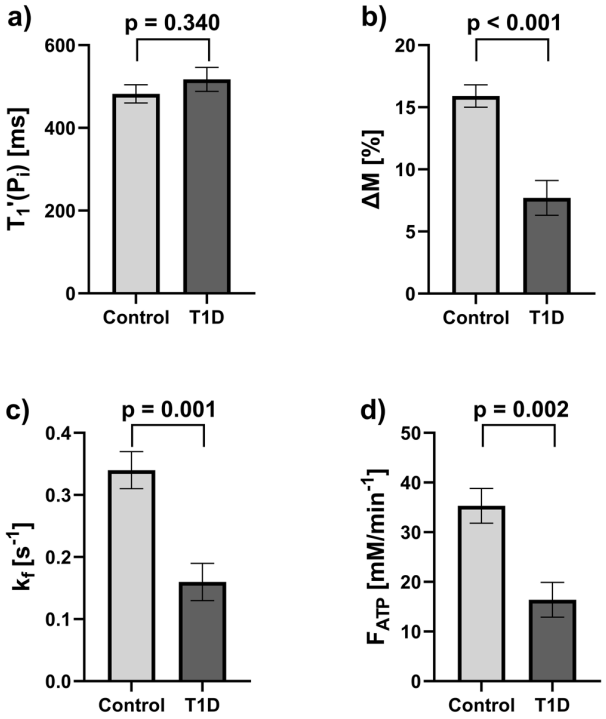

Fig. 6 Results of the comparison of subgroups of control volunteers and type 1 diabetes (T1D) hepatic saturation transfer experiments. Comparison is shown for: (**a**) the apparent spin-lattice relaxation time of P_i ($T'_{1,Pi}$); (**b**) the percentage difference in P_i amplitude between saturating and control irradiation (ΔM); (**c**) the forward rate constant (k_f); and (**d**) the forward ATP synthesis rate (F_{ATP}). All graphs show mean ± standard error of the mean

Table 3 Determined ^{31}P-magnetic resonance spectroscopy parameters for the subgroups of control volunteers and type 1 diabetes

	Control volunteers	Type 1 diabetes	*p*-value
Number	9	8	
$T'_{1,Pi}$ (ms)	482 [431; 533]	517 [449; 585]	0.340
ΔM (%)	15.9 [13.7; 18.2]	7.7 [4.3; 11.0]	< 0.001*
k_f (s^{-1})	0.34 [0.26; 0.42]	0.16 [0.08; 0.23]	0.001*
F_{ATP} (mM/min)	35.3 [27.3; 43.3]	16.4 [8.2; 24.7]	0.002*

All values are reported as numbers of participants or mean [95% CI]
ΔM Percentage difference in P_i amplitude between saturating and control irradiation, F_{ATP} Forward adenosine triphosphate synthesis rate, k_f Forward rate constant, P_i Inorganic phosphate, $T'_{1,Pi}$ Apparent spin-lattice relaxation time of P_i
* $p < 0.05$ indicates statistical significance

what the source of error was. Biological factors seem unlikely, possibly breathing artifacts may have influenced the outcome. While UHF offers clear advantages in spectral quality and reduced measurement time, it is usually not available for wider application in a clinical setting; the possibility to perform these measurements at clinical field strength was crucial for us and the driver to optimize the protocol at 3-T.

At clinical field strengths, hepatic k_f and F_{ATP} have been previously reported in control volunteers [14, 15] and in T2D [32]. The results for $T'_{1,Pi}$ and k_f in control participants are in good agreement with literature, where a range from 520 ± 20 ms to 580 ± 60 ms for $T'_{1,Pi}$ and 0.27 ± 0.03 s^{-1} to 0.3 ± 0.02 s^{-1} for k_f was found [14, 15]. Also F_{ATP} results fall within the reported range, but literature shows more variation from 29.5 ± 1.8 mM/min [15] to 48.6 ± 7.4 mM/min [14] due to differences in assumed P_i concentrations. The P_i concentration used here (1.73 mM) agrees with the values reported by Schmid et al (1.64 mM) [15], but is much lower than the values reported by Buehler et al [14] (3.0 mM), explaining differences in F_{ATP} across studies.

At 7-T, k_f was found to be lower in people with MASH [19, 20] and in one study on T1D [21]. For T1D, their reported mean k_f value of 0.17 ± 0.03 s^{-1} [21] is in excellent agreement with the findings of the current study (k_f = 0.16 ± 0.03 s^{-1}). The significantly reduced k_f and F_{ATP} in T1D may indicate an impaired mitochondrial function. It is worth mentioning that this reduction occurred despite the very low hepatic lipid content in T1D in our study (0.67 ± 0.07%), agreeing with findings of Wolf et al (2.1 ± 0.4%) [21]. This is in contrast to results in T2D

and MASLD/MASH, where increased hepatic lipid content often correlates with reduced F_{ATP} [19, 20]. Of note, the decrease in F_{ATP} was primarily shown in people with MASH, but not in people with MASL alone [19, 20] and one should note that the phenotype in T1D is quite different from MASLD/MASH with a decrease in F_{ATP} while hepatic lipid content and liver enzymes are expected to be in the normal range.

When applying FRiST at 3-T, we confirmed lowered k_f in T1D, showing that the method is sensitive enough to noninvasively detect clinical differences between control volunteers and people with T1D.

Since the FRiST method was developed at clinical field strength, it is possible to be integrated into clinical workflows as its noninvasive approach represents a valuable alternative to invasive liver biopsies. Furthermore, monitoring of treatment responses in MASLD/MASH and also risk stratification in MASLD may arise as a future application of the method, as changes in F_{ATP} may be an early indicator of progression of liver disease, as shown by the decrease in k_f and F_{ATP} between MASL and MASH [19]. Being a quantitative measurement of hepatic F_{ATP}, it may also contribute to a more personalized treatment therapy for people with hepatic disorders. However, it should be noted that the duration of FRiST amounts to 90 min, preventing the method from being routinely implemented as an additional measurement into standard MRI/S workflows. Future work may focus on speeding up the measurements without impairing data quality.

Although we successfully detected significant changes in F_{ATP} between T1D and controls, this study has several limitations. First, the interpretation of ST results is complex, with studies demonstrating that assessed metabolic fluxes in human skeletal muscle overestimate oxidative ATP synthesis [33]. ATP is produced through both anaerobic glycolysis and aerobic oxidative phosphorylation, so that F_{ATP} measurements will include a significant glycolytic component [33, 34]. Reactions near equilibrium have a larger impact, as forward and backward reactions occur simultaneously, determining the unidirectional flux rather than the net flux. While ST data does not directly measure purely oxidative net ATP synthesis, k_f and F_{ATP} remain sensitive markers of energy metabolism, mostly changing in parallel with other related metabolic measures [35]. Second, we used mean values of P_i concentration from a previous study to calculate F_{ATP} in control participants, rather than measuring individual absolute P_i concentration. However, P_i concentration in control volunteers typically shows only little variation, and the used concentration comes from a group with similar age and BMI. Third, the relatively small sample size used (nine controls, eight T1D) may limit the generalizability of our findings. Larger cohort studies need to be performed in the future to investigate milder clinical phenotypes and validate these results in a broader population. Future research should aim to provide a more comprehensive metabolic profile of the volunteers with more detailed clinical characterization, including assessment of additional metabolic markers such as HbA1c, insulin resistance, and fibrosis markers, as well as consideration of medication.

In conclusion, we developed FRiST, a new noninvasive ^{31}P-MRS ST method to assess hepatic F_{ATP} on a clinical scanner. This method demonstrates acceptable reproducibility, which allows meaningful sample size calculations for future biomedical research and clinical studies. FRiST demonstrates a sensitivity allowing to detect a decrease in F_{ATP} in people with T1D compared to control volunteers and shows potential as a noninvasive tool for enhancing the understanding of liver diseases and improving diagnosis and monitoring of treatment.

Abbreviations

F_{ATP}	Forward ATP synthesis rate
$T'_{1,Pi}$	Apparent spin-lattice relaxation time of inorganic phosphate
k_f	Equilibrium forward rate constant
ATP	Adenosine triphosphate
BMI	Body mass index
CV	Coefficient of variation
DANTE	Delays alternating with nutations for tailored excitation
FRiST	Four repetition time saturation transfer
MASH	Metabolic dysfunction-associated steatohepatitis
MASLD	Metabolic dysfunction-associated steatotic liver disease
MRS	Magnetic resonance spectroscopy
PCr	Phosphocreatine
P_i	Inorganic phosphate
SNR	Signal-to-noise ratio
ST	Saturation transfer
T1D	Type 1 diabetes
T2D	Type 2 diabetes
TR	Repetition time
UHF	Ultrahigh field

Supplementary information

The online version contains supplementary material available at https://doi.org/10.1186/s41747-025-00588-9.

Additional file 1: Supplementary Fig. S1: Planning of the FRiST protocol. a) Coronal and b) transverse MRI slices of the liver of a 30 years old control volunteer showing coil placement and position of the 2D-voxel of interest (VOI) (open in feet-head direction). White dots within the coil housing show position of reference spheres. **Supplementary Fig. S2:** Representative raw hepatic phosphorus magnetic resonance spectroscopy spectrum. No postprocessing was performed except zero order phasing. The spectral region between 10 ppm and 20 ppm served to determine the noise for calculation of signal-to-noise for spectral quality assessment. **Supplementary Fig. S3:** Position of the delays alternating with nutations for tailored excitation (DANTE) saturation bands with m = 3 saturation bands which were δ = 12 Hz (M3D12) apart on an entire hepatic phosphorus magnetic resonance spectroscopy spectrum. In the saturation experiment, the saturation pulse was centered on the γ-ATP resonance at ~-2.48 ppm (saturation bands displayed in red). Two aliased saturation bands (~-23.6 ppm and ~18.7 ppm) occur every ~21.2 ppm (1/τ = 1100 Hz) from the center of saturation frequency due to a DANTE subpulse duration of τ = 0.91 ms. In the mirrored experiment, the mirrored

saturation frequency was set to ~12.7 ppm resulting in aliased saturation bands at ~33.82 ppm (not shown) and ~-8.5 ppm (blue dashed lines). Note that in the mirrored experiment α-ATP is partly affected by the aliased sideband resulting in a decreased signal amplitude. For better representation, the spectrum is apodized with a 5 Hz Gaussian filter. **Supplementary Table S1:** MRSinMRS checklist [14]. **Supplementary Table S2:** 3TR *versus* 5TR. Results of apparent spin-lattice relaxation time ($T1'_{1,Pi}$) fitting of a saturation experiment to find the best suited three repetition time (TR) set. Two control volunteers underwent a saturation recovery experiment consisting of five TRs. The experimentally determined $T1'_{1,Pi}$ together with the calculated coefficient of determination (R^2) were compared to find the most accurate set of three TRs. **Supplementary Table S3:** Calculated phosphorus-MR spectroscopy parameters for the subgroups of control volunteers and type 1 diabetes using ANOVA adjusted for age, sex and BMI.

Acknowledgements
The authors thank Franziska Paumen and Neele Midding (Institute for Clinical Diabetology, German Diabetes Center, Düsseldorf, Germany) for their help with the experiments. We thank all GDS participants and all physicians for their continued encouragement of their volunteers to participate in GDS. We declare that this manuscript was written without any use of Large Language Models (LLMs).

Author contributions
MJ contributed to conceptualization, formal analysis, investigation, methodology, software, validation, visualization, and wrote the original draft. BK contributed to formal analysis, investigation, and methodology. MS contributed to methodology, resources, and software. JM contributed to software. SW and PB contributed to formal analysis. TS and SK contributed to resources. MR contributed to conceptualization, funding acquisition, project administration, resources, and supervision. VS contributed to conceptualization, project administration, resources, and supervision. All authors contributed to the manuscript revision & editing, read, and approved the submitted version.

Funding
This study was supported in part by the German Diabetes Center (DDZ), the German Federal Ministry of Health (BMG), by grants of the Federal Ministry for Research (BMBF) and the Ministry of Culture and Science of the State of North Rhine Westphalia to the German Center for Diabetes Research (DZD e. V.). MR is also supported by grants from the European Community (HORIZON-HLTH-2022-STAYHLTH-02-01: Panel A) to the INTERCEPT-T2D consortium, the German Research Foundation (DFG, GRK 2576) and the Schmutzler-Stiftung. The funding sources had no role in study design, data collection, data analysis, data interpretation, or writing of the report. Open Access funding enabled and organized by Projekt DEAL.

Data availability
The datasets used and/or analyzed during the current study are available from the corresponding author on reasonable request.

Declarations

Ethics approval and consent to participate
Institutional Review Board approval was obtained. All procedures performed in studies involving human participants were in accordance with the ethical standards of the institutional committee (Medical Faculty, Heinrich Heine University, Düsseldorf; ref#4508) and with the 1964 Helsinki declaration and its later amendments or comparable ethical standards.

Consent for publication
All participants provided written informed consent.

Competing interests
The authors of this manuscript declare relationships with the following companies. MR received fees consulting, lecturing or serving on advisory boards from Astra Zeneca, Boehringer-Ingelheim, Echosens, Eli Lilly, Madrigal, Merck-MSD, and Novo Nordisk and has performed investigator-initiated research with support from Boehringer-Ingelheim, Novo Nordisk, and Nutricia/Danone to the German Diabetes Center (DDZ). The other authors declare that they have no competing interests.

Author details
[1]Institute for Clinical Diabetology, German Diabetes Center, Leibniz Center for Diabetes Research at Heinrich Heine University Düsseldorf, Düsseldorf, Germany. [2]German Center for Diabetes Research (DZD e.V.), Partner Düsseldorf, München-Neuherberg, Germany. [3]Division of Magnetic Resonance Research, Department of Radiology, Johns Hopkins University School of Medicine, Baltimore, United States of America. [4]Department of Radiology and Nuclear Medicine, Maastricht University Medical Center, Maastricht, The Netherlands. [5]Institute for Biometrics and Epidemiology, German Diabetes Center, Leibniz Center for Diabetes Research at Heinrich Heine University Düsseldorf, Düsseldorf, Germany. [6]Department of Endocrinology and Diabetology, Medical Faculty and University Hospital Düsseldorf, Heinrich Heine University Düsseldorf, Düsseldorf, Germany.

Received: 22 January 2025 Accepted: 14 April 2025
Published online: 13 May 2025

References

1. Fromenty B, Roden M (2023) Mitochondrial alterations in fatty liver diseases. J Hepatol 78:415–429. https://doi.org/10.1016/j.jhep.2022.09.020
2. Koliaki C, Szendroedi J, Kaul K et al (2015) Adaptation of hepatic mitochondrial function in humans with non-alcoholic fatty liver is lost in steatohepatitis. Cell Metab 21:739–746. https://doi.org/10.1016/j.cmet.2015.04.004
3. Harrison SA, Bedossa P, Guy CD et al (2024) A phase 3, randomized, controlled trial of Resmetirom in NASH with liver fibrosis. N Engl J Med 390:497–509. https://doi.org/10.1056/NEJMoa2309000
4. Gancheva S, Kahl S, Pesta D et al (2022) Impaired hepatic mitochondrial capacity in nonalcoholic steatohepatitis associated with type 2 diabetes. Diabetes Care 45:928–937. https://doi.org/10.2337/dc21-1758
5. Oberhaensli RD, Galloway GJ, Hilton-Jones D et al (1987) The study of human organs by phosphorus-31 topical magnetic resonance spectroscopy. Br J Radiol 60:367–373. https://doi.org/10.1259/0007-1285-60-712-367
6. Meyerhoff DJ, Karczmar GS, Matson GB et al (1990) Non-invasive quantitation of human liver metabolites using image-guided ^{31}P magnetic resonance spectroscopy. NMR Biomed 3:17–22. https://doi.org/10.1002/nbm.1940030103
7. Szendroedi J, Chmelik M, Schmid AI et al (2009) Abnormal hepatic energy homeostasis in type 2 diabetes. Hepatology 50:1079–1086. https://doi.org/10.1002/hep.23093
8. Gancheva S, Bierwagen A, Kaul K et al (2016) Variants in genes controlling oxidative metabolism contribute to lower hepatic ATP independent of liver fat content in type 1 diabetes. Diabetes 65:1849–1857. https://doi.org/10.2337/db16-0162
9. Forsén S, Hoffman RA (1963) Study of moderately rapid chemical exchange reactions by means of nuclear magnetic double resonance. J Chem Phys 39:2892–2901. https://doi.org/10.1063/1.1734121
10. Fear EJ, Torkelsen FH, Zamboni E et al (2023) Use of ^{31}P magnetisation transfer magnetic resonance spectroscopy to measure ATP changes after 670 nm transcranial photobiomodulation in older adults. Aging Cell 22:e14005. https://doi.org/10.1111/acel.14005
11. Chen C, Stephenson MC, Peters A et al (2018) ^{31}P magnetization transfer magnetic resonance spectroscopy: assessing the activation induced change in cerebral ATP metabolic rates at 3 T. Magn Reson Med 79:22–30. https://doi.org/10.1002/mrm.26663
12. Valkovič L, Chmelík M, Just Kukurova I et al (2013) Time-resolved phosphorous magnetization transfer of the human calf muscle at 3 T and 7 T: a feasibility study. Eur J Radiol 82:745–751. https://doi.org/10.1016/j.ejrad.2011.09.024
13. Schmid AI, Schrauwen-Hinderling VB, Andreas M et al (2012) Comparison of measuring energy metabolism by different ^{31}P-magnetic resonance

spectroscopy techniques in resting, ischemic, and exercising muscle. Magn Reson Med 67:898–905. https://doi.org/10.1002/mrm.23095
14. Buehler T, Kreis R, Boesch C (2015) Comparison of ^{31}P saturation and inversion magnetization transfer in human liver and skeletal muscle using a clinical MR system and surface coils. NMR Biomed 28:188–199. https://doi.org/10.1002/nbm.3242
15. Schmid AI, Chmelík M, Szendroedi J et al (2008) Quantitative ATP synthesis in human liver measured by localized ^{31}P spectroscopy using the magnetization transfer experiment. NMR Biomed 21:437–443. https://doi.org/10.1002/nbm.1207
16. Valkovič L, Bogner W, Gajdošík M et al (2014) One-dimensional image-selected in vivo spectroscopy localized phosphorus saturation transfer at 7T. Magn Reson Med 72:1509–1515. https://doi.org/10.1002/mrm.25058
17. Fellinger P, Beiglböck H, Semmler G et al (2023) Increased GH/IGF-I axis activity relates to lower hepatic lipids and phosphor metabolism. J Clin Endocrinol Metab 108:e989–e997. https://doi.org/10.1210/clinem/dgad206
18. Fellinger P, Wolf P, Pfleger L et al (2020) Increased ATP synthesis might counteract hepatic lipid accumulation in acromegaly. JCI Insight 5:e134638. https://doi.org/10.1172/jci.insight.134638
19. Traussnigg S, Kienbacher C, Gajdošík M et al (2017) Ultra-high-field magnetic resonance spectroscopy in non-alcoholic fatty liver disease: novel mechanistic and diagnostic insights of energy metabolism in non-alcoholic steatohepatitis and advanced fibrosis. Liver Int 37:1544–1553. https://doi.org/10.1111/liv.13451
20. Valkovič L, Gajdošík M, Traussnigg S et al (2014) Application of localized ^{31}P MRS saturation transfer at 7 T for measurement of ATP metabolism in the liver: reproducibility and initial clinical application in patients with non-alcoholic fatty liver disease. Eur Radiol 24:1602–1609. https://doi.org/10.1007/s00330-014-3141-x
21. Wolf P, Fellinger P, Pfleger L et al (2019) Reduced hepatocellular lipid accumulation and energy metabolism in patients with long standing type 1 diabetes mellitus. Sci Rep 9:2576. https://doi.org/10.1038/s41598-019-39362-4
22. Schär M, El-Sharkawy A-MM, Weiss RG et al (2010) Triple repetition time saturation transfer (TRiST) ^{31}P spectroscopy for measuring human creatine kinase reaction kinetics. Magn Reson Med 63:1493–1501. https://doi.org/10.1002/mrm.22347
23. Szendroedi J, Saxena A, Weber KS et al (2016) Cohort profile: the German Diabetes Study (GDS). Cardiovasc Diabetol 15:59. https://doi.org/10.1186/s12933-016-0374-9
24. Jonuscheit M, Wierichs S, Rothe M et al (2024) Reproducibility of absolute quantification of adenosine triphosphate and inorganic phosphate in the liver with localized ^{31}P-magnetic resonance spectroscopy at 3-T using different coils. NMR Biomed 37:e5120. https://doi.org/10.1002/nbm.5120
25. Morris GA, Freeman R (1978) Selective excitation in Fourier transform nuclear magnetic resonance. J Magn Reson 29:433–462. https://doi.org/10.1016/0022-2364(78)90003-3
26. Schär M, Kozerke S, Fischer SE et al (2004) Cardiac SSFP imaging at 3 tesla. Magn Reson Med 51:799–806. https://doi.org/10.1002/mrm.20024
27. Ordidge R, Connelly A, Lohman J (1986) Image-selected in vivo spectroscopy (ISIS). A new technique for spatially selective NMR spectroscopy. J Magn Reson 66:283–294. https://doi.org/10.1016/0022-2364(86)90031-4
28. Lin A, Andronesi O, Bogner W et al (2021) Minimum reporting standards for in vivo magnetic resonance spectroscopy (MRSinMRS): experts' consensus recommendations. NMR Biomed 34:e4484. https://doi.org/10.1002/nbm.4484
29. Kreis R, Boer V, Choi I-Y et al (2020) Terminology and concepts for the characterization of in vivo MR spectroscopy methods and MR spectra: background and experts' consensus recommendations. NMR Biomed 34:e4347. https://doi.org/10.1002/nbm.4347
30. Roumans KHM, Lindeboom L, Veeraiah P et al (2020) Hepatic saturated fatty acid fraction is associated with de novo lipogenesis and hepatic insulin resistance. Nat Commun 11:1891. https://doi.org/10.1038/s41467-020-15684-0
31. Du F, Zhang Y, Chen W (2012) Relayed magnetization transfer from nuclear Overhauser effect and chemical exchange observed by in vivo ^{31}P MRS in rat brain. Magn Reson Imaging 30:716–721. https://doi.org/10.1016/j.mri.2012.01.005
32. Schmid AI, Szendroedi J, Chmelik M et al (2011) Liver ATP synthesis is lower and relates to insulin sensitivity in patients with type 2 diabetes. Diabetes Care 34:448–453. https://doi.org/10.2337/dc10-1076
33. Kemp GJ (2008) The interpretation of abnormal ^{31}P magnetic resonance saturation transfer measurements of Pi/ATP exchange in insulin-resistant skeletal muscle. Am J Physiol Endocrinol Metab 294:E640–E642; author reply E643– E644. https://doi.org/10.1152/ajpendo.00797.2007
34. Balaban RS, Koretsky AP (2011) Interpretation of ^{31}P NMR saturation transfer experiments: what you can't see might confuse you. Focus on "Standard magnetic resonance-based measurements of the Pi→ATP rate do not index the rate of oxidative phosphorylation in cardiac and skeletal muscles". Am J Physiol Cell Physiol 301:C12–C15. https://doi.org/10.1152/ajpcell.00100.2011
35. Valkovič L, Chmelík M, Krššák M (2017) In-vivo ^{31}P-MRS of skeletal muscle and liver: a way for non-invasive assessment of their metabolism. Anal Biochem 529:193–215. https://doi.org/10.1016/j.ab.2017.01.018

Publisher's Note

Chapter 7

7 Overall Discussion

The presented studies show improvements and advancements in non-invasive assessment of hepatic energy metabolism using ^{31}P-MRS methods on a clinical system. The results of the two studies demonstrate that dedicated method development in combination with specialized post-processing routines allows a robust and coil-independent absolute quantification of hepatic metabolites and assessment of ATP synthesis rates on a clinically available scanner without the need for an UHF system. With an acceptable reproducibility, both methods have the potential to be applied in further research studies, contributing to the elucidation of the etiology of chronic metabolic disease.

^{31}P-MRS methods show the potential for wide applications in human studies for assessment of energy metabolism [19,130,131]. However, in the past, absolute concentrations largely differed even in healthy volunteers between different sites with values ranging from 1.39–3.7 mM for ATP and 1.18–2.8 mM for P_i, respectively [57, 59, 73, 123, 132–134]. The here described phantom replacement technique, introduced by Meyerhoff et al. [57], proposes one way to report absolute concentrations of metabolites, which are independent of the used coil and further corrects for sequence-specific characteristics of the used sequence. It was shown that the results obtained with both surface coils, which differ in size and geometry, are comparable and that the method provides a small CV, and can thereby be seen as highly reproducible. However, sticking to an exact procedure in terms of phantom setup as well as a well-controlled, precise quantification of spectra is mandatory. As a result, absolute quantification is a tedious process with many pitfalls, where errors can quickly be introduced. But once established, it turns out to be a very robust method, which is capable to completely remove coil-dependent characteristics as source of variation. The correction factors used to obtain coil-independent results are the spatial $\boldsymbol{B_1}$ field distribution, the excitation pulse profile, and the coil loading. The first two of these are also affected by the choice of MRS sequence used, making them indispensable to be assessed and to be accounted for. There are also other factors like T_1 relaxation which can be a cause for discrepancies, especially when a short TR is used, leading to partial saturation of some metabolites. However, there are also volunteer-specific factors, because larger amounts of HL content replace signal from ^{31}P-metabolites in the observed VOI, which is why this factor needs to be corrected for, too.

The results of the reproducibility study show that both coils provided similar day-to-day reproducibilities for ATP and P_i with CVs <11%, which are in agreement with literature [45, 60, 135] and show that the method is highly reproducible. Even an additional measurement after three months did not introduce extra variation, showing that in healthy people, basal concentrations of hepatic metabolites do not change quickly. The results of the intra-day measurements with CVs <5% and <7% for ATP in measurements without and with repositioning of the volunteer

indicate that methodological variations are minimal. Also a deliberate replanning of the VOI to a suboptimal position within the liver yielded a CV <8%, showing that the established method is able to compensate for smaller misplacements of the VOI. Another factor indicating the robustness of the method is that only one out of 86 spectra needed to be excluded due to low SNR and there was no reason to exclude any spectrum because of high contamination from abdominal muscle. Looking at the SNRs obtained with both coils for ATP and P_i (8.2 and 7.3 single-loop coil; 8.0 and 6.8 quadrature coil), similar values were calculated. At first glance, this may seem strange since the coil sizes vary greatly and one might expect that the bigger loops of the quadrature coil introduce more noise than the small single-loop coil within the same sized VOI. However, its quadrature geometry seems to compensate this issue by a boost in sensitivity, which can theoretically increase SNR by a factor of $\sqrt{2}$ [136]. On the other hand, the bigger coil elements should be favorable in people with high BMI, because due to the rule of reciprocity, its penetration depth should increase with loop size. This effect could not be confirmed in the current study as also the single-loop coil yielded good measurements in all volunteers, although two volunteers were obese (BMIs of 31–32 $^{kg}/_{m^2}$). It should be noted that even though the SNR and reproducibility of absolute concentrations did not indicate any improvement with the quadrature coil, it was shown in later measurements, which are not part of this work, that the larger curved coil allows measurements in very obese people (BMI >35$^{kg}/_{m^2}$) that would not have led to analyzable results with the previously used single-loop coil. The driving force behind this study was the fact that over recent years, more and more obese people were measured in the framework of the German Diabetes Study (GDS) study and the failure rate continued to increase due to high BMI. This observation is in accordance with an older report which claimed that every unit increase in BMI lowers the successful application of ^{31}P-MRS by 14% [135]. The custom-made bigger coil design addresses this issue successfully. The phantom replacement technique eliminates a major barrier in the assessment of absolute concentrations across different vendors and coils. By successful implementation of this technique it is possible to switch between coils in case a coil has a malfunction and needs to be replaced. Due to the constant progress in coil design, a coil exchange may also be desirable if an improved version of a coil is available, as it was the case in this study, and exchanging the coil should be possible without introducing a bias in the measurement results.

However, it is to mention that even when using this technique, still significant differences in concentrations can be observed between different sites. One study dealing with conductivity of the used phosphate phantom for in-vitro establishment of the phantom replacement technique showed that a large bias in data can be introduced in cases the conductivity of the phantom does not match the in-vivo situation [134]. As the range of acceptable conductivity heavily decreases with increasing B_0, studies performed at 3 T need to take this into account when mixing the phantom and it becomes even more important at UHF. Nevertheless, even if the conductivity is not in the desired region, this factor can be calculated and corrected later, as it is independent of both the used coil and the measurement protocol. According to the work of Purvis et al. [134], the phantom used in this study introduced an approximately 20% bias because of too high conductivity, which would increase the reported values for ATP and P_i from 2.32 mM and 1.73 mM to 2.78 mM and 2.08 mM. These conductivity-corrected values are

exactly in the center of the range of concentrations given in the literature. Nevertheless, they were not used here because the GDS study already exists for years and no bias should arise in the data. However, to better understand conductivity- and permittivity-related biases, future studies should develop more complex phantoms, as proposed by Purvis et al. [134], and validate these across field strengths (3T vs. UHF) to ensure robust multi-center reproducibility. Another factor introducing a bias if not taken into account is the HL content of the volunteers. As the liver is usually considered as homogeneous tissue, an accumulation of TGs diminishes the volume of the VOI that is occupied by cytoplasm (containing phosphorus metabolites) leading to a smaller apparent concentration. However, since the healthy cohort in this study was expected to be characterized by normal levels of hepatic TGs, the reported concentrations are at most 1–2 percentage points higher. It should be emphasized that this had no influence on the results of the reproducibility and the coil comparison, as this factor is person-dependent and constant in repeated measurements. Still, correcting for HL content should be applied routinely, especially when investigating people with MASLD and T2D. The first study used the Java magnetic resonance user interface (jMRUI) software [137, 138] with the Advanced Method for Accurate, Robust and Efficient Spectral fitting (AMARES) algorithm [139, 140] for data post-processing and peak fitting, in accordance with data analysis in GDS. Establishing custom prior knowledge, including chemical shifts, linewidths, and lineshapes allows both an accurate and highly reproducible fitting as well as a fast analysis. This is of particular importance, since variations in metabolite concentrations in the literature were found partly caused by differences in post-processing and quantification methods [53]. Today, jMRUI software is frequently applied for analysis of ^{31}P-MRS spectra [33, 35, 49, 59–61, 132] and uses the time domain signal for quantification. Next to custom written MATLAB scripts, there are approaches to use software quantifying metabolites in the frequency domain like LCModel [141], which requires data from in vitro or simulated spectra and is mostly used for ^{1}H-MRS. In the last years, LCModel was adapted to a basis set of ^{31}P-MRS spectra at 3 T and first results showed comparable fitting results as obtained with jMRUI [30]. Because analysis with jMRUI is done semi-automatically and requires considerable operator-dependent input, a more automatized approach might be favorable to assure observer-independence and speed up processing for routine analysis of larger data sets.

The second study went one step further by analyzing a biochemical reaction rather than 'solely' measuring metabolite concentrations. For this purpose, a method capable of assessing hepatic ATP synthesis rates at clinical field strength with a high degree of spatial localization was developed. Here, the ^{31}P-MRS ST technique was used, which required implementation of a saturation pulse within the vendor-provided pulse program. Because pulse programming within the environment of the vendors system is necessary, this technique is mostly applied in a research environment and not clinically used. However, once established it is possible to assess parameters that are otherwise difficult to determine, such as hepatic ATP synthesis rates.

Whereas the technique itself is not novel and the theoretical background was already proposed in 1963 by Forsen et al. [18], ^{31}P-MRS ST has mainly been applied in the human brain [63–66] and skeletal muscle [77–86], being non-moving organs and the tissues of interest are close to the body surface. The application of ST in the liver is rather complex, because application of

spatial localization is mandatory, which heavily decreases SNR and therefore leads to highly increased measurement times of 2 h at clinical field strength. Up to now, only two methods were published to assess hepatic ATP synthesis in humans at clinical field strength [51, 52]. Both studies have in common that the applied protocols were very long (up to 2 h), requiring two separate measurement sessions. Also, these protocols were applied with limited signal localization to liver tissue either localizing the signal only by FA [52] or with a one-dimensional localization sequence [51]. Furthermore, no data on reproducibility has been reported. The described method in this doctoral thesis developed a new approach that addresses all these limitations: The overall duration of the protocol amounts to 90 min. Therefore, the whole protocol can be applied within one session, the signal is localized in two-dimensions and the reproducibility of the method was assessed. A reduction of total measurement time was achieved by acquisition of only four spectra. The otherwise time-consuming IR protocol to assess the hepatic apparent spin-lattice relaxation time $T'_{1,Pi}$ was replaced by a 3TR approach. Moreover, shimming was performed on $\boldsymbol{B_0}$ maps based on manually segmented liver volume which in combination with the acquisition of two-dimensional localized spectra resulted in high SNR spectra of 12.0 and 6.2 for ATP and P_i, respectively, and spectra showed negligible contamination from the abdominal muscle, which can be verified by minimal signal from PCr in the spectra.

Day-to-day reproducibility of the method in healthy volunteers resulted in CVs of 7.1% for $T'_{1,Pi}$ and 21.3% for k_f, respectively, which is slightly higher than the sparse literature values available of 11.2% for $T'_{1,Pi}$ and 9.0% for k_f that were assessed at UHF [76]. Excluding one outlier in the present study, the CV of k_f would reduce to 14.6%, being even more similar to the values of Valkovič et al. at UHF [76]. The reason for this outlier in the data, however, could not be found; one possibility could be breathing artifacts. It is to highlight that the acceptable reproducibility in the current study is achieved, although at UHF the signal intensity difference between the saturated and unsaturated experiment is larger compared to 3 T (21% from [76] vs. 15% in this study) due to increased B_0. This work shows that methodological optimizations mitigate inherent limitations of clinical field strength, bridging the gap between UHF research and clinical applications for hepatic energy metabolism. Looking at the obtained values in healthy controls at clinical field strength, a range from 520 ± 20 ms to 580 ± 60 ms for $T'_{1,Pi}$ and 0.27 ± 0.03 $^1/_s$ to 0.3 ± 0.02 $^1/_s$ for k_f was found [51, 52] and is agreement with data obtained from the current study ($T'_{1,Pi}$ = 482 ± 22 ms and k_f = 0.34 ± 0.03 $^1/_s$). In both studies from the literature, also F_{ATP} values were reported, which surprisingly show more variation from 29.5 ± 1.8 $^{mM}/_{min}$ [51] to 48.6 ± 7.4 $^{mM}/_{min}$ [52]. The discrepancies in F_{ATP} emerge by differences in assumed P_i concentrations. The average P_i concentration used in this study (1.73 mM) was taken from the reproducibility study (Study 1) and this value agreed well with the mean value reported in the literature and also by Schmid et al. (1.64 mM) [51], leading to a F_{ATP} value of 35.3 ± 3.5 $^{mM}/_{min}$. The calculated F_{ATP} is much lower compared to the value reported by Buehler et al., since they used P_i = 3.0 mM [52]. However, this P_i concentration appears extraordinarily high and is outside the range usually published in the literature. To assess the sensitivity of the method, the protocol was in a second step also applied in people with T1D, as literature using an UHF system has previously indicated reduced ATP synthesis rates for T1D compared

to healthy controls [142]. Indeed, a lower k_f of 0.16 ± 0.03 $^1/_s$ was found which is in excellent agreement with the data reported at UHF of $k_f = 0.17 \pm 0.03\,^1/_s$ [142]. Thus the current protocol is able to pick up relevant differences and report ATP synthesis rates which are comparable to data obtained at UHF.

Although similar CVs were obtained compared to the UHF study, it is noteworthy that the whole experiment took 90 min in this study. In contrast, the study conducted at 7 T only lasts 24 min, including a 7-point IR experiment for assessment of $T'_{1,Pi}$, which clearly shows the advantage of higher spectral resolution and SNR at UHF [76]. In another study Valkovič et al. performed and compared hepatic ^{31}P-MRS ST between 3 T and 7 T and concluded that at 7 T both the SNR and fitting precision improved more than double within the same scan duration (SNR 2.09 vs. 4.28, Cramer-Rao lower bound (CRLB) 30.5 vs. 13.1), respectively [75]. Even adding up two datasets at 3 T proved to be far inferior than 7 T (SNR 2.76, CRLB 26.7). Due to this insurmountable difference in spectral quality caused by the field strength, sequences should be specifically optimized for clinical field strength, but an increase in measurement time, at the expense of volunteer comfort and throughput, is unpreventable. Since the critical parameter for this method is the assessment of the difference in P_i amplitude between the saturated and unsaturated spectrum (△M), the acquisition of these two spectra alone required about 1 h. In addition to the duration of the measurement time ($SNR \propto \sqrt{NSA}$), the processing of the spectrum also plays a major role for the accuracy of the results. To address this specifically, a fully-automated, custom-written analysis script was established in MATLAB for post-processing of all spectra for Study 2. The major advantage is that the script allows simultaneous pre-processing of all four spectra in order to find an overall mean phase angle and subsequently perform a simultaneous fitting procedure, which ensures exactly consistent handling of all relevant spectra and precise estimation of peak differences for P_i. Using jMRUI software, this is only possible in a fully manual manner which is why the procedure is susceptible to user-dependent inputs. Additionally, the automated procedure enabled a mixture of Gaussian and Lorentzian line shapes to be applied in the fitting process, which was unfortunately not available in jMRUI and increases fitting accuracy of P_i in respect to its neighboring PDE and PME resonances.

An important aspect of the ST technique is the interpretation of the results obtained. In skeletal muscle, where determination of ATP synthesis rates have already been applied more thoroughly, it has been noticed that the calculated metabolic flux overestimates the purely oxidative ATP synthesis [143]. This makes the interpretation of the results more complex than initially assumed. Since ATP in the liver can be synthesized via two processes, anaerobic glycolysis and aerobic oxidative ATP synthesis (creatine kinase reaction is negligible), the assessed k_f value may include a significant glycolytic component [143, 144]. Moreover, the measured k_f represents the unidirectional flux, not the net flux of the system. Therefore, in case the reaction runs close to the equilibrium, forward and backward reaction rates become comparable, leading to a larger contribution of the reverse flux (ATP hydrolysis) to the measured unidirectional k_f. Consequently, the ST derived k_f reflects the total unidirectional ATP synthesis rate and should not be interpreted as the net oxidative ATP synthesis rate. This note emphasizes that ST results must be interpreted depending on the context. Although the method is sensitive to metabolic

dysfunction, it does not provide isolated information on mitochondrial activity. Combinations with other techniques, such as hyperpolarized ^{13}C-MRS for detection of glycolysis by infusion of ^{13}C-labeled pyruvate as a substrate, offer a measure of pyruvate-lactate interconversion and would be necessary to decouple the contributions of individual metabolic pathways [145]. This approach has been validated in murine skeletal muscle, where simultaneous increase in pyruvate dehydrogenase-derived bicarbonate (oxidative ATP synthesis) and lactate (glycolytic ATP synthesis) during induced exercise was observed [146]. Still, although not reflecting only net oxidative ATP synthesis, the assessed values by ST remain a sensitive marker of energy metabolism, mostly changing in parallel with other related metabolic markers [19].

It should be noted that it was not possible to include an age-matched T1D cohort in the current study, which is why the statistical testing of anthropometric data revealed a significant difference in age between the two groups. Nevertheless, the results remained unchanged when testing without and with sex, age, and BMI as a covariate.

As long scan times are demanding in terms of volunteer cooperation, speeding up the protocols is particularly important for implementation in future studies, and even more so for successful integration into everyday clinical practice. The phantom replacement technique described in this doctoral thesis has a great advantage over other absolute quantification methods, as the phantom is only measured once, but in a very lengthy and detailed manner. The process described here assesses the entire three-dimensional space in which the voxel can potentially be positioned. Other methods require the phantom to be placed in a similar position in the scanner right after each in-vivo measurement and then measure the VOI at exactly the same spatial location as in vivo. This is an impractical procedure, as the measurement time is doubled. The spectroscopy sequence used in this study has a duration of about thirteen minutes, owning a TR of six seconds and 128 averages. As long as only ATP and P_i are the metabolites of interest, one could decrease TR to, for example, four seconds to reduce the measurement time to about nine minutes without losing any signal quality for both metabolites. The underlying reason behind this is that due to the presence of increased iron in the liver, relaxation times of the metabolites are shorter compared to other organs. This applies especially for ATP and P_i with $T_{1,ATP} = 430$ ms and $T_{1,P_i} = 730$ ms at 3 T [51], respectively. In case TR is decreased by one third from six to four seconds, both metabolites will still be fully relaxed after four seconds ($TR > 5T_1$).

The ST method itself needs an acquisition duration of 90 min, which is mainly caused by the necessity of two-dimensional localization to prevent signal contamination from abdominal muscle. Even this time was already a significant improvement compared to other methods at the same field strength, though it is still very long compared to clinical protocols. One way of reducing time would be to carry out the method with one-dimensional localization. However, in order for this to work without significant contamination, a smaller coil would be required, which in turn may have a too low penetration depth to obtain sufficient signal in people with higher BMI and is therefore only applicable in lean people. As only three spectra with different TRs are acquired for determination of $T'_{1,Pi}$ and one of them is simultaneously required for determining $\triangle M$, there is no large potential for speeding up the measurement. One could consider using group mean values for clinical studies instead of individual $T'_{1,Pi}$ measurements,

which would reduce the measurement time by 30 min, however, this approach decreases the sensitivity of the method as differences in k_f also influence $T'_{1,Pi}$. Otherwise, the number of averages of both spectra at $TR = 1.7$ s could be reduced to assess $\triangle M$ faster. Also here, the extent to which this affects the reproducibility of the measurement must be checked in advance.

In summary, this doctoral thesis contributes novel developments in diabetes research and spectroscopy with particular focus on hepatic energy metabolism using a clinical scanner. A method for coil-independent determination of absolute metabolite concentrations was introduced and validated. The herewith obtained absolute concentrations allow insights into energy metabolism without the necessity of relying on assumed concentrations or metabolite ratios, enhancing the interpretability of the findings. The subsequent study presented a novel method for contamination-free assessment of unidirectional hepatic ATP synthesis rates, being a marker for hepatic mitochondrial activity. Finally, this doctoral thesis highlights the feasibility of using MRS for studying hepatic energy metabolism in vivo and in detail at clinical field strength.

Chapter 8

8 Conclusion and Outlook

Both studies conducted in this doctoral thesis developed and validated ^{31}P-MRS methods for investigation of hepatic metabolism, particularly at clinical field strength. The aim was to establish robust and reproducible non-invasive methods which allow the calculation of absolute metabolite concentrations such as ATP and P_i, but also detect biochemical reaction rates as the ATP synthesis rate in the human liver. Both methods represent a technique for translational research since they enable characterization of hepatic energy metabolism on an individual basis as well as paving the way for longitudinal monitoring and assessment of treatment effects in metabolic research. This enables a more personalized characterization of metabolism and gives insights into disease progression and treatment responses without the need for an invasive biopsy.

Study 1 developed a three-dimensional MR sequence together with a post-processing routine for assessment of absolute quantification of hepatic metabolites using the phantom replacement technique [57]. Two surface coils with different size and geometry were used and evaluated regarding obtained concentrations, SNR and reproducibility in a healthy cohort. The results of this study show that the implemented method yields consistent and reproducible results which are independent of the coil in use, showing the potential of this method to allow consistent reports of physiological concentrations without bias caused by the used hardware.

Study 2 introduced an innovative ^{31}P-MRS ST method aiming to determine the hepatic ATP synthesis rate with a high degree of spatial localization at clinical field strength, which addresses a critical gap in metabolic imaging. While current methods for ATP synthesis rate assessment have been largely confined to UHF systems due to SNR and localization challenges [19, 75], this study developed a time-efficient, spatially localized approach using a two-dimensional localization sequence combined with optimized DANTE saturation pulses. The method was established in vitro and in vivo, before applying it in healthy volunteers and people with T1D. As a result, the method showed acceptable reproducibility and was sensitive enough to detect significant changes in ATP synthesis rates between healthy controls and people with T1D.

Both studies demonstrate the feasibility of ^{31}P-MRS at clinical field strength, despite the challenges of low SNR and long measurement times compared to UHF systems [60, 75, 134]. The developed methods are reproducible and sensitive enough to detect differences between groups and are ready for future application in clinical studies. While the method for absolute quantification of hepatic ^{31}P-metabolites has been used for more than a decade within the framework of the GDS in Germany [147], larger multi-center cohorts are still lacking and might be needed to confirm the findings in other diverse populations. For this purpose, a harmonization of protocols between sites and vendors is essential in order to be able to compare the obtained absolute

values. The current work may serve as a foundation for application of multi-center studies and protocol harmonization efforts with the ultimate aim to support the broader clinical adoption of the ^{31}P-MRS for hepatic metabolism research.

On the other hand, the method of ^{31}P-MRS ST is very sophisticated, which hampers its widespread application. Being technically complex together with a total measurement time of 90 min, including this method into clinical routine might be very difficult. However, this thesis has set up automatic routines and extensive standardization, so that this method can be applied in further research-driven studies to investigate possible changes in ATP synthesis rates in various diseases. For example, the technique can be applied in T2D to characterize liver metabolism across the recently defined clusters of T2D, enabling metabolic profiling within these distinct subgroups. Preliminary observations in people with diabetes indicate that the hepatic ATP synthesis rate F_{ATP} may differ mechanistically between subtypes: While in T2D reduced F_{ATP} appears linked to lower hepatic P_i concentrations [35,76], people with T1D showed significantly decreased k_f values despite stable P_i concentrations [142]. These differences highlight the potential of ^{31}P-MRS ST for metabolic phenotyping but require further validation in larger, multi-center cohorts to confirm subtype-specific patterns and their clinical relevance. Also studies investigating short-term treatment scenarios as the effect of the recently approved liver-selective thyroid hormone receptor ß-agonist, resmetirom, for MASH, may be of interest, as resmetirom's working mechanism is currently thought to be an improvement of overall mitochondrial function [148].

This doctoral thesis deals exclusively with the application of ^{31}P-MRS to characterize hepatic metabolism. The described methods can also be included into more complex protocols that additionally apply ^{1}H- and ^{13}C-MRS to link the obtained data with lipid quantification and data on glycogen metabolism. Especially ^{1}H-MRS of the liver provides important information on TGs as for example the HL content can be assessed with high precision within a few minutes [61, 117, 149] and even more information can be assessed by investigation of the fatty acid composition which takes about 15 min [115, 116]. Although ^{13}C-MRS requires the use of an additional coil and suffers even more regarding SNR compared to ^{31}P-MRS, the possibility to detect metabolites such as glucose and glycogen offers complementary information on hepatic metabolism. Conventional ^{13}C-MRS is limited by low sensitivity, necessitating long acquisition times. However, recent developments in hyperpolarized ^{13}C-pyruvate MRS overcome this issue. This technique enables detection of real-time metabolism and is therefore a promising field for synergy with ^{31}P-MRS. In this context, a recent study performed real-time quantification of both oxidative and glycolytic fluxes during exercise in vivo in skeletal muscle of murine animals [146]. This technique may also be transferred for hepatic applications and combined with the investigation of redox shifts using also hyperpolarized ^{13}C-pyruvate MRS as reported by Lewis et al., who investigated metformin-induced changes in cytosolic NADH/NAD$^+$ ratios in the heart and the liver of rats [150]. Combining all these techniques, an even more detailed insight into hepatic metabolism can be obtained.

The presented methodologies may spark new research and eventually may even transform ^{31}P-MRS from an only research-focused tool into a clinically valuable option for metabolic liver assessment. Because it is non-invasive and does not use ionizing radiation, its ability to

provide assessment of hepatic energy metabolism may allow us to better understand chronic metabolic disease and enable treatment monitoring. Future work should - in addition to further technical refinements to decrease the scan time - focus on an integration of these methods into clinical workflows, where applicable. The overall aim will always be to improve the outcome for each individual with hepatic and metabolic disorders and these techniques might help to achieve a personalized medicine approach for precision medicine in the future.

Bibliography

[1] American Diabetes Association, "2. Diagnosis and classification of diabetes: Standards of care in diabetes-2024," *Diabetes Care*, vol. 47, no. Suppl 1, pp. 20–42, 2024.

[2] World Health Organization, *Diabetes country profiles: Germany 2016.* Geneva: WHO, 2016.

[3] NCD Risk Factor Collaboration, "Worldwide trends in diabetes prevalence and treatment from 1990 to 2022: A pooled analysis of 1108 population-representative studies with 141 million participants," *The Lancet*, vol. 404, no. 10467, pp. 2077–2093, 2024.

[4] GBD 2021 Diabetes Collaborators, "Global, regional, and national burden of diabetes from 1990 to 2021, with projections of prevalence to 2050: A systematic analysis for the Global Burden of Disease Study 2021," *The Lancet*, vol. 402, no. 10397, pp. 203–234, 2023.

[5] D. J. Magliano, E. J. Boyko, I. Genitsaridi, L. Piemonte, P. Riley, and P. Salpea, *International Diabetes Federation Diabetes Atlas: 11th Edition.* Brussels: IDF, 2025.

[6] World Health Organization, *Global Health Estimates 2021: Global Deaths by Cause, Age and Sex, 2000-2021.* Geneva: WHO Press, 2024.

[7] C. D. Mathers and D. Loncar, "Projections of global mortality and burden of disease from 2002 to 2030," *PLOS Medicine*, vol. 3, no. 11, p. e442, 2006.

[8] D. Voeltz, M. Vetterer, E. Seidel-Jacobs, R. Brinks, T. Tönnies, and A. Hoyer, "Projecting the economic burden of type 1 and type 2 diabetes mellitus in Germany from 2010 until 2040," *Population Health Metrics*, vol. 22, no. 1, p. 17, 2024.

[9] S. Tsipas, T. Khan, F. Loustalot, K. Myftari, and G. Wozniak, "Spending on glucagon-like peptide-1 receptor agonists among US adults," *JAMA Network Open*, vol. 8, no. 4, p. e252964, 2025.

[10] M. Roden and G. I. Shulman, "The integrative biology of type 2 diabetes," *Nature*, vol. 576, no. 7785, pp. 51–60, 2019.

[11] D. Leith, Y. Y. Lin, and P. Brennan, "Metabolic dysfunction-associated steatotic liver disease and type 2 diabetes: A deadly synergy," *touchREVIEWS in Endocrinology*, vol. 20, no. 2, pp. 5–9, 2024.

[12] A. Gastaldelli and K. Cusi, "From NASH to diabetes and from diabetes to NASH: Mechanisms and treatment options," *Journal of Hepatology Reports*, vol. 1, no. 4, pp. 312–328, 2019.

[13] C. Herder and M. Roden, "A novel diabetes typology: Towards precision diabetology from pathogenesis to treatment," *Diabetologia*, vol. 65, no. 11, pp. 1770–1781, 2022.

[14] E. Ahlqvist, P. Storm, A. Käräjämäki, M. Martinell, M. Dorkhan, A. Carlsson, P. Vikman, R. B. Prasad, D. M. Aly, P. Almgren, Y. Wessman, N. Shaat, P. Spégel, H. Mulder, E. Lindholm, O. Melander, O. Hansson, U. Malmqvist, Å. Lernmark, K. Lahti, T. Forsén, T. Tuomi, A. H. Rosengren, and L. Groop, "Novel subgroups of adult-onset diabetes and their association with outcomes: A data-driven cluster analysis of six variables," *Lancet Diabetes & Endocrinology*, vol. 6, no. 5, pp. 361–369, 2018.

[15] O. P. Zaharia, K. Strassburger, A. Strom, G. J. Bönhof, Y. Karusheva, S. Antoniou, K. Bódis, D. F. Markgraf, V. Burkart, K. Müssig, J.-H. Hwang, O. Asplund, L. Groop, E. Ahlqvist, J. Seissler, P. Nawroth, S. Kopf, S. M. Schmid, M. Stumvoll, A. F. H. Pfeiffer, S. Kabisch, S. Tselmin, H. U. Häring, D. Ziegler, O. Kuss, J. Szendroedi, and M. Roden, "Risk of diabetes-associated diseases in subgroups of patients with recent-onset diabetes: A 5-year follow-up study," *Lancet Diabetes & Endocrinology*, vol. 7, no. 9, pp. 684–694, 2019.

[16] M. Schön, K. Prystupa, T. Mori, O. P. Zaharia, K. Bódis, M. Bombrich, C. Möser, I. Yurchenko, Y. Kupriyanova, K. Strassburger, P. Bobrov, A. T. N. Nair, G. J. Bönhof, A. Strom, G. E. Delgado, S. Kaya, R. Guthoff, N. Stefan, A. L. Birkenfeld, H. Hauner, J. Seissler, A. Pfeiffer, M. Blüher, S. Bornstein, J. Szendroedi, S. Meyhöfer, S. Trenkamp, V. Burkart, V. B. Schrauwen-Hinderling, M. E. Kleber, A. Niessner, C. Herder, O. Kuss, W. März, E. R. Pearson, M. Roden, and R. Wagner, "Analysis of type 2 diabetes heterogeneity with a tree-like representation: Insights from the prospective German Diabetes Study and the LURIC cohort," *Lancet Diabetes & Endocrinology*, vol. 12, no. 2, pp. 119–131, 2024.

[17] R. A. de Graaf, *In Vivo NMR Spectroscopy: Principles and Techniques*. Hoboken, NJ: Wiley, 3rd ed., 2019.

[18] S. Forsén and R. A. Hoffman, "Study of moderately rapid chemical exchange reactions by means of nuclear magnetic double resonance," *The Journal of Chemical Physics*, vol. 39, no. 11, pp. 2892–2901, 1963.

[19] L. Valkovič, M. Chmelík, and M. Krššák, "In-vivo 31P-MRS of skeletal muscle and liver: A way for non-invasive assessment of their metabolism," *Analytical Biochemistry*, vol. 529, pp. 193–215, 2017.

[20] F. Bloch, "Nuclear Induction," *Physical Review*, vol. 70, no. 7-8, pp. 460–474, 1946.

[21] E. M. Purcell, H. C. Torrey, and R. v. Pound, "Resonance absorption by nuclear magnetic moments in a solid," *Physical Review*, vol. 69, no. 1-2, pp. 37–38, 1946.

[22] Paul C. Lauterbur, "Image formation by induced local interactions: Examples employing nuclear magnetic resonance," *Nature*, vol. 242, pp. 190–191, 1973.

[23] P. Mansfield and P. K. Grannell, "NMR 'diffraction' in solids?," *Journal of Physics C: Solid State Physics*, vol. 6, no. 22, pp. L422–L426, 1973.

[24] B. M. Dale, M. A. Brown, and R. C. Semelka, *MRI: Basic Principles and Applications*. Chichester: Wiley-Blackwell, 5th ed., 2015.

[25] H. Friebolin, *Basic One- and Two-Dimensional NMR Spectroscopy*. Weinheim: Wiley-VCH, 5th ed., 2011.

[26] Bruker, *Almanac 2012: Analytical Tables and Product Overview*. Billerica, MA: Bruker, 2012.

[27] M. A. Brown and R. C. Semelka, *MRI: Basic principles and applications*. Hoboken, NJ: Wiley-Interscience, 3rd ed., 2003.

[28] S. F. Keevil, "Spatial localization in nuclear magnetic resonance spectroscopy," *Physics in Medicine and Biology*, vol. 51, no. 16, pp. R579–636, 2006.

[29] P. A. Bottomley, *Handbook of Magnetic Resonance Spectroscopy in Vivo: MRS Theory, Practice and Applications*. New York: John Wiley & Sons Incorporated, 1st ed., 2015.

[30] P. Sedivy, T. Dusilova, M. Hajek, M. Burian, M. Krššák, and M. Dezortova, "In vitro 31P MR chemical shifts of in vivo-detectable metabolites at 3T as a basis set for a pilot evaluation of skeletal muscle and liver 31P spectra with LCModel software," *Molecules*, vol. 26, no. 24, p. 7571, 2021.

[31] W. I. Jung, A. Staubert, S. Widmaier, T. Hoess, M. Bunse, F. van Erckelens, G. Dietze, and O. Lutz, "Phosphorus J-coupling constants of ATP in human brain," *Magnetic Resonance in Medicine*, vol. 37, no. 5, pp. 802–804, 1997.

[32] L. van den Wildenberg, A. Gursan, L. W. F. Seelen, T. A. van der Velden, M. W. J. M. Gosselink, M. Froeling, W. J. M. van der Kemp, D. W. J. Klomp, and J. J. Prompers, "In vivo phosphorus magnetic resonance spectroscopic imaging of the whole human liver at 7 T using a phosphorus whole-body transmit coil and 16-channel receive array: Repeatability and effects of principal component analysis-based denoising," *NMR in Biomedicine*, vol. 36, no. 5, p. e4877, 2023.

[33] J. Szendroedi, M. Chmelik, A. I. Schmid, P. Nowotny, A. Brehm, M. Krssak, E. Moser, and M. Roden, "Abnormal hepatic energy homeostasis in type 2 diabetes," *Hepatology*, vol. 50, no. 4, pp. 1079–1086, 2009.

[34] Y. Kupriyanova, O. P. Zaharia, P. Bobrov, Y. Karusheva, V. Burkart, J. Szendroedi, J.-H. Hwang, and M. Roden, "Early changes in hepatic energy metabolism and lipid content in recent-onset type 1 and 2 diabetes mellitus," *Journal of Hepatology*, vol. 74, no. 5, pp. 1028–1037, 2021.

[35] A. I. Schmid, J. Szendroedi, M. Chmelik, M. Krssák, E. Moser, and M. Roden, "Liver ATP synthesis is lower and relates to insulin sensitivity in patients with type 2 diabetes," *Diabetes Care*, vol. 34, no. 2, pp. 448–453, 2011.

[36] A. Shaka, J. Keeler, and R. Freeman, "Evaluation of a new broadband decoupling sequence: WALTZ-16," *Journal of Magnetic Resonance*, vol. 53, no. 2, pp. 313–340, 1983.

[37] T. C. Ford and D. P. Crewther, "A comprehensive review of the 1H-MRS metabolite spectrum in autism spectrum disorder," *Frontiers in Molecular Neuroscience.*, vol. 9, no. 9, p. 14, 2016.

[38] J. Pfeuffer, I. Tkác, S. W. Provencher, and R. Gruetter, "Toward an in vivo neurochemical profile: Quantification of 18 metabolites in short-echo-time 1H NMR spectra of the rat brain," *Journal of Magnetic Resonance*, vol. 141, no. 1, pp. 104–120, 1999.

[39] H. Günther, *NMR Spectroscopy: Basic Principles, Concepts, and Applications in Chemistry*. Weinheim: Wiley-VCH, 3rd ed., 2013.

[40] L. Schröder and C. Faber, *In vivo NMR Imaging: Methods and Protocols*, vol. 771. Totowa, NY: Humana Press, 2011.

[41] P. A. Bottomley, "Selective volume method for performing localized NMR spectroscopy, patent US4480228A," 1984.

[42] J. Frahm, H. Bruhn, M. L. Gyngell, K. D. Merboldt, W. Hänicke, and R. Sauter, "Localized high-resolution proton NMR spectroscopy using stimulated echoes: Initial applications to human brain in vivo," *Magnetic Resonance in Medicine*, vol. 9, no. 1, pp. 79–93, 1989.

[43] R. Ordidge, A. Connelly, and J. Lohman, "Image-selected in vivo spectroscopy (ISIS). A new technique for spatially selective NMR spectroscopy," *Journal of Magnetic Resonance*, vol. 66, no. 2, pp. 283–294, 1986.

[44] K. V. R. Chary and G. Govil, *NMR in Biological Systems: From Molecules to Humans*, vol. 6. Dordrecht: Springer, 2008.

[45] I. J. Cox, D. K. Menon, J. Sargentoni, D. J. Bryant, A. G. Collins, G. A. Coutts, R. A. Iles, J. D. Bell, I. S. Benjamin, and S. Gilbey, "Phosphorus-31 magnetic resonance spectroscopy of the human liver using chemical shift imaging techniques," *Journal of Hepatology*, vol. 14, no. 2-3, pp. 265–275, 1992.

[46] R. M. Dixon, P. W. Angus, B. Rajagopalan, and G. K. Radda, "Abnormal phosphomonoester signals in 31P MR spectra from patients with hepatic lymphoma. A possible marker of liver infiltration and response to chemotherapy," *British Journal of Cancer*, vol. 63, no. 6, pp. 953–958, 1991.

[47] D. K. Menon, J. Sargentoni, S. D. Taylor-Robinson, J. D. Bell, I. J. Cox, D. J. Bryant, G. A. Coults, K. Rolles, A. K. Burroughs, and M. Y. Margan, "Effect of functional grade and etiology on in vivo hepatic phosphorus-31 magnetic resonance spectroscopy in cirrhosis: Biochemical basis of spectral appearances," *Hepatology*, vol. 21, no. 2, pp. 417–427, 1995.

[48] R. D. Oberhaensli, G. J. Galloway, D. Hilton-Jones, P. J. Bore, P. Styles, B. Rajagopalan, D. J. Taylor, and G. K. Radda, "The study of human organs by phosphorus-31 topical magnetic resonance spectroscopy," *British Journal of Radiology*, vol. 60, no. 712, pp. 367–373, 1987.

[49] A. Hakkarainen, J. Lundbom, E. K. Tuominen, M.-R. Taskinen, K. H. Pietiläinen, and N. Lundbom, "Measuring short-term liver metabolism non-invasively: Postprandial and post-exercise ^{1}H and ^{31}P MR spectroscopy," *Magnetic Resonance Materials in Physics, Biology and Medicine*, vol. 28, no. 1, pp. 57–66, 2015.

[50] T. Munakata, R. D. Griffiths, P. A. Martin, S. A. Jenkins, R. Shields, and R. H. Edwards, "An in vivo 31P MRS study of patients with liver cirrhosis: Progress towards a non-invasive assessment of disease severity," *NMR in Biomedicine*, vol. 6, no. 2, pp. 168–172, 1993.

[51] A. I. Schmid, M. Chmelík, J. Szendroedi, M. Krssák, A. Brehm, E. Moser, and M. Roden, "Quantitative ATP synthesis in human liver measured by localized 31P spectroscopy

using the magnetization transfer experiment," *NMR in Biomedicine*, vol. 21, no. 5, pp. 437–443, 2008.

[52] T. Buehler, R. Kreis, and C. Boesch, "Comparison of 31P saturation and inversion magnetization transfer in human liver and skeletal muscle using a clinical MR system and surface coils," *NMR in Biomedicine*, vol. 28, no. 2, pp. 188–199, 2015.

[53] P. E. Sijens, P. C. Dagnelie, S. Halfwerk, P. van Dijk, K. Wicklow, and M. Oudkerk, "Understanding the discrepancies between 31P MR spectroscopy assessed liver metabolite concentrations from different institutions," *Magnetic Resonance Imaging*, vol. 16, no. 2, pp. 205–211, 1998.

[54] L. A. B. Purvis, W. T. Clarke, L. Valkovič, C. Levick, M. Pavlides, E. Barnes, J. F. Cobbold, M. D. Robson, and C. T. Rodgers, "Phosphodiester content measured in human liver by in vivo 31P MR spectroscopy at 7 tesla," *Magnetic Resonance in Medicine*, vol. 78, no. 6, pp. 2095–2105, 2017.

[55] E. Hultman, L. H. Nilsson, and K. Sahlin, "Adenine nucleotide content of human liver. Normal values and fructose-induced depletion," *Scandinavian Journal of Clinical and Laboratory Investigation*, vol. 35, no. 3, pp. 245–251, 1975.

[56] D. J. Meyerhoff, M. D. Boska, A. M. Thomas, and M. W. Weiner, "Alcoholic liver disease: Quantitative image-guided P-31 MR spectroscopy," *Radiology*, vol. 173, no. 2, pp. 393–400, 1989.

[57] D. J. Meyerhoff, G. S. Karczmar, G. B. Matson, M. D. Boska, and M. W. Weiner, "Noninvasive quantitation of human liver metabolites using image-guided 31P magnetic resonance spectroscopy," *NMR in Biomedicine*, vol. 3, no. 1, pp. 17–22, 1990.

[58] R. Buchli, D. Meier, E. Martin, and P. Boesiger, "Assessment of absolute metabolite concentrations in human tissue by 31P MRS in vivo. Part II: Muscle, liver, kidney," *Magnetic Resonance in Medicine*, vol. 32, no. 4, pp. 453–458, 1994.

[59] M. Chmelík, A. I. Schmid, S. Gruber, J. Szendroedi, M. Krssák, S. Trattnig, E. Moser, and M. Roden, "Three-dimensional high-resolution magnetic resonance spectroscopic imaging for absolute quantification of 31P metabolites in human liver," *Magnetic Resonance in Medicine*, vol. 60, no. 4, pp. 796–802, 2008.

[60] L. Pfleger, M. Gajdošík, P. Wolf, S. Smajis, P. Fellinger, A. Kuehne, P. Krumpolec, S. Trattnig, Y. Winhofer, M. Krebs, M. Kršš ák, and M. Chmelík, "Absolute quantification of phosphor-containing metabolites in the liver using 31P MRSI and hepatic lipid volume correction at 7T suggests no dependence on body mass index or age," *Journal of Magnetic Resonance Imaging*, vol. 49, no. 2, pp. 597–607, 2019.

[61] A. Laufs, R. Livingstone, B. Nowotny, P. Nowotny, F. Wickrath, G. Giani, J. Bunke, M. Roden, and J.-H. Hwang, "Quantitative liver 31P magnetic resonance spectroscopy at 3T on a clinical scanner," *Magnetic Resonance in Medicine*, vol. 71, no. 5, pp. 1670–1675, 2014.

[62] M. Jonuscheit, S. Wierichs, M. Rothe, B. Korzekwa, J. Mevenkamp, P. Bobrov, Y. Kupriyanova, M. Roden, and V. B. Schrauwen-Hinderling, "Reproducibility of absolute quantification of adenosine triphosphate and inorganic phosphate in the liver with

localized 31P–magnetic resonance spectroscopy at 3–T using different coils," *NMR in Biomedicine*, vol. 37, no. 8, p. e5120, 2024.

[63] C. Chen, M. C. Stephenson, A. Peters, P. G. Morris, S. T. Francis, and P. A. Gowland, "31P magnetization transfer magnetic resonance spectroscopy: Assessing the activation induced change in cerebral ATP metabolic rates at 3 T," *Magnetic Resonance in Medicine*, vol. 79, no. 1, pp. 22–30, 2018.

[64] E. J. Fear, F. H. Torkelsen, E. Zamboni, K.-J. Chen, M. Scott, G. Jeffery, H. Baseler, and A. J. Kennerley, "Use of 31P magnetisation transfer magnetic resonance spectroscopy to measure ATP changes after 670 nm transcranial photobiomodulation in older adults," *Aging Cell*, vol. 22, no. 11, p. e14005, 2023.

[65] H. Lei, K. Ugurbil, and W. Chen, "Measurement of unidirectional Pi to ATP flux in human visual cortex at 7 T by using in vivo 31P magnetic resonance spectroscopy," *Proceedings of the National Academy of Sciences of the United States of America*, vol. 100, no. 24, pp. 14409–14414, 2003.

[66] J. Ren, A. D. Sherry, and C. R. Malloy, "31P-MRS of healthy human brain: ATP synthesis, metabolite concentrations, pH, and T1 relaxation times," *NMR in Biomedicine*, vol. 28, no. 11, pp. 1455–1462, 2015.

[67] X.-H. Zhu, H. Qiao, F. Du, Q. Xiong, X. Liu, X. Zhang, K. Ugurbil, and W. Chen, "Quantitative imaging of energy expenditure in human brain," *NeuroImage*, vol. 60, no. 4, pp. 2107–2117, 2012.

[68] W. T. Clarke, M. D. Robson, S. Neubauer, and C. T. Rodgers, "Creatine kinase rate constant in the human heart measured with 3D-localization at 7 Tesla," *Magnetic Resonance in Medicine*, vol. 78, no. 1, pp. 20–32, 2017.

[69] W. T. Clarke, M. A. Peterzan, J. J. Rayner, R. A. Sayeed, M. Petrou, G. Krasopoulos, H. A. Lake, B. Raman, W. D. Watson, P. Cox, M. J. Hundertmark, A. P. Apps, C. A. Lygate, S. Neubauer, O. J. Rider, and C. T. Rodgers, "Localized rest and stress human cardiac creatine kinase reaction kinetics at 3 T," *NMR in Biomedicine*, vol. 32, no. 6, p. e4085, 2019.

[70] P. A. Bottomley and C. J. Hardy, "Mapping creatine kinase reaction rates in human brain and heart with 4 tesla saturation transfer 31P NMR," *Journal of Magnetic Resonance*, vol. 99, no. 2, pp. 443–448, 1992.

[71] P. A. Bottomley, R. Ouwerkerk, R. F. Lee, and R. G. Weiss, "Four-angle saturation transfer (FAST) method for measuring creatine kinase reaction rates in vivo," *Magnetic Resonance in Medicine*, vol. 47, no. 5, pp. 850–863, 2002.

[72] R. G. Weiss, G. Gerstenblith, and P. A. Bottomley, "ATP flux through creatine kinase in the normal, stressed, and failing human heart," *Proceedings of the National Academy of Sciences of the United States of America*, vol. 102, no. 3, pp. 808–813, 2005.

[73] P. Fellinger, P. Wolf, L. Pfleger, P. Krumpolec, M. Krssak, K. Klavins, S. Wolfsberger, A. Micko, P. Carey, B. Gürtl, G. Vila, W. Raber, C. Fürnsinn, T. Scherer, S. Trattnig,

A. Kautzky-Willer, M. Krebs, and Y. Winhofer, "Increased ATP synthesis might counteract hepatic lipid accumulation in acromegaly," *JCI Insight*, vol. 5, no. 5, p. e134638, 2020.

[74] S. Traussnigg, C. Kienbacher, M. Gajdošík, L. Valkovič, E. Halilbasic, J. Stift, C. Rechling, H. Hofer, P. Steindl-Munda, P. Ferenci, F. Wrba, S. Trattnig, M. Kršš̌ák, and M. Trauner, "Ultra-high-field magnetic resonance spectroscopy in non-alcoholic fatty liver disease: Novel mechanistic and diagnostic insights of energy metabolism in non-alcoholic steatohepatitis and advanced fibrosis," *Liver International*, vol. 37, no. 10, pp. 1544–1553, 2017.

[75] L. Valkovič, W. Bogner, M. Gajdošík, M. Považan, I. J. Kukurová, M. Kršš̌ák, S. Gruber, I. Frollo, S. Trattnig, and M. Chmelík, "One-dimensional image-selected in vivo spectroscopy localized phosphorus saturation transfer at 7T," *Magnetic Resonance in Medicine*, vol. 72, no. 6, pp. 1509–1515, 2014.

[76] L. Valkovič, M. Gajdošík, S. Traussnigg, P. Wolf, M. Chmelík, C. Kienbacher, W. Bogner, M. Krebs, M. Trauner, S. Trattnig, and M. Kršš̌ák, "Application of localized ^{31}P MRS saturation transfer at 7 T for measurement of ATP metabolism in the liver: Reproducibility and initial clinical application in patients with non-alcoholic fatty liver disease," *European Radiology*, vol. 24, no. 7, pp. 1602–1609, 2014.

[77] D. E. Befroy, D. L. Rothman, K. F. Petersen, and G. I. Shulman, "31P-magnetization transfer magnetic resonance spectroscopy measurements of in vivo metabolism," *Diabetes*, vol. 61, no. 11, pp. 2669–2678, 2012.

[78] A. Brehm, M. Krssak, A. I. Schmid, P. Nowotny, W. Waldhäusl, and M. Roden, "Increased lipid availability impairs insulin-stimulated ATP synthesis in human skeletal muscle," *Brazilian Archives of Biology and Technology*, vol. 55, no. 1, pp. 136–140, 2006.

[79] E. L. Lim, K. G. Hollingsworth, P. E. Thelwall, and R. Taylor, "Measuring the acute effect of insulin infusion on ATP turnover rate in human skeletal muscle using phosphorus-31 magnetic resonance saturation transfer spectroscopy," *NMR in Biomedicine*, vol. 23, no. 8, pp. 952–957, 2010.

[80] M. Meyerspeer, S. Robinson, C. I. Nabuurs, T. Scheenen, A. Schoisengeier, E. Unger, G. J. Kemp, and E. Moser, "Comparing localized and nonlocalized dynamic 31P magnetic resonance spectroscopy in exercising muscle at 7 T," *Magnetic Resonance in Medicine*, vol. 68, no. 6, pp. 1713–1723, 2012.

[81] J. Ren, A. D. Sherry, and C. R. Malloy, "A simple approach to evaluate the kinetic rate constant for ATP synthesis in resting human skeletal muscle at 7 T," *NMR in Biomedicine*, vol. 29, no. 9, pp. 1240–1248, 2016.

[82] A. I. Schmid, V. B. Schrauwen-Hinderling, M. Andreas, M. Wolzt, E. Moser, and M. Roden, "Comparison of measuring energy metabolism by different 31P-magnetic resonance spectroscopy techniques in resting, ischemic, and exercising muscle," *Magnetic Resonance in Medicine*, vol. 67, no. 4, pp. 898–905, 2012.

[83] J. Szendroedi, E. Zwettler, A. I. Schmid, M. Chmelik, G. Pacini, G. Kacerovsky, G. Smekal, P. Nowotny, O. Wagner, C. Schnack, G. Schernthaner, K. Klaushofer, and M. Roden, "Re-

duced basal ATP synthetic flux of skeletal muscle in patients with previous acromegaly," *PLOS ONE*, vol. 3, no. 12, p. e3958, 2008.

[84] L. Valkovič, M. Chmelík, I. Just Kukurova, M. Krššák, S. Gruber, I. Frollo, S. Trattnig, and W. Bogner, "Time-resolved phosphorous magnetization transfer of the human calf muscle at 3 T and 7 T: A feasibility study," *European Journal of Radiology*, vol. 82, no. 5, pp. 745–751, 2013.

[85] L. Valkovič, B. Ukropcová, M. Chmelík, M. Baláž, W. Bogner, A. I. Schmid, I. Frollo, E. Zemková, I. Klimeš, J. Ukropec, S. Trattnig, and M. Krššák, "Interrelation of 31P-MRS metabolism measurements in resting and exercised quadriceps muscle of overweight-to-obese sedentary individuals," *NMR in Biomedicine*, vol. 26, no. 12, pp. 1714–1722, 2013.

[86] K. F. Petersen, S. Dufour, D. Befroy, R. Garcia, and G. I. Shulman, "Impaired mitochondrial activity and insulin-resistant offspring of patients with type 2 diabetes," *The New England Journal of Medicine*, vol. 350, no. 23, pp. 2419–21; author reply 2419–21, 2004.

[87] E. Baguet and C. Roby, "Off-resonance irradiation effect in steady-state NMR saturation transfer," *Journal of Magnetic Resonance*, vol. 128, no. 2, pp. 149–160, 1997.

[88] R. E. Gabr, R. G. Weiss, and P. A. Bottomley, "Correcting reaction rates measured by saturation-transfer magnetic resonance spectroscopy," *Journal of Magnetic Resonance*, vol. 191, no. 2, pp. 248–258, 2008.

[89] A. Horská and G. S. Spencer, "Correctly accounting for radiofrequency spillover in saturation transfer experiments: Application to measurement of the creatine kinase reaction rate in human forearm muscle," *Magnetic Resonance Materials in Physics, Biology and Medicine*, vol. 5, no. 2, pp. 159–163, 1997.

[90] G. A. Morris and R. Freeman, "Selective excitation in Fourier transform nuclear magnetic resonance," *Journal of Magnetic Resonance*, vol. 29, no. 3, pp. 433–462, 1978.

[91] M. Jonuscheit, B. Korzekwa, M. Schär, J. Mevenkamp, S. Wierichs, P. Bobrov, T. Sarabhai, S. Kahl, M. Roden, and V. B. Schrauwen-Hinderling, "31P-MRS saturation transfer for assessing human hepatic ATP synthesis at clinical field strength," *European Radiology Experimental*, vol. 9, no. 1, p. 51, 2025.

[92] M. Schär, A.-M. M. El-Sharkawy, R. G. Weiss, and P. A. Bottomley, "Triple repetition time saturation transfer (TRiST) 31P spectroscopy for measuring human creatine kinase reaction kinetics," *Magnetic Resonance in Medicine*, vol. 63, no. 6, pp. 1493–1501, 2010.

[93] K. Zilles and B. Tillmann, *Anatomie*. Berlin, Heidelberg: Springer-Verlag Berlin Heidelberg, 2010.

[94] C. Couinaud, "Lobes et segments hépatiques: Notes sur l'architecture anatomiques et chirurgicale du foie," *Presse Médicalele*, vol. 62, no. 33, pp. 702–712, 1954.

[95] R. F. Schmidt and F. Lang, eds., *Physiologie des Menschen: Mit Pathophysiologie*. Berlin, Heidelberg: Springer Medizin Verlag Heidelberg, 30th ed., 2007.

[96] R. Williams, S. Karuranga, B. Malanda, P. Saeedi, A. Basit, S. Besançon, C. Bommer, A. Esteghamati, K. Ogurtsova, P. Zhang, and S. Colagiuri, "Global and regional estimates

and projections of diabetes-related health expenditure: Results from the International Diabetes Federation Diabetes Atlas, 9th edition," *Diabetes Research and Clinical Practice*, vol. 162, p. 108072, 2020.

[97] B. Goffrier, M. Schulz, and J. Bätzing-Feigenbaum, *Administrative Prävalenzen und Inzidenzen des Diabetes mellitus von 2009 bis 2015: Versorgungsatlas-Bericht Nr. 17/03.* Berlin, Germany: Zentralinstitut für die kassenärztliche Versorgung in Deutschland, 2017.

[98] C. Heidemann, Y. Du, R. Paprott, M. Haftenberger, W. Rathmann, and C. Scheidt-Nave, "Temporal changes in the prevalence of diagnosed diabetes, undiagnosed diabetes and prediabetes: Findings from the German Health Interview and Examination Surveys in 1997-1999 and 2008-2011," *Diabetic Medicine*, vol. 33, no. 10, pp. 1406–1414, 2016.

[99] R. Hering, M. Schulz, C. Kohring, M. K. Akmatov, J. Holstiege, and D. Müller, *Administrative Prävalenz und Inzidenz des diagnostizierten Diabetes mellitus Typ 2 – Daten von 2011 bis 2023: Kurzbericht Nr. 24/02.* Berlin, Germany: Zentralinstitut für die kassenärztliche Versorgung in Deutschland, 2024.

[100] World Health Organization, *Diabetes country profile: Germany.* Geneva: WHO, 2025.

[101] World Health Organization, *Classification of diabetes mellitus.* Geneva: WHO, 2019.

[102] M. Battaglia, S. Ahmed, M. S. Anderson, M. A. Atkinson, D. Becker, P. J. Bingley, E. Bosi, T. M. Brusko, L. A. DiMeglio, C. Evans-Molina, S. E. Gitelman, C. J. Greenbaum, P. A. Gottlieb, K. C. Herold, M. J. Hessner, M. Knip, L. Jacobsen, J. P. Krischer, S. A. Long, M. Lundgren, E. F. McKinney, N. G. Morgan, R. A. Oram, T. Pastinen, M. C. Peters, A. Petrelli, X. Qian, M. J. Redondo, B. O. Roep, D. Schatz, D. Skibinski, and M. Peakman, "Introducing the endotype concept to address the challenge of disease heterogeneity in type 1 diabetes," *Diabetes Care*, vol. 43, no. 1, pp. 5–12, 2020.

[103] J. M. Berg, J. L. Tymoczko, and G. J. Gatto, *Stryer Biochemie.* Berlin, Heidelberg, Germany: Springer Spektrum, 8th ed., 2018.

[104] G. J. Kemp, R. E. Ahmad, K. Nicolay, and J. J. Prompers, "Quantification of skeletal muscle mitochondrial function by 31P magnetic resonance spectroscopy techniques: A quantitative review," *Acta Physiologica*, vol. 213, no. 1, pp. 107–144, 2015.

[105] D. M. Dawson and I. H. Fine, "Creatine kinase in human tissues," *Archives of Neurology*, vol. 16, no. 2, pp. 175–180, 1967.

[106] J. Machann, N. Stefan, and F. Schick, "1H MR spectroscopy of skeletal muscle, liver and bone marrow," *European Journal of Radiology*, vol. 67, no. 2, pp. 275–284, 2008.

[107] R. Carvalho-Gontijo, C. Han, L. Zhang, V. Zhang, M. Hosseini, K. Mekeel, B. Schnabl, R. Loomba, M. Karin, D. A. Brenner, and T. Kisseleva, "Metabolic injury of hepatocytes promotes progression of NAFLD and AALD," *Seminars in Liver Disease*, vol. 42, no. 3, pp. 233–249, 2022.

[108] K. Pafili and M. Roden, "Nonalcoholic fatty liver disease (NAFLD) from pathogenesis to treatment concepts in humans," *Molecular Metabolism*, vol. 50, p. 101122, 2021.

[109] A. E. Bohte, J. R. van Werven, S. Bipat, and J. Stoker, "The diagnostic accuracy of US, CT, MRI and 1H-MRS for the evaluation of hepatic steatosis compared with liver biopsy: A meta-analysis," *European Radiology*, vol. 21, no. 1, pp. 87–97, 2011.

[110] A. Tyagi, O. Yeganeh, Y. Levin, J. C. Hooker, G. C. Hamilton, T. Wolfson, A. Gamst, A. K. Zand, E. Heba, R. Loomba, J. Schwimmer, M. S. Middleton, and C. B. Sirlin, "Intra- and inter-examination repeatability of magnetic resonance spectroscopy, magnitude-based MRI, and complex-based MRI for estimation of hepatic proton density fat fraction in overweight and obese children and adults," *Abdominal Imaging*, vol. 40, no. 8, pp. 3070–3077, 2015.

[111] J. H. Runge, P. J. Bakker, I. C. Gaemers, J. Verheij, T. B. M. Hakvoort, R. Ottenhoff, A. J. Nederveen, and J. Stoker, "Measuring liver triglyceride content in mice: Non-invasive magnetic resonance methods as an alternative to histopathology," *Magnetic Resonance Materials in Physics, Biology and Medicine*, vol. 27, no. 4, pp. 317–327, 2014.

[112] H. Kramer, P. J. Pickhardt, M. A. Kliewer, D. Hernando, G.-H. Chen, J. A. Zagzebski, and S. B. Reeder, "Accuracy of liver fat quantification with advanced CT, MRI, and ultrasound techniques: Prospective comparison with MR spectroscopy," *American Journal of Roentgenology*, vol. 208, no. 1, pp. 92–100, 2017.

[113] J.-P. Kühn, D. Hernando, B. Mensel, P. C. Krüger, T. Ittermann, J. Mayerle, N. Hosten, and S. B. Reeder, "Quantitative chemical shift-encoded MRI is an accurate method to quantify hepatic steatosis," *Journal of Magnetic Resonance Imaging*, vol. 39, no. 6, pp. 1494–1501, 2014.

[114] I. S. Idilman, O. Keskin, A. Celik, B. Savas, A. H. Elhan, R. Idilman, and M. Karcaaltincaba, "A comparison of liver fat content as determined by magnetic resonance imaging-proton density fat fraction and MRS versus liver histology in non-alcoholic fatty liver disease," *Acta Radiologica*, vol. 57, no. 3, pp. 271–278, 2016.

[115] P. Peterson, L. Trinh, and S. Månsson, "Quantitative 1H MRI and MRS of fatty acid composition," *Magnetic Resonance in Medicine*, vol. 85, no. 1, pp. 49–67, 2021.

[116] K. H. M. Roumans, L. Lindeboom, P. Veeraiah, C. M. E. Remie, E. Phielix, B. Havekes, Y. M. H. Bruls, M. C. G. J. Brouwers, M. Ståhlman, M. Alssema, H. P. F. Peters, R. de Mutsert, B. Staels, M.-R. Taskinen, J. Borén, P. Schrauwen, and V. B. Schrauwen-Hinderling, "Hepatic saturated fatty acid fraction is associated with de novo lipogenesis and hepatic insulin resistance," *Nature Communications*, vol. 11, no. 1, p. 1891, 2020.

[117] G. Hamilton, T. Yokoo, M. Bydder, I. Cruite, M. E. Schroeder, C. B. Sirlin, and M. S. Middleton, "In vivo characterization of the liver fat ^{1}H MR spectrum," *NMR in Biomedicine*, vol. 24, no. 7, pp. 784–790, 2011.

[118] K. Strobel, J. van den Hoff, and J. Pietzsch, "Localized proton magnetic resonance spectroscopy of lipids in adipose tissue at high spatial resolution in mice in vivo," *Journal of Lipid Research*, vol. 49, no. 2, pp. 473–480, 2008.

[119] S. B. Reeder, I. Cruite, G. Hamilton, and C. B. Sirlin, "Quantitative assessment of liver

fat with magnetic resonance imaging and spectroscopy," *Journal of Magnetic Resonance Imaging*, vol. 34, no. 4, pp. 729–749, 2011.

[120] J. Ren, I. Dimitrov, A. D. Sherry, and C. R. Malloy, "Composition of adipose tissue and marrow fat in humans by 1H NMR at 7 Tesla," *Journal of Lipid Research*, vol. 49, no. 9, pp. 2055–2062, 2008.

[121] L. S. Szczepaniak, P. Nurenberg, D. Leonard, J. D. Browning, J. S. Reingold, S. Grundy, H. H. Hobbs, and R. L. Dobbins, "Magnetic resonance spectroscopy to measure hepatic triglyceride content: Prevalence of hepatic steatosis in the general population," *American Journal of Physiology. Endocrinology and Metabolism*, vol. 288, no. 2, pp. E462–8, 2005.

[122] K. F. Petersen, S. Dufour, F. Li, D. L. Rothman, and G. I. Shulman, "Ethnic and sex differences in hepatic lipid content and related cardiometabolic parameters in lean individuals," *JCI Insight*, vol. 7, no. 7, 2022.

[123] C. W. Li, W. G. Negendank, J. Murphy-Boesch, K. Padavic-Shaller, and T. R. Brown, "Molar quantitation of hepatic metabolites in vivo in proton-decoupled, nuclear Overhauser effect enhanced 31P NMR spectra localized by three-dimensional chemical shift imaging," *NMR in Biomedicine*, vol. 9, no. 4, pp. 141–155, 1996.

[124] K. Sevastianova, A. Hakkarainen, A. Kotronen, A. Cornér, P. Arkkila, J. Arola, J. Westerbacka, R. Bergholm, J. Lundbom, N. Lundbom, and H. Yki-Järvinen, "Nonalcoholic fatty liver disease: Detection of elevated nicotinamide adenine dinucleotide phosphate with in vivo 3.0-T 31P MR spectroscopy with proton decoupling," *Radiology*, vol. 256, no. 2, pp. 466–473, 2010.

[125] A. Bierwagen, P. Begovatz, P. Nowotny, D. Markgraf, B. Nowotny, C. Koliaki, G. Giani, B. Klüppelholz, J. Lundbom, and M. Roden, "Characterization of the peak at 2.06 ppm in 31P magnetic resonance spectroscopy of human liver: Phosphoenolpyruvate or phosphatidylcholine?," *NMR in Biomedicine*, vol. 28, no. 7, pp. 898–905, 2015.

[126] M. Chmelík, L. Valkovič, P. Wolf, W. Bogner, M. Gajdošík, E. Halilbasic, S. Gruber, M. Trauner, M. Krebs, S. Trattnig, and M. Krššák, "Phosphatidylcholine contributes to in vivo 31P MRS signal from the human liver," *European Radiology*, vol. 25, no. 7, pp. 2059–2066, 2015.

[127] L. Pfleger, E. Halilbasic, M. Gajdošík, D. Benčíková, M. Chmelík, T. Scherer, S. Trattnig, M. Krebs, M. Trauner, and M. Krššák, "Concentration of gallbladder phosphatidylcholine in cholangiopathies: A phosphorus-31 magnetic resonance spectroscopy pilot study," *Journal of Magnetic Resonance Imaging*, vol. 55, no. 2, pp. 530–540, 2022.

[128] R. M. de Guia, M. Agerholm, T. S. Nielsen, L. A. Consitt, D. Søgaard, J. W. Helge, S. Larsen, J. Brandauer, J. A. Houmard, and J. T. Treebak, "Aerobic and resistance exercise training reverses age-dependent decline in NAD+ salvage capacity in human skeletal muscle," *Physiological Reports*, vol. 7, no. 12, p. e14139, 2019.

[129] J. Mevenkamp, Y. M. H. Bruls, R. Mancilla, L. Grevendonk, J. E. Wildberger, K. Brouwers, M. K. C. Hesselink, P. Schrauwen, J. Hoeks, R. H. Houtkooper, M. Buitinga, R. A. d.

Graaf, L. Lindeboom, and V. B. Schrauwen-Hinderling, "Development of a 31P magnetic resonance spectroscopy technique to quantify NADH and NAD+ at 3 T," *Nature Communications*, vol. 15, no. 1, p. 9159, 2024.

[130] M. Meyerspeer, C. Boesch, D. Cameron, M. Dezortová, S. C. Forbes, A. Heerschap, J. A. L. Jeneson, H. E. Kan, J. Kent, G. Layec, J. J. Prompers, H. Reyngoudt, A. Sleigh, L. Valkovič, and G. J. Kemp, "31P magnetic resonance spectroscopy in skeletal muscle: Experts' consensus recommendations," *NMR in Biomedicine*, vol. 34, no. 5, p. e4246, 2020.

[131] A. Santos-Díaz and M. D. Noseworthy, "Phosphorus magnetic resonance spectroscopy and imaging (31P-MRS/MRSI) as a window to brain and muscle metabolism: A review of the methods," *Biomedical Signal Processing and Control*, vol. 60, p. 101967, 2020.

[132] A. Bashir, R. Gropler, and J. Ackerman, "Absolute quantification of human liver phosphorus-containing metabolites in vivo using an inhomogeneous spoiling magnetic field gradient," *PLOS ONE*, vol. 10, no. 12, p. e0143239, 2015.

[133] I. R. Corbin, L. N. Ryner, H. Singh, and G. Y. Minuk, "Quantitative hepatic phosphorus-31 magnetic resonance spectroscopy in compensated and decompensated cirrhosis," *American Journal of Physiology. Gastrointestinal and Liver Physiology*, vol. 287, no. 2, pp. G379–84, 2004.

[134] L. A. B. Purvis, L. Valkovič, M. D. Robson, and C. T. Rodgers, "Feasibility of absolute quantification for 31P MRS at 7 T," *Magnetic Resonance in Medicine*, vol. 82, no. 1, pp. 49–61, 2019.

[135] S. F. Solga, A. Horska, S. Hemker, S. Crawford, C. Diggs, A. M. Diehl, F. L. Brancati, and J. M. Clark, "Hepatic fat and adenosine triphosphate measurement in overweight and obese adults using 1H and 31P magnetic resonance spectroscopy," *Liver International*, vol. 28, no. 5, pp. 675–681, 2008.

[136] D. I. Hoult, C. N. Chen, and V. J. Sank, "Quadrature detection in the laboratory frame," *Magnetic Resonance in Medicine*, vol. 1, no. 3, pp. 339–353, 1984.

[137] A. Naressi, C. Couturier, I. Castang, R. de Beer, and D. Graveron-Demilly, "Java-based graphical user interface for MRUI, a software package for quantitation of in vivo/medical magnetic resonance spectroscopy signals," *Computers in Biology and Medicine*, vol. 31, no. 4, pp. 269–286, 2001.

[138] D. Stefan, F. Di Cesare, A. Andrasescu, E. Popa, A. Lazariev, E. Vescovo, O. Strbak, S. Williams, Z. Starcuk, M. Cabanas, D. van Ormondt, and D. Graveron-Demilly, "Quantitation of magnetic resonance spectroscopy signals: The jMRUI software package," *Measurement Science and Technology*, vol. 20, no. 10, p. 104035, 2009.

[139] Š. Mierisová, A. van den Boogaart, I. Tkáč, P. van Hecke, L. Vanhamme, and T. Liptaj, "New approach for quantitation of short echo time in vivo 1H MR spectra of brain using AMARES," *NMR in Biomedicine*, vol. 11, no. 1, pp. 32–39, 1998.

[140] L. Vanhamme, A. van den Boogaart, and S. van Huffel, "Improved method for accurate and efficient quantification of MRS data with use of prior knowledge," *Journal of Magnetic Resonance*, vol. 129, no. 1, pp. 35–43, 1997.

[141] S. W. Provencher, "Estimation of metabolite concentrations from localized in vivo proton NMR spectra," *Magnetic Resonance in Medicine*, vol. 30, no. 6, pp. 672–679, 1993.

[142] P. Wolf, P. Fellinger, L. Pfleger, S. Smajis, H. Beiglböck, M. Gajdošík, C.-H. Anderwald, S. Trattnig, A. Luger, Y. Winhofer, M. Krššák, and M. Krebs, "Reduced hepatocellular lipid accumulation and energy metabolism in patients with long standing type 1 diabetes mellitus," *Scientific Reports*, vol. 9, no. 1, p. 2576, 2019.

[143] G. J. Kemp, "The interpretation of abnormal 31P magnetic resonance saturation transfer measurements of Pi/ATP exchange in insulin-resistant skeletal muscle," *American Journal of Physiology. Endocrinology and Metabolism*, vol. 294, no. 3, pp. E640–2; author reply E643–4, 2008.

[144] R. S. Balaban and A. P. Koretsky, "Interpretation of ^{31}P NMR saturation transfer experiments: What you can't see might confuse you. Focus on "Standard magnetic resonance-based measurements of the Pi→ATP rate do not index the rate of oxidative phosphorylation in cardiac and skeletal muscles"," *American Journal of Physiology. Cell Physiology.*, vol. 301, no. 1, pp. C12–5, 2011.

[145] A. E. Hansen, H. Gutte, P. Holst, H. H. Johannesen, S. Rahbek, A. E. Clemmensen, M. M. E. Larsen, C. Schøier, J. Ardenkjaer-Larsen, T. L. Klausen, A. T. Kristensen, and A. Kjaer, "Combined hyperpolarized 13C-pyruvate MRS and 18F-FDG PET (hyperPET) estimates of glycolysis in canine cancer patients," *European Journal of Radiology*, vol. 103, pp. 6–12, 2018.

[146] M. K. Curtis, J. J. McGing, B. J. Stubbs, V. Ball, L. E. Cochlin, D. P. O'Neill, C. Laustsen, M. A. Cole, P. A. Robbins, D. J. Tyler, and J. J. Miller, "Hyperpolarized 13C-MRS can quantify lactate production and oxidative PDH flux in murine skeletal muscle during exercise," *NMR in Biomedicine*, vol. 38, no. 5, p. e70020, 2025.

[147] J. Szendroedi, A. Saxena, K. S. Weber, K. Strassburger, C. Herder, V. Burkart, B. Nowotny, A. Icks, O. Kuss, D. Ziegler, H. Al-Hasani, K. Müssig, and M. Roden, "Cohort profile: The German Diabetes Study (GDS)," *Cardiovascular Diabetology*, vol. 15, p. 59, 2016.

[148] S. A. Harrison, P. Bedossa, C. D. Guy, J. M. Schattenberg, R. Loomba, R. Taub, D. Labriola, S. E. Moussa, G. W. Neff, M. E. Rinella, Q. M. Anstee, M. F. Abdelmalek, Z. Younossi, S. J. Baum, S. Francque, M. R. Charlton, P. N. Newsome, N. Lanthier, I. Schiefke, A. Mangia, J. M. Pericàs, R. Patil, A. J. Sanyal, M. Noureddin, M. B. Bansal, N. Alkhouri, L. Castera, M. Rudraraju, and V. Ratziu, "A phase 3, randomized, controlled trial of resmetirom in NASH with liver fibrosis," *The New England Journal of Medicine*, vol. 390, no. 6, pp. 497–509, 2024.

[149] J. Machann, C. Thamer, B. Schnoedt, N. Stefan, H.-U. Haring, C. D. Claussen, A. Fritsche, and F. Schick, "Hepatic lipid accumulation in healthy subjects: A comparative study using spectral fat-selective MRI and volume-localized 1H-MR spectroscopy," *Magnetic Resonance in Medicine*, vol. 55, no. 4, pp. 913–917, 2006.

[150] A. J. M. Lewis, J. J. J. Miller, C. McCallum, O. J. Rider, S. Neubauer, L. C. Heather, and

D. J. Tyler, “Assessment of metformin-induced changes in cardiac and hepatic redox state using hyperpolarized 1-13C pyruvate,” *Diabetes*, vol. 65, no. 12, pp. 3544–3551, 2016.

Nomenclature

13C	Carbon-13
1H	Hydrogen-1
23Na	Sodium-23
31P	Phosphorus-31
Acetyl-CoA	Acetyl coenzyme A
ADA	American Diabetes Association
AFP	Adiabatic full passage
AHP	Adiabatic half passage
AMARES	Advanced Method for Accurate, Robust and Efficient Spectral fitting
ATP	Adenosine triphosphate
BMI	Body mass index
BW	Bandwidth
CI	Confidence interval
CK	Creatine kinase
Cr	Creatine
CRLB	Cramer-Rao lower bound
CSD	Chemical shift displacement
CT	Computer tomography
CV	Coefficient of variation
DANTE	Delays Alternating with Nutations for Tailored Excitation
ETC	Electron transport chain
FA	Flip angle

FID	Free induction decay
FOV	Field of view
FT	Fourier transformation
GDS	German Diabetes Study
GLP-1	Glucagon-like peptide-1
GPC	Glycero-phosphocholine
GPE	Glycero-phosphoethanolamine
HbA1c	Hemoglobin A1c
HCC	Hepatocellular carcinoma
HEP	High-energy phosphate
HF	High-frequency
HL	Hepatic lipid
HS	Hyperbolic secant
IDF	International Diabetes Federation
IR	Inversion recovery
ISIS	Image-Selected In vivo Spectroscopy
jMRUI	Java magnetic resonance user interface
MASH	Metabolic dysfunction-associated steatohepatitis
MASLD	Metabolic dysfunction-associated steatotic liver disease
MODY	Maturity-onset diabetes of the young
MR	Magnetic resonance
MRI	Magnetic resonance imaging
MRS	Magnetic resonance spectroscopy
MT	Magnetization transfer
MUFA	Monounsaturated fatty acid
MVS	Multi-voxel localized spectroscopy
NAD	Nicotinamide adenine dinucleotide

NLS	Non-localized spectroscopy
NMR	Nuclear magnetic resonance
NOE	Nuclear Overhauser effect
NSA	Number of signal averages
OGTT	Oral glucose tolerance test
PC	Phosphocholine
PCr	Phosphocreatine
PDE	Phosphodiesters
PE	Phosphoethanolamine
PEP	Phosphoenolpyruvate
Pi	Inorganic phosphate
PME	Phosphomonoesters
PPM	Parts per million
PRESS	Point RESolved Spectroscopy
PtdC	Phosphatidylcholine
PUFA	Polyunsaturated fatty acid
RF	Radio frequency
SD	Standard deviation
SFA	Saturated fatty acid
SIRD	Severe insulin-resistant diabetes
SNR	Signal-to-noise ratio
ST	Saturation transfer
STEAM	STimulated Echo Acqisition Mode
SVS	Single-voxel localized spectroscopy
T1D	Type 1 diabetes
T2D	Type 2 diabetes
TCA cycle	Tricarboxylic acid cycle

TE	Echo time
TG	Triglyceride
TMS	Tetramethylsilane
TR	Repetition time
UDPG	Uridine diphosphate glucose
UHF	Ultrahigh field
US	Ultrasound
VOI	Voxel of interest
WALTZ	Wideband Alternating-phase Low-power Techniqe for Zero-residual splitting
WHO	World Health Organization

Reproducibility of absolute quantification of ATP and P_i in the liver with localized ^{31}P-MRS at 3T using different coils

Marc Jonuscheit[1,2], Stefan Wierichs[1,2], Maik Rothe[1,2,3], Benedict Korzekwa[1,2], Julian Mevenkamp[4], Pavel Bobrov[2,5], Yuliya Kupriyanova[1,2], Michael Roden[6,1,2] and Vera B. Schrauwen-Hinderling[1,2,4]

Supplementary material

Table of contents

1. **Supplementary Table S1. MRS in MRS checklist.**
2. **Supplementary Figure S1. Results of the in vitro excitation pulse offset correction for the A) single loop and B) quadrature coil.**
3. **Supplementary Table S2. Starting values and prior knowledge for the AMARES algorithm in jMRUI for peak fitting of ^{31}P-metabolites in the human liver.**
4. **Supplementary Table S3. Analytical results using a repeated measures ANCOVA for GLMM adjusted for both coil and visit for the metabolites GPC and GPE of the single loop and quadrature coil day-to-day reproducibility study (three visits).**
5. **Supplementary Table S4. Analytical results using a repeated measures ANCOVA for GLMM adjusted for both coil and visit for the metabolites PC and PE of the single loop and quadrature coil day-to-day reproducibility study (three visits).**
6. **Supplementary Table S5. Estimated CVs and absolute concentrations of GPC, GPE, PC and PE of the day-to-day and intra-day reproducibility studies of the ^{31}P-MRS method including both coils.**
7. **Supplementary Figure S2. Individual results of the day-to-day (three visits) reproducibility study for the six prominent metabolites γ-ATP, P_i, GPC, GPE, PC and PE.**

Supplementary Table S1. MRS in MRS checklist.

German Diabetes Center Düsseldorf	^{31}P MRS
1. Hardware	
a. Field strength [T]	3T
b. Manufacturer	Philips, Best, the Netherlands
c. Model (software version if available)	Achieva 3T dStream, R5.6
d. RF coils: nuclei (transmit/ receive), number of channels, type, body part	1. ^{31}P flat circular single loop surface coil 14 cm dia., transmit & receive PhilipsP140 2. ^{31}P curved quadrature surface coil, total loop size 220 x 160 mm^2, transmit & receive, Rapid Biomedical
e. Additional hardware	-
2. Acquisition	
a. Pulse sequence	Image Selected In Vivo Spectroscopy (ISIS), vendor supplied
b. Volume of Interest (VOI) locations	Lateral side of liver
c. Nominal VOI size [mm^3]	60 x 60 x 60 mm^3
d. Repetition Time (TR), Echo Time (TE) [ms]	TR 6000 ms, TE 0.096 ms
e. Total number of Excitations or acquisitions per spectrum	NSA 128
f. Additional sequence parameters (spectral width in Hz, number of spectral points, frequency offsets)	Bandwith 3000 Hz Datapoints 2048 Broadband decoupling (WALTZ-4, B_1 ampl. 7 µT) Continuous wave NOE with mixing time 3500 ms, B_1 ampl. 0.5 µT Excitation pulse center was set to -1.0 ppm (between γ-ATP and P_i) Chemical shift displacement: γ-ATP ↔ Pi = ~7.7 ppm → ~6.7 mm
g. Water Suppression Method	-
h. Shimming Method, reference peak, and thresholds for "acceptance of shim" chosen	Vendor second order pencil beam VOI (shim size 60 x 60 x 60 mm^3) System reported FWHM between 20 and 45 Hz
i. Triggering or motion correction method	-
3. Data analysis methods and outputs	
a. Analysis software	jMRUI
b. Processing steps deviating from quoted reference or product	Apodization (15 Hz), frequency adjustment to γ-ATP = -2.48 ppm, zero order phasing
c. Output measure (e.g. absolute concentration, institutional units, ratio)Processing steps deviating from quoted reference or product	Absolute units (millimolar [mM]) Correction for T_1, individual metabolite frequency offset, coil loading and distance in all three dimensions

d. Quantification references and assumptions, fitting model assumptions	AMARES in jMRUI, custom created prior knowledge (Gaussian line shapes, estimated amplitudes, fixed relative phases, individual line width and chemical frequencies kept in soft constraints, see Supplementary Table S2)
4. Data Quality	
a. Reported variables (SNR, Linewidth (with reference peaks))	Good quality data: SNR (γ-ATP and P_i) Potential signal contamination from abdominal muscle: PCr/γ-ATP peak ratio
b. Data exclusion criteria	SNR of γ-ATP and P_i: SNR: γ-ATP < 4 SNR: P_i < 2.5 Potential signal contamination from abdominal muscle: PCr/γ-ATP > 0.5 Spectra were excluded for distances between coil and center of ISIS voxel > 9.5 cm for the single loop and > 13.5 cm for the quadrature coil
c. Quality measures of postprocessing Model fitting (e.g. CRLB, goodness of fit, SD of residual)	-
d. Sample Spectrum	Figure 5

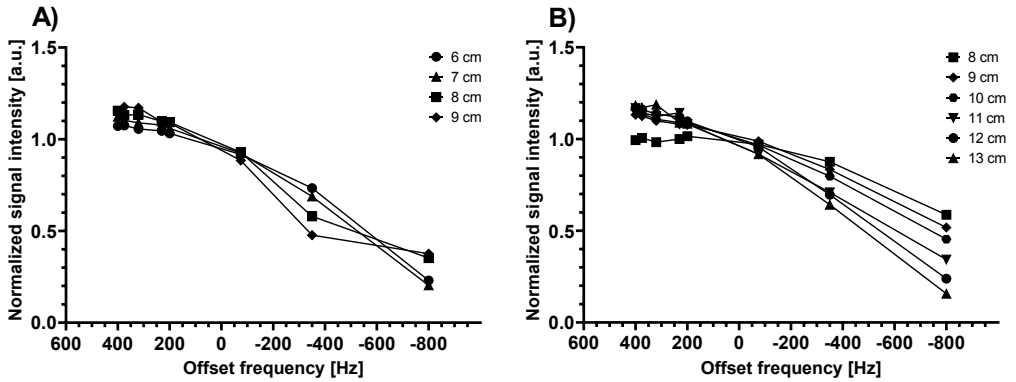

Supplementary Figure S1. Results of the in vitro excitation pulse offset correction for the A) single loop and B) quadrature coil. In each of the acquired distances between coil and VOI, 8 different frequency offsets corresponding to the position of the most prominent ^{31}P-metabolites (PE, PC, P_i, GPE, GPC, γ-ATP, α-ATP, β-ATP) in regard to the center of the excitation pulse offset (0 Hz) of the HS AHP pulse in vivo were set in order to be able to correct for the pulse profile. All signals were normalized to the respective zero offset frequency.

Supplementary Table S2. Starting values and prior knowledge for the AMARES algorithm in jMRUI for peak fitting of ^{31}P-metabolites in the human liver. A custom created prior knowledge file ensured that all resonances were fitted together with 'estimated' amplitudes and Gaussian line shapes, whereas all relative phases were fixed to zero and individual line widths as well as chemical frequencies were fitted with soft constraints.

Metabolite	Abbreviation	Chemical shift [ppm]	Soft constraints for peak fitting	
			Line width [Hz]	Frequency [ppm]
Phosphoethanolamine	PE	6.82	Estimated	6.8 – 7.4
Phosphocholine	PC	6.35	1 x PE	6.1 – 6.6
Inorganic phosphate	Pi	5.18	0 – 35	5.0 – 5.4
Glycero-phosphoethanolamine	GPE	3.51	Estimated	3.4 – 3.8
Glycero-phosphocholine	GPC	2.94	1 x GPE	2-7 – 3.1
Phosphoenolpyruvate/Phosphatidylcholine	PEP/PtdC	1.99	1 x GPE	1.7 – 2.2
Phosphocreatine	PCr	0.31	0 – 20	-1.5 – 1.5
γ-adenosine triphosphate	γ-ATP	-2.48	0 – 35	-2.6 – -2.36
α-adenosine triphosphate	α-ATP	-7.61	Estimated	-7.8 – -7.2
Nicotinamide adenine dinucleotide	NADH	-8.24	1 x α-ATP	-8.5 – -8.1
Uridine diphosphate glucose	UDPG	-9.67	1 x α-ATP	-9.7 – -9.3
β-adenosine triphosphate	β-ATP	-16.2	0 – 20	-16.3 – -15.7

Supplementary Table S3. Analytical results using a repeated measures ANCOVA for GLMM adjusted for both coil and visit for the metabolites GPC and GPE of the single loop and quadrature coil day-to-day reproducibility study (three visits). Estimated absolute concentrations of GPC and GPE with 95% CI are listed for each individual coil or visit and their individual differences are shown. Significant differences ($p < 0.05$) are highlighted with a *. SC: Single loop coil, QC: Quadrature coil.

Effect	Concentration mM [95% CI]	
	GPC	GPE
Least squares means		
All spectra of SC coil	2.78 [2.41; 3.16]	3.16 [2.88; 3.44]
All spectra of QC coil	2.70 [2.32; 3.07]	2.93 [2.65; 3.20]
Visit 1 (SC & QC)	2.56 [2.18; 2.95]	3.05 [2.75; 3.34]
Visit 2 (SC & QC)	2.91 [2.52; 3.29]	3.05 [2.75; 3.34]
Visit 3 (SC & QC)	2.76 [2.37; 3.14]	3.04 [2.74; 3.34]
Differences of least squares means		
SC – QC	0.0864 [-0.0857; 0.258]	0.231 [0.00846; 0.454]*
Visit 1 – Visit 2 (SC & QC)	-0.343 [-0.551; -0.135]*	-0.00269 [-0.272; 0.267]
Visit 1 – Visit 3 (SC & QC)	-0.195 [-0.407; 0.0174]	0.00687 [-0.268; 0.282]
Visit 2 – Visit 3 (SC & QC)	0.149 [-0.0634; 0.361]	0.00956 [-0.265; 0.284]

Supplementary Table S4. Analytical results using a repeated measures ANCOVA for GLMM adjusted for both coil and visit for the metabolites PC and PE of the single loop and quadrature coil day-to-day reproducibility study (three visits). Estimated absolute concentrations of PC and PE with 95% CI are listed for each individual coil or visit and their individual differences are shown. SC: Single loop coil, QC: Quadrature coil.

Effect	Concentration mM [95% CI]	
	PC	PE
Least squares means		
All spectra of SC coil	0.91 [0.78; 1.04]	0.97 [0.82; 1.12]
All spectra of QC coil	0.94 [0.82; 1.07]	0.83 [0.68; 0.99]
Visit 1 (SC & QC)	0.94 [0.79; 1.08]	0.92 [0.75; 1.09]
Visit 2 (SC & QC)	0.91 [0.76; 1.05]	0.89 [0.73; 1.06]
Visit 3 (SC & QC)	0.94 [0.79; 1.09]	0.89 [0.72; 1.06]
Differences of least squares means		
SC – QC	-0.0343 [-0.175; 0.106]	0.137 [-0.00265; 0.277]
Visit 1 – Visit 2 (SC & QC)	0.0296 [-0.140; 0.200]	0.0263 [-0.143; 0.195]
Visit 1 – Visit 3 (SC & QC)	-0.00648 [-0.180; 0.167]	0.0262 [-0.146; 0.198]
Visit 2 – Visit 3 (SC & QC)	-0.0361 [-0.209; 0.137]	-0.00013 [-0.172; 0.172]

Supplementary Table S5. Estimated CVs and absolute concentrations of GPC, GPE, PC and PE of the day-to-day and intra-day repeatability & reproducibility studies of the ^{31}P-MRS method including both coils.

	No. volunteers	% CV intra-volunteer ± SD				Concentration mM [mean ± SD]			
		GPC	GPE	PC	PE	GPC	GPE	PC	PE
Single loop coil – three sessions (V1-V3)	8	9.8 ± 10.3	5.9 ± 4.2	19.8 ± 20.1	19.4 ± 26.0	2.76 ± 0.61	3.15 ± 0.31	0.91 ± 0.26	0.96 ± 0.30
Quadrature coil – three sessions (V1-V3)	8	7.5 ± 3.2	5.0 ± 4.2	14.0 ± 9.2	18.5 ± 17.8	2.70 ± 0.52	2.93 ± 0.59	0.94 ± 0.25	0.83 ± 0.26
Quadrature coil – single session without repositioning (M1-M3)	6	7.0 ± 2.0	7.3 ± 2.9	14.2 ± 4.6	13.1 ± 9.4	2.22 ± 0.59	2.60 ± 0.76	0.82 ± 0.17	0.85 ± 0.27
Quadrature coil – single session with different VOI placement (M3-M5)	3	10.4 ± 6.1	13.5 ± 11.0	22.9 ± 10.6	37.4 ± 1.9	2.23 ± 0.29	2.59 ± 0.40	0.69 ± 0.22	0.72 ± 0.25
Quadrature coil – single session with volunteer repositioning (M1,M6,M7)	6	8.2 ± 2.7	6.3 ± 3.3	19.3 ± 11.3	21.1 ± 9.4	2.28 ± 0.53	2.60 ± 0.72	0.82 ± 0.20	0.76 ± 0.28

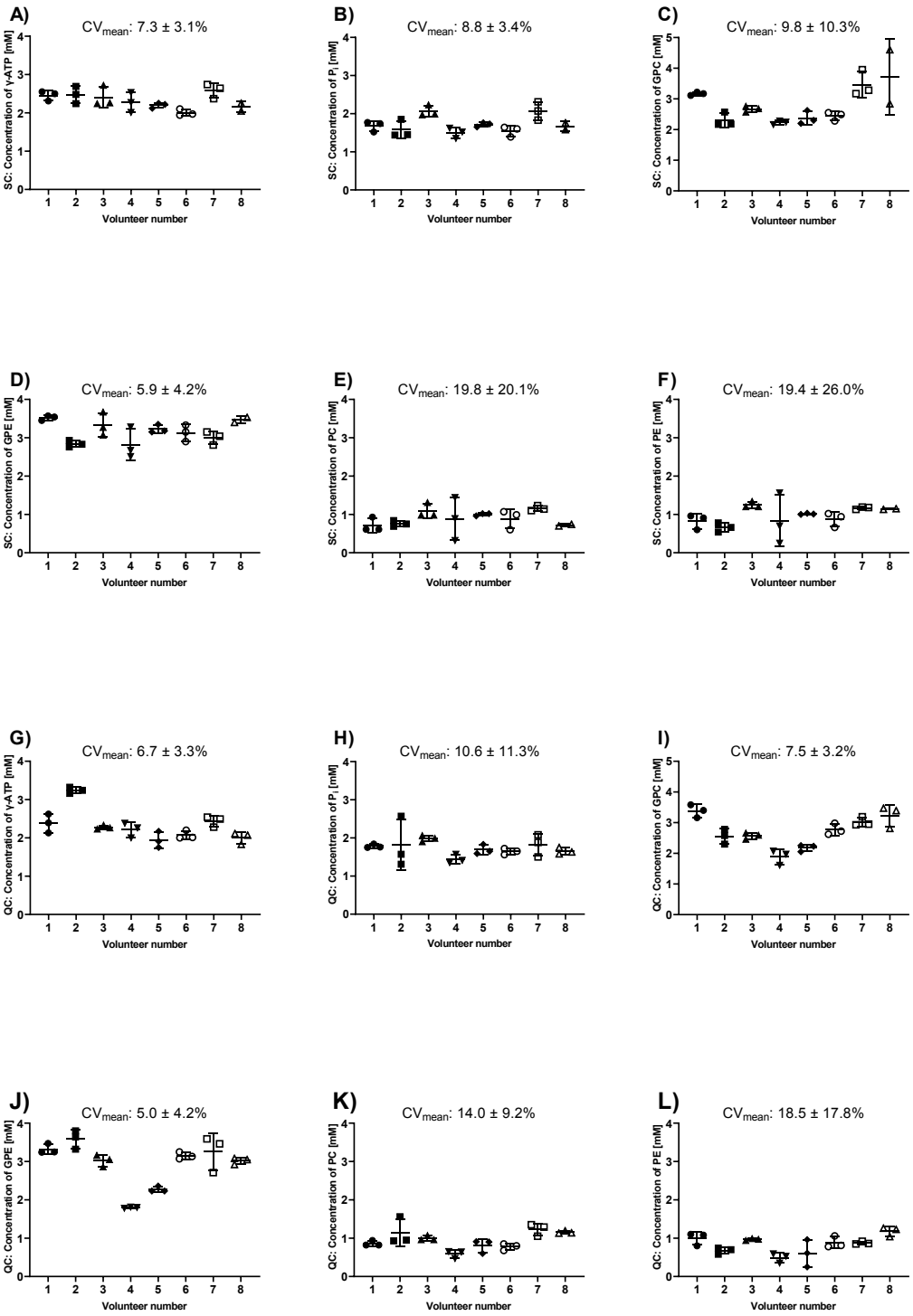
A)
CVmean: 7.3 ± 3.1%
SC: Concentration of γ-ATP [mM]
B)
CVmean: 8.8 ± 3.4%
SC: Concentration of Pi [mM]
C)
CVmean: 9.8 ± 10.3%
SC: Concentration of GPC [mM]
D)
CVmean: 5.9 ± 4.2%
SC: Concentration of GPE [mM]
E)
CVmean: 19.8 ± 20.1%
SC: Concentration of PC [mM]
F)
CVmean: 19.4 ± 26.0%
SC: Concentration of PE [mM]
G)
CVmean: 6.7 ± 3.3%
QC: Concentration of γ-ATP [mM]
H)
CVmean: 10.6 ± 11.3%
QC: Concentration of Pi [mM]
I)
CVmean: 7.5 ± 3.2%
QC: Concentration of GPC [mM]
J)
CVmean: 5.0 ± 4.2%
QC: Concentration of GPE [mM]
K)
CVmean: 14.0 ± 9.2%
QC: Concentration of PC [mM]
L)
CVmean: 18.5 ± 17.8%
QC: Concentration of PE [mM]
Volunteer number

Supplementary Figure S2. Individual results of the day-to-day (three visits) reproducibility study for the six prominent metabolites γ-ATP, P_i, GPC, GPE, PC and PE. A-F) Results of the single loop coil (SC), G-L) results of the quadrature coil (QC). All obtained metabolite concentrations are denoted as a single datapoint. Metabolite concentrations are presented in mM concentrations, quantified by the replacement method using a phantom with known concentration.

^{31}P-MRS saturation transfer for assessing human hepatic ATP synthesis at clinical field strength

ELECTRONIC SUPPLEMENTARY MATERIAL

Eur Radiol Exp (2025) Jonuscheit M, Korzekwa B, Schär M, et al.

Supplemental material S1:

Inclusion and exclusion criteria

Cohort profile: The German Diabetes Study (GDS)

The GDS is an ongoing prospective observational study comprising intensive phenotyping within 12 months after clinical diagnosis, at 5-year intervals for at least 20 years and annual telephone interviews in between. The study is performed according to the Declaration of Helsinki, approved by the ethics committee of the University of Düsseldorf and was registered at Clinicaltrials.gov (Identifier number: NCT01055093). A detailed description can be found in Szendroedi et al [1].

Inclusion criteria

a) Age of 18–69 years
b) Type 1 diabetes mellitus
    a. Diagnosis of T1D, diabetes onset within the last 12 months.
    b. T1D diagnosis based on ketoacidosis or immediate insulin requirement, presence of at least one islet cell directed autoantibody or C- peptide levels below detection limit
c) Healthy volunteers
    a. No diagnosis of diabetes

Exclusion criteria

a) Diabetes due to specific causes (“Type 3”; e.g., pancreoprive diabetes, genetically-induced diabetes)
b) Gestational diabetes, pregnancy
c) Poor glycemic control (HbA1c >9.0 %)
d) Hyperlipidemia (triglycerides and low- density lipoproteins ≥double upper reference limit)
e) Heart failure (New York Heart Association class ≥II)
f) Renal disease (serum creatinine ≥1.6 mg/dL)
g) Clinically relevant Liver disease (aspartate aminotransferase and/or alanine aminotransferase and/or gamma glutamyltransferase ≥double upper reference limit)
h) Peripheral artery occlusive disease stage IV
i) Venous thromboembolic events
j) Anemia or blood donation
k) Participation in a clinical study within the past 3 months

l) Acute infection, increased leukocytes, immunosuppressive therapy, autoimmune diseases, infection with human immunodeficiency virus, other severe diseases (e.g., active cancer disease)
m) Psychiatric disorders
n) Specific exclusion criteria for MRI/S studies
    a. pacemaker
    b. metallic and magnetic implants
    c. claustrophobia

Supplemental material S2:

In vitro & in vivo MR protocols for establishing FRiST

Frequency selective saturation using DANTE pulses

In order to saturate the γ-ATP resonance over its full linewidth in the human liver, the amplitude of the delays alternating with nutations for tailored excitation (DANTE) pulse train is modulated according to the flip angle function $\alpha(k)$ to produce multiple adjacent suppression bands [2, 3]:

$$\alpha(k) = \beta \sum_{n=0}^{m-1} \cos\left(2\pi\left(n - \frac{m-1}{2}\right)k\tau\delta\right)$$

In the above formula k denotes the number of subpulses, m is the number of suppression bands, δ represents the frequency separation in Hz between the individual suppression bands, β denotes the average subpulse flip angle per suppression band and τ represents the repetition time of the subpulses.

Using such short hard pulses allows for a narrow suppression band at a specific frequency. By splitting the applied irradiation into subpulses aliased suppression bands occur in the spectrum at frequency intervals set as the inverse of τ. In order to avoid any potential influence on the peak of interest (P_i), τ = 0.91 ms was chosen to generate aliased suppression bands 1/τ = 1100 Hz apart from the γ-ATP resonance which is far from any ^{31}P-metabolite and especially P_i (frequency offset γ-ATP ↔ P_i = ~400 Hz at 3T).

To find an optimal saturation scheme for successful saturation of the γ-ATP resonance in the liver, first in vitro experiments were performed. For this, a cylindrical 3 liter bottle containing 50 mM dipotassium phosphate (K_2HPO_4) served as phantom and a 2D-ISIS [4] localization sequence was used to test different DANTE pulse train schemes at a depth of 10 cm between coil and center of the voxel of interest (VOI) using a repetition time (TR) of 0.7 s, number of signal averages (NSA) 256, t_{exp} ~3 min. Here, two saturation schemes were tested using m = 5 suppression bands which were δ = 9 Hz apart (M5D9) and m = 3 with δ = 12 Hz (M3D12), respectively. In both experiments the subpulse flip angle β was varied between 0° and 6° in +0.5° steps in order to determine the minimal necessary β to saturate γ-ATP to < 5% of its unsaturated peak intensity. Additionally, the same β flip angle series was repeated with saturation at the mirrored frequency and finally, one spectrum without any saturation was acquired in order to calculate the spillover Q, representing the amount of signal decrease resulting from the presence of the saturation scheme at the respective pulse power. Q was calculated as the ratio between M_0 of the resonance of interest (P_i) with and without saturation [5]. Based on the results of the in vitro experiments, a similar β-series was performed in vivo to confirm the low power β-values obtained in vitro and also confirm good saturation of γ-ATP

in vivo. Therefore, the scheme M5D9 was examined between β = 1.2°–6.0° in +0.3° steps and the second scheme M3D12 was evaluated between β = 1.5°–2.3° in +0.4° steps and 2.3°–4.9° in +0.2° steps. Two control volunteers male volunteers (age 26.5 ± 3.5 years, BMI 25.7 ± 0.9 kg/m^2) underwent all measurements. Due to the long duration of this experiment, all experiments were performed with the shortest TR (TR 0.7 s) and NSA were limited to 512, which resulted in a measurement time of ~6 min per spectrum.

After evaluating the results, the protocol with the DANTE pulse train scheme that yielded the best outcome was applied together with the optimal β-value in both volunteers in a separate session to determine the Q-values of the chosen parameters. Here, spectra were acquired at mirrored saturation frequency with and without active saturation at TR 6 s, NSA 128, t_{exp} ~12.8 min.

Optimization of $T'_{1,Pi}$ determination

In order to determine the apparent spin-lattice relaxation time of P_i ($T'_{1,Pi}$), a saturation recovery experiment with 2D-localization and a range of different TRs was tested. Initial experiments showed that TR = 700 ms was the shortest successful TR for the DANTE saturation schemes and the following five TRs were applied and tested in 2 volunteers: TR 700, 1200, 1700, 2200 and 2700 ms with 1368, 840, 564, 496, 472 and 464 NSA (t_{exp} ~68 min), respectively. NSAs for each TR were adapted in order to keep SNR stable. Subsequently, it was tested to what extent data quality of $T'_{1,Pi}$ determination is compromised when only three of the five TRs are measured and which of the three TRs can best be chosen for reliable $T'_{1,Pi}$ determination.

Choice of TR for detecting the saturation effect

For assessment of the equilibrium ($M_{0,Pi}$) and apparent longitudinal magnetization of P_i ($M'_{0,Pi}$), a TR of 1.7 s was chosen based on reported values for $T'_{1,Pi}$ of 520 ms [6] or 580 ms [7] as well as $T_{1,Pi}$ of 730 ms [6] thereby keeping a good compromise between signal strength and measurement time. Because the expected difference in P_i amplitude (ΔM) between experiments is small (about 15%) [6] 768 NSA were acquired for each spectrum to achieve excellent SNR.

Supplemental material S3:

Extended MRI/S protocol parameters for FRiST

B_0 shimming

A three-dimensional (3D) isotropic fast field echo (FFE) was acquired during a single breath hold to acquire a B_0 map (field of view (FOV) 350 × 292 × 160 mm^3, acquisition voxel size 5 × 5 × 10 mm^3, reconstruction voxel size 2.43 × 2.43 × 10 mm^3, 16 transverse slices, t_{exp} 12 s).

Nonlocalized spectroscopy and calculation of frequency offsets for the FRiST experiment

Nonlocalized spectroscopy was applied with a 3.83 ms hyperbolic secant (HS) adiabatic half passage pulse for excitation (excitation bandwidth 1.63 kHz) TR 10 s, NSA 4, total acquisition time ~1 min, number of sample points (N) 512, spectral bandwidth (BW) 3 kHz, excitation pulse center ~1.0 ppm).

The unlocalized spectrum was used for determination of the individually frequencies of γ-ATP and P_i, in order to i) set the transmitter frequency of the successive ST experiments exactly in between both resonances, ii) calculate the participant specific frequency offset of the saturation pulse for the on-resonance experiments and iii) determine the frequency offset for the saturation pulse in case of the mirrored experiment.

FRiST experiment

All ST experiments were acquired using a 2D-localized image-selected in vivo spectroscopy (ISIS) [4] sequence with a 40 × 90 mm^2 voxel of interest (VOI) and a 3.83 ms HS adiabatic pulse for excitation (excitation bandwidth 1.63 kHz), N 512 and BW 3 kHz. The duration of the HS inversion pulse for slice selection was 3.9 ms, HS inversion bandwidth 3.18 kHz. The TRs and number of signal averages of the four acquired spectra were 0.7 s (TR_{short}), 1.7 s (TR_{center}), 1.7 s ($TR_{mirrored}$) and 2.7 s (TR_{long}) with 1024, 768, 768 and 548, respectively.

In order to determine k_f the FRiST method acquires 4 spectra. The partially saturated magnetization of P_i ($M'_{z,Pi}$) is measured at three different TRs: TR_{short}, TR_{center} and TR_{long} during continuous saturation of γ-ATP in order to calculate $T'_{1,Pi}$. As a fourth spectrum, $M_{0,Pi}$ is measured at TR_{center} in the presence of control irradiation applied at the mirrored frequency (further called mirrored spectrum). This compensates for possible spill over, originating from partially saturating the P_i resonance while aiming for the saturation of γ-ATP in the TR_{short}, TR_{center} and TR_{long} setup. From the difference in P_i amplitude between the spectrum with γ-ATP saturation and the spectrum with saturation at the mirrored frequency, the P_i exchange can be assessed.

The chemical shift between γ-ATP and P_i amounts ~7.7 ppm, resulting in a chemical shift displacement (CSD) of ~6.7 mm between these two metabolites. No respiratory triggering was used for the ST experiment. However, a sandbag was placed on the coil to restrict both coil and volunteer movement during the scans. 2D-localization was achieved by carefully placing a 40 × 90 × open mm^3 (AP,RL,FH) voxel of interest parallel to the coil in the transverse plane within the liver tissue, avoiding immediate proximity to the abdominal muscle (Supplemental Figure S1).

Supplemental material S4:

Data processing and quantification

Matlab script for processing of ST spectra

The script processes any number of spectra simultaneously and sorts them by their TR before fitting. All spectra were zero filled to 8192 points, apodized by a Gaussian filter of 18 Hz, frequency drift corrected, averaged and zero order phase optimized in the time domain by phasing spectra with the angle of the first complex data point. Hereby all spectra, independent of TR, were corrected with the overall mean phase angle. Subsequently, in total 13 resonances were fitted corresponding to all expected resonances in the obtained ^{31}P-MRS spectra. Briefly the following resonances were accounted for: α-, β-, γ-adenosine triphosphate (ATP), Glycero-phosphocholine (GPC), Glycero-phosphoethanolamine (GPE), inorganic phosphate (P_i), 2× nicotinamide adenine dinucleotide (NAD/NADH), Phosphocholine (PC), phosphocreatine (PCr), phosphoenolpyruvate/phosphatidylcholine (PEP/PtdC), Phosphoethanolamine (PE) and uridine diphosphate glucose (UDPG). PCr was included into the analysis to additionally account for potential contamination from abdominal muscles. All TR identical spectra were fitted with the same fitting model, incorporating T_2 estimates of resonances, J-coupling, and relative chemical shifts. A mix of Gaussian and Lorentzian line shapes was assumed and iteratively adjusted to match spectra. Furthermore, the fitting model takes the delay between excitation and acquisition of the FID into account and thereby fits the first order phase, making correction during post processing unnecessary.

Absolute quantification of P_i

^{31}P-spectra for absolute P_i quantification were processed using Java magnetic resonance user interface (jMRUI) software [8, 9] together with the advanced method for accurate, robust, and efficient spectral fitting (AMARES) [10, 11] algorithm and a custom created prior knowledge file was used for fitting as previously described [12].

Hepatic lipid content (HLC)

HL content was quantified as the ratio of intensities of the methylene (CH_2) peak in triglycerides at 1.3 ppm of liver ^{1}H-spectra to the combined signal intensities of the water and methylene peaks $HLC\ (\%) = \frac{S_{lipid}}{S_{lipid}+S_{water}}$. The difference in transverse relaxation times of water and lipid peaks was corrected based on a previous publication [13].

Supplemental material S5:

Theoretical background: Calculation of k_f

In order to calculate the pseudo-first order equilibrium forward rate constant (k_f) in human liver, a two-site model of chemical exchange between P_i and γ-ATP, as shown in equation 1, is typically assumed. Hepatic ATP is continuously synthesized from adenosine diphosphate (ADP) and P_i primarily in the mitochondria by oxidative phosphorylation, catalyzed by the enzyme ATP synthase:

$$ADP + P_i \underset{k_r}{\overset{k_f}{\rightleftharpoons}} ATP + H_2O \quad (1)$$

k_f and k_r represent the pseudo-first order equilibrium forward and reverse exchange rate constants, respectively.

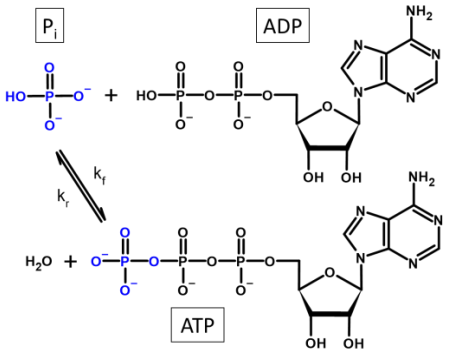

Schematic representation of adenosine triphosphate (ATP) synthesis. Adeonsine diphosphate (ADP) and inorganic phosphate (P_i) bind to ATP synthase, where they are joined to form ATP, releasing energy for cellular processes. k_f forward rate constant, k_r reverse rate constant.

During the ST experiment, the γ-ATP resonance is constantly saturated by frequency-selective irradiation, reducing the magnetization of γ-ATP to zero. Due to the chemical exchange described above, the equilibrium longitudinal magnetization of P_i is also reduced from its initial condition $M_{0,Pi}$ to $M'_{0,Pi}$ in presence of saturation. In addition, the spin-lattice relaxation time (T_1) of P_i also shifts from $T_{1,Pi}$ to an apparent $T'_{1,Pi}$ caused by chemical exchange of P_i with the saturated γ-ATP pool. From this, the longitudinal magnetization of P_i at an arbitrary time t during active saturation of γ-ATP, $M'_{Pi}(t)$, can be calculated by:

$$M'_{Pi}(t) = M'_{0,Pi} + \left(M'_{Pi}(t=0) - M'_{0,Pi}\right)e^{-\frac{t}{T'_{1,Pi}}} \quad (2)$$

$$\text{with } \frac{1}{T'_{1,Pi}} = \frac{1}{T_{1,Pi}^{intrinsic}} + k_f \text{ and } M'_{0,Pi} = \frac{M_{0,Pi}}{1 + T_{1,Pi}^{intrinsic} k_f} \quad (3)$$

In equation 3, $T_{1,Pi}^{intrinsic}$ denotes the intrinsic longitudinal relaxation time of P_i in case no exchange is present. From these formulas, one can deduce the reaction rate:

$$k_f = \frac{1}{T'_{1,Pi}}\left(1 - \frac{M'_{0,Pi}}{M_{0,Pi}}\right) \quad (4)$$

In summary, three variables are required to assess k_f: The apparent spin-lattice relaxation time of P_i ($T'_{1,Pi}$), the equilibrium ($M_{0,Pi}$) and apparent longitudinal magnetization of P_i ($M'_{0,Pi}$).

Supplemental Fig. S1:

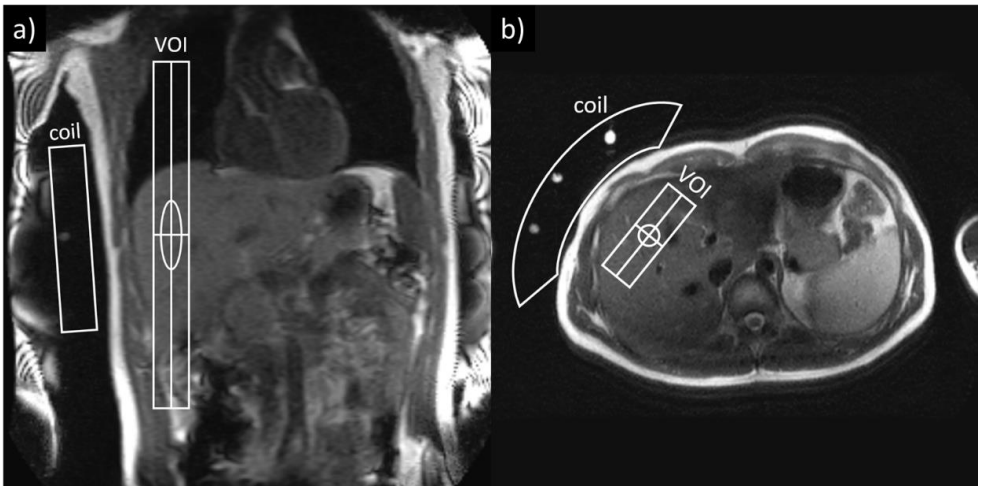

Supplemental Fig. S1: Planning of the FRiST protocol. a) Coronal and b) transverse MRI slices of the liver of a 30 years old control volunteer showing coil placement and position of the 2D-voxel of interest (VOI) (open in feet-head direction). White dots within the coil housing show position of reference spheres. *FRiST* Four Repetition time Saturation Transfer.

Supplemental Fig. S2:

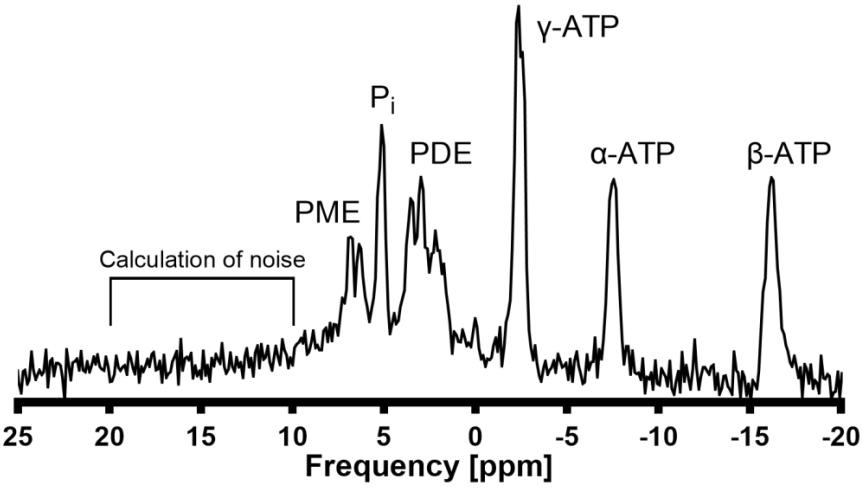

Supplemental Fig. S2: Representative raw hepatic phosphorus magnetic resonance spectroscopy spectrum. No postprocessing was performed except zero order phasing. The spectral region between 10 ppm and 20 ppm served to determine the noise for calculation of signal-to-noise for spectral quality assessment. *ATP* adenosine triphosphate, *PDE* phosphodiesters, P_i inorganic phosphate, *PME* phosphomonoesters.

Supplemental Fig. S3:

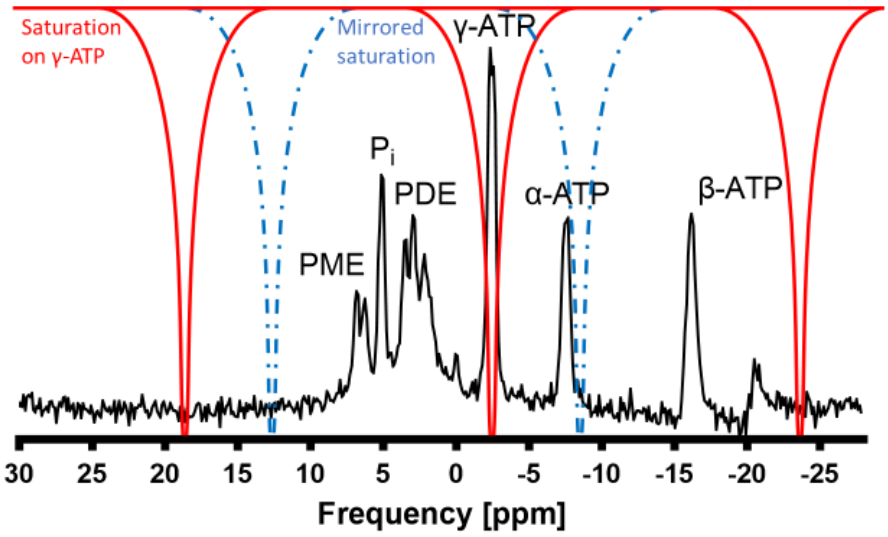

Supplemental Fig. S3: Position of the delays alternating with nutations for tailored excitation (DANTE) saturation bands with m = 3 saturation bands which were δ = 12 Hz (M3D12) apart on an entire hepatic phosphorus magnetic resonance spectroscopy spectrum. In the saturation experiment, the saturation pulse was centered on the γ-ATP resonance at ~-2.48 ppm (saturation bands displayed in red). Two aliased saturation bands (~-23.6 ppm and ~18.7 ppm) occur every ~21.2 ppm (1/τ = 1100 Hz) from the center of saturation frequency due to a DANTE subpulse duration of τ = 0.91 ms. In the mirrored experiment, the mirrored saturation frequency was set to ~12.7 ppm resulting in aliased saturation bands at ~33.82 ppm (not shown) and ~-8.5 ppm (blue dashed lines). Note that in the mirrored experiment α-ATP is partly affected by the aliased sideband resulting in a decreased signal amplitude. For better representation, the spectrum is apodized with a 5 Hz Gaussian filter.
ATP adenosine triphosphate, *PDE* phosphodiesters, P_i inorganic phosphate, *PME* phosphomonoesters.

Supplemental Table S1:

Supplemental Table S1: MRSinMRS checklist [14].

German Diabetes Center Düsseldorf 1. Hardware	^{31}P MRS ST	^{31}P MRS	^{1}H MRS
a. Field strength [T]	3T		
b. Manufacturer	Philips, Best, the Netherlands		
c. Model (software version if available)	Achieva 3T dStream, R5.6/R.5.7		
d. RF coils: nuclei (transmit/ receive), number of channels, type, body part	^{31}P curved quadrature surface coil, total loop size 220 × 160 mm^2, transmit & receive, Rapid Biomedical		Body coil, Philips, Best, the Netherlands
e. Additional hardware	-		
2. Acquisition			
a. Pulse sequence	Basic pulse sequence: Image Selected In Vivo Spectroscopy (ISIS), vendor supplied Research patch added implementation of frequency-selective DANTE saturation pulse trains		STimulated Echo Acquisition Mode (STEAM), vendor supplied
b. Volume of Interest (VOI) locations	Lateral side of liver		
c. Nominal VOI size	40 × 90 × 300 mm^3 (AP,RL,FH)	60 × 60 × 60 mm^3	25 × 25 × 25 mm^3
d. Repetition Time (TR), Echo Time (TE) [ms, s]	TR 700, 1700, 2700 ms, TE 0.096 ms	TR 6000 ms, TE 0.096 ms	TR 4000 ms, TE 10 ms
e. Total number of Excitations or acquisitions per spectrum	TR 700 ms: 1024 NSA TR 1700 ms: 768 NSA TR 2700 ms: 548 NSA	128 NSA	16 NSA for both non-water suppressed and water suppressed spectra
f. Additional sequence parameters	Bandwidth 3000 Hz Datapoints 512	Bandwidth 3000 Hz Datapoints 2048	Bandwidth 2000 Hz Datapoints 1024

Eur Radiol Exp (2025) Jonuscheit M, Korzekwa B, Schär M, et al.

(spectral width in Hz, number of spectral points, frequency offsets)	Excitation pulse center was set exactly in between γ-ATP and P_i Chemical shift displacement: γ-ATP ↔ Pi = ~7.7 ppm → ~6.7 mm	Broadband decoupling (WALTZ-4, B_1 ampl. 7 µT) Continuous wave NOE with mixing time 3500 ms, B_1 ampl. 0.5 µT Excitation pulse center was set to -1.0 ppm (between γ-ATP and P_i) Chemical shift displacement: γ-ATP ↔ Pi = ~7.7 ppm → ~6.7 mm	TM 16 ms Excitation pulse center was set to water frequency
g. Water Suppression Method	-		CHEmical Shift Selective saturation (CHESS)
h. Shimming Method, reference peak, and thresholds for “acceptance of shim” chosen	3D-FFE, 1 BH FOV 350 × 292 × 160 mm^3, acq. voxel size 5 × 5 × 10 mm^3, rec. voxel size 2.43 × 2.43 × 10 mm^3, 16 transverse slices	Vendor second order pencil beam VOI (shim size 60 × 60 × 60 mm^3) System reported FWHM between 20 and 45 Hz	Vendor second order pencil beam VOI (shim size 50 × 50 × 50 mm^3)
i. Triggering or motion correction method	-		
3. Data analysis methods and outputs			
a. Analysis software	Matlab	jMRUI	Matlab
b. Processing steps deviating from quoted reference or product	Gaussian apodization 18 Hz, zero filling to 8192 points, frequency drift corrected, zero order phase optimization	Gaussian apodization 15 Hz, frequency adjustment to γ-ATP = -2.48 ppm, zero order phasing	Gaussian apodization 15 Hz, zero filling to 4096 points, frequency adjustment to water = 4.7ppm or methylene = 1.3ppm

c. Output measure (e.g. absolute concentration, institutional units, ratio) Processing steps deviating from quoted reference or product	P_i amplitudes [a.u.]	Absolute units (millimolar [mM]) Correction for T_1, individual metabolite frequency offset, coil loading and distance in all three dimensions	Hepatic lipid content (HLC) [%]
d. Quantification references and assumptions, fitting model assumptions	13 resonances were fitted with a mix of Gaussian and Lorentzian line shapes incorporating T_2 estimates of resonances, J-coupling, relative chemical shifts	AMARES in jMRUI, custom created prior knowledge (Gaussian line shapes, estimated amplitudes, fixed relative phases, individual line width and chemical frequencies kept in soft constraints	22 resonances were fitted in the water spectrum and 23 in the water-suppressed spectrum with a mix of Gaussian and Lorentzian line shapes incorporating T_2 estimates of resonances, J-coupling, relative chemical shifts
4. Data Quality			
a. Reported variables (SNR, Linewidth (with reference peaks))	Good quality data: SNR (γ-ATP and P_i) Potential signal contamination from abdominal muscle: PCr/γ-ATP peak ratio Only for ST: Degree of γ-ATP saturation		-
b. Data exclusion criteria	SNR of γ-ATP and P_i: SNR: γ-ATP < 4 SNR: P_i < 2.5 Potential signal contamination from abdominal muscle: PCr/γ-ATP > 0.5	SNR of γ-ATP and P_i: SNR: γ-ATP < 4 SNR: P_i < 2.5 Potential signal contamination from abdominal muscle: PCr/γ-ATP > 0.5 Spectra were excluded for distances between coil and center of ISIS voxel > 13.5 cm	Malfunction of water-suppression
c. Quality measures of postprocessing Model fitting (e.g. CRLB,	-	-	-

goodness of fit, SD of residual)			
d. Sample Spectrum	Figure 4 & Figure 5	See 10.1002/nbm.5120	See 10.1038/s41467-020-15684-0

Supplemental Table S2:

Supplemental Table S2: 3TR versus 5TR. Results of apparent spin-lattice relaxation time ($T'_{1,Pi}$) fitting of a saturation experiment to find the best suited three repetition time (TR) set. Two control volunteers underwent a saturation recovery experiment consisting of five TRs. The experimentally determined $T'_{1,Pi}$ together with the calculated coefficient of determination (R^2) were compared to find the most accurate set of three TRs.

TR combination [ms]	Control volunteer #1		Control volunteer #2	
	$T'_{1,Pi}$ [ms]	R^2	$T'_{1,Pi}$ [ms]	R^2
700, 1200, 1700, 2200 & 2700	699	0.9962	432	0.9962
700, 1200 & 1700	598	0.9996	492	1
700, 1200 & 2200	743	0.9975	402	0.9978
700, 1200 & 2700	666	0.9989	455	0.9996
700, 1700 & 2200	693	0.9969	430	0.9964
700, 1700 & 2700	645	0.9993	465	0.9995
700, 2200 & 2700	665	0.9986	433	0.9982

Supplemental Table S3:

Supplemental Table S3: Calculated phosphorus-MR spectroscopy parameters for the subgroups of control volunteers and type 1 diabetes using ANOVA adjusted for age, sex and BMI.

	Control volunteers	Type 1 diabetes	*p*-value
Number	9	8	
$T'_{1,Pi}$ [ms]	488 [419; 557]	513 [437; 588]	0.640
ΔM [%]	16.0 [13.2; 18.8]	8.3 [5.3; 11.3]	0.003*
k_f [s^{-1}]	0.33 [0.26; 0.41]	0.18 [0.09; 0.26]	0.017*
F_{ATP} [mM/min]	35.4 [27.3; 43.4]	18.3 [9.6; 27.1]	0.014*

All values are reported as numbers of participants or mean [95% CI]. *$p < 0.05$ indicates statistical significance

ΔM Percentage difference in P_i amplitude between saturating and control irradiation, F_{ATP} Forward adenosine triphosphate synthesis rate, k_f Forward rate constant, *P_i* Inorganic phosphate, $T'_{1,Pi}$ Apparent spin-lattice relaxation time of P_i.

References

1. Szendroedi J, Saxena A, Weber KS et al (2016) Cohort profile: the German Diabetes Study (GDS). Cardiovasc Diabetol 15:59. https://doi.org/10.1186/s12933-016-0374-9
2. Schär M, El-Sharkawy A-MM, Weiss RG et al (2010) Triple repetition time saturation transfer (TRiST) ^{31}P spectroscopy for measuring human creatine kinase reaction kinetics. Magn Reson Med 63:1493–1501. https://doi.org/10.1002/mrm.22347
3. Eberhardt KW, Schär M, Barmet C et al (2006) Linear response equilibrium. J Magn Reson 178:142–154. https://doi.org/10.1016/j.jmr.2005.09.005
4. Ordidge R, Connelly A, Lohman J (1986) Image-selected in vivo spectroscopy (ISIS). A new technique for spatially selective NMR spectroscopy. J Magn Reson 66:283–294. https://doi.org/10.1016/0022-2364(86)90031-4
5. Bottomley PA, Ouwerkerk R, Lee RF et al (2002) Four-angle saturation transfer (FAST) method for measuring creatine kinase reaction rates in vivo. Magn Reson Med 47:850–863. https://doi.org/10.1002/mrm.10130
6. Schmid AI, Chmelík M, Szendroedi J et al (2008) Quantitative ATP synthesis in human liver measured by localized ^{31}P spectroscopy using the magnetization transfer experiment. NMR Biomed 21:437–443. https://doi.org/10.1002/nbm.1207
7. Buehler T, Kreis R, Boesch C (2015) Comparison of ^{31}P saturation and inversion magnetization transfer in human liver and skeletal muscle using a clinical MR system and surface coils. NMR Biomed 28:188–199. https://doi.org/10.1002/nbm.3242
8. Naressi A, Couturier C, Castang I et al (2001) Java-based graphical user interface for MRUI, a software package for quantitation of in vivo/medical magnetic resonance spectroscopy signals. Comput Biol Med 31:269–286. https://doi.org/10.1007/BF02668096
9. Stefan D, Di Cesare F, Andrasescu A et al (2009) Quantitation of magnetic resonance spectroscopy signals: the jMRUI software package. Meas Sci Technol 20:104035. https://doi.org/10.1088/0957-0233/20/10/104035
10. Mierisová Š, van den Boogaart A, Tkáč I et al (1998) New approach for quantitation of short echo time in vivo 1H MR spectra of brain using AMARES. NMR Biomed 11:32–39. https://doi.org/10.1002/(sici)1099-1492(199802)11:1<32:aid-nbm501>3.0.co;2-
11. Vanhamme L, van den Boogaart A, van Huffel S (1997) Improved method for accurate and efficient quantification of MRS data with use of prior knowledge. J Magn Reson 129:35–43. https://doi.org/10.1006/jmre.1997.1244
12. Jonuscheit M, Wierichs S, Rothe M et al (2024) Reproducibility of absolute quantification of adenosine triphosphate and inorganic phosphate in the liver with localized ^{31}P-magnetic resonance spectroscopy at 3-T using different coils. NMR Biomed 37:e5120. https://doi.org/10.1002/nbm.5120
13. Hamilton G, Yokoo T, Bydder M et al (2011) In vivo characterization of the liver fat ^{1}H MR spectrum. NMR Biomed 24:784–790. https://doi.org/10.1002/nbm.1622
14. Lin A, Andronesi O, Bogner W et al (2021) Minimum reporting standards for in vivo magnetic resonance spectroscopy (MRSinMRS): experts' consensus recommendations. NMR Biomed 34:e4484. https://doi.org/10.1002/nbm.4484

Publications

The doctoral thesis at hand is based on:

Study 1:

M. Jonuscheit, S. Wierichs, M. Rothe, B. Korzekwa, J. Mevenkamp, P. Bobrov, Y. Kupriyanova, M. Roden and V. B. Schrauwen-Hinderling.

Reproducibility of absolute quantification of adenosine triphosphate and inorganic phosphate in the liver with localized 31P-magnetic resonance spectroscopy at 3-T using different coils.

Published in: *NMR in Biomedicine* 2024 Aug;37(8):e5120.

DOI: 10.1002/nbm.5120.

Reprint from NMR in Biomedicine can be found in chapter 5. The original paper is available online at https://analyticalsciencejournals.onlinelibrary.wiley.com/doi/10.1002/nbm.5120. John Wiley and Sons granted the permission of reprint to the author.

Journal Impact Factor 2023: 2.7

Personal contribution: 80% (Conceptualization, formal analysis, investigation, methodology, software, validation, visualization, writing the original draft of the manuscript).

Study 2:

M. Jonuscheit, B. Korzekwa, M. Schär, J. Mevenkamp, S. Wierichs, P. Bobrov, T. Sarabhai , S. Kahl, M. Roden, V. B. Schrauwen-Hinderling

31P-MRS saturation transfer for assessing human hepatic ATP synthesis at clinical field strength.

Published in: *European Radiology Experimental* 2025 May;13;9(1):51.

DOI: 10.1186/s41747-025-00588-9.

Reprint from European Radiology Experimental can be found in chapter 6. The original paper is available online at https://eurradiolexp.springeropen.com/articles/10.1186/s41747-025-00588-9. This is an open access article distributed under the terms of the Creative Commons CC BY license by Springer Nature, permitting unrestricted use for reproduction.

Journal Impact Factor 2023: 3.7

Personal contribution: 80% (Conceptualization, formal analysis, investigation, methodology, software, validation, visualization, writing the original draft of the manuscript).

Co-author Publications

The methods described in this thesis were also applied in other publications:

- Sarabhai T, Mastrototaro L, Kahl S, Bönhof GJ, Jonuscheit M, Bobrov P, Katsuyama H, Guthoff R, Wolkersdorfer M, Herder C, Meuth SG, Dreyer S, and Roden M, "Hyperbaric oxygen rapidly improves tissue-specific insulin sensitivity and mitochondrial capacity in humans with type 2 diabetes: A randomised placebo-controlled crossover trial," *Diabetologia*, vol. 66, no. 1, p. 57-69, 2023. doi:10.1007/s00125-022-05797-0
- Kupriyanova Y, Yurchenko I, Bobrov P, Bartels F, Wierichs S, Jonuscheit M, Korzekwa B, Prystupa K, Schön M, Mendez D, Trenkamp S, Burkart V, Wagner R, Schrauwen-Hinderling V, and Roden M, "Alterations of hepatic lipid content following COVID-19 in persons with type 2 diabetes," *BMJ Open Diabetes Research & Care*, vol. 13, no. 1, p. e004727, 2025. doi:10.1136/bmjdrc-2024-004727

List of Figures

2.1 (a) Quantized precession cone for ^{1}H- and ^{31}P-spins. (b) Single spin precessing at angle θ to $\boldsymbol{B_0}$. . . . 8
2.2 (a) $\triangle E \propto B_0$ for spin $I = 1/2$ nuclei. (b) Spin population distribution across Zeeman levels. . . . 10
2.3 Range of ^{31}P-chemical shifts. . . . 16
2.4 Structural formula and ^{31}P-MRS spectrum of ATP in a solution. . . . 18
2.5 NOE effects on energy levels and populations in a dipolar-coupled ^{1}H–^{31}P two-spin system. . . . 21
2.6 FID signal and Fourier transformed spectrum of a single frequency and a mixture of frequencies. . . . 23
2.7 k-space data image reconstruction. . . . 26
2.8 Pulse shapes and slice profiles of common RF pulses. . . . 32
2.9 Volume selection using static magnetic field gradients. . . . 33
2.10 Pulse sequence diagrams for STEAM and ISIS. . . . 35
2.11 Overview of the different calibration methods for estimation of metabolite concentrations. . . . 39
2.12 $\boldsymbol{B_1}$ excitation pulse offset correction for eight ^{31}P-metabolites. . . . 41
2.13 Spatial $\boldsymbol{B_1}$ excitation profiles of two different surface coils. . . . 42
2.14 $\boldsymbol{B_1}$ excitation pulse correction for VOI placement using surface coil sensitivity profiles. . . . 43
2.15 DANTE saturation bands for hepatic ATP synthesis rate detection. . . . 47

3.1 Frontal view of the human liver. . . . 50
3.2 Representative localized ^{1}H-MRS spectra of the human liver (a) without and (b) with water-suppression at 3 T. . . . 58
3.3 Representative ^{31}P-MRS spectrum of the human liver at 3 T. . . . 60

List of Tables

2.1 Key nuclear properties of isotopes commonly used for in-vivo NMR spectroscopy. 7
2.2 Experimental ISIS cycle diagram. 36
2.3 T_1 relaxation times of ^{31}P-metabolites at 3 T in the human liver. 43

3.1 Peak identification and chemical shift values for hepatic triglycerides in the ^{1}H-MRS spectrum. 57
3.2 Peak identification and chemical shift values for hepatic metabolites in the ^{31}P-MRS spectrum. 61